Title
STUDIES OF NONLINEAR AND CHAOTIC PHENOMENA IN SOLID STATE SYSTEMS

Author
Bryant, P.H.

Publication Date
1987-09-01

Lawrence Berkeley Laboratory
UNIVERSITY OF CALIFORNIA

Materials & Chemical Sciences Division

Studies of Nonlinear and Chaotic Phenomena in Solid State Systems

P.H. Bryant
(Ph.D. Thesis)

September 1987

Prepared for the U.S. Department of Energy under Contract DE-AC03-76SF00098

DISCLAIMER

LBL-23975

Studies of Nonlinear and Chaotic Phenomena in Solid State Systems

Paul Henry Bryant

Ph.D. Thesis

September 1987

Materials and Chemical Sciences Division
Lawrence Berkeley Laboratory
Berkeley, CA 94720

and

Department of Physics
University of California
Berkeley, CA 94720

This work was supported by the Director, Office of Energy Research, Office of Basic Energy Sciences, Materials Sciences Division of the U.S. Department of Energy under Contract No. DE-AC03-76SF00098.

Studies of Nonlinear and Chaotic Phenomena in Solid State Systems

Paul Henry Bryant

To Gayle,

Verity, Charles, and Elayna

CONTENTS

PREFACE

During my graduate study at Berkeley, I focussed on the study of nonlinear phenomena occurring in solid state systems. This led me to work on a number of problems, all linked by this common theme. The three most significant of these projects have been combined to form this thesis. These are given as three parts, each of which is self contained and may be read independently of the other parts. Each part has its own introduction, conclusion, and references. The first part concerns itself with the dynamics of spin waves excited by microwaves in a sphere of yttrium iron garnet. This study yielded a variety of interesting experimental results which were then analyzed both analytically and by numerical integration of the equations of motion. The second part is a study of the dynamics of a forced magnetic oscillator. The system here is a toroidal magnetic core which displays the nonlinear effects of magnetic saturation and hysteresis. It is excited by a winding connected to a linear external circuit driven by a signal generator. This system was primarily developed to study a number of nonlinear phenomena in an experimental system - particularly resonance effects related to the emergence of a second frequency in the dynamics. The third part is concerned with a practical problem – an anomalous "noise rise" that was observed to occur in Josephson Junction parametric amplifiers. A theory is presented which offers an explanation for this effect. The theory is based on a "dynamical systems" approach to the problem, the results of which may be applied to a broad class of similar systems.

Berkeley 1987 Paul Bryant

ACKNOWLEDGEMENTS

I would first of all like to thank my wife Gayle for her support and encouragement during my graduate studies and also for typing the first part of this thesis.

I am very grateful for the guidance and encouragement of my research advisor Professor Carson Jeffries.

I would like to thank Professors John Clarke and Shyh Wang for being on my thesis committee.

I would like to thank Professor Katsuhiro Nakamura who collaborated on the spin wave research (part 1 of this thesis), and also Professor Harry Suhl, Xinyun Zhang, and Joe Smyth for their comments on this work.

I would like to thank Jim Swift for his helpful comments on the magnetic oscillator research (part 2 of this thesis).

I would like to thank Kurt Wiesenfeld and Bruce McNamara who collaborated on the noise rise research (part 3 of this thesis), and also Professors John Clarke, Marc Feldman, and Paul Richards for their comments on this research.

Finally I would like to thank Jim Crutchfield for setting up our group's computer system and developing the graphics programs which were used to make many of the figures in parts one and three of this thesis.

ABSTRACT

This work consists of three parts. These are linked by the common theme of nonlinear phenomena in solid state systems, but are otherwise independent and self contained.

Part 1: In this part an experimental study is made of the interactions between spin wave modes excited in a sphere of yttrium iron garnet by pumping the Suhl subsidiary absorption at 9.2 GHz with the dc field parallel to [111]. The dynamical behavior of the magnetization is observed under high resolution by varying two control parameters, dc field ($580 < H < 2100$ Oe) and microwave pump power ($1 < P < 200$ mW). Within this parameter space quite varied behavior is found: (i) onset of the Suhl instability by excitation of a single spin wave mode with very narrow linewidth (< 0.5 G); (ii) when two or more modes are excited, interactions lead to auto-oscillations with a systematic dependence of frequency (10^4 to 10^6 Hz) on pump power, these oscillations displaying period-doubling to chaos; (iii) quasiperiodicity, locking, and chaos occur when three or more modes are excited; (iv) abrupt transition to wide band power spectra (i.e., turbulence), with hysteresis; (v) irregular relaxation oscillations and aperiodic spiking behavior. A theoretical model is developed from first principles, using the plane wave approximation and including anisotropy effects, obtaining the lowest order non-linear interaction terms between the excited modes. Extension of this analysis to the true spherical spin-modes is discussed. Bifurcation behavior is examined, and dynamical behavior is numerically computed and compared to the experimental data, explaining a number of features. A theory is developed regarding the nature of the experimentally observed relaxation oscillations and spiking behavior based on the interaction of "weak" and "strong" modes, and this is demonstrated in the numerical simulations for two modes. Quasiperiodicity is shown to occur in the numerical study when at least 3 modes are excited with appropriate parameter values. A

possible mechanism for generating microwave subharmonics at half of the pumping frequency is discussed.

Part 2: This is an experimental study of a forced symmetric oscillator containing a saturable inductor with magnetic hysteresis. It displays a Hopf bifurcation to quasiperiodicity, entrainment horns, and chaos. The bifurcations and hysteresis occurring near points of resonance (particularly "strong resonance") are studied in detail and it is shown how the observed behavior can be understood using Arnold's theory. Much of the behavior relating to the entrainment horns is explored: period doubling and symmetry breaking bifurcations; homoclinic bifurcations; and crises and other bifurcations taking place at the horn boundaries. Important features of the behavior related to symmetry properties of the oscillator are studied and explained through the concept of a half-cycle map. The system is shown to exhibit a Hopf bifurcation from a phase-locked state to periodic "islands," similar to those found in Hamiltonian systems. An initialization technique is used to observe the manifolds of saddle orbits and other hidden structure. An unusual differential equation model is developed which is irreversible and generates a noninvertible Poincare map of the plane. Noninvertibility of this planar map has important effects on the behavior observed. The Poincare map may also be approximated through experimental measurements, resulting in a planar map with parameter dependence. This model gives good correspondence with the system in a region of the parameter space.

Part 3: This part takes a new look at an old problem, namely the observed "noise rise" in superconducting Josephson junction parametric amplifiers. By exploiting recent insights from dynamical systems theory, it is shown how the interplay of random noise and (nonchaotic) deterministic dynamics can result in a noise rise like that observed in experiments. This analysis leads to a *universal* first order equation which applies to all similar systems in the high-gain regime. several predictions are proposed which can be tested experimentally, including that a similar noise rise should occur in modulated semiconductor injection lasers. An

analysis is also made of a previously unknown mode of operation – a "six-photon" mode associated with a symmetry breaking bifurcation – and its potential advantages over the previously studied three-photon and four-photon modes are discussed.

PART 1:

SPIN WAVE DYNAMICS IN YIG SPHERES

1 INTRODUCTION

This part is concerned with the dynamics of interacting spin wave modes in single crystal spherical samples of YIG (yttrium iron garnet: $Y_3Fe_5O_{12}$), which is ferrimagnetic. Although the existence of spin waves has been known for some time, the recent emergence of interest in dynamical systems theory has warranted making a detailed study of the many phenomena that can arise from the nonlinear interaction of excited spin waves. In order to orient the reader, we will start with a discussion of spin waves and how they may be excited.

When ferro- or ferri- magnetic materials are placed in a strong d.c. magnetic field H_0, excited states exist which involve an ordered precession of the spins about the axis of the applied field. The simplest of these is the uniform or Kittel mode,[1] in which all of the spins process in phase, as shown in Fig. 1(a). This mode can be excited not only by thermal excitation, but directly by applying a microwave field **h** transverse to the d.c. field at the precession frequency. In addition to this mode there are spin wave modes in which there is a periodic variation of the precessional phase across the sample as shown in Fig. 1(b). The quanta of these excitations are called magnons. In many cases useful information and insight into the behavior of spin waves may be obtained by studying Bloch spin waves in which the medium is approximated as infinite and the spatial variation takes the form of $e^{i\mathbf{k}\cdot\mathbf{r}}$. Naturally, to make correspondence to a spin wave resonance in a finite sample we will assume a "standing spin wave" is

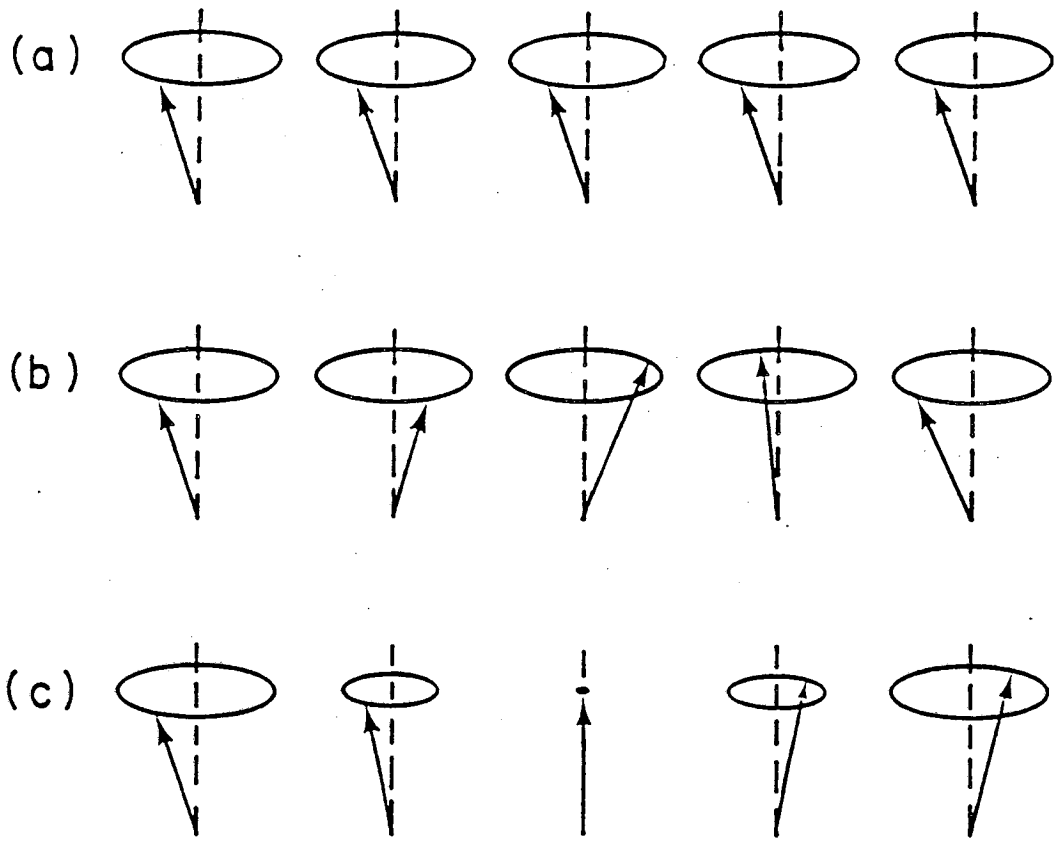

Figure 1. (a) Spins in uniform precession. (b) Spins in a traveling wave. (c) Spins in a standing wave.

formed by combination of a k and –k magnon. Such a spin wave is shown in Fig. 1(c).

Although full theoretical details are given in Sec. 3, it is useful to introduce now a few equations. For a spherical sample the frequency of the uniform precession is (ignoring effects of crystalline anisotropy):

$$\omega_0 = \gamma H_0 \tag{1}$$

where γ, the gyromagnetic ratio, is approximately 1.76×10^7 $G^{-1}sec^{-1}$. The basic dispersion relation for spin waves in a ferromagnetic sphere is (again neglecting anisotropy):[2]

$$\omega_k^2 = (\gamma H_0 - \frac{1}{3}\omega_m + \gamma D k^2)(\gamma H_0 - \frac{1}{3}\omega_m + \gamma D k^2 + \omega_m \sin^2\theta_k) \tag{2}$$

for spin waves of frequency ω_k, wavevector k, and azimuthal angle θ_k of k relative to H_0. Here M_s is the saturation magnetization of the material, $4\pi M_s \simeq 1750$ G for YIG, $\omega_m = \gamma 4\pi M_s$, and D, the exchange constant, is approximately 5.4×10^{-9} Gcm^2 for YIG. These equations follow from the more general expressions derived in Sec. 3.1 – see Eqs. (59), (48) and (49). In Fig. 2 we show a typical dispersion curve for spin waves in YIG sphere. The frequency depends not only on the magnitude of k but also on its azimuthal angle θ_k. There is also a slight dependence on polar angle ϕ_k resulting from anisotropy effects not included in Eq. (2) or Fig. 2.

Excitation of a spin wave mode may be accomplished in a variety of ways. On the quantum mechanical level, these include various scattering processes of magnons with other magnons and with other types of excitations e.g. photons and phonons. On the classical level, these correspond to various nonlinear mode couplings. Low wave number modes may couple directly to a nonuniform microwave magnetic field. This effect produces a series of diminishing peaks (Walker modes[3-11]) near the main resonance. Spin waves of all wave numbers may be excited parametrically, through nonlinear coupling with the uniform mode or other spin wave modes. In such cases Suhl[12-14,2] showed that excitation of spin waves by this means can only occur when the driving field exceeds a certain threshold (now called the Suhl threshold) beyond which the power coupled into the mode parametrically is in excess of that lost due to damping. This analysis was able to explain two important experimental observations: 1) The subsidiary resonance absorption and 2) premature saturation of the main resonance, effects which were first observed by Bloembergen and Wang[15] and by Damon.[16] The subsidiary resonance results from the first order Suhl instability. Here the pump frequency ω_p is roughly double the uniform resonance ω_0, and consequently this mode is excited very weakly. However,

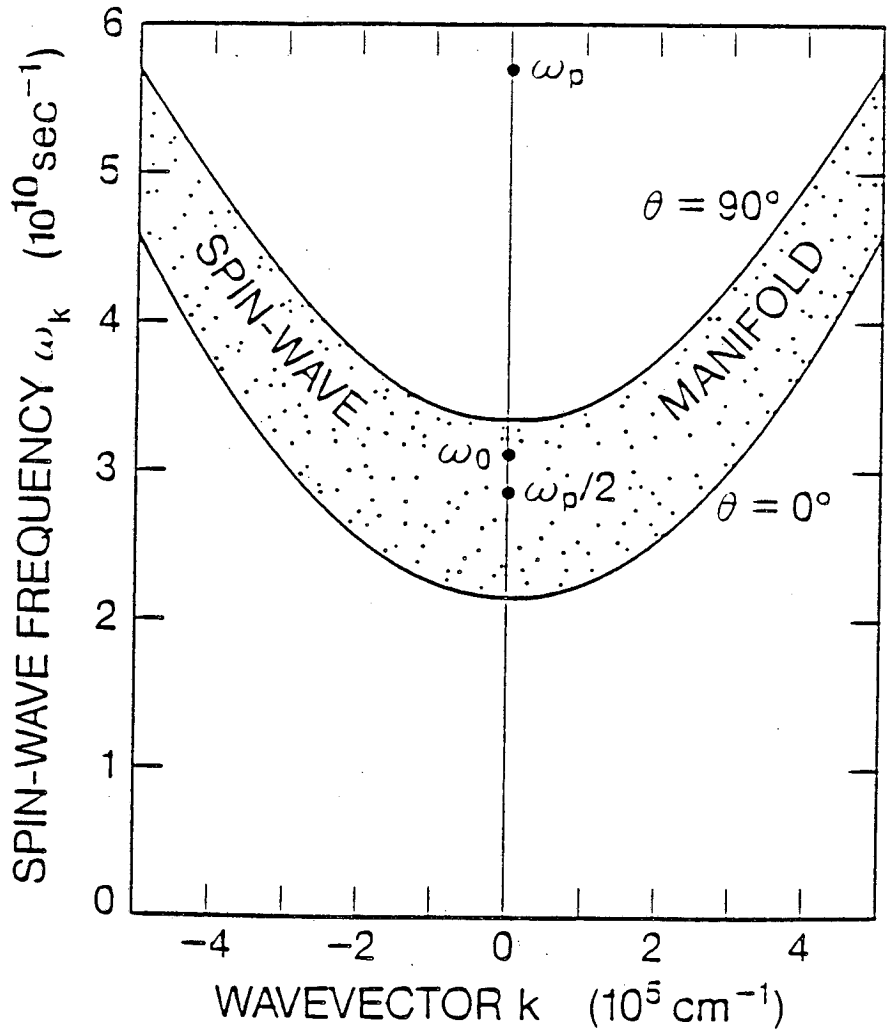

Figure 2. Dispersion diagram ω_k vs. **k** for YIG sphere. θ_k is the azimuthal angle of **k** with respect to the d.c. magnetic field. Obtained from Eq. (2) for $H_0 = 1700$ G.

when there are spin wave modes whose frequency is very close to $\omega_p/2$ (typically within $\pm 10^{-5}\omega_p$) then these modes can absorb power parametrically from the uniform mode and build up to a large amplitude. Since the spin wave modes occur over a wide range of frequency the subsidiary absorption peak is very broad, and under certain circumstances can even extend past

the uniform resonance.[17] In premature saturation, one observes a second order Suhl instability. One drives the resonance for the uniform mode, which is strongly excited, and couples parametrically to spin wave modes at very nearly the same frequency. This coupling is of higher order than for the subsidiary resonance, but this is compensated for by the much higher amplitude of the uniform mode. The term "premature saturation" comes from the fact that the Suhl threshold occurs at a significantly lower microwave power (several orders of magnitude) than that required to saturate the uniform mode in the absence of spin waves. Above the threshold the effective damping of the uniform mode increases dramatically due to the large number of accessible spin wave modes.

There is one additional means of coupling to the spin wave modes, that is generally referred to as "parallel pumping". Like the Walker modes discussed earlier, this is a direct coupling between the spin waves and the external field. Unlike them, however, this is a parametric coupling, and the frequency of the spin waves must be very close to $\omega_p/2$ (as for the subsidiary case). This process was first proposed (independently) by Morgenthaler,[18] Schlömann, Green and Milano,[19] and Kaganov and Tsukernik.[20] It results from the fact that standing spin wave modes (made up of k and –k magnons) exhibit elliptical procession orbits when k is not parallel to the d.c. field. The ellipticity results from the volume (as opposed to surface) demagnetizing field. Elliptic orbits have a nonconstant z component of magnetization which oscillates a frequency $2\omega_k$ and thus can couple to ω_p. The parallel pumping absorption is very broad and is found in the same frequency region as the subsidiary absorption.

Although these instabilities were extensively studied earlier (see Damon[21] and Zakharov[22] for review), no clear evidence of low dimensional chaotic motion was reported. Nakamura et al.[23, 24] and Ohta and Nakamura[25] re-examined the theory for parallel pumping, numerically iterated the equations of motion assuming two modes, and found onset of instability, collective oscillations, and a period doubling cascade to chaos, with a Henon-like return map. Gibson and Jeffries[26] observed a period doubling route to chaos, periodic windows, and a

single-hump return map for the second order instability in YIG. Zhang and Suhl[27] iterated the original equations for this instability and found a period doubling cascade to chaos. Similar theoretical conclusions were reported by Rezende et al.;[28] and de Aguiar and Rezende[29] reported theory and experiments on parallel pumping.

In this thesis is reported a detailed experimental study of the subsidiary absorption instability in a YIG sphere, along with a theoretical interpretation of these results. Above the threshold one or more spin wave modes may become excited and these modes may interact with each other nonlinearly, resulting in a variety of interesting phenomena. Some new effects discussed in the present work include:

1) The regions and boundaries of behavior are found in a high resolution parameter space diagram.

2) Fine structure is observed in the parameter space. Previous studies focused on the dynamics that occur when large numbers of spin wave modes are simultaneously excited. However, under appropriate conditions excitations can be limited to a few (1, 2, 3,...) very closely spaced modes. With two modes phenomena include low frequency (typically $10^{-5}\omega_p$) auto-oscillations exhibiting period doubling and chaos, aperiodic relaxation oscillations and aperiodic spiking. With three modes, quasiperiodicity (two incommensurate auto-oscillation frequencies) quasiperiodic route to chaos, and various aperiodic and chaotic orbits.

3) Hysteresis is found at the Suhl threshold.

4) Transitions to a wideband noisy state is found corresponding to hyper-chaos or turbulence.

5) An approximate relationship between the auto-oscillation frequency and forcing amplitude, is found

Although the primary focus in this study is on the subsidiary resonance, some additional data is given for parallel pumping. YIG has some asymmetry and unless specified otherwise,

data is with the d.c. field along the [111] or easy axis of the crystal.

2 EXPERIMENT

2.1 Experimental Setup

The basic experimental arrangement is shown in Fig. 3. Microwave power of 200mW at 9.2GHz is supplied by a klystron tube (this can be mechanically tuned from 8 to 12GHz). This is coupled via x-band wave guide (3cm) to a precision attenuator. The microwaves enter port 1 of a 3-port circulator and exit through port 2 to the sample. Microwave power reflected by the sample returns by the same wave guide entering port 2 of the circulator, from which it is directed through port 3 to a tunable video crystal detector which is sensitive to changes in microwave power from dc to frequencies of several megahertz. The sample is mounted in a loop gap resonator[30] located approximately 1 cm from an adjustable sliding short at the end of the wave guide. The loaded resonator, shown in Fig. 4, is designed to resonate at the klystron frequency. Adjustment of the resonator frequency is accomplished by either changing the gap thickness or by inserting some dielectric material into the gap. The resonator is brass, plated with silver to improve the Q ($Q \approx 500$). The resonator has a significant advantage over a T_{102} cavity – it can produce a larger microwave h field (5 Gauss compared to 0.25 Gauss at 100mW) while providing a broader resonance. The system is fine tuned by adjusting the klystron frequency to the resonator. One can achieve near perfect coupling between the wave guide and the resonator by adjustment of the sliding short. Input microwave power P_{in} to the resonator is measured with a power meter attached to a 20 dB cross guide coupler. A balancing reference arm is attached to the detector via an attenuator and phase shifter. This is particularly useful for locating the Suhl threshold. One first nulls the detector output by adjusting the attenuator and

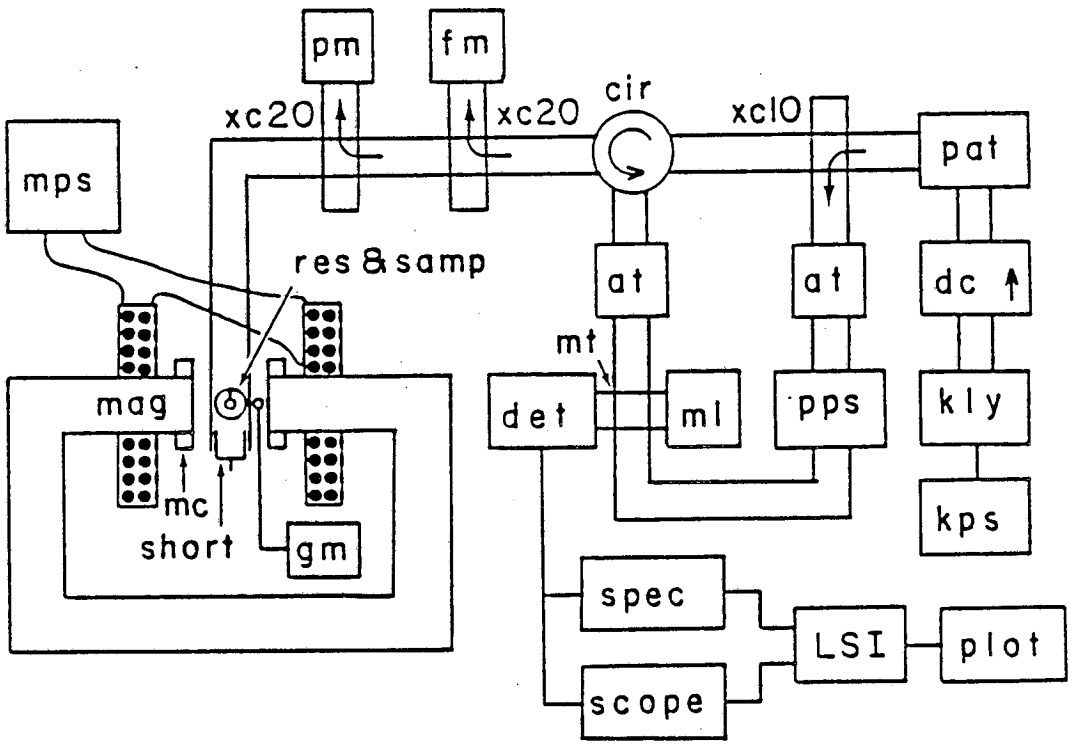

Figure 3. Diagram of the experimental setup. Notation: at = variable attenuator, cir = circulator, (microwaves entering port 1 exit port 2; microwaves entering port 2 exit port 3), dc = directional coupler (absorbs microwaves traveling opposite to arrow), det = tunable video crystal detector (type 1N23B), fm = frequency meter (HP model 2590B microwave frequency converter connected to 5245L electronic counter with 5253B plug-in), gm = Gauss meter, kly = klystron (Varian V-58), kps = klystron power supply (FXR model Z815B), LSI = LSI-11 computer, mag = electromagnet 0 to 19 kG, mc = modulation coils for magnet, ml = matched load, mps = magnet power supply (Harvey-Wells model HSR-1365B), mt = 4 arm magic T, res & samp = resonator and sample (see Fig. 4), pat = precision 0 to 50 dB attenuator (HP model X382A), plot = digitally controlled x-y plotter (HP model 7470A), pm = power meter (HP 431C), pps = precision phase shifter (HP model X885A), scope = digital storage ocilloscope (Tektronics 468), short = adjustable sliding short at end of waveguide, spec = spectrum analyzer 0 to 40 MHz (HP model 3585A), xc10 = 10dB crossguide coupler (10% of power follows arrow while remainder passes straight through), xc20 = 20dB crossguide coupler (1% of power follows arrow while remainder passes straight through).

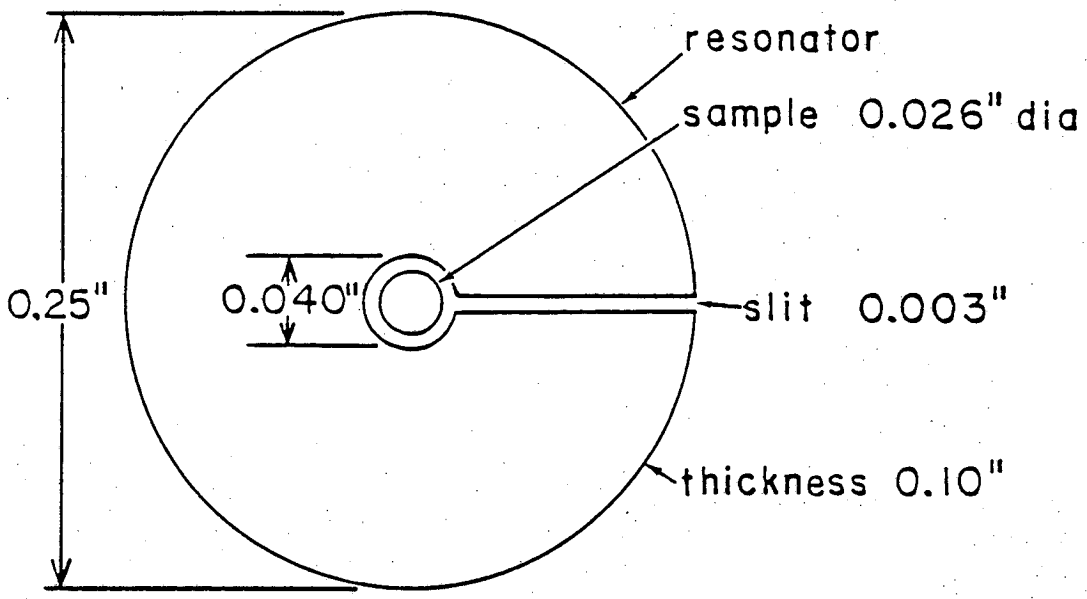

Figure 4. Loop-gap resonator with sample. Dimensions in inches.

phase shifter in the reference arm, at some point well below threshold. When power is increased by adjusting the precision attenuator (pat) the detector output remains zero until threshold is reached. Beyond this point the detector response increases abruptly due to the increasing level of the effective damping resulting from spin wave excitation. The sample is centered on a large precision electromagnet with field stability of better than 0.1G. The magnet can be rotated about the wave guide allowing one to vary the angle θ_R between $\mathbf{H}_0$ and $\mathbf{h}$, thereby choosing perpendicular, parallel or oblique pumping angles with a resolution of better than 1 degree. The sample itself may be rotated about the axis of the resonator to sample angle θ_S – also with better than 1 degree resolution.

A variety of parameters may be varied to study the behavior. Most frequently, the d.c. magnetic field H_0 and the applied microwave power P are adjusted to produce a two

dimensional parameter space plot. Other parameters, usually kept fixed, include: microwave frequency ω_p (typically 9.2GHz), the position of the sliding short which controls the coupling between the wave guide and the resonator, the rotation angles θ_R and θ_S, the resonant frequency ω_R of the resonator, and the temperature of the sample (unregulated unless stated otherwise – roughly 300K at low power but increasing significantly at full input power of 150mW.)

Efforts have been made to minimize noise, but some remains and limits the ultimate resolution of various dynamical phenomena such as high order phase locking and period doubling cascades. Sources include: intrinsic klystron noise, thermal magnons in the sample, klystron power supply noise (60 Hz and broadband), magnet power supply noise, temperature fluctuations effecting the klystron and the sample, crystal detector noise, and microphonics.

2.2 Sample Description and Properties of YIG

The sample used is a sphere of pure YIG (yttrium iron garnet) having a radius of 0.033 cm. It is a spherical to within $\Delta R/R = 6\times10^{-5}$ and highly polished, to within 0.15μm.

In order to orient the crystalline axes of the sample we plot the resonance field H_0 of the uniform mode as a function of sample angle θ_S as shown in Fig. 5. By adjusting the magnet angle as well, one can easily find the [111] directions (absolute minima for the resonant field strength) and the [100] directions (absolute maxima). The 8 [111] directions are the "easy axes" for YIG – if left free to rotate in a strong field the sample will tend to align itself with a [111] axis parallel to the field; also, the anisotropy energy is a minimum when the magnetization is aligned with [111]. By contrast, the 6 [100] directions are "hard axes" or direction of unstable equilibrium, and the 12 [110] directions are "saddle axes", i.e., they are saddle points for the anisotropy energy.

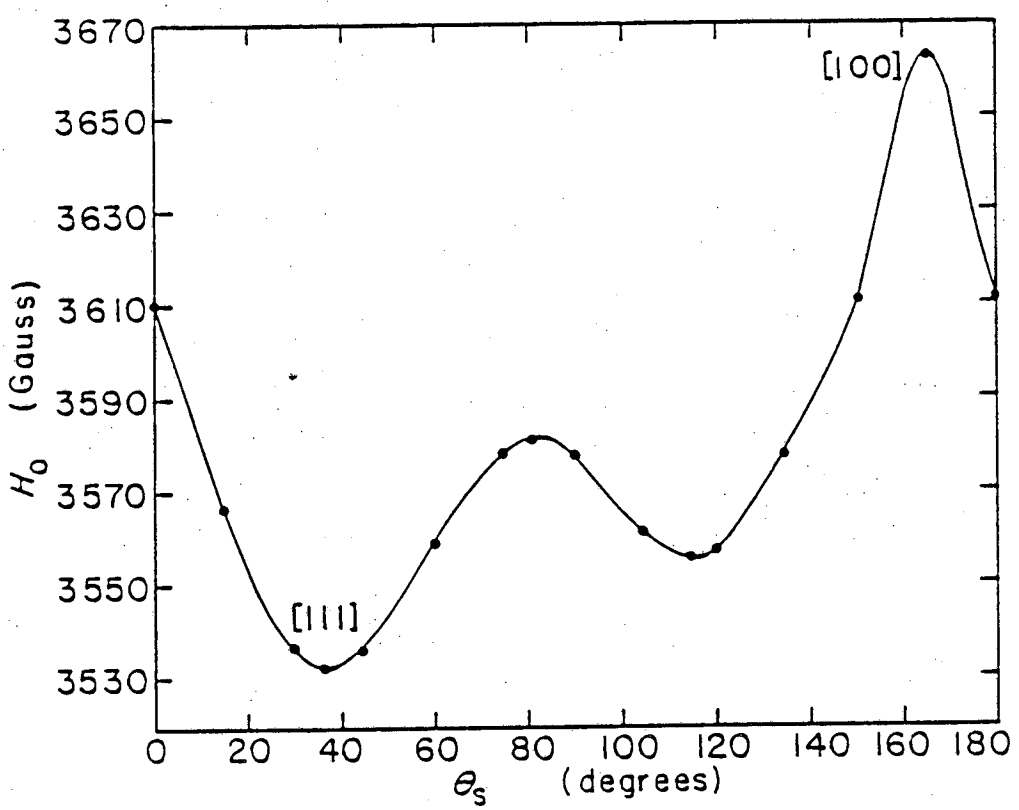

Figure 5. Field for uniform resonance as a function of sample angle θ_S. Axis of rotation is roughly [110]. Minimum occurs for [111] parallel to d.c. field H_0, maximum occurs for [100]. Relative maximum at 80° is [110]. If rotation axis was precisely [110] both minima in the figure would be the same. By rotating the magnet angle θ_R as well, the location of the axes may be determined precisely. The first minimum is within 5° of a [111] axis and is the orientation used in the experiment unless stated otherwise.

Yttrium iron garnet has the chemical formula $Y_3Fe_5O_{12}$. The name garnet was originally given to certain silicates found to occur naturally (although usually in impure form). The

general formula for such garnets is $\{A_3^{2+}\}[B_2^{3+}](Si_3)O_{12}$, where the A and B can be any of a number elements, e.g., $\{Ca_3^{2+}\}[Cl_2^{3+}](Si_3)O_{12}$ is a commonly occurring form. The brackets represent locations at different sites:{ } = c–site, [ ] = a–site, ( ) = d–site and no brackets = h–site in the space group $Ia3d(O_h^{10})$ – see Geller.[31] The only cations on symmetry centers are those on the a–sites. The a–sites form a BCC lattice, however a full unit cube for a garnet has a side twice the length of the a–site lattice and contains 8 formula units. Each d–site ion is tetrahedrally bonded to four oxygen atoms, and each a–site ion is octahedrally surrounded by 6 oxygens.

The iron garnets have the general form $\{A_3\}[Fe_2](Fe_3)O_{12}$, where A can be Y^{3+} or any of a number of rare earth ions. Note that iron ions fill both the a– and the d–sites. YIG is an ideal Neel ferrimagnet. The a– and d–site ions have opposite spin polarization because of a super exchange interaction through the intervening O^{2-} ions. This produces a negative a–d exchange field: $B_a \approx -1.5\times10^4 M_d$. These ferric ions have S=5/2 and L=0, hence there is a net magnetization of $5\mu_B$ per formula unit or $40\mu_B$ per unit cell at zero Kelvin. The lattice constant is 12.376 Angstroms (at room temperature) and from this we can calculate the saturation magnetization per unit volume: $4\pi M_s = 2459$G. The magnetization falls with temperature however, dropping to 3.65 μ_B per formula unit at 300K.[32] This lowers $4\pi M_s$ to 1795G. The sample used in this thesis is specified to have $4\pi M_s = 1750\pm50$G at room temperature. At still higher temperatures the saturation magnetization continues to decline, going to zero at the Curie temperature of 559K.

Technically, the presence of a spontaneous magnetization implies that YIG cannot have perfect cubic symmetry. The fact that its easy axis is the [111] axis indicates that the structure is actually rhombohedral. Determination of the deviation from cubic structure have been carried out by various researchers (see Geller[31]).

Y^{3+} is diamagnetic, and the ferric ions being in an L = 0 state have very weak interactions with lattice phonons. As a result, YIG has a very narrow line width, typically 0.4 Gauss at room temperature. In contrast, rare earth ions are paramagnetic and when replacing Y in iron garnets they have a weak exchange coupling to the ferric ions, resulting in a magnetization which opposes the $5\mu_B$ of the Fe^{3+} ions. This results in a strong temperature dependence of M_s and also an increased line width. Rare earth impurities in YIG can lead to significant broadening of the line width.[31]

The anisotropy energy for cubic crystals may be expanded as[33]

$$W_A = K_1 f_1 + K_2 f_2 + K_3 f_1^2 + K_4 f_1 f_2 + \cdots,$$

where f_1 and f_2 are certain symmetry invariant functions (this is discussed in more detail in Sec. 3.1, Eqs. (36) to (41)). The most significant of these coefficients have been measured by Hansen[34,33] for YIG and are given in Table 1. Some values for K_3 were measured by Escudier.[35]

Table 1: Anisotropy Factors for YIG

T (K)	$4\pi M_s$ (G)	$-K_1$ (10^3erg cm^{-3})	$-K_2$ (10^3erg cm^{-3})
4.2	2460	24.8	2.3
77	2435	22.1	2.1
295	1750	6.1	0.05

The effect of exchange in YIG (and other cubic ferromagnets) may well be approximated by an exchange field, $\mathbf{H}_E = (D/M_s)\nabla^2\mathbf{M}(\mathbf{r})$ where D is the exchange constant, which for YIG is 5.4×10^{-9}G cm^2.

2.3 Experimental Results

In Fig. 6 we show an overall parameter space diagram, pump power P_{in} vs H_0, for a [111] orientation of the sample along the d.c. field, and perpendicular pumping of the subsidiary resonance. The solid lower boundary line represents the Suhl threshold for absorption by the spin waves. Below this line the system behaves linearly – the reflected power being some fixed fraction of the incident power that depends on the coupling between resonator and wave guide.

For comparison purposes we show in Fig. 7 the behavior for parallel pumping. Note that here the threshold has a minimum at lower field than for perpendicular pumping. Most often the data to be presented is for perpendicular pumping - one may assume this is the case unless stated otherwise.

Near the absolute minimum of the threshold curve for perpendicular pumping (Fig. 6) the dynamics of individual spin wave modes may be observed. These modes are very closely spaced (typically 0.16 G) and give an oscillatory character to the Suhl threshold on a scale which is too fine to be seen in Fig. 6. In Fig.8 we plot the d.c. microwave absorption as a function of applied field over a very narrow range of field. This d.c. effect was first observed by Jantz et al.[36-39] As seen in Eq. (2), changing the field H_0 shifts the frequencies of the spin wave modes in the sample so that in the figure we are scanning through a sequence of modes. The frequency is related to field approximately as γH_0, so this implies that the mode frequency spacing in this sequence is roughly 450 kHz. Just slightly above the Suhl threshold, neighboring modes interact via nonlinear coupling. This gives rise to auto-oscillations in the reflected power as shown in Fig. 9a. These are very low frequency compared to the applied microwaves - typically 100 kHz. They appear as a modulation of the reflected microwave signal and directly in the video detector output signal $S(t)$. The oscillation can undergo period doubling bifurcations as shown in Fig. 9b. This occurs when a peak at half of the fundamental frequency begins to

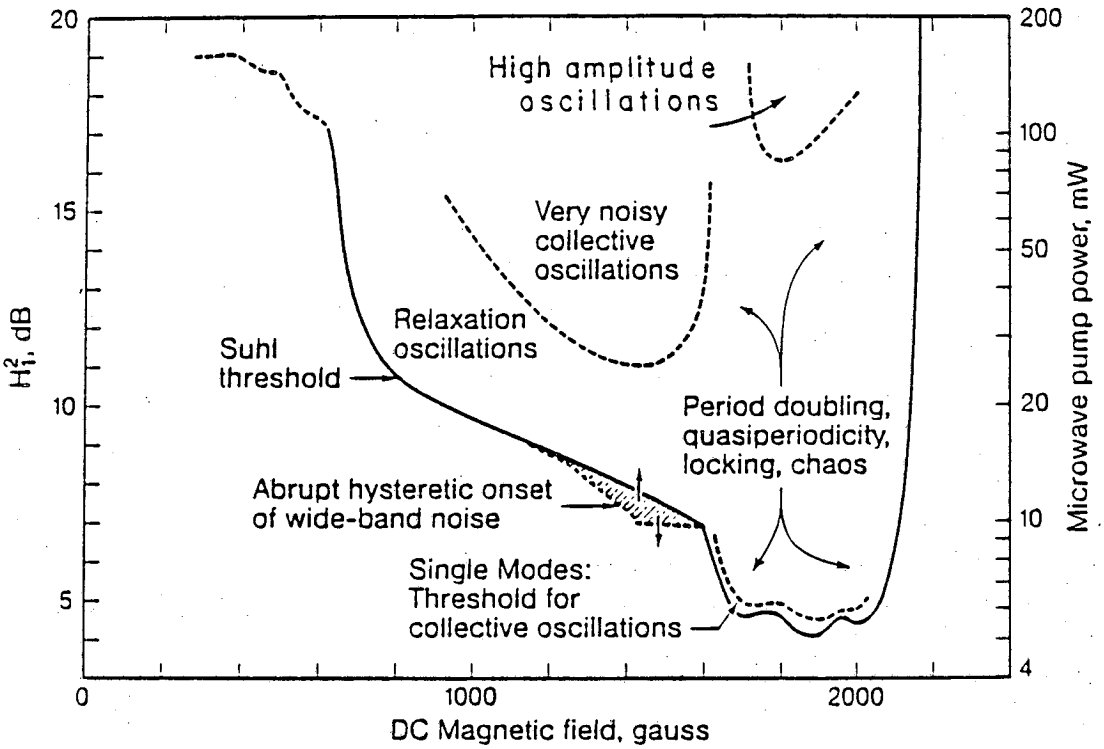

Figure 6. Parameter space diagram for perpendicular pumping with the [111] axis parallel to the d.c. magnetic field.

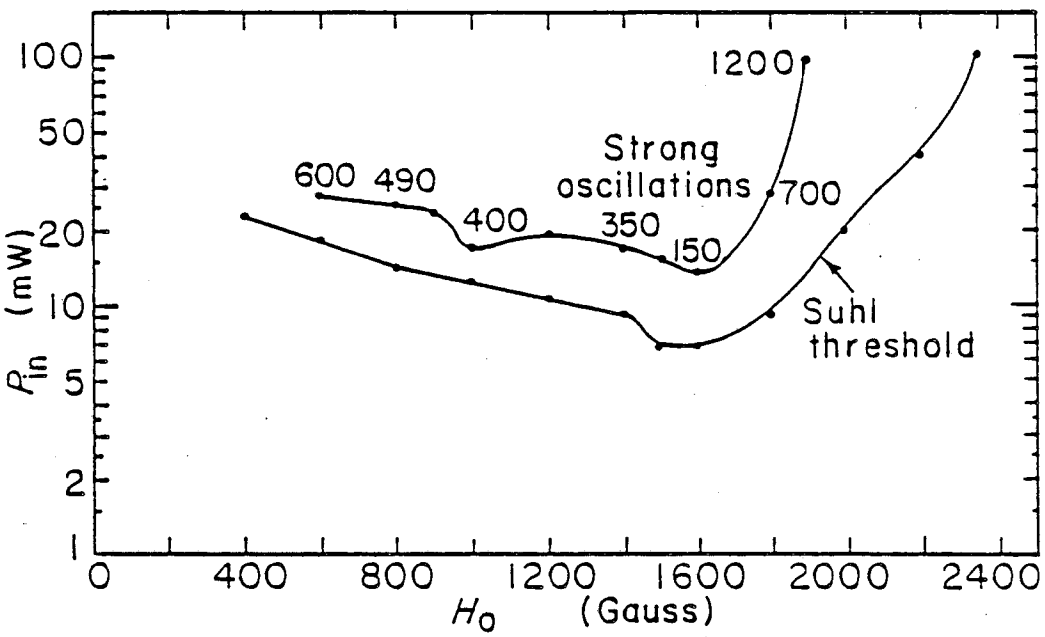

Figure 7. Parameter space diagram for (nearly) parallel pumping with the [111] axis parallel (within 2°) to the d.c. magnetic field. Upper threshold marks the onset of high amplitude auto-oscillations. These occur over a much broader range of field than was observed for perpendicular pumping. Oscillation frequencies given in kHz. Actual pumping angle: $\theta_R = 18°$ off parallel.

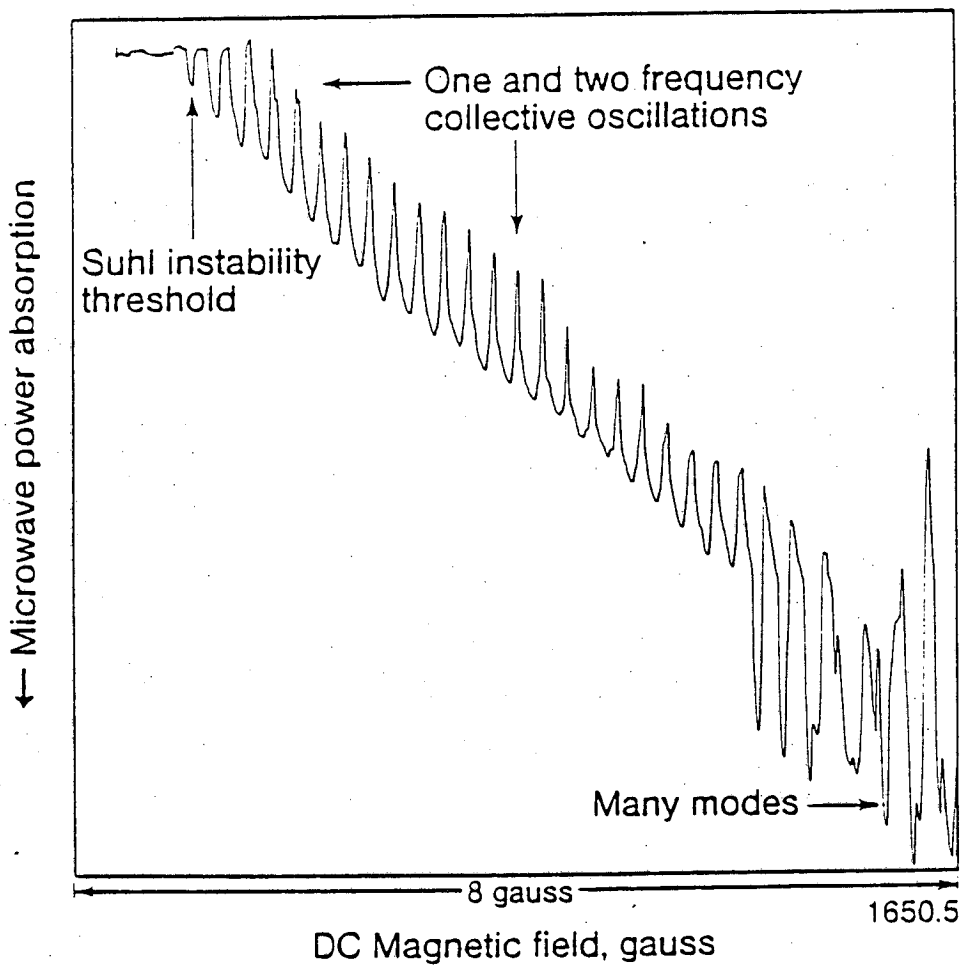

Figure 8. Observed single mode resonances. Located as indicated in Fig. 6. Mode spacing approximately 0.16 G.

emerge in the power spectrum, as shown in Fig. 9c. This process may repeat and a cascade of period doublings occurs culminating in a chaotic orbit as shown in Fig. 9d with power spectrum shown in Fig. 9e. (However, due to the extreme sensitivity of the fine structure region, only the first 2 or 3 bifurcations can be clearly observed). As will be demonstrated in Section 4, these behavior patterns require only the presence of two excited spin wave modes. For the sequence

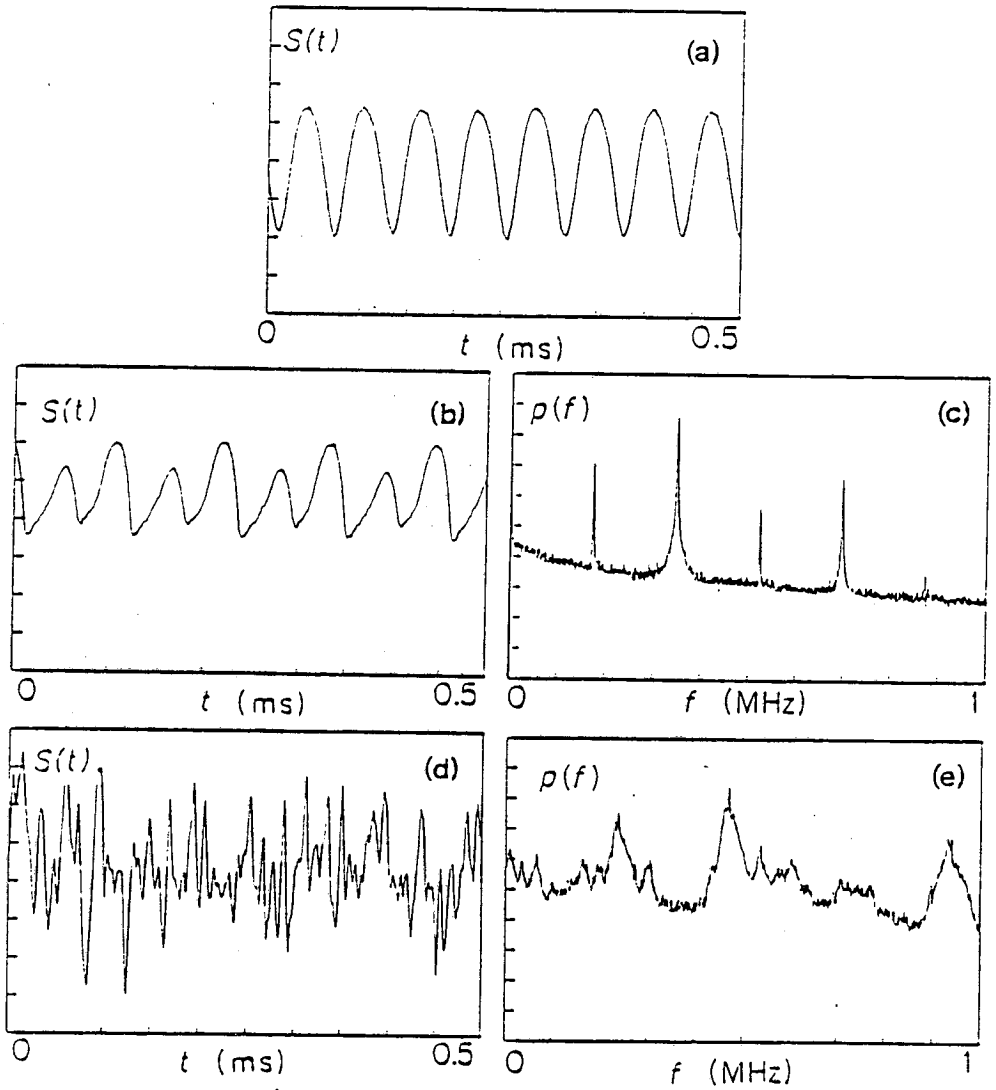

Figure 9. (a) Periodic auto-oscillations at approximately 16 kHz, observed in the single mode region of Fig. 6. Note: typical frequencies range from 10 kHz to 500 kHz. (b) Period doubling (c) Period doubling power spectrum (d) Chaotic auto-oscillations (e) Power spectrum of chaotic oscillations.

of peaks in Fig. 8, the first few starting at the left involve only single mode excitation and no auto-oscillations are observed - here the only observed effect is a d.c. shift in power absorption. Moving to the right, the threshold for the successive modes is decreasing (we are approaching

the absolute minimum of the Suhl curve in Fig. 6.) Thus, being higher above the threshold, we can excite neighboring modes as well as the mode with the smallest detuning from resonance. (The detuning $\Delta\omega_k$ is defined to be $\omega_k - \omega_p/2$). The a.c. effects we have described then occur in conjunction with the d.c. shift of Fig. 8. Hysteresis is also observed, the dynamics may switch suddenly into and out of oscillatory modes and the pattern is slightly changed when the sweep direction is reversed. The a.c. as well as the d.c. behavior repeats approximately when the field is swept through intervals of 0.16 Gauss. Farther to the right, as more modes become involved, quasiperiodic behavior is sometimes observed, as shown in Fig. 10a. In this case the power spectrum [Fig. 10b] shows two fundamental peaks (ω_1 and ω_2) which are irrationally related, along with all of their 2-component harmonics of the form $\omega_{mn} = m\,\omega_1 + n\,\omega_2$. These harmonics may be found arbitrarily close to any chosen frequency, however the amplitude of the peaks decay rapidly with increasing m and n . These orbits can exhibit the quasiperiodic route to chaos, which has been the subject of much theoretical study (see e.g.[40,41]) however, it is difficult to resolve much of the details of the transition in this case due to the extreme sensitivity in the fine structure region. The computer results in section 4 however do show that quasiperiodicity can occur when three or more modes are involved and exhibit the transition to chaos.

Referring back to Fig.6 there is a region between 1200 and 1600 Gauss where the boundary displays hysteresis – on increasing power, spin wave absorption is not observed until the upper curve, while on decreasing power, it continues until the lower one. The attractors exist for the system in the crosshatched zone, only one of which involves excited spin waves. In the excited spin wave state, the system exhibits noisy oscillations as well as an increased d.c. absorption. These do not appear to emerge through any bifurcation sequence from a simple oscillation. Also, the fine structure of the absorption cannot be observed in this region, which may be due to a higher density of modes, and/or modes with higher damping (and therefore greater overlap with neighboring modes). The essential origin of the hysteresis effect can be

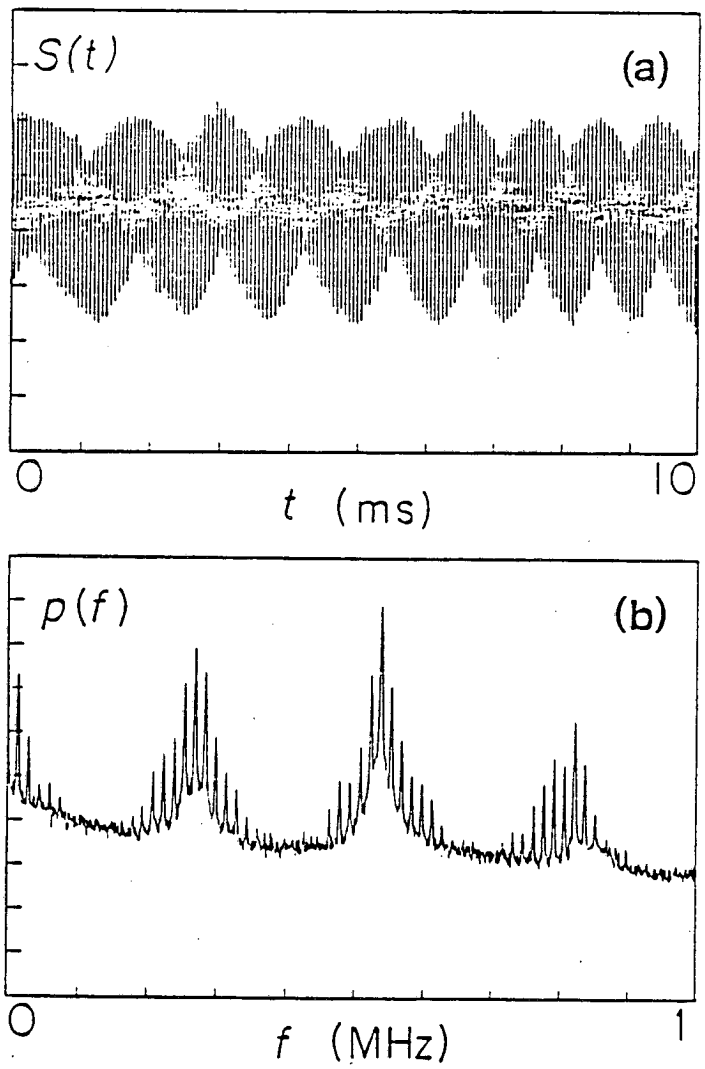

Figure 10. (a) Quasiperiodic time series from single mode region of Fig. 6. (b) Quasiperiodic power spectrum

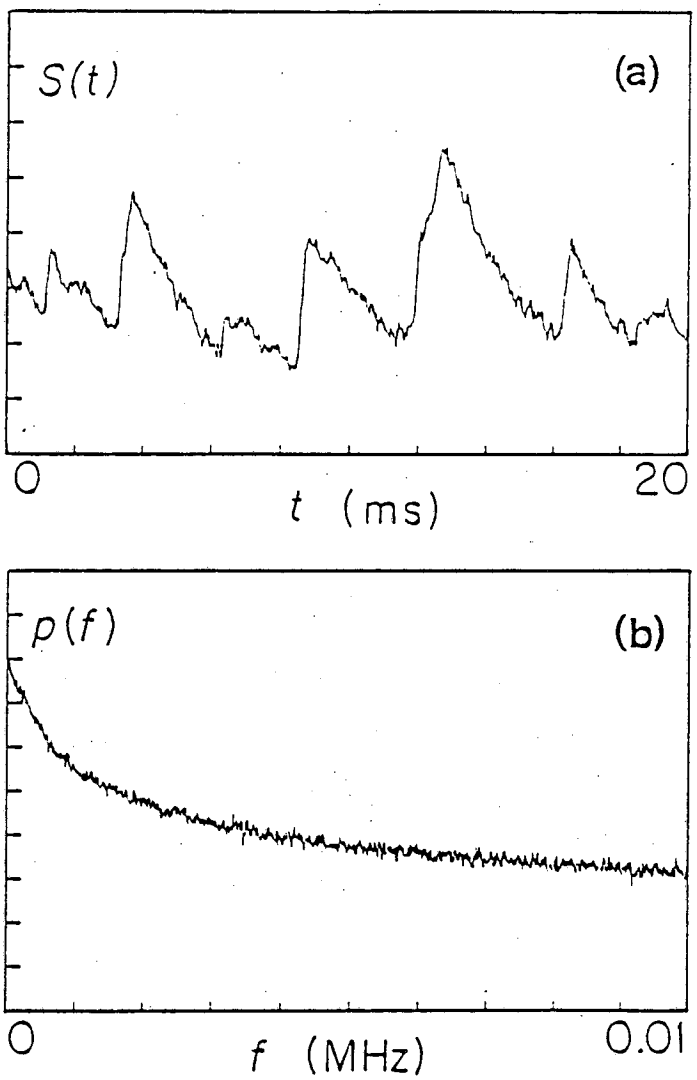

Figure 11. (a) Relaxation oscillations time series. Located as indicated in Fig. 6. (b) Relaxation oscillations power spectrum.

understood theoretically in the dynamics of a single mode as discussed in Section 3.4.

Between 700 and 1200 Gauss in Fig.6 we find that just above the Suhl threshold a form of aperiodic relaxation oscillation occurs. An example of this is shown in Fig. 11a. These have a characteristic "fast phase" during which the response of the system changes very rapidly which

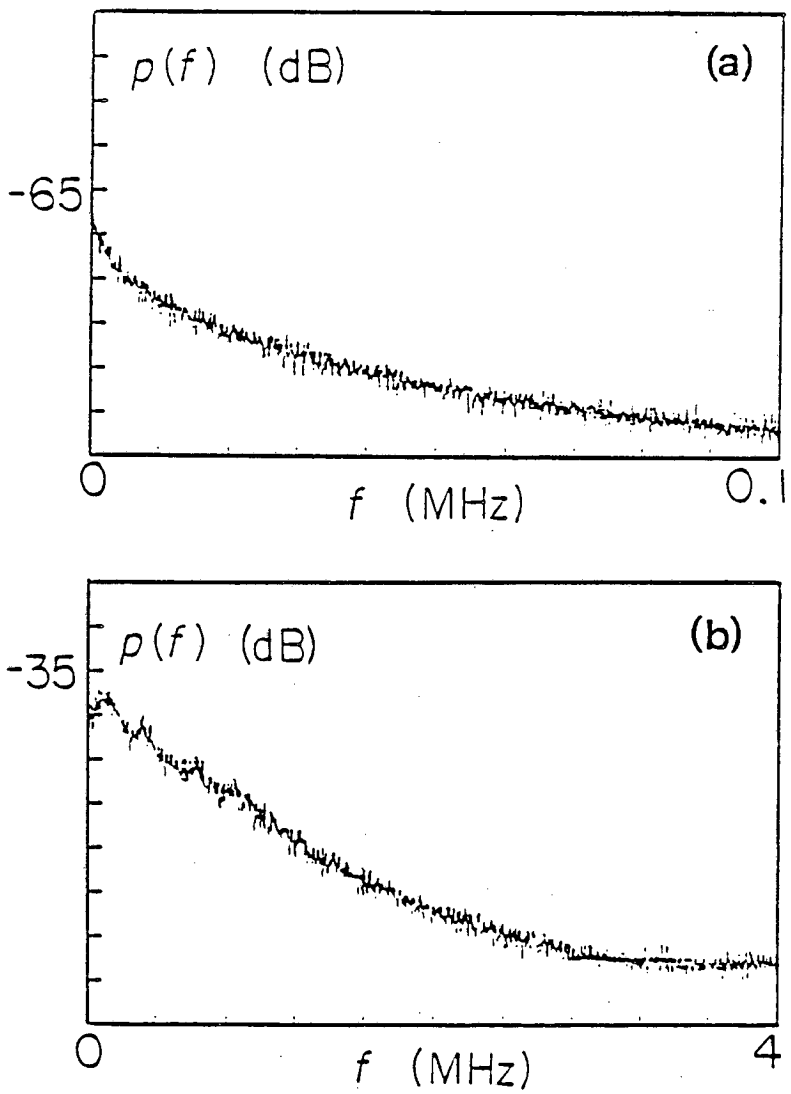

Figure 12. (a) Low frequency noise spectrum. Below transition to high frequency noise in Fig. 6. (b) High frequency noise spectrum. Above transition to high frequency noise in Fig. 6. For both figures the vertical scale is 10 dB per division.

alternates with a "slow phase". Typically the fast phase is at least an order of magnitude faster and shorter (in duration) than the slow phase. These oscillations show no periodicity as can be seen from the featureless power spectrum in Fig.11b. This behavior may be related to the interaction of "weak" and "strong" modes as discussed in Sec. 3.5.

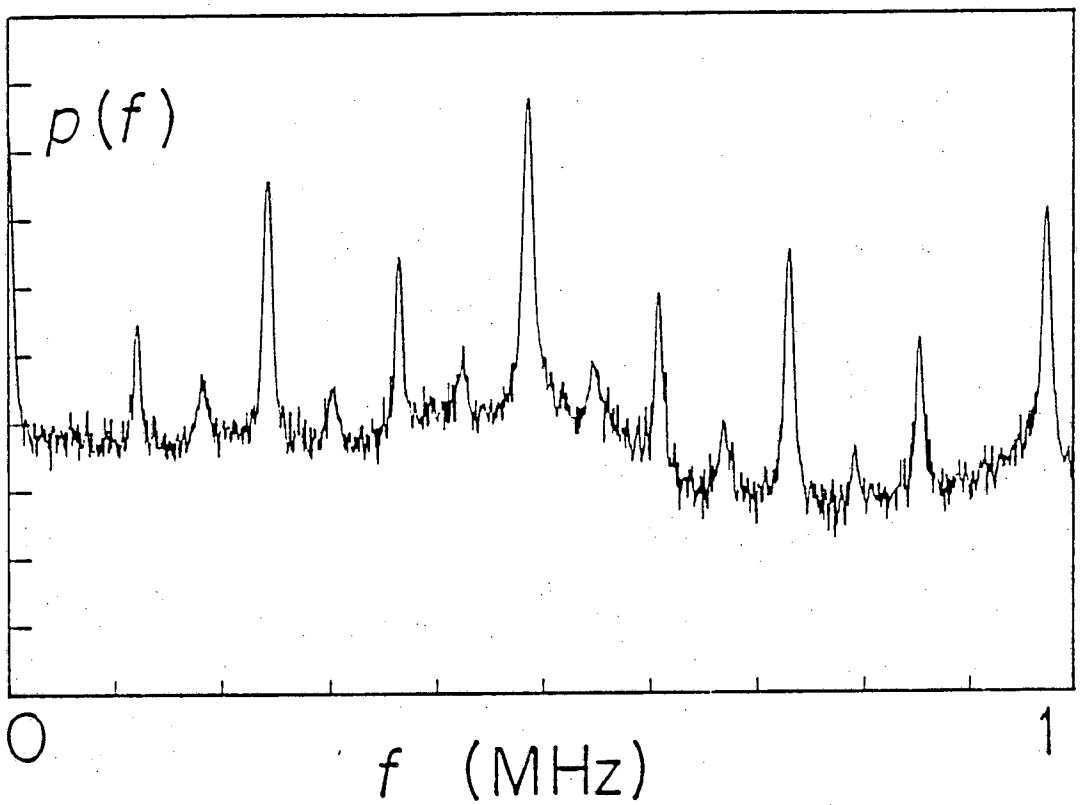

Figure 13. Period 8 observed for parallel pumping. $P_{in} \approx 50\text{mW}$, $H_0 \approx 1800\text{G}$ – see Fig. 7.

At a somewhat higher level of excitation, for d.c. fields in the range 1000 to 1400 Gauss, the relaxation oscillations are superceded with the noisy oscillations of much higher amplitude and frequency. The emergence of this new behavior occurs abruptly at the threshold curve indicated by the dashed line in Fig. 6. In Fig. 12(a) and (b) we compare the power spectra for the low and high frequency noise occurring just below and above the threshold. In both cases these

curves are nearly featureless, as was the case for the relaxation oscillations in Fig. 11b.

At still higher pumping power, with H_0 in the range 1800 to 2000 Gauss, there are high level periodic oscillations. These are typically at least an order of magnitude greater in amplitude and frequency (typical frequency now 1MHz) than those of the fine structure regime. At

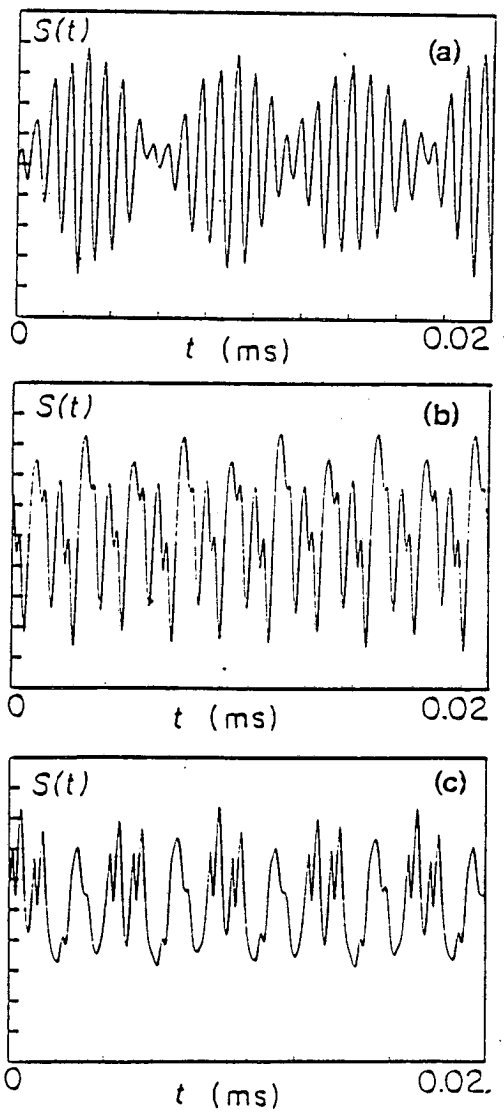

Figure 14. Data for d.c. field parallel to [100] (a) Quasi periodic time series (b) Phase locking of period 8 (c) Phase locking of period 14

these power levels, a large number of spin wave modes become accessible, and the oscillations may be a cooperative effect involving many modes. Thus analysis for the interaction of only a few modes which is presented in Secs. 3 and 4 may be of only limited applicability in this region. (However, see the analysis of Suhl and Zhang[42-44] related to this behavior). These oscillations exhibit all of the dynamical phenomena previously described for the fine structure regime, e.g. period doubling, quasiperiodicity and chaos. They emerge in a Hopf bifurcation at the threshold indicated in Fig. 6. Their emergence does not eliminate the noisy oscillations which exist below this point, however this noise is nearly negligible compared to the oscillations when they reach full amplitude.

These high level oscillations are also observed for parallel pumping where it occurs over a much wider range of the d.c. field, as shown in Fig. 7. In Fig. 13 we show the spectrum following three period doublings to Period 8. Other crystalline orientations were also examined. Perpendicular pumping in the [100] (hard axis) orientation showed some excellent examples of quasiperiodicity and phase locking. Fig. 14(a) shows the beating of two incommensurate frequencies separated by about 12% in frequency. Figs 14(b) and (c) show two examples of high order phase lockings.

In many cases the auto-oscillation frequency shows a trend of increasing with applied microwave power. In Fig. 15(a) an example of such behavior is shown. This data agrees well with the form $f^2 \propto (P/P_c)-1$, where f is the auto-oscillation frequency, P is the pump power, and P_c is the threshold power. This form is suggested by the work of Zautkin et al.[45] This behavior can also be found in the numerical simulations of Sec. 4, as shown in Fig. 15(b).

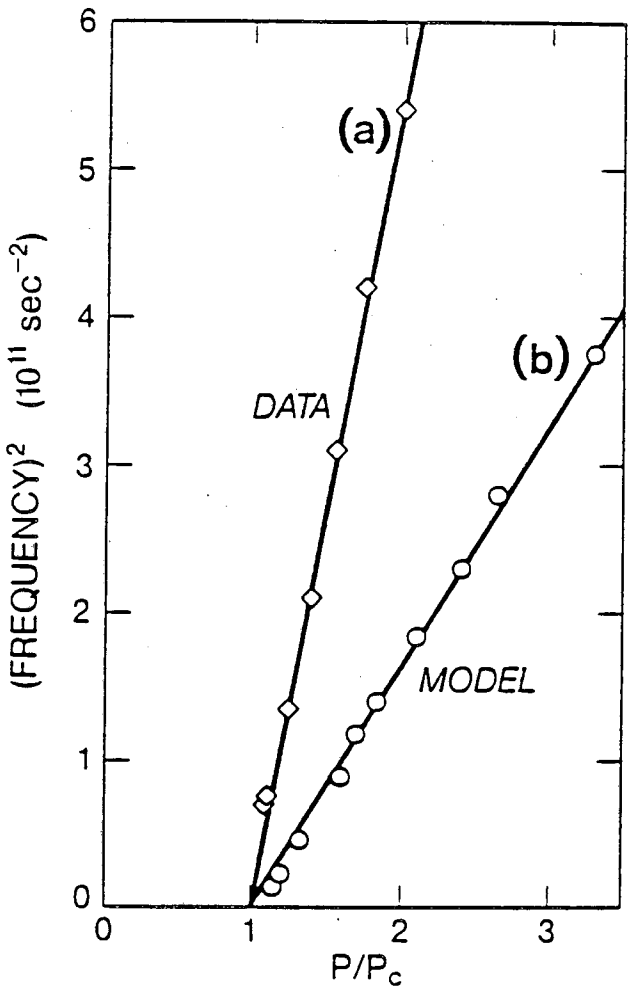

Figure 15. (a) Square of observed auto-oscillation frequency f^2 vs. pump power P relative to threshold value at P_c. The line is a fit to the data. (b) $10 \times f^2$ vs. P/P_c, computed for 2 mode model (Sec. 4): The line has the same functional form as that of (a), $f^2 \propto [(P/P_c) - 1]$.

3 THEORY

This section deals with the analytical formulation of a model of spin wave dynamics that may be useful in understanding the experimental results of Sec. 2. The model equation [Eq. (109)] will be numerically iterated in Sec. 4 and compared to the experimental dynamics.

3.1 Classical Hamiltonian Formulation of the Equations of Motion

We review spin wave theory and present a semiclassical derivation of the fundamental equations governing the relevant spin wave dynamics (which we will go on to study in detail in later sections). In this approach the classical magnetization M is considered to be an analytic function of position $\mathbf{r}$ and time t, and its dynamics are considered to be governed by its interaction with an effective field $H(\mathbf{r},t)$. Suhl's original analysis of spin wave instabilities[13] is also a semiclassical one which starts with classical equations of motion for $\mathbf{M}(\mathbf{r},t)$ and goes on to find the normal modes of the system and stability criteria for their calculation. Although this approach may be extended to obtain equations of motion for the spin waves and their mutual interactions, we take a slightly different approach here, working with the Hamiltonian for the system and utilizing many results due to Schlömann[46] and Zakharov et al.[22, 47, 48] in order to put it in the most desirable form. Much of this development has its roots in the quantum treatment of spin waves by Holstein and Primakoff[49] in which they developed a sequence of transformations to diagonalize their spin Hamiltonian. The Hamiltonian formulation has the advantage of giving the equations of motion in their canonical form. They are obtained easily from the Hamiltonian, which is equal to the total energy of the system. In this representation certain symmetries occur between the coefficients, resulting from the fact that the Hamiltonian is real, while the variables used are complex. The form of the Hamiltonian is essentially the same as of the quantum Hamiltonian, which we discuss in Sec. 3.2. In the analysis, (Secs. 3.4, 3.5, 3.6 and 4), however we will use only the classical form of the equations since the excitation levels of the experiment are usually far above the quantum regime. Damping is treated

phenomenologically, by adding a linear damping term to the equations of motion for each spin wave mode.

An effort is made to make the equations general – we consider oblique pumping showing quite clearly the connection between parallel and perpendicular pumping in the subsidiary resonance regime. We also consider many details omitted in some earlier works such as the effects of crystalline anisotropy and interactions with the resonator or cavity used to couple the microwaves to the sample. Explicit expressions are obtained for the various coupling coefficients – although some of these are very lengthy indeed. Following the derivation of the equations, we discuss in Sec. 3.3 the main approximation - the use of planar spin waves rather than spherical spin- modes which should be the true modes of the sample. We also discuss the possibility of obtaining a subharmonic response at half the microwave pumping frequency in Sec. 3.6.

In the process of obtaining the equations of motion in their final form, we must change variables a number of times. For a Hamiltonian these must take the form of canonical transformations so that the form of Hamilton's equations of motion will be preserved. We list these different representations for the magnetization in Table 2 in approximately the same order in which they appear in the text, and ending with c_k, the final form which we use throughout the rest of this work.

We start by noting that provided we are well below the Curie temperature (559K for YIG), the magnitude of the magnetization is approximately a constant M_s, called the saturation magnetization. ($4\pi M_s$ = 1750 G at 300 K for YIG). Thus M_x, M_y, and M_z are not all independent; it is sufficient to know just M_x and M_y. These are the appropriate variables to choose since the d.c. field H_0 points along the z axis and hence M_z will deviate only slightly from M_s, while M_x and M_y will oscillate about zero. Aside from anisotropy effects (which we discuss later in this section) the system possesses axial symmetry, and this symmetry suggests the use of a complex

Table 2: Nomenclature for Magnetization		
$\mathbf{M}(\mathbf{r})$	$[M_x(\mathbf{r}),M_y(\mathbf{r}),M_z(\mathbf{r})]$ = magnetization.	Eq. (3)
$\mathbf{M}_\mathbf{k}$	Fourier component of $\mathbf{M}(\mathbf{r})$: $\mathbf{M}(\mathbf{r}) = \sum_\mathbf{k} \mathbf{M}_\mathbf{k} e^{i\mathbf{k}\cdot\mathbf{r}}$.	Eq. (25)
$M_T(\mathbf{r})$	Transverse magnetization $= M_x + iM_y$.	Eq. (3)
$M_{T\mathbf{k}}$	Fourier component of M_T: $M_T = \sum_\mathbf{k} M_{T\mathbf{k}} e^{i\mathbf{k}\cdot\mathbf{r}}$	Eq. (28)
s, s^*	Canonically conjugate complex magnetization variables: $M_T = s(2\gamma M_s - \gamma^2 s^* s)^{1/2}$.	Eq. (4)
$s_\mathbf{k}, s_\mathbf{k}^*$	Fourier component of s: $s = V_s^{-1/2} \sum_\mathbf{k} s_\mathbf{k} e^{i\mathbf{k}\cdot\mathbf{r}}$, where V_s is the sample volume.	Eq. (17)
$\nu_\mathbf{k}, \nu_\mathbf{k}^*$	Diagonalizes quadratic part of Hamiltonian: $s_\mathbf{k} = \lambda_\mathbf{k}\nu_\mathbf{k} - \mu_\mathbf{k}\nu_\mathbf{k}^*$ where $\lambda_\mathbf{k}$ and $\mu_\mathbf{k}$ are constants.	Eq. (56)
$b_\mathbf{k}, b_\mathbf{k}^*$	Obtained from $\nu_\mathbf{k}, \nu_\mathbf{k}^*$ by near identity canonical transformation effecting only terms of order $\nu_\mathbf{k}^3$ and higher. Transformation chosen to eliminate all terms of order $\nu_\mathbf{k}^3$.	Eq. (71)
$\tilde{c}_\mathbf{k}$	Slow variables: $\tilde{c}_\mathbf{k} e^{i\omega_p t/2} = b_\mathbf{k}$. Exhibits dynamics on a slow time scale when the resonance condition $\omega_\mathbf{k} = \omega_p/2$ is approximately satisfied ($\omega_\mathbf{k}$ = spin wave frequency, ω_p = pump frequency).	Eq. (98)
$c_\mathbf{k}$	Phase adjusted slow variables: $\tilde{c}_\mathbf{k} = c_\mathbf{k} e^{-iq_\mathbf{k}/2}$, $q_\mathbf{k}$ is appropriate phase shift so that $c_\mathbf{k} = c_{-\mathbf{k}}$.	Eq. (107)

representation: we define the transverse magnetization M_T as:

$$M_T = M_x + iM_y \tag{3}$$

For small amplitudes, M_x and M_y behave essentially as though they were canonically conjugate, while at higher amplitudes they deviate from this behavior. However, a weakly nonlinear transformation exists to new variables s_x and s_y which are canonically conjugate for all amplitudes. This transformation previously used by Schlömann[46] and Zakharov et al[22, 47, 48] is essentially a classical version of the Holstein-Primakoff[49] transformation for the quantum treatment of spin waves. The transformation is

$$M_T = s(2\gamma M_s - \gamma^2 s s^*)^{1/2} \tag{4}$$

where $s = s_x + is_y$ is a complex representation of the canonical variables s_x and s_y, and γ is the gyromagnetic ratio. (Note: in linear approximation $s \propto M_T$ and s has units of Gsec$^{1/2}$.) Since

the magnitude of the magnetization is constrained to equal M_s, we can also express M_z in terms of s and s^* (the complex conjugate of s):

$$M_z = M_s - \gamma s s^* \tag{5}$$

The inverse relationship (s in terms of M_T) can be put in the form

$$s = M_T \gamma^{-1/2} (M_s + M_z)^{-1/2} \tag{6}$$

where $M_z = (M_s^2 - M_T M_T^*)^{1/2}$ To verify that s_x and s_y represent canonically conjugate variables, we will show that Hamilton's equations give the correct equations of motion when the total energy expressed in terms of the complex variable s.

The magnetization changes in response to an effective field H(r) which is defined to be:

$$\mathbf{H}(\mathbf{r}) = -\frac{\delta W}{\delta \mathbf{M}(\mathbf{r})} \tag{7}$$

where $\delta W / \delta \mathbf{M}(\mathbf{r})$ is the functional derivative of the total energy W of the ferromagnet with respect to the magnetization as a function of **r**. To obtain the variation in W one must integrate the functional derivative times the variation in the function M(**r**) over r, i.e.:

$$\delta W = \int \frac{\delta W}{\delta \mathbf{M}(\mathbf{r})} \cdot \delta \mathbf{M}(\mathbf{r}) d^3 r \tag{8}$$

(This relationship defines the functional derivative) The torque per unit volume on the spin system is given by the cross product M×H. Multiplying this by the gyro magnetic ratio γ ($\gamma = g \mu_B / \hbar \approx 1.76 \times 10^7 G^{-1} s^{-1}$ for YIG) we obtain an expression for $\dot{\mathbf{M}}(\mathbf{r})$:

$$\begin{aligned} \dot{\mathbf{M}}(r) &= -\gamma \mathbf{M}(r) \times \mathbf{H}(r) \\ &= \gamma \mathbf{M}(\mathbf{r}) \times \frac{\delta W}{\delta \mathbf{M}(\mathbf{r})} \end{aligned} \tag{9}$$

H(**r**) may be broken down into the applied d.c. field H_0, applied microwave field h, the exchange field H_E, the demagnetization or dipolar field H_D and the crystalline anisotropy field H_A. Similarly the energy may be broken down into the energy due to applied fields W_0, the exchange energy W_E, the demagnetizing energy W_D and the crystalline anisotropy energy W_A. We will obtain explicit forms for each of these later in this section.

The equations of motion take a somewhat simpler form when expressed in terms of M_T:

$$\frac{\partial M_T}{\partial t} = 2i\gamma M_z \frac{\delta W}{\delta M_T^*} \tag{10}$$

$$\frac{\partial M_T^*}{\partial t} = 2i\gamma M_z \frac{\delta W}{\delta M_T}$$

Note that in evaluating $\delta W/\delta M_T^*$ (or similar derivatives) W is to be expressed in terms of $M_T(\mathbf{r})$ and $M_T^*(\mathbf{r})$ and $M_T(\mathbf{r})$ is to be treated like an independent function from $M_T^*(\mathbf{r})$. One can show that Eq. (10) is equivalent to Eq. (9) using:

$$\frac{\delta W}{\delta M_T^*} = \frac{\delta W}{\delta M_x}\frac{\partial M_x}{\partial M_T^*} + \frac{\delta W}{\delta M_y}\frac{\partial M_y}{\partial M_T^*} + \frac{\delta W}{\delta M_z}\frac{\partial M_z}{\partial M_T^*} \tag{11}$$

where

$$\frac{\partial M_x}{\partial M_T^*} = \frac{1}{2}$$

$$\frac{\partial M_y}{\partial M_T^*} = \frac{i}{2}$$

and

$$\frac{\partial M_z}{\partial M_T^*} = \frac{-M_T}{2M_z}$$

We may now proceed to show that the equations of motion for s and s^* are

$$\frac{\partial s(\mathbf{r})}{\partial t} = i\frac{\delta \tilde{H}}{\delta s^*(\mathbf{r})} \quad \text{and} \quad \frac{\partial s^*(\mathbf{r})}{\partial t} = -i\frac{\delta \tilde{H}}{\delta s(\mathbf{r})} \tag{12}$$

where the Hamiltonian $\tilde{H}$ is obtained by expressing the total energy W as a functional of $s(\mathbf{r})$ and $s^*(\mathbf{r})$. Eq. (12) is an appropriate form for Hamilton's equations when using the complex representation of the conjugate variables s_x and s_y. (Note: if desired the i may be included in $\tilde{H}$ so that the equations have exactly the same form as the ordinary Hamilton's equations). To obtain Eq. (12) we first expanded $i\,\delta\tilde{H}/\delta s^*$ using the chain rule:

$$i\frac{\delta \tilde{H}}{\delta s^*} = i\frac{\delta W}{\delta M_T^*}\frac{\partial M_T^*}{\partial s^*} + i\frac{\delta W}{\delta M_T}\frac{\partial M_T}{\partial s^*} \tag{13}$$

then, using Eq. (10) we obtain

$$i\frac{\delta\tilde{H}}{\delta s^*} = \frac{1}{2\gamma M_z}\left[\frac{\partial M_T^*}{\partial s^*}\frac{\partial M_T}{\partial t} - \frac{\partial M_T}{\partial s^*}\frac{\partial M_T^*}{\partial t}\right] \tag{14}$$

again using the chain rule we may express $\partial s/\partial t$ as:

$$\frac{\partial s}{\partial t} = \frac{\partial s}{\partial M_T}\frac{\partial M_T}{\partial t} + \frac{\partial s}{\partial M_T^*}\frac{\partial M_T^*}{\partial t} \tag{15}$$

Using Eq. (4) and Eq. (6), one can easily verify that

$$\frac{\partial s}{\partial M_T} = \frac{1}{2\gamma M_z}\frac{\partial M_T^*}{\partial s*} \quad \text{and} \quad \frac{\partial s}{\partial M_T*} = \frac{-1}{2\gamma M_z}\frac{\partial M_T}{\partial s*} \tag{16}$$

This shows that the right hand sides of Eq. (14) and Eq. (15) are equal and hence Hamilton's equations [Eq. (13)] are correct.

The next step is to expand s and s^* in Fourier series:

$$s = V_s^{-1/2}\sum_{\mathbf{k}} s_{\mathbf{k}} e^{i\mathbf{k}\cdot\mathbf{r}} \tag{17}$$

$$s* = V_s^{-1/2}\sum_{\mathbf{k}} s^*_{-\mathbf{k}} e^{i\mathbf{k}\cdot\mathbf{r}}$$

where V_s is the sample volume ($V_s \approx 1.51\times10^{-4} cm^3$ in the experiment). For Hamiltonian expressed in terms of Fourier components $s_{\mathbf{k}}$ and $s^*_{\mathbf{k}}$, we may express $i\,\partial\tilde{H}/\partial S^*_{\mathbf{k}}$ as

$$i\frac{\partial\tilde{H}}{\partial s^*_{\mathbf{k}}} = i\int\frac{\delta\tilde{H}}{\delta s*(r)}\frac{\partial s*(r)}{\partial s^*_k} + \frac{\delta\tilde{H}}{\delta s(r)}\frac{\partial s(r)}{\partial s^*_{\mathbf{k}}}d^3r \tag{18}$$

where the integral is required because we have functional derivatives on the right hand side. Noting that $\partial s(r)/\partial s^*_{\mathbf{k}} = 0$ and $\partial s^*(r)/\partial s^*_{\mathbf{k}} = V_s^{-1/2}e^{-i\mathbf{k}\cdot\mathbf{r}}$ we find

$$i\frac{\partial\tilde{H}}{\partial S^*_k} = \int\frac{\partial s(r)}{\partial t}V_s^{-1/2}e^{-i\mathbf{k}\cdot\mathbf{r}}d^3r \tag{19}$$

from which we obtain Hamilton's equations in the form:

$$\frac{\partial s_k}{\partial t} = i\frac{\partial\tilde{H}}{\partial s^*_{\mathbf{k}}} \quad \text{and} \quad \frac{\partial s^*_{\mathbf{k}}}{\partial t} = -i\frac{\partial\tilde{H}}{\partial s_{\mathbf{k}}} \tag{20}$$

[Note: if k was considered continuous rather than discrete then we would still have functional derivatives, i.e., $\partial s(\mathbf{k})/\partial t = i\,\delta\tilde{H}/\delta s^*(\mathbf{k})$].

At this point we need to find explicit expressions for the different components of the total energy W. We will then form the Hamiltonian by expressing W in terms of s_k and s_k^*.

W_0 – The Interaction Energy with External Field

The external field has an interaction energy W_0 with the magnetization of the ferromagnet given by

$$W_0 = \int -[\mathbf{H}_0 + \mathbf{h}(t)] \cdot \mathbf{M} d^3 r \tag{21}$$

where $\mathbf{H}_0$ is the d.c. magnetic field (oriented along the z axis) and $\mathbf{h}(t)$ is the microwave magnetic pumping field which has arbitrary orientation and frequency ω_p. Defining a transverse pumping field $h_T \equiv h_x + ih_y$ we may express W_0 as:

$$W_0 = -\int d^3 r \left[(H_0 + h_z) M_z + \frac{1}{2}(h_T M_T^* + h_T^* M_T) \right] \tag{22}$$

or in terms of the constant Fourier components M_{T0} and M_{z0} and sample volume V_s:

$$W_0 = -V_s (H_0 + h_z) - \frac{1}{2} V_s (h_T M_{T0}^* + h_T^* M_{T0}) \tag{23}$$

W_E – The Exchange Energy

The exchange field can be shown to be[50]

$$\mathbf{H}_E = \frac{D}{M_s} \nabla^2 \mathbf{M} \tag{24}$$

where D is the exchange constant ($D \approx 2JSa^2/\hbar\ \gamma Gcm^2$ where J is the Heisenberg exchange energy. $D \approx 5.4 \times 10^{-9} Gcm^2$ for YIG). In terms of the Fourier components $\mathbf{M}_k$ of the magnetization ($\mathbf{M}(\mathbf{r}) = \sum_{\mathbf{k}} \mathbf{M}_k e^{i\mathbf{k}\cdot\mathbf{r}}$) we find that the exchange field is

$$\mathbf{H}_E = \frac{-D}{M_s} k^2 \mathbf{M}_\mathbf{k} e^{i\mathbf{k}\cdot\mathbf{r}}. \tag{25}$$

It follows from Eq. (7) that

$$\partial W_E / \partial M_{-\mathbf{k}} = -V_s \mathbf{H}_{E\mathbf{k}} \tag{26}$$

where $\mathbf{H}_{E\mathbf{k}}$ is a Fourier component of $\mathbf{H}_E$. An expression for W_E which satisfies (26) is

$$W_E = \frac{DV_s}{2M_s} \sum_{\mathbf{k}} k^2 \mathbf{M}_\mathbf{k} \cdot \mathbf{M}_{-\mathbf{k}} \tag{27}$$

We can express this in terms of $M_{T\mathbf{k}}$ and $M_{z\mathbf{k}}$ (the Fourier components of M_T and M_Z) obtaining:

$$W_E = \frac{DV_s}{2M_s} \sum_{\mathbf{k}} k^2 (M_{T\mathbf{k}} M_{T\mathbf{k}}^* + M_{z\mathbf{k}} M_{z\mathbf{k}}^*) \tag{28}$$

Note that $M_{T\mathbf{k}}^*$ is to be interpreted as $(M_{T\mathbf{k}})^*$ not as $(M_T^*)_\mathbf{k}$.

W_D – The Demagnetizing or Dipolar Energy

Here we follow the approach of Suhl[13] and break the demagnetizing field into two components. First, the $k = 0$, case where for certain sample shapes including infinite sheets, infinite rods, and spheres (or more generally ellipsoids), a uniform demagnetizing field $\mathbf{H}_{D0}$ within the sample exactly solves the magnetostatic boundary conditions:

$$\mathbf{H}_{D0} = -4\pi(N_x M_{x0}, N_y M_{y0}, N_z M_{z0}) \tag{29}$$

where M_{x0}, M_{y0}, M_{z0} are the constant Fourier components of M and where N_x, N_y, N_z are the demagnetizing factors (note – these must be generalized to a tensor if the ellipsoid is not oriented with its principle axes corresponding to x, y, and z). The demagnetizing factors satisfy $N_x + N_y + N_z = 1$ and their values for the main cases of interest are given in Table 3. For the more general case of ellipsoidal samples see Osborn[51] and Stoner.[52] We define symmetric and asymmetric demagnetizing factors N_{D+} and N_{D-} as

Table 3: Demagnetizing Factors					
Shape	N_x	N_y	N_z	N_{D+}	N_{D-}
Sphere	$\frac{1}{3}$	$\frac{1}{3}$	$\frac{1}{3}$	$\frac{1}{3}$	0
Rod, along z	$\frac{1}{2}$	$\frac{1}{2}$	0	$\frac{1}{2}$	0
Rod, along y	$\frac{1}{2}$	0	$\frac{1}{2}$	$\frac{1}{4}$	$\frac{1}{4}$
Rod, along x	0	$\frac{1}{2}$	$\frac{1}{2}$	$\frac{1}{4}$	$-\frac{1}{4}$
Sheet, normal z	0	0	1	0	0
Sheet, normal y	0	1	0	$\frac{1}{2}$	$-\frac{1}{2}$
Sheet, normal x	1	0	0	$\frac{1}{2}$	$\frac{1}{2}$

$$N_{D+} = (N_x + N_y)/2 \quad and \quad N_{D-} = (N_x - N_y)/2 \tag{30}$$

The corresponding energy W_{D0} is given by

$$W_{D0} = 2\pi V_s (N_x M_{x0}^2 + N_y M_{y0}^2 + N_z M_{z0}^2) \tag{31}$$

or in terms of the transverse magnetization

$$W_{D0} = 2\pi V_s (N_{D+} M_{T0} M_{T0}^* + \frac{1}{2} N_{D-} (M_{T0}^2 + M_{T0}^{*2}) + N_z M_{z0}^2) \tag{32}$$

The components with $k \neq 0$ are very difficult to determine precisely for a spherical sample, but the problem becomes relatively easy if we neglect the boundary conditions. This is not really a very good approximation – especially since individual spherical modes have been observed to be excited experimentally - however, this approximation has been used in all previous studies of spin wave instabilities because it leads to equations which can be solved analytically. Starting with the Maxwell Equation $\nabla \cdot B = 0$, we express B as $H_D + H_0 + h + 4\pi M$ and obtain:

$$\nabla \cdot H_D = -4\pi \nabla \cdot M \tag{33}$$

expanding in Fourier components we find

$$\sum_{\mathbf{k}} \mathbf{H}_{D\mathbf{k}} e^{i\mathbf{k}\cdot\mathbf{r}} = \sum_{k} -4\pi \frac{\mathbf{k}}{k^2} \mathbf{k}\cdot\mathbf{M}_{\mathbf{k}} e^{i\mathbf{k}\cdot\mathbf{r}} \tag{34}$$

The corresponding term in the total energy (which satisfies $\partial W_{D\mathbf{k}}/\partial \mathbf{M}_{-\mathbf{k}} = -V_s \mathbf{H}_{D\mathbf{k}}$) including all nonzero values for k is given by:

$$W_{D\mathbf{k}} = 2\pi V_s \sum_{\mathbf{k}\neq 0} \frac{|\,\mathbf{k}\cdot\mathbf{M}_{\mathbf{k}}\,|^2}{k^2} \tag{35}$$

$$= 2\pi V_s \sum_{\mathbf{k}\neq 0} \frac{1}{4k^2} |\, k_T M^*_{T,-\mathbf{k}} + k_T^* M_{T,\mathbf{k}} + 2k_z M_{z\mathbf{k}}\,|^2$$

W_A – The Anisotropy Energy

For crystals with cubic symmetry there are two symmetry invariant functions f_1 and f_2 [with $m\,3m\,(O_h)$ point group symmetry]:[33]

$$f_1 = \alpha_1^2\alpha_2^2 + \alpha_2^2\alpha_3^2 - \alpha_3^2\alpha_1^2 \tag{36}$$

$$f_2 = \alpha_1^2\alpha_2^2\alpha_3^2$$

where $(\alpha_1, \alpha_2, \alpha_3)$ is a representation of a unit vector with respect to the crystallographic (rather than experimental) axes. We therefore expect that the anisotropy energy density for such a crystal must be expressible as a function of f_1 and f_2 where alpha is a unit vector in the direction of the magnetization. This assumes that the crystal is unstrained and that the exchange field is large compared to external fields. Also, there may be a uniaxial component, especially in thin films, resulting from stress induced by a mismatch between film and substrate or related to the direction of crystal growth – see Hansen.[33] Expanding W_A in terms of f_1 and f_2 we find:

$$W_A = \int d^3r\,(K_1 f_1 + K_2 f_2 + K_3 f_1^2 + K_4 f_1 f_2 + \ldots) \tag{37}$$

Values for the anisotropy constants K_1 and K_2 for YIG are given in Table 1 in Sec. 2.2. Values for other garnets may be found in Hansen.[33] In order to use Eq. (37) we must express it in terms of $M_{T\mathbf{k}}$. The procedure is as follows: first find the linear transformation R which

relates $(\alpha_1,\alpha_2,\alpha_3)$ with (M_x,M_y,M_z) and hence with M_T i.e.

$$\begin{bmatrix}\alpha_1\\ \alpha_2\\ \alpha_3\end{bmatrix} = \mathbf{R}\begin{bmatrix}M_x\\ M_y\\ M_z\end{bmatrix} = \mathbf{R}\begin{bmatrix}(M_T+M_T^*)/2\\ -i\,(M_T-M_T^*)/2\\ (1-M_T M_T^*)^{1/2}\end{bmatrix} \tag{38}$$

then express f_1 and f_2 in terms of M_T. Finally expand M_T as a Fourier series, eliminate oscillatory terms from the integral with nonoscillatory terms being multiplied by V_s, the sample volume. The easiest case to evaluate is for H_0 oriented along [001]. In this case we can normally make the additional conditions $\hat{x} = [100]$ and $\hat{y} = [010]$. [However some other choice might be required for a sample which is not azimuthally symmetric if its principle axes (for evaluating the demagnetizing field) do not agree with the crystallographic axes]. In this case $\mathbf{R} = M_s^{-1}\mathbf{I}$ where $\mathbf{I}$ is the identity matrix. From this we obtain (for [100] orientation):

$$f_1 = m_T m_T^* - \frac{9}{8}(m_T m_T^*)^2 + \frac{1}{16}(m_T^4 + m_T^{*4}) \tag{39}$$

$$f_2 = \frac{1}{16}(m_T^4 + m_T^{*4} - 2m_T^2 m_T^{*2})(1 - m_T m_T^*) \tag{40}$$

where we have defined $m_T = M_T/M_s$. In order to obtain all terms through order M_T^4 in W_A we need to include the first three terms in Eq. (37) with coefficients K_1, K_2, and K_3. Similar expressions to Eq. (39) above may be obtained for other orientations of interest. However relatively simple results may be obtained if we restrict ourselves to the lowest order contributions (order M_T^2) with the z axis corresponding to [001], [110], or [111], and the y axis corresponding to $[1\bar{1}0]$ (the three orientations indicated for the z axis may be obtained by rotating about the $[1\bar{1}0]$ axis). In this case the anisotropy energy has the form

$$W_A = 2\pi V_s \sum_{\mathbf{k}}\left[N_{A+} M_{T\mathbf{k}} M_{T\mathbf{k}}^* + \frac{1}{2}N_{A-}(M_{T\mathbf{k}}^2 + M_{T\mathbf{k}}^{*2})\right] + Order\,(M_{T\mathbf{k}}^4) \tag{41}$$

where:

$$\text{for [001]}\quad N_{A+} = 2K_1/4\pi M_s^2,\quad N_{A-} = 0$$

$$\text{for [111]}\quad N_{A+} = (-\frac{4}{3}K_1 - \frac{4}{9}K_2)/4\pi M_s^2,\quad N_{A-} = 0$$

$$\text{for [110]} \quad N_{A+}=(-\frac{1}{2}K_1+\frac{1}{4}K_2)/4\pi M_s^2, \quad N_{A-}=(\frac{3}{2}K_1+\frac{1}{4}K_2)/4\pi M_s^2$$

This notation was chosen because of its similarity to the demagnetizing factors N_{D+} and N_{D-} appearing in Eq. (32). Note that for $\hat{z}$ = [001] or [111] the results are independent of the orientation of $\hat{x}$ and $\hat{y}$, although there will be differences in higher order terms omitted in Eq. (41). Only the $\hat{z}$ = [110] case leads to a nonzero value of N_{A-}. This term breaks azimuthal symmetry and leads to elliptical rather than circular orbits for the uniform mode (as does the factor N_{D-} in Eq. (32) which results from shape anisotropy). Values for N_{A+} and N_{A-} for YIG may be found in Table 4.

Table 4: Anisotropy Factors for YIG

T (K)	[100] N_{A+}	[111] N_{A+}	[110] N_{A+}	[110] N_{A-}
4.2	-0.1030	0.0708	0.0246	-0.0784
77	-0.0937	0.0644	0.0223	-0.0714
295	-0.0501	0.0335	0.0125	-0.0376

Now that the various contributions to the energy have been evaluated [Eqs. (23), (28), (32), (35), and (41)] we may combine them to form to obtain an expression for the Hamiltonian:

$$\bar{H}=W_0+W_E+W_{DO}+W_{D\mathbf{k}}+W_A \tag{42}$$

Naturally, we will want to express the Hamiltonian in terms of the canonical variables $s_{\mathbf{k}}$ and $s_{\mathbf{k}}^*$ This may be accomplished using:

$$M_{T\mathbf{k}}=M_s\left[Y^{1/2}s_{\mathbf{k}}-\frac{1}{8}Y^{3/2}\sum_{\mathbf{k}_1,\mathbf{k}_2}s_{\mathbf{k}_1}s_{\mathbf{k}_2}s^*_{\mathbf{k}_1+\mathbf{k}_2-\mathbf{k}}\right]+Order(s_{\mathbf{k}}^5) \tag{43}$$

and

$$M_{z\mathbf{k}}=M_s(\delta_k-\frac{1}{2}Y\sum_{\mathbf{k}_1}s_{\mathbf{k}_1}s^*_{\mathbf{k}_1-\mathbf{k}}) \tag{44}$$

where $Y\equiv 2\gamma/M_sV_s$ and $\delta_k\equiv 1$ for $\mathbf{k}\equiv 0$ and $\delta_k\equiv 0$ for $\mathbf{k}\neq 0$. Since the resulting Hamiltonian is

a lengthy expression, we break it into components as follows:

$$\tilde{H} = const. + \tilde{H}_p + \tilde{H}_2 + \tilde{H}_3 + \tilde{H}_4 + \cdots \tag{45}$$

where $\tilde{H}_p$ consists of terms involving the pumping fields h_T and h_z, $\tilde{H}_2$ consists of quadratic terms in s_k, $\tilde{H}_3$ of cubic terms, and $\tilde{H}_4$ quartic terms. The results are:

$$\tilde{H}_p = \gamma h_z \sum_{\mathbf{k}} s_{\mathbf{k}}^* s_{\mathbf{k}} - \gamma Y^{-1/2}(h_T s_0^* + h_T^* s_0) \tag{46}$$

$$\tilde{H}_2 = \sum_{\mathbf{k}} A_{\mathbf{k}} s_k^* s_{\mathbf{k}} + \frac{1}{2}(B_{\mathbf{k}}^* s_{\mathbf{k}} s_{-\mathbf{k}} + c.c.) \tag{47}$$

where

$$A_{\mathbf{k}} = \gamma(H_0 + Dk^2) + \omega_m(\delta_k N_{D+} - N_z + N_{A+} + (1-\delta_k)\frac{|k_T|^2}{2k^2}), \tag{48}$$

$$B_{\mathbf{k}} = \omega_m(\delta_k N_{D-} + N_{A-} + (1-\delta_k)\frac{k_T^{*2}}{2k^2}), \tag{49}$$

$\omega_m = 4\pi M_s \gamma$, and c.c. denotes complex conjugate

$$\tilde{H}_3 = -Y^{1/2} \sum_{\mathbf{k},\mathbf{k}_1} J_k^* s_{\mathbf{k}} s_{\mathbf{k}_1} s_{\mathbf{k}_1+\mathbf{k}}^* + c.c. \tag{50}$$

where

$$J_{\mathbf{k}} = \omega_m \frac{k_z k_T}{2k^2}(1 - \delta_k) \tag{51}$$

and

$$\tilde{H}_4 = \frac{1}{8} Y \left[\sum_{k_1,k_2,k_3} (2E_{\mathbf{k}_1-\mathbf{k}_3} - Q_{\mathbf{k}_1} - Q_{\mathbf{k}_3}) s_{\mathbf{k}_1} s_{\mathbf{k}_2} s_{\mathbf{k}_3}^* s_{\mathbf{k}_1+\mathbf{k}_2-\mathbf{k}_3}^* - (F_{\mathbf{k}_1}^* s_{\mathbf{k}_1} s_{\mathbf{k}_2} s_{\mathbf{k}_3} s_{\mathbf{k}_1+\mathbf{k}_2+\mathbf{k}_3}^* + c.c.) \right] \tag{52}$$

where

$$Q_{\mathbf{k}} = \gamma D k^2 + \omega_m(\delta_k N_{D+} + (1-\delta_k)\frac{|k_T|^2}{2k^2} + N_{A+}) \tag{53}$$

$$E_{\mathbf{k}} = \gamma D k^2 + \omega_m(\delta_k N_z + (1-\delta_k)\frac{k_z^2}{k^2}) \tag{54}$$

and

$$F_k = \omega_m[(1-\delta_k)\frac{k_T^2}{2k^2} + \delta_k N_{D-} + N_{A-}] \tag{55}$$

Note that while we have included in $\tilde{H}_4$ its dependence on the anisotropy factors N_{A+} and N_{A-}, there are additional contributions to $\tilde{H}_4$ from terms of order M_T^4 in the anisotropy energy such as those given explicitly in Eq. (39) for the [100] orientation, and requiring knowledge of the coefficients $k_1 k_2$ and k_3 in Eq. (37). However, anisotropy is not very strong in pure YIG and it may be reasonable to neglect these terms in first approximation.

In the absence of dipolar and anisotropy effects, the s_k variables would be the appropriate normal coordinates for the problem since in that case $\tilde{H}_2$ would have the "diagonal" form $A_k s_k^* s_k$. However we have the additional terms $\frac{1}{2} B_k^* s_k s_{-k}$ and $\frac{1}{2} B_k s_k^* s_{-k}^*$ whose presence means that s_k and s_{-k} are coupled. Fortunately, $\tilde{H}_2$ can be diagonalized by means of a canonical transformation to the new variables v_k and v_k^*:

$$s_k = \lambda_k v_k - \mu_k v_{-k}^* \tag{56}$$

with inverse transformation

$$v_k = \lambda_k s_k + \mu_k s_{-k}^* \tag{57}$$

This is sometimes referred to as the Bogoliubov transformation. The coefficients λ_k and μ_k are given by

$$\lambda_k = \left[\frac{A_k + \omega_k}{2\omega_k} \right]^{1/2} \tag{58}$$

and

$$\mu_k = \frac{B_k}{|B_k|} \left[\frac{A_k - \omega_k}{2\omega_k} \right]^{1/2}$$

where

$$\omega_k \equiv (A_k^2 - |B_k|^2)^{1/2} \tag{59}$$

is the spin wave dispersion relation. λ_k and μ_k satisfy

$$\lambda_k^2 - |\mu_k|^2 = 1 \tag{60}$$

which is required in order that the transformation be canonical, i.e., that Hamilton's equations give the correct equations of motion:

$$\dot{v}_k = i\frac{\partial \tilde{H}}{\partial v_k^*} \quad and \quad \dot{v}_k^* = -i\frac{\partial \tilde{H}}{\partial v_k} \tag{61}$$

The other useful relations are:

$$\lambda_k \mu_k = B_k / 2\omega_k \tag{62}$$

and

$$\lambda_k^2 + |\mu_k|^2 = A_k/\omega_k \tag{63}$$

Note that there is no real solution for ω_k in Eq. (59) in the event that $A_k^2 < |B_k|^2$. This first occurs in the limit of small (but nonzero) k when

$$H_0 < 4\pi M_s (N_z + N_{A-} - N_{A+}) \tag{64}$$

below this field the ferromagnet is unstable against the formation of domains (roughly 600 G for YIG). A typical dispersion diagram was shown previously in Fig. 2. Note that ω_k depends not only on $|k|$ but also on θ_k, the azimuthal angle of k. Neglecting the anisotropy factor N_{A-}, ω_k is a minimum for $\theta_k = 0$ and a maximum for $\theta_k = 90°$. The presence of N_{A-} changes the minimum to a nonzero value of θ_k and also makes ω_k dependent on the ϕ_k the polar angle of k. For N_{A-} positive, the minimum occurs for $\phi_k = 90°[\phi_k = arg(k_T)]$, while N_{A-} negative gives a minimum for $\phi_k = 0$. (These conditions are reversed for the maximum). The uniform mode frequency ω_0 always lies within the band of allowed frequencies for small but nonzero k. Its location depends primarily on the sample shape - for a sphere it has approximately the same frequency as a spin wave with $k \approx 0$ and $\theta_k \approx 54.7°$; for a thin disc with $\hat{z}$ normal the frequency corresponds to $\theta_k \approx 0°$; for a thin disc with $\hat{z}$ parallel to the surface the frequency corresponds to $\theta_k \approx 90°$.

The Bogoliubov transformation puts the quadratic term in the desired form

$$\tilde{H}_2 = \omega_k v_k^* v_k \tag{65}$$

The pumping term now has the form

$$\tilde{H}_p = \gamma h_z \sum_k \left[\frac{A_k}{\omega_k} v_k^* v_k - \frac{1}{2}\left(\frac{B_k}{\omega_k} v_k^* v_{-k}^* + c.c. \right) \right] \tag{66}$$

$$-\gamma Y^{-1/2}\left[(\lambda_0 h_T - \mu_0 h_T^*)v_0^* + c.c\right]$$

note, if $N_{D-}+N_{A-}$ is negligibly small then $\lambda_0 = 1$ and $\mu_0 = 0$ and therefore $v_0 = s_0$. The $h_z v_k^* v_{-k}^*$ term gives parallel pumping and the $h_T v_0^*$ term gives perpendicular pumping. The transformed cubic term is:

$$\tilde{H}_3 = -Y^{1/2}\sum_{k_1,k_2}\left[U_{k_1,k_2} v_{k_1} v_{k_2} v_{-(k_1+k_2)} + c.c.\right) + X_{k_1,k_2} v_{k_1} v_{k_2} v_{-(k_1+k_2)}^* + c.c.\right) \tag{67}$$

where

$$U_{k_1,k_2} = J_{k_1}\mu_{k_1}^*\mu_{k_2}^*\lambda_{k_1+k_2} - J_{k_1}^*\lambda_{k_1}\lambda_{k_2}\mu_{k_1+k_2} \tag{68}$$

$$X_{k_1+k_2} = J_{k_1}^*\lambda_{k_1}\lambda_{k_2}\lambda_{k_1+k_2} + J_{k_2}^*\mu_{k_1}^*\lambda_{k_2}\mu_{k_1+k_2} + J_{k_1+k_2}^*\lambda_{k_1}\mu_{k_2}^*\mu_{k_1+k_2} \tag{69}$$

$$-J_{k_1}\mu_{k_1}^*\mu_{k_2}^*\mu_{k_1+k_2} - J_{k_2}\lambda_{k_1}\mu_{k_2}^*\lambda_{k_1+k_2} - J_{k_1+k_2}\mu_{k_1}^*\lambda_{k_2}\lambda_{k_1+k_2}$$

For the quartic term $\tilde{H}_4$, we will keep only those terms which couple two spin wave modes of interest, say, k and k′. We will also ignore all terms with fast time dependence. Only those terms with slow time dependence, of the same order of magnitude as the damping rate (to be introduced later into the equation of motion), Will be needed. We naturally assume that $\omega_k \approx \omega_{k'} \approx \omega_p/2$. Factors v_k and v_{-k} have time dependence $e^{i\omega_k t}$ while v_k^* and v_{-k}^* have time dependence $e^{-i\omega_k t}$ As a result, $\tilde{H}_4$ is reduced to just two terms:

$$\tilde{H}_4 = \hat{T}_{kk'} v_k v_k^* v_{k'} v_{k'}^* + \frac{1}{2}\hat{S}_{kk'} v_k^* v_{-k}^* v_{k'} v_{-k'} \tag{70}$$

where the parameters $\hat{T}_{kk'}$ and $\hat{S}_{kk'}$ may be obtained in terms of the previous parameters by substituting Eq. (56) into Eq. (52) and collecting all terms of the indicated types.

While we have found terms in $\tilde{H}_4$ which directly couple two spin wave modes (of the same frequency) there are no such terms in $\tilde{H}_3$. Why then do we need $\tilde{H}_3$? The reason is that the $\tilde{H}_3$ terms are much larger than the $\tilde{H}_4$ terms and there are second order contributions from $\tilde{H}_3$ which do couple k and k′. These occur through the off resonance or virtual excitation of the mode k+k′ or k−k′. These modes will not normally have the same resonant frequency as k and k^1, however they may nevertheless be forced into a weak response at this frequency, which in

turn produces a weak coupling between k and k′ which may be of the same order as the terms in $\tilde{H}_4$. There are two essentially equivalent ways of dealing with this problem. First, one may explicitly determine the response of these off resonance modes from the equations of motion. Since these modes are strongly detuned they will not behave as dynamical variables – their amplitudes may be expressed directly as a function of v_k and $v_{k'}$. A second method is to introduce another canonical transformation[47] to new variables b_k and b_k^* which eliminates all of the cubic terms in the Hamiltonian. The appropriate transformation is:

$$v_k = b_k + Y^{1/2}\sum_{k'}\left\{ \frac{X_{k',k-k'}b_{k'}b_{k'-k}}{\omega_k-\omega_k-\omega_{k+k'}} + \frac{(X^*_{k,k'} + X^*_{k',k})b_{k'}b^*_{k'-k}}{\omega_k-\omega_k+\omega_{k+k'}} \right. \\ \left. + \frac{(U^*_{k,k'} + U^*_{k',k} + U^*_{k',k-k'})b^*_{k'}b^*_{k'-k}}{\omega_k+\omega_k+\omega_{k'+k}} \right\} \tag{71}$$

Hamilton's equations in the b_k variables are correct through quadratic terms but deviate from the correct equations of motion by cubic terms. These errors can be canceled by adding the appropriate quartic terms to the Hamiltonian. [Note: These correction terms could be generated by adding the appropriate cubic terms to Eq. (71)]. The transformation itself also generates new quartic terms and as a result $\hat{T}_{kk'}$ and $\hat{S}_{kk'}$ are "renormalized" to new values $T_{kk'}$ and $S_{kk'}$. Thus we now have

$$\tilde{H}_3 = 0 \tag{72}$$

and

$$\tilde{H}_4 = T_{kk'}b_k b^*_k b_{k'}b^*_{k'} + \frac{1}{2}S_{kk'}b^*_k b^*_{-k}b_{k'}b_{-k'} \tag{73}$$

The transformation leaves the quadratic part of the Hamiltonian in diagonal form:

$$\tilde{H}_2 = \omega_k b^*_k b_k \tag{74}$$

However, there are some very important consequences for the perpendicular pumping term [see Eq. (66)]. In the v_k notation, the transverse field h_T only couples to the uniform mode v_0 which is off resonance. This in turn couples to a spin wave pair, v_k,v_{-k}, via terms in $\tilde{H}_3$ like $X^*_{k,-k}v^*_k v^*_{-k}v_0$. In the b_k notation however, $\tilde{H}_3$ has been eliminated so this mechanism no

longer exists. Instead, we now have new terms appearing in $\tilde{H}_p$ whereby the external field couples directly to spin wave pairs just as it does for the parallel pumping term. The important part of $\tilde{H}_p$ may now be expressed:

$$\tilde{H}_p = \sum_{k'}\left[-\frac{1}{2}\gamma h_z \frac{B_k}{\omega_k} - \gamma(\lambda_0 h_T - \mu_0 h_T^*)\frac{X^*_{k,k'}}{\omega_0 - 2\omega_k}\right. \tag{75}$$

$$\left. - \gamma(\lambda_0 h_T^* - \mu_0^* h_T)\frac{U^*_{0,k} + U^*_{k,0} + U^*_{k,-k}}{\omega_0 + 2\omega_k}\right] b_k^* b_{-k}^* \quad + c.c.$$

Where we have omitted the direct coupling terms $h_T b_0 + c.c.$, since these are now unimportant for the subsidiary absorption, however they are required for the second order Suhl instability since this involves the excitation of the uniform mode. Noting that $U_{k,k'}$ and $X_{k,k'}$ were given by Eqs. (68) and (69) we see that the coefficient of $b_k^* b_{-k}^*$ in Eq. (75) can in general be very complicated. However, if we restrict our attention to the case where N_{D-} and N_{A-} are both zero, as occurs for example with a spherical sample with H_0 parallel to [111] or [100], then $\lambda_0 = 1$ and $\mu_0 = 0$ and Eq. (75) simplifies to:

$$\tilde{H}_p = \sum_{k'}\left[-\frac{1}{2}\gamma h_z \frac{B_k}{\omega_k} - \gamma h_T\left[\frac{J_k^* \lambda_k^2 - J_k \lambda_k \mu_k}{\omega_0 - 2\omega_k}\right]\right. \tag{76}$$

$$\left. -\gamma h_T^*\left[\frac{J_k^* \mu_k^2 - J_k \lambda_k \mu_k^*}{\omega_0 + 2\omega_k}\right]\right] b_k^* b_{-k}^* \quad + c.c.$$

The first term corresponds to parallel pumping by the z component of the microwave field h_z. The second term corresponds to perpendicular pumping by the component of the transverse field with c.c.w. circular polarization. The third term corresponds to perpendicular pumping by the component of the c.w. circular polarization. The reader may be surprised that this last case can contribute since it is opposed to the direction of precession of the uniform mode. However the important factor is how far the excitation is detuned from ω_0: the c.c.w. case is typically detuned by $\frac{1}{2}\omega_p$ while the c.w. case is typically detuned by $\frac{3}{2}\omega_p$. Noting that $\omega_k \approx \frac{1}{2}\omega_p$ we see that these factors appear in the denominators of the respective terms, hence the third term

will be at least 3 times smaller than the second (in the subsidiary resonance regime) and may be considerably smaller still due to factors in the numerator.

Effects of Resonator and Waveguide

In the experimental setup, the microwave pumping field is generated by a resonator which surrounds the sample, as was discussed in Sec. 2.1. This device serves the same purpose as a cavity, i.e., to intensify the field, and a similar analysis to that presented can be applied to that case. The resonator amplitude will be represented by R, a complex variable, chosen so that R and R^* behave as canonical variables and contribute a term $\tilde{H}_R$ to the Hamiltonian:

$$\tilde{H}_R = \omega_R R^* R \tag{77}$$

where ω_R is the resonator frequency. The resonator can be represented as a series LC circuit. This has total energy $\frac{1}{2}LI^2 + \frac{1}{2}CV^2$ where L is the inductance, C is the capacitance, V is the voltage and I is the current. In terms of these variables a suitable expression for R is:

$$R = \left[\frac{L}{4C}\right]^{1/4} I + i\left[\frac{C}{4L}\right]^{1/4} V \tag{78}$$

and ω_R is given by

$$\omega_R = (LC)^{-1/2} \tag{79}$$

The magnetic field at the center of the resonator (excluding the sample) is proportional to I and hence to $R+R^*$ By equating the maximum field energy with $\tilde{H}_R$ we find that the field h_R is given by

$$h_R = \left[\frac{2\pi\omega_R}{V_R}\right]^{1/2} (R + R^*) \tag{80}$$

where V_R is the effective volume of the resonator. (V_R may include corrections for end effects but we will ignore these and use $V_R \approx 2.06\times10^{-3} cm^3$, the experimental volume within the

resonator used.) Since we wish to consider oblique pumping we assume that h_R is linearly polarized, lies in the x-z plane and makes an angle θ_R with the z axis. Thus the z component is given by

$$h_z = \left[\frac{2\pi\omega_R}{V_R}\right]^{1/2} (\cos\theta_R)(R+R^*) \tag{81}$$

and the transverse component is given by

$$h_z = \left[\frac{2\pi\omega_R}{V_R}\right]^{1/2} (\sin\theta_R)(R+R^*) \tag{82}$$

We may now insert this into the expression for $\tilde{H}_p$ (Eq. (76) or the more general case Eq. (75)) to obtain (keeping only terms with slow time dependence assuming $\omega_R \simeq 2\omega_k$)

$$\tilde{H}_p = \sum_k G_k R b_k^* b_{-k}^* + c.c. \tag{83}$$

where for the simpler case [Eq. (76)]

$$G_k = -\frac{1}{2}\gamma\left[\frac{2\pi\omega_R}{V_R}\right]^{1/2} \frac{B_k}{\omega_k}\cos\theta_R \tag{84}$$

$$-\gamma\left[\frac{2\pi\omega_R}{V_R}\right]^{1/2} \sin\theta_R \left[\frac{J_k^*\lambda_k^2 - J_k\lambda_k\mu_k}{\omega_0 - 2\omega_k} + \frac{J_k^*\mu_k^2 - J_k\lambda_k\mu_k^*}{\omega_0 + 2\omega_k}\right]$$

We will now consider the coupling of the resonator to the wave guide. In the wave guide there is an incoming wave h_{in} and an outgoing wave h_{out}. For simplicity we will assume a complex representation with the amplitude of h_{in} equal to the square root of the input power P_{in}

$$h_{in} = P_{in}^{1/2} e^{i\omega_p t} \tag{85}$$

Both h_{in} and h_{out} are taken to be the effective amplitude of the waves at the location of the sample. The outgoing wave h_{out} is made up of two components: h_{in} is reflected at the end of the wave guide and becomes the first component; the second component is the emission from the resonator and is assumed to be directly proportional to the resonator amplitude R:

$$h_{out} = h_{in} + i\beta R \tag{86}$$

where β is a complex constant. From this expression we can determine the power entering the

wave guide from the sample P_w:

$$P_w = |h_{out}|^2 - |h_{in}|^2 = \beta\beta^* RR^* + i\beta Rh_{in}^* - i\beta^* R^* h_{in} \tag{87}$$

This must be balanced by the power entering the resonator $\frac{d}{dt}(\omega_R R^* R)$ (less resistive damping and sample interaction terms) and by the rate of change of the interaction energy, E_{int}, between the resonator and wave guide fields. We can expect the slowly varying part of E_{int} to be of the form

$$E_{int} = \xi h_{in}^* R + \xi^* h_{in} R^* \tag{88}$$

where ξ is a complex constant. The term $\beta\beta^* RR^*$ in Eq. (87) must be balanced by a radiative damping term $-\Gamma_{rad} R$ in the equation for $\dot{R}$. There must also be a term coupling to the incoming wave h_{in} so we expect that :

$$\dot{R} = -(\Gamma_{res} + \Gamma_{rad})R + i(\omega_R R + \alpha h_{in} + \sum_{\mathbf{k}} G_{\mathbf{k}}^* b_{\mathbf{k}} b_{-\mathbf{k}}) \tag{89}$$

where Γ_{res} is the resistive damping (Γ_{res} and Γ_{rad} are both assumed real) and α is a complex parameter. (Note that we have omitted the coupling term to the uniform mode, of the form $G^* b_0$, since it is of no importance if $\omega_p \neq \omega_0$. Its only effect is to slightly shift the resonant frequency ω_R). The balance of power determines the relationship between α, β, ξ, and Γ_{rad}:

$$\Gamma_{rad} = \frac{1}{2}\alpha\alpha^*\omega_R \tag{90}$$

$$\beta = \alpha^* \omega_R \tag{91}$$

$$\xi = \alpha^* \tag{92}$$

Thus we only need to know the complex parameter α.

One case of particular interest is critical coupling. In this case we choose α so that $h_{out} = 0$ to obtain maximum efficiency, thus

$$h_{in} = -i\alpha^* R\,\omega_R \tag{93}$$

For steady state the right hand side of Eq. (89) must equal $i\omega_p R$. Assuming $\omega_{\mathbf{k}} = \omega_p$ and all b_k's are zero (below threshold) the condition for critical coupling is:

$$\Gamma_{rad} = \Gamma_{res} = \frac{1}{2}\alpha\alpha^{*}\omega_R \tag{94}$$

or:

$$|\alpha| = (2\Gamma_{res}/\omega_R)^{1/2} = Q^{-1/2} \tag{95}$$

where Q is the quality factor of the resonator ($Q \equiv \omega_R/2\Gamma_{res}$). If we take $Q \approx 500$ for the experimental resonator, then $|\alpha| \approx 0.045$. The fact that the critical condition depends only on the magnitude of α implies that this can be achieved in general by the adjustment of only one experimental parameter. This is found to be the case – adjustment of the sliding short alone is sufficient to achieve a null in the reflected power.

Elimination of the Resonator Variable

Under certain conditions the resonator may be eliminated as a dynamical variable. The main requirement is that the damping of the resonator, $\Gamma_{res} + \Gamma_{rad}$, must be much greater than the effective damping, γ_k, for the spin wave modes being excited. γ_k represents the combined effects of a variety of mechanisms whereby the energy of the excited spin waves couples to the thermal reservoir of phonons and magnons. γ_k is introduced phenomenologically into the equations of motion by modifying Hamilton's equations:

$$\frac{\partial b_k}{\partial t} = i\frac{\partial \bar{H}}{\partial b_k^{*}} - \gamma_k b_k \tag{96}$$

thus the equation for $\dot{b}_k$ is:

$$\dot{b}_k = (i\omega_k - \gamma_k)b_k + 2G_k R b_{-k}^{*} + i\sum_{k'}(2T_{kk'}|b_{k'}|^2 b_k + S_{kk'}b_{k'}b_{-k'}b_{-k}^{*}) \tag{97}$$

We will now change to show variables:

$$b_k = \tilde{c}_k e^{i\omega_p t/2} \tag{98}$$

$$R = R_0 e^{i\omega_p t} \tag{99}$$

substituting these expressions into Eqs. (89) and (97) and using Eq. (85) for h_{in} we obtain:

$$\dot{R}_0 = -\Gamma R_0 + i(\Delta\Omega_R R_0 + \alpha P_{in}^{1/2} + \sum_k G_k^* \tilde{c}_k \tilde{c}_{-k}) \tag{100}$$

$$\dot{\tilde{c}}_k = (-\gamma_k + i\Delta\Omega_k)\tilde{c}_k + 2iG_k R_0 \tilde{c}_{-k}^* + i\sum_{k'}(2T_{kk'}|\tilde{c}_{k'}|^2 \tilde{c}_k + S_{kk'}\tilde{c}_{k'}\tilde{c}_{-k'}\tilde{c}_{-k}^*) \tag{101}$$

where $\Gamma = \Gamma_{rad} + \Gamma_{res}$, $\Delta\Omega_R = \omega_p - \omega_R$, and $\Delta\Omega_k = \omega_k - \omega_p/2$. Assuming that $\Gamma \gg \gamma_k$ we can expect R_0 to be in quasi-equilibrium with $\dot{R}_0 \ll \Gamma R_0$ so that we may set $\dot{R}_0 \simeq 0$. Eq. (100) may then be solved for R_0:

$$R_0 = \frac{i}{\Gamma - i\Delta\Omega_R}(\alpha P_{in}^{1/2} + \sum_k G_k^* \tilde{c}_k \tilde{c}_{-k}) \tag{102}$$

Using this in the equation for $\dot{\tilde{c}}_k$ we obtain

$$\dot{\tilde{c}}_k = (-\gamma_k + i\Delta\Omega_k)\tilde{c}_k - g_k P_{in}^{1/2}\tilde{c}_{-k}^* + i\sum_{k'} 2T_{kk'}|\tilde{c}_{k'}|^2 \tilde{c}_k + (S_{kk'} + R_{kk'})\tilde{c}_{k'}\tilde{c}_{-k'}\tilde{c}_{-k}^* \tag{103}$$

where

$$R_{kk'} = 2iG_k^* G_k/(\Gamma - i\Delta\Omega_R) \tag{104}$$

and

$$g_k = \frac{2G_k\alpha}{\Gamma - i\Delta\Omega_R} \tag{105}$$

We must now discuss the relationship between c_k and c_{-k}. Since we are dealing with a sample of finite size, it makes no sense to talk of traveling spin waves. Instead, the theory must be compatible to the fact that the sample must exhibit standing waves. In order to create standing waves, we must require

$$\tilde{c}_{-k} = e^{iq_k}\tilde{c}_k \tag{106}$$

where q_k is a real phase factor. If we take this as an initial condition, then an examination of the equations for c_k and c_{-k} shows that the condition will remain true [noting that $T_{k,k'} = T_{-k,-k'}$ and $S_{k,k'} = S_{-k,-k'}$]. If we define a new variable c_k by:

$$\tilde{c}_k = c_k e^{-iq_k/2} \tag{107}$$

so that by Eq. (106):

$$\tilde{c}_{-k} = c_k e^{iq_k/2} \tag{108}$$

then we may write Eq. (103) as

$$\dot{c}_{\mathbf{k}} = (-\gamma_k + i\Delta\Omega_k)c_{\mathbf{k}} - g_{\mathbf{k}}P_{in}^{1/2}c_{\mathbf{k}}^{*} + i\sum_{\mathbf{k}'} 2T_{\mathbf{k}\mathbf{k}'}|c_{\mathbf{k}'}|^2 c_{\mathbf{k}} + (S_{\mathbf{k}\mathbf{k}'} + R_{\mathbf{k}\mathbf{k}'})c_{\mathbf{k}'}^{2}c_{\mathbf{k}}^{*} \tag{109}$$

Note that this equation still includes a sum over positive and negative values of k′ – these may be combined if desired. Eq. (109) is the main analytical result and will be numerically solved in Sec. 4.

There are a number of symmetries satisfied by the spin wave coupling coefficients $T_{\mathbf{k}\mathbf{k}'}$ and $S_{\mathbf{k}\mathbf{k}'}$. First, we note that certain terms are equivalent: $S_{\mathbf{k},\mathbf{k}'}$, $S_{\mathbf{k},-\mathbf{k}'}$, $S_{-\mathbf{k},\mathbf{k}'}$, and $S_{-\mathbf{k},-\mathbf{k}'}$ all multiply the same term ($c_{\mathbf{k}'}c_{-\mathbf{k}'}c_{\mathbf{k}}^{*}c_{-\mathbf{k}}^{*}$) in the Hamiltonian and similarly, $T_{\mathbf{k}\mathbf{k}'}$ and $T_{\mathbf{k}'\mathbf{k}}$ both multiply the same term ($c_{\mathbf{k}'}c_{\mathbf{k}'}^{*}c_{\mathbf{k}}c_{\mathbf{k}}^{*}$). Thus we are free to choose these coefficients so that

$$T_{\mathbf{k}'\mathbf{k}} = T_{\mathbf{k}\mathbf{k}'} \tag{110}$$

and

$$S_{\mathbf{k},\mathbf{k}'} = S_{\mathbf{k},-\mathbf{k}'} = S_{-\mathbf{k},\mathbf{k}'} = S_{-\mathbf{k},-\mathbf{k}'}. \tag{111}$$

These relations were used in obtaining Eq. (101). We also find from simple inversion symmetry that

$$T_{-\mathbf{k},-\mathbf{k}'} = T_{\mathbf{k}\mathbf{k}'} \tag{112}$$

However, $T_{\mathbf{k},-\mathbf{k}'}$ and $T_{\mathbf{k},\mathbf{k}'}$ are not required to be equal. Some additional conditions follow from the fact that the Hamiltonian is real:

$$S_{\mathbf{k}\mathbf{k}'} = S_{\mathbf{k}'\mathbf{k}}^{*} \tag{113}$$

and

$$T_{\mathbf{k}\mathbf{k}'} = T_{\mathbf{k}'\mathbf{k}}^{*} \tag{114}$$

From Eqs. (110) and (114) we see that $T_{\mathbf{k}\mathbf{k}'}$ must be real while $S_{\mathbf{k}\mathbf{k}'}$ may be complex except for the diagonal terms $S_{\mathbf{k}\mathbf{k}}$ which must be real. As can be seen from Eqs. (104) and (84), $R_{\mathbf{k}\mathbf{k}'}$ satisfies the same conditions as $S_{\mathbf{k}\mathbf{k}'}$ in Eq. (111). The fact that $T_{\mathbf{k}\mathbf{k}'}$ is real implies that these terms cannot result in energy transfer between modes as they only effect the phase and not the amplitude – all energy transfer takes place via the $S_{\mathbf{k}\mathbf{k}'}$ and $R_{\mathbf{k}\mathbf{k}'}$ terms.

3.2 Quantum Formulation – Outline

The various steps which were required to obtain the classical Hamiltonian all have their analogs using quantum operators. However, we will not go through this development in full detail but instead will give only a brief outline.

The first step is to express the Hamiltonian in terms of transverse spin operators – analogous to the transverse magnetization M_T:

$$S_{n+} = S_{nx} + iS_{ny} \quad and \quad S_{n-} = S_{nx} - iS_{ny} \tag{115}$$

One then performs the Holstein-Primakoff transformation to new variables a_n and $a_n\dagger$:

$$S_{n+} = (2S)^{1/2} a_n\dagger \left[1 - \frac{a_n\dagger a_n}{2S}\right]^{1/2} \tag{116}$$

$$S_{n-} = (2S)^{1/2} \left[1 - \frac{a_n\dagger a_n}{2S}\right]^{1/2} a_n$$

$$S_{nz} = -S + a_n\dagger a_n$$

where the square roots are interpreted formally as infinite series. The a_n's satisfy the commutation relations

$$[a_n, a_{n'}\dagger] = \delta_{nn'}. \tag{117}$$

$a_n\dagger$ and a_n correspond to $s(\mathbf{r})$ and $s(\mathbf{r})^*$ in the classical treatment. These are then expanded in a Fourier series:

$$a_n = \frac{1}{\sqrt{N}} \sum_{\mathbf{k}} a_{\mathbf{k}} \exp(i\,\mathbf{k}\cdot\mathbf{r}_n) \tag{118}$$

$$a_n\dagger = \frac{1}{\sqrt{N}} \sum_{\mathbf{k}} a_{\mathbf{k}} \exp(-i\,\mathbf{k}\cdot\mathbf{r}_n)$$

Where N is the total number of unit cells in the sample. One then performs the Bogoliubov transformation

$$a_{\mathbf{k}} = \lambda_{\mathbf{k}} \nu_{\mathbf{k}} - \mu_{\mathbf{k}} \nu_{-\mathbf{k}}\dagger \tag{119}$$

where the magnon raising and lowering operators $\nu_{\mathbf{k}}\dagger$ and ν_k correspond to the spin wave vari-

ables v_k^* and v_k in the classical treatment. Finally, we may make the transformation to $b_k\dagger$ and b_k, corresponding to Eq. (71), which eliminates cubic terms from the Hamiltonian, alters the nature of the coupling to the resonator, and renormalizes the quartic terms.

One may convert the classical expression to the corresponding quantum expression by replacing b_k with $\hbar^{1/2} b_k\dagger$, and replacing b_k^* with $\hbar^{1/2} b_k$. Note that in the conventional notation it is the raising operators $b_k\dagger$ which have positive frequency and therefore correspond to our classical b_k. The state of the resonator may also be quantized – we similarly replace R with $\hbar^{1/2} R\dagger$ and R^* with $\hbar^{1/2} R$, where $R\dagger$ and R are the raising and lowering operators for the electromagnetic state of the resonator. The number of k-magnons in the sample or of photons in the resonator are determined by the number operators $b_k\dagger b_k$ and $R\dagger R$ respectively. The Hamiltonian including resonator terms becomes:

$$\bar{H} = \hbar\,\omega_k b_k\dagger b_k + \hbar\,\omega_R R\dagger R \tag{120}$$

$$+\hbar^{3/2}\sum_k G_k R b_k^* b_{-k}^* + h.c. + \hbar^{1/2}\alpha h_{in} R^* + h.c.$$

$$+\hbar^2\sum_{kk'}\frac{1}{4}(S_{kk'} b_{k'} b_{-k'} b_k\dagger b_{-k}\dagger + h.c.) + \frac{1}{2}(T_{kk'} b_k\dagger b_k b_{k'} b_{k'} + h.c.)$$

where h.c. = hermitian conjugate. The equations of motion for the magnon operators are now given by:

$$\frac{\partial b_k}{\partial t} = \frac{-i}{\hbar}\frac{\partial \bar{H}}{\partial b_k\dagger} - \gamma_k b_k \tag{121}$$

and for the resonator by:

$$\frac{\partial R}{\partial t} = \frac{-i}{\hbar}\frac{\partial \bar{H}}{\partial R\dagger} - \Gamma R \tag{122}$$

where we have included the phenomenological damping rates γ_k and Γ.

3.3 Spherical Spin-Modes

In deriving our spin wave equations of motion, we have made one major approximation – we have used an expression in planar spin waves rather than spherical spin-modes. The theory of these modes was first developed by Walker[3-5] and they are often referred to as Walker modes or magnetostatic modes. Walker's analysis covers spheroids, axially aligned with the d.c. field, but does not include the effects of exchange or anisotropy. The spherical case was studied in much greater detail by Fletcher and Bell.[6,7] Damon and Eshbach[10] discuss the modes of a ferromagnetic slab.

Walker assumes, as we did in the previous analysis, that propagation effects may be neglected (i.e. $\nabla \times \mathbf{B} = 0$). This allows one to define a magnetic potential ψ such that

$$\mathbf{H} = \nabla \psi \tag{123}$$

The Maxwell equation $\nabla \cdot B = 0$ leads to an equation relating ψ and M:

$$\nabla^2 \psi + 4\pi \nabla \cdot \mathbf{M} = 0 \tag{124}$$

additionally we have the gyromagnetic equation:

$$\frac{\partial \mathbf{M}}{\partial t} = -\gamma \mathbf{M} \times \mathbf{H} \tag{125}$$

by performing a linearized analysis and imposing appropriate boundary conditions a general solution may be found for ψ both inside and outside of the sphere. Solutions are characterized by three indices (n, m, r). ψ_{nmr} has $n - |m|$ zero's (not counting end points) as θ is varied from 0° to 180°. The ϕ and time dependence of ψ (in complex representation) is of the form $\exp(im\phi + i\omega t)$ while the other part of ψ may be taken to be real. The index n is restricted to positive integers, while m may be positive or negative in the range $-n$ to n. For $m > 0$ there are $[n - |m|/2] + 1$ values of r (labeled 0, 1, 2, ...) while for $m < 0$ there are $[n - |m|/2]$ values (labeled 1, 2, 3, ...) where [x] is the largest integer in x. Modes with $r = 0$ take the form of surface waves[11] (particularly for large n); the frequency of these modes lie in a band which

is just above the band occupied by planar spin waves (for no exchange). The modes with $r \neq 0$ and the uniform mode (1,1,0) lie in a band that corresponds to the planar spin wave band. If we express ψ as $\psi_0 e^{i(m\phi+\omega t)}$ then the magnetization can be expressed as

$$4\pi M_r = \mathrm{Re}\left[\left[\kappa\frac{\partial\psi_0}{\partial r} + \nu\frac{m\psi_0}{r}\right] e^{i(m\phi+\omega t)}\right] \tag{126}$$

$$4\pi M_\phi = -\mathrm{Im}\left[\left[\nu\frac{\partial\psi_0}{\partial r} + \kappa\frac{m\psi_0}{r}\right] e^{i(m\phi+\omega t)}\right]$$

where M_r is the radial magnetization and M_ϕ is the angular magnetization. κ and ν are related to the frequency of the mode by

$$\kappa \equiv \frac{(\gamma H_0 - \omega_m/3)\omega_m}{(\gamma H_0 - \omega_m/3)^2 - \omega^2} \tag{127}$$

$$\nu \equiv \frac{\omega\omega_m}{(\gamma H_0 - \omega_m/3)^2 - \omega^2}$$

where $\omega_m = 4\pi M_s \gamma$. Note: κ and ν are both ordinarily negative. The spins precess in elliptical orbits with either the major or minor axis of the ellipse oriented radially. Spins on an axially aligned circle in the sample all precess on identical ellipses with relative phases varying as $m\phi$, as shown in Fig. 16 for several values of m. Thus modes with $m \neq 0$ take the form of circulating waves moving with angular phase velocity ω/m. The case of $m = 0$ is a "breather mode" in which all spins on the circle move inwards and outwards (on the ellipses) together. Note that the uniform mode (1, 1, 0) is not a breather mode, it has $m = 1$ not $m = 0$. The eccentricity of the ellipses is a necessary factor in their coupling to both the uniform mode and to parallel microwave fields. Because of the traveling wave nature of the solutions, m is similar to k in the plane wave expansion in that products of spin wave variables in the Hamiltonian should have a summed m value of zero, where the summed m value is just the sum of the m values of each variable, with the sign of m changed for those variables which are conjugated. A circularly polarized microwave field has $m = 1$, while a parallel microwave field has $m = 0$. If a spherical spin mode is represented as v_{nmr} (a complex amplitude) and if we normalize v_{nmr} so that the

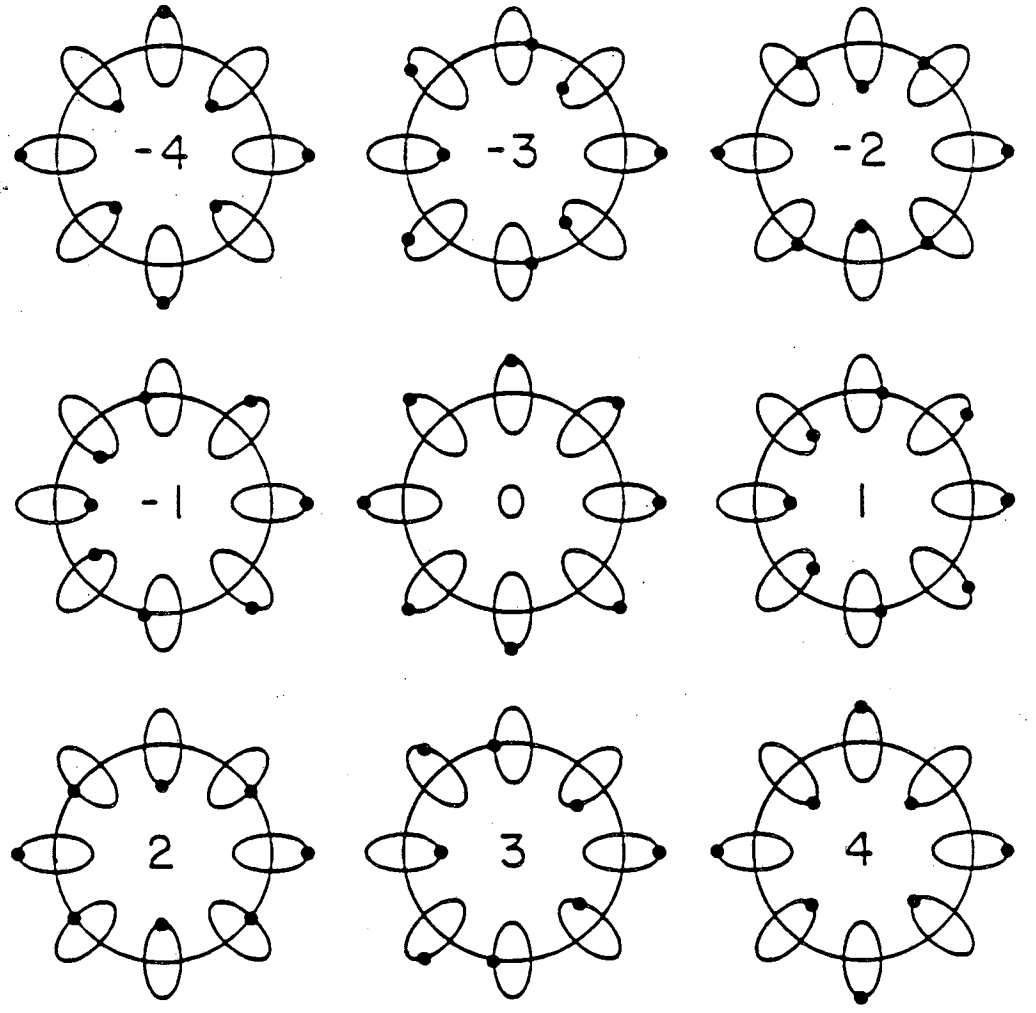

Figure 16. Spherical spin-mode: behavior of spins on an axially alligned circle for several values of m as indicated.

energy of the mode is in the usual canonical form $\omega_{nmr}\, v^{\bullet}_{nmr}\, v_{nmr}$ then we can expect the following terms in the Hamiltonian:

$$\bar{H} = \sum \omega_{nmr} v^*_{nmr} v_{nmr} + U^*_{nmr} R^* v_{n,m,r} v_{n,-m,r} + c.c. \qquad (128)$$

$$+ g^*_{nmr} v^*_{110} v_{nmr} v_{n,1-m,r} + c.c. + \hat{g}^*_{nmr} v_{110} v_{nmr} v_{n,-1-m,r} + c.c$$

$$+ G^* R^* v_{110} + c.c. + \textit{other triple products and higher order terms.}$$

The parallel pumping term $U^*_{nmr} R^* v_{nmr} v_{n,-m,r}$ is relatively easy to justify. Here we just compute the z component of the magnetization and integrate this with the applied parallel field over the sample. The z component of the magnetization is approximately M_s minus one half of the square of the transverse magnetization. The transverse magnetization in turn can be expressed as a linear combination of the v_{nmr} amplitudes times appropriate phase factors. After squaring and integrating the only contributing terms are products of the form shown. The coefficient U^*_{nmr} is determined primarily by the eccentricity of the precession orbits.

The triple terms which couple the uniform and spin wave modes (the terms with coefficients g^*_{nmr} and $\hat{g}^*_{nmr}$) are more difficult to justify. Here we rely on analogy with the plane wave analysis. Since the uniform mode has $m = 1$, the other two modes in the triple product do not have exactly opposite values of m as they did in the parallel case. We have required n and r (as we did in the parallel case) to be the same for these two modes as otherwise we would expect the interaction to integrate to zero. Other than to point out the importance of having some eccentricity, little is known at present about the dependence of the coupling coefficients on n, m, and r.

The coupling to the uniform mode $G^* R^* v_{110}$ is of the expected form and the coefficient G may be obtained from Eqs. (66) and (82) where v_{110} was called v_0 and which includes anisotropy effects. This form of the Hamiltonian is equivalent to the one we derived previously for planar spin waves with one exception – the modes (n, m, r), $(n, -m, r)$, $(n, 1-m, r)$, and $(n, -1-m, r)$ will not have exactly the same frequency as each other (while the k and -k modes did in the planar case). For low order modes the difference in frequency can be significant – the driving frequency will be split not in half but rather into two different values. This might then

have a significant impact on the resultant dynamics – in particular our assumption that $c_k = c_{-k}$ may not carry over to the corresponding conditions: $c_{nmr} = c_{n,-m,r} = c_{n,1-m,r} = c_{n,-1-m,r}$. However, for high order modes (n large) it would seem reasonable to expect the condition of frequency equality to be nearly satisfied.

It is desirable to find out the approximate values for n, m, and r in various regions of the parameter space, particularly the fine structure region. This cannot be stated with any certainty as yet, however we can discuss some possibilities. The main experimental fact we have is that the mode spacing is $\Delta H = 0.16$ Gauss in the fine structure region (see Sec. 2.3). One possibility is that this results from the increase in exchange energy with increasing wave number. Exchange effects are not included in Walker's analysis, however we can estimate this effect from our plane wave analysis. Using the dispersion relation Eqs. (59), (48) and (49), and neglecting anisotropy we have:

$$\omega_k^2 = (\gamma H_0 - \frac{1}{3}\omega_m + \gamma D k^2)(\gamma H_0 - \frac{1}{3}\omega_m + \gamma D k^2 + \omega_m \sin^2\theta_k) \tag{129}$$

if we assume $\Delta\omega_k = 0$ and $\Delta\theta = 0$ then we can obtain:

$$\Delta H_0 = 2Dk\Delta k \tag{130}$$

we can take Δk from the sphere's radius r_0 as $\Delta k \simeq \pi/r_0 = 95.2\text{cm}^{-1}$ assuming that the effective k value is determined primarily from oscillations in the radial direction. The experimental value of ΔH_0 allows us to compute k:

$$k \simeq 1.56\times10^5 cm^{-1}$$

using this k value we may determine the number n_r of half wavelengths along the radius of the sample:

$$n_r \simeq 1640$$

While this value of k is consistent with the operating conditions (see Fig. 2) the value of n_r seems excessively large for a high Q resonant mode. One might expect such a mode to have much higher damping due to surface roughness and other effects. Another reason why we

might doubt the calculated value of k is the fact that the work of Patton et al[53] suggests that a certain kink in the threshold curve is associated with the availability of low k, high Q modes, occurring when $\omega_p/2$ coincides with the upper ($\theta_k = 90°$) boundary of the spin wave manifold (Fig. 2). In the experiment this kink occurs just below the field at which the fine structure behavior is most clearly observed. In view of these facts another option may be considered – assume k is small so Δk is unimportant and allow $\Delta\theta$ to be nonzero. From Eq. (129) we can relate $\Delta\theta$, ΔH_0 and θ. Unfortunately, we do not have a simple relation giving the effective angle θ in terms of n, m, and r. However, on examining the literature on Walker modes, one finds that their frequencies do strongly depend on the field and the indices n, m, and r so that a sequence of modes could certainly be found which exhibit the observed behavior.

3.4 Fixed Points and Stability

As a first step to understanding the behavior of excited spin wave modes, we will consider the case where only one spin wave is excited. Examining Eq. (109) we find that $c_k = 0$ is always a fixed point - this is true regardless of how many spin wave modes are excited to nonzero values. However, this fixed point need not be stable, it's stability depends on the relative strength of the damping term - $\gamma_k c_k$ and forcing term $-g_k P_{in}^{1/2} c_k^*$. An important feature to note about Eq. (109) is that there is inversion symmetry - if $c_k(t)$ is a solution then so is $-c_k(t)$. This is also true for arbitrarily many modes, the sign of each may be changed independently without effecting the validity of the solution. To determine the stability of the fixed point $c_k = 0$, we need only consider the linear part of the equation:

$$\dot{c}_k = (-\gamma_k + i\Delta\Omega_k)c_k - g_k P_{in}^{1/2} c_k^* \tag{131}$$

This leads to the eigenvalue equation (in complex form):

$$\begin{bmatrix} A & B \\ B^* & A^* \end{bmatrix} \begin{bmatrix} \xi \\ \xi^* \end{bmatrix} = E \begin{bmatrix} \xi \\ \xi^* \end{bmatrix} \tag{132}$$

where

$$A = -\gamma_k + i\Delta\Omega_k B = -g_k P_{in}^{1/2}$$

E is the eigenvalue and ξ is the complex eigenvector. We set the determinant equal to zero:

$$\det \begin{bmatrix} A-E & B \\ B^* & A^*-E \end{bmatrix} = 0 \tag{133}$$

and solve for E obtaining:

$$E_{\pm} = \frac{A+A^*}{2} \pm \left[\left[\frac{A+A^*}{2} \right]^2 - (AA^* - BB^*) \right]^{1/2} \tag{134}$$

since $(A + A^*)/2 = -\gamma_k$ is always negative it is clear that both eigenvalues are negative if and only if $AA^* > BB^*$ or equivalently:

$$|M| > 1 \quad \text{for stability of } c_k = 0$$

where

$$M = (-\gamma_k - i\ \Delta\Omega_k)/g_k^* P_{in}^{1/2} \tag{135}$$

The condition $|M| = 1$ corresponds to the "Suhl threshold" for the mode k. Since $|M|$ is inversely related to input power P_{in}, $|M|>0$ is below threshold and $|M|<0$ is above threshold. Above threshold the origin is a saddle point as it always retains one stable eigenvalue. Immediately below threshold the origin is a stable node with two negative real eigenvalues. However, the eigenvalues may split into a conjugate pair below a lower threshold, which corresponds to a change from a stable node to a stable focus. This occurs for:

$$P_{in} < \Delta\Omega_k^2 / |g_k|^2$$

We will now consider nontrivial (or nonzero) fixed points. Since we are still considering the behavior of a single mode, the equation $\dot{c}_k = 0$ [from Eq. (109)] can be put in the simple form

$$M + N|c_k|^2 = \frac{c_k^2}{|c_k|^2} = \text{point on unit circle} \tag{136}$$

where $N = -i(2T_{kk} + S_{kk} + R^*_{kk})/g_k^* P_{in}^{1/2}$ and M is as defined previously, [Eq. (135)]. This equation has a simple geometrical interpretation, as shown in Fig. 17. We plot the point M and the unit circle in the complex plane. If we are below threshold then M lies outside the circle. We draw a line from the point M making an angle arg (N) with respect to the real axis. Typically this line will either miss the circle as in (a) in which case there are no nontrivial fixed points, or it will intersect the circle in two points as in (c) in which case there are two pairs of nontrivial fixed points $\pm c_k^{[1]}$ and $\pm c_k^{[2]}$. Nontrivial fixed points always come in pairs because of the symmetry of the equations mentioned previously. The transition between the two cases

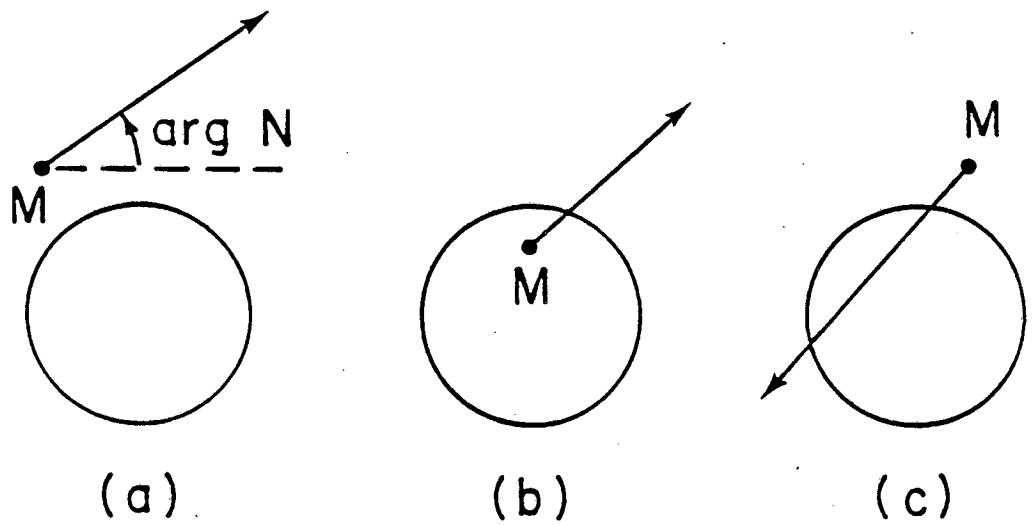

Figure 17. Nontrivial fixed point analysis: (a) No intersections with unit circle ⇒ no nontrivial fixed points. (b) One intersection with unit circle ⇒ one pair of nontrivial fixed points. (c) Two intersections with unit circle ⇒ two pairs of nontrivial fixed points.

occurs when the line is just tangent to the circle. This is a saddle-node bifurcation with the saddle being the intersection point closest to M. Above the Suhl threshold M is inside the circle and there is always one intersection point as in (b). There are two possibilities for what may occur when crossing the Suhl threshold and these are illustrated in Fig. 18. In the first case, which occurs for $\mathrm{Re}(M/N) > 0$, we obtain a supercritical symmetry breaking bifurcation as a complimentary pair of stable nontrivial fixed points emerge from the origin as the origin is changing stability. The second case, which occurs for $\mathrm{Re}(M/N) < 0$, involves the existence of the saddle and node below threshold. In this case we obtain a subcritical symmetry breaking bifurcation, where the unstable nontrivial fixed points (the saddle points) converse on the origin as it changes stability. There is a hysteresis loop as shown because the system must jump from the origin to one of the stable nodes which are at finite amplitude.

In the event that R_{kk} may be neglected, the type of bifurcation can be changed by changing the sign of $\Delta\Omega_k$. We find this experimentally in the region where the fine structure is observed (as mentioned previously in Sec. 2.3) but here the hysteresis is also a very fine effect,

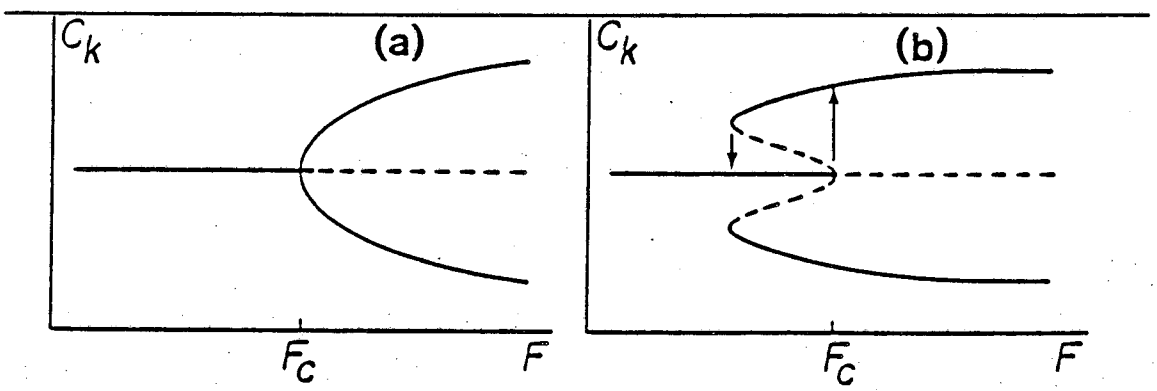

Figure 18. (a) Supercritical symmetry breaking bifurcation. F is the level of forcing (pump power), F_c is the bifurcation point or Suhl threshold. Solid lines – stable fixed points, dashed lines – unstable fixed points. (b) Subcritical symmetry breaking bifurcation, preceded by saddle node bifurcation of nonzero fixed points. Displays hysteresis as shown.

occurring over very small distances in parameter space. However, there is a region indicated in Fig. 6 in which the hysteresis occurs over a substantial distance in parameter – much more than can be attributed to a single mode. This is likely to be due to a related effect in which more than one mode is simultaneously excited.

3.5 Relaxation and Spiking Behavior Analysis

In the experiment it was observed that in certain regimes aperiodic relaxation type oscillations are observed which are characterized by alternating fast and slow phases, where in the fast phase, the amplitude of the reflected microwaves changes very rapidly and in the slow phase it changes much more gradually, typically by an order of magnitude or more (see Fig. 11). There has also been observed a related behavior pattern in which rapid spikes in the response are separated by long dormant periods of irregular length. This latter case has been the subject of much interest recently and there has been the suggestion that there may be a route to chaos by irregular periods.[54,55] We will now present a mechanism which can explain both types of behavior and discuss some of its effects on the dynamics of the experimental system.

The simplest system which can exhibit this type of behavior is a 2 mode system, represented by the complex variables c_1 and c_2. The mode c_1 will be called the "strong mode"; it is assumed that the pumping level is above the Suhl threshold for this mode. The mode c_2 will be called the "weak mode"; it is assumed that the pumping level is below the Suhl threshold for this mode. In the absence of coupling between c_1 and c_2, we would expect that the origin of c_1 would be a saddle point so that this mode would be attracted to a nonzero fixed point, while the origin would be stable for c_2 so this mode would decay to zero. However, due to intermodal coupling, the stability of the origin for c_2 can be affected by the amplitude of c_1. When coupling is included the stability criterion for $c_2 = 0$ is

$$\left| \frac{A + D|c_1|^2}{B + Fc_1^2} \right| \begin{matrix} > 1 & \textit{stable} \\ < 1 & \textit{unstable} \end{matrix} \tag{137}$$

where

$$A = -\gamma_2 - i\Delta\Omega_2$$

$$B = -g_2 P_{in}^{1/2}$$

$$D = -2iT_{2,1}$$

and

$$F = -i(S_{2,1} + R_{2,1}).$$

The assumption that c_2 is below its Suhl threshold (for $c_1 = 0$) implies that

$$|A| > |B|$$

There are four general cases for the behavior of the stability of c_2 as a function of c_1. Case 1: $|F| > |D|$. In this case, as $|c_1|$ is increased for any particular phase $\phi = arg\ c_1$ a point is reached beyond which the denominator in Eq. (137) becomes larger in magnitude than the numerator and stability is lost. The point of stability loss is a function of ϕ and has inversion symmetry as shown in Fig. 19 (a). Case 2: $|F| < |D|$ and $K > |BF|$, where $K \equiv [(|A|^2 - |B|^2)(|D|^2 - |F|^2)]^{1/2} + \mathrm{Re}\,AD^*$. In this case the point $c_2 = 0$ is a stable fixed point for all values of c_1 as shown in Fig. 19 (b). Case 3: $|F| < |D|$ and $-|BF| < K < |BF|$. In this case there are two symmetrically located stability zones in the c_1 plane as shown in Fig. 19 (c). Case 4: $|F| < |D|$ and $K < -|BF|$. This case has a annulus of instability as shown in Fig. 19(d). The general stability boundary for all three cases can be expressed as a quadratic solution:

$$|c_1|^2 = \frac{-b \pm (b^2 - 4ac)^{1/2}}{2a} \tag{138}$$

where

$$a = |D|^2 - |F|^2$$

$$b = AD^* + DA^* - BF^* e^{-i\phi} - FB^* e^{i\phi}$$

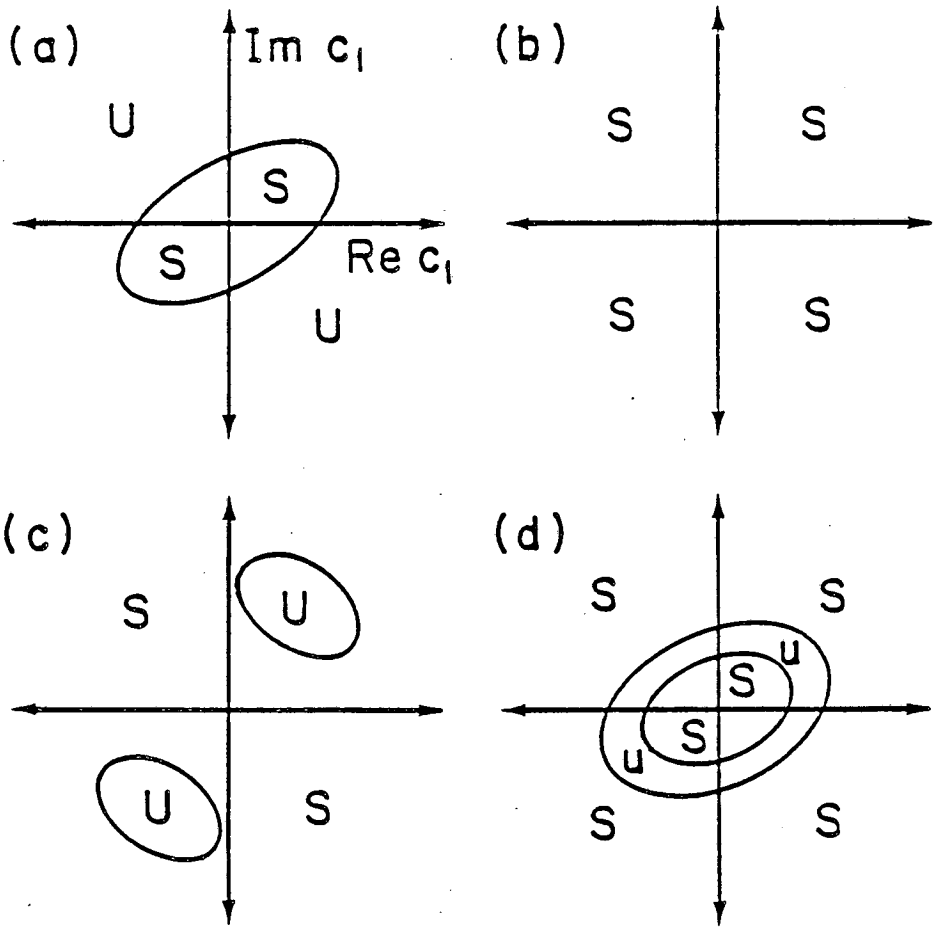

Figure 19. Stability curve for $c_2 = 0$ as a function of c_1. S = stable, U = unstable. (a) Case 1. (b) Case 2. (c) Case 3. (d) Case 4.

$$c = |A|^2 - |B|^2$$

Since for cases 2, 3, and 4, a and c are both positive, a solution for $|c_1|$ exists only if b is more negative than $-\sqrt{4ac}$ (in which case there are two solutions).

Now that we have analyzed the stability of the weak mode, we can proceed to explain the nature of the oscillations. We will suppose that c_1 and c_2 both start at some small but finite value. Then c_1 will increase, approaching a nontrivial fixed point and c_2 will decrease towards zero. Assuming that the nontrivial fixed point for c_1 lies in (or possibly across) a zone of instability for c_2, the phase path of c_1 will eventually enter this zone. Beyond this point c_2 will begin to increase. Under certain conditions, which we will not specify precisely but we will demonstrate in Sec 4, this can lead to a relaxation oscillation, with the fast phase occurring after c_1 reaches the instability boundary and the slow phase occurring when c_1 and c_2 both go back to values near 0. The reason that c_1 can return to a point near zero is that the origin for c_1 is a saddle point and therefore an orbit near the stable manifold may come quite close to the origin before escaping again. Orbits of the type we are describing are nearly homoclinic as they pass very close to a saddle point in the four-dimensional c_1,c_2 space. In the event that the weak mode has a focus at the origin, the orbit may be of the Silnikov type (see Guchenheimer and Holmes[56] for discussion) which is known to imply the existence of horseshoes and other complicated behavior. The distinction between relaxation oscillations and aperiodic spiking lies in the length of the dormant phase for the weak mode (examples of both are given in Sec. 4). During the dormant phase, the amplitude of c_2 decays exponentially. Consequently a moderately long dormant phase can easily result in the amplitude of c_2 decaying to the thermal magnon level. This introduces stochasticity into the dynamics – something which might not ordinarily be expected for oscillators whose peak amplitude is many orders of magnitude above the thermal level.

3.6 Generation of Microwave Subharmonics

We will now briefly discuss mechanisms whereby a subharmonic response at half the applied microwave frequency might be obtained from the spin system. No experimental data was taken of this effect (or lack of it), primarily because the wave guide used in the experimental setup has a lower cut off frequency of about 8 GHz and hence will not transmit the half frequency response at 4.6 GHz. However, this experiment could easily be done at some future time.

Although the parametrically excited spin waves we have been discussing have half of the pump frequency, these modes do not couple directly to the wave guide and no microwave subharmonic response will normally be obtained. There are, however, two mechanisms which might, under appropriate circumstances, allow a response at $\omega_p/2$. The first is the possibility of achieving a parametric excitation of the uniform mode at $\omega_p/2$. In the absence of crystalline anisotropy or shape anisotropy this can not occur because of symmetry. Crystalline anisotropy becomes important when the sample is not aligned with $\mathbf{H}_0$ along [111] or [100], and in particular if it is aligned along [110] (a saddle point in the anisotropy energy). Then there is a difference between the x and y anisotropy factors (N_{A-} in table 4) which gives the uniform mode an elliptical character to its motion. This ellipticity allows parametric coupling to the uniform mode for parallel pumping if $\omega_0 \approx \omega_p/2$. The coupling coefficient is $G_{\mathbf{k}}$ for $k = 0$ [see Eq. (84)] which is nonzero if N_{A-} is nonzero. In order to observe the response it will be necessary to pump obliquely so that there is a parallel component for excitation, and a perpendicular component allowing a direct coupling between the uniform mode and the resonator / wave guide so that the subharmonic response may be detected by the experimenter. The main difficulty in achieving this is that the anisotropy is not very large for YIG, and consequently the threshold for subharmonic excitation (or period doubling bifurcation point) will be relatively high, and one may expect that spin wave modes will begin to absorb power at a lower threshold - making

it very difficult to reach the subharmonic threshold. This difficulty might be countered by using a rare earth iron garnet some of which have very high anisotropies[33] at low temperature. Unfortunately, however, these garnets also have higher damping rates and thus have higher excitation thresholds.

The possibility of using shape anisotropy to couple parametrically to the uniform mode seems much more promising. This is because the asymmetric demagnetizing factor N_{D-} can be large (0.5 or 1) compared to N_{A-} (typically 0.1) and also because this term is only present in the equations for the uniform mode and will not enhance coupling to spin wave modes. In a loop gap resonator one could use an ellipsoidally shaped sample with two equal axes and one elongated axis along the resonator axis (but not the d.c. field axis) which could achieve an N_{D-} of nearly one half. In a cavity, a disc shaped sample could produce an N_{D-} of nearly 1 with H_0 parallel to the plane of the disc.

A second approach is to try to parametrically excite low order Walker modes[3] in the sample. These are the spherical spin modes which have sufficiently few spatial oscillations across the sample so that they can couple directly to a nonuniform microwave field. If there is a d.c. field for which such modes are parametrically excited at a lower threshold than the many high order modes, then a subharmonic response could be achieved since they may also couple directly to the applied microwave field. This effect may be distinguished from the parametric excitation of the uniform mode in that it may be achieved in a purely perpendicular pumping configuration, whereas the uniform mode case requires oblique pumping.

4 NUMERICAL SOLUTION OF SPIN WAVE EQUATIONS

In order to fully explore the behavior of the spin wave equation [Eq. (109)], it is necessary to use numerical methods, particularly when 2 or more interacting modes are involved. In this section we will discuss the procedures used to perform the numerical analysis and then present the results, many of which can be compared to the experimental results of Sec 2.3.

4.1 Procedures

Each spin wave mode is represented by a complex variable c_k which contains both amplitude and phase information for that mode. From Eq. (109), we obtain one equation for each mode which is coupled to all other excited modes through the interaction parameters $R_{kk'}$, $S_{kk'}$, and$T_{kk'}$, and to the microwave pumping field through the parameter g_k. The analytic results provide rough estimates for these parameters. They cannot be specified exactly from the theory for two reasons: 1) we do not know for certain which spin wave modes in the sample are being excited and involved in the dynamics, and 2) the plane wave approximation used in Sec. 3.1 can yield only approximate values for the interaction parameters of the spherical modes. We typically set the spin wave damping γ_k to $1\times10^6 s^{-1}$ and g_k to $1.414\times10^7 W^{-1/2}s^{-1}$, which results in a Suhl threshold of about 5 mW as is observed experimentally in the single mode region. $T_{kk'}$ and $S_{kk'}$ are estimated to be on the order of 10^{19} or 10^{20} $erg^{-1}sec^{-2}$, but may vary considerably depending on which modes are involved. In order to simulate the effect of a sequence of modes as was observed experimentally, we will not assume that the modes all have zero detuning, but will instead choose a sequence of equally spaced values for Δf_k which will typically extend from some negative value to some positive value, where $\Delta f_k \equiv \Delta\omega_k/2\pi$. If the excitation level is low, only those modes with detunings closest to zero will be excited. The

remaining modes will be below threshold and will remain at zero amplitude. From the observed field spacing of the modes (0.16 G) we can estimate the frequency spacing using $\Delta f_{mode} = \gamma \Delta H / 2\pi$ and obtain about 500 kHz.

The equations with appropriately chosen parameter values are numerically integrated using a 4-point Runge-Kutta Algorithm[57] on a Sun 3.0 computer. Initial conditions must always be chosen to be nonzero since zero is always a fixed point of the equations. Results are displayed on a graphics screen and may be printed on a laser printer to produce the figures given in Sec. 4.2. The Fortran code used to obtain these results is given in the Appendix.

4.2 Results

In the case of excitation of a single mode alone, the analytic results of Sec. 3.4 determine the location and stability of all fixed points. There is always at least one stable fixed point and the numerical results indicate that the system is always attracted to one of these; no periodic or chaotic attractors are observed. For appropriate parameter values hysteresis may be observed as was indicated in the theoretical treatment.

For two modes excited we first see periodic auto-oscillations. A particularly interesting form is observed, as shown in Fig. 20 (a) and (b). Here mode 2 is exhibiting an asymmetric orbit while mode 1 is exhibiting a symmetrical orbit of twice the period. Symmetrical orbits are possible because of the inherent inversion symmetry of the equations. When asymmetric orbits occur they always come in complimentary pairs ($C'(t) = -C(t)$). The nature of the coupling between modes allows the type of behavior observed - since the square of C_1 appears in the equation for C_2, a change sign of C_1 (to the opposite point on the symmetric orbit) has the identical influence on C_2.

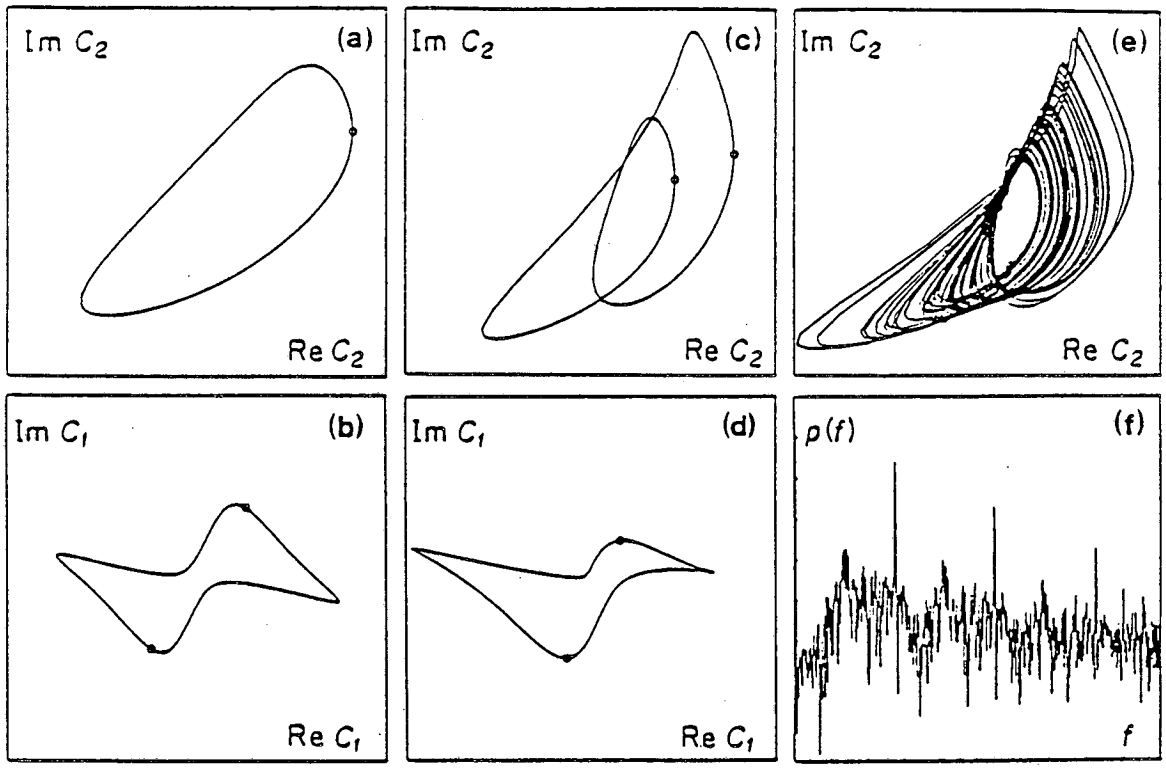

Figure 20. Computed behavior for two modes: (a) Phase portrait for periodic oscillations, asymmetric mode. Δf_1 = -300kHz, Δf_2 = 200kHz. (b) Symmetric mode. (c) Period doubling of asymmetric mode. Δf_1 = -385kHz, Δf_1 = 115kHz. (d) Symmetry breaking of symmetric mode. (e) Chaotic orbit following period doubling cascade; Δf_1 = -410kHz, Δf_1 = 90kHz. (f) Power spectrum of chaotic orbit, $f_{max} = 2.5$ MHz. For all figures, P_{in} = 0.027W, $\gamma_k = 1\times10^6 s^{-1}$, $g_k = 1.414\times10^7 W^{-1/2}s^{-1}$, $S_{kk'} = 4.078\times10^{19}G^{-2}s^{-2}$ for all k and k′, $T_{kk'} = -1.896\times10^{19}G^{-2}s^{-2}$ for k = k′ and = 0 for k ≠ k′, and $R_{kk'} = 0$ (assumed negligible) for all k and k′.

By changing the parameters this orbit may undergo a bifurcation. There are many parameters which could be adjusted to accomplish this, such as power input or pump frequency, however in Fig. 20c and d we have chosen to synchronously shift the detunings of the spin modes. This is equivalent to shifting the level of the d.c. magnetic field in the experiment. (We are assuming that all modes in the sequence have identical field dependence of their frequencies). The result is interesting - mode 1 exhibits a symmetry breaking bifurcation while mode 2 simultaneously exhibits period doubling. Further shifting the frequencies leads to a cascade of period doubling bifurcations for both modes, leading to a chaotic orbit (Figs 20e and f).

The numerical study for two modes also reveals behavior similar to the relaxation oscillations and aperiodic spiking behaviors of the experimental system. An example of this behavior is shown in Fig. 21 The mechanism for this behavior was discussed previously in Sec. 3.5. There is a "strong mode" which is above its threshold, and a "weak mode" which is initially below threshold but which can become excited for brief periods when sufficient excitation is supplied via the nonlinear coupling of the strong mode. Characteristically there is a slow or dormant phase during which the weak mode is decaying closer and closer to zero and the strong mode is changing at a relatively slow rate. At a certain critical point in the orbit of the strong mode, which is marked with an arrow in Fig. 21(a), a fast or active phase commences during which both modes (Figs. 21a and b) change rapidly. This is typically two or more orders of magnitude faster and shorter in duration than the slow phase. The decay of the mode during the dormant phase may be extreme - it has been observed in some cases in the numerical study to decay by over 10 orders of magnitude. This will easily take any experimental system to the thermal level, thus introducing a stochastic element into the dynamics. Orbits with a short dormant phase tend to have the relaxation oscillation appearance as in Fig. 21(c) [compare to experimental Fig. 11(a)] while orbits with a long dormant phase may tend to have the spiking appearance - Fig. 21(d). This dormant period may become arbitrarily long for certain parameter values. This is because the orbit is approaching a saddle loop bifurcation which occurs when

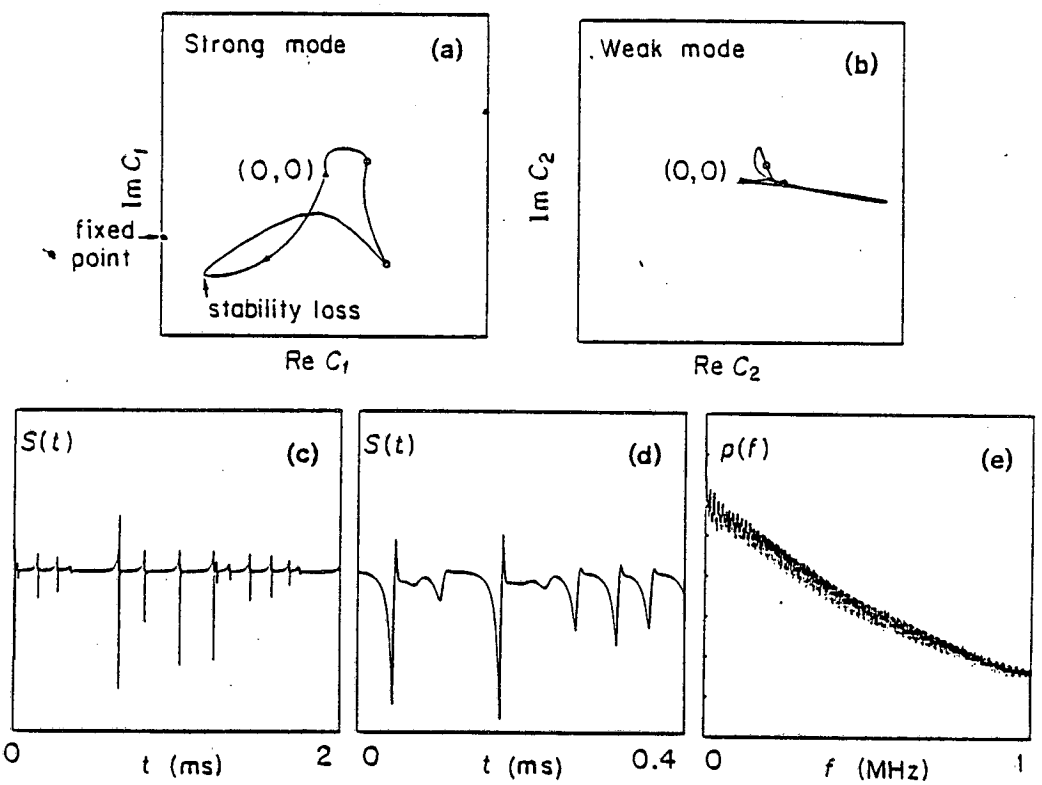

Figure 21. (a) aperiodic spiking – strong mode (mode 1). Arrow marks point of stability loss for weak mode (mode 2). Origin is at center of figure as indicated. Δf_1 = -200kHz, Δf_2 = 300kHz. (b) Weak mode. (c) Time series for aperiodic spiking behavior. (d) Time series for relaxation oscillations. Δf_1 = -175kHz, Δf_2 = 325kHz. (e) Fast Fourier transform for time series in (d). All figures have P_{in} = 0.0135W and the other parameters are the same as in Fig. 20.

the orbit connects the saddle point at the origin. Beyond this point a transition must occur to another attractor - typically a nonzero fixed point for the strong mode and zero for the weak

mode. It should also be noted that the relaxation and spiking behaviors do not have to be irregular - they may, for appropriate parameter values, be perfectly periodic. In some cases a cascade period doubling bifurcations to chaos has been observed to occur over extremely small changes in parameters (< 0.1% change). This has the appearance, on first examination, as an emergence of irregularity of the orbit starting at a critical parameter value.

With three modes some new phenomena emerge. One of these is the occurrence of quasiperiodic behavior with two incommensurate frequencies. An example of this is shown in Fig. 22. The three modes do not have exactly the same frequency, but rather are spaced equally in frequency by a small amount to simulate the effect of a series of modes as was observed in the experiment. Naturally all must be very near to half of the pumping frequency, and it is the detuning which plays an important role in the dynamics. The quasiperiodic orbit lies on a 2-torus in the phase space. By strobing every cycle we can make a Poincare section of the orbit. For a quasiperiodic orbit below the transition to chaos these points all lie on a closed curve – the intersection of the 2-torus with the surface of section. The section may be defined in various ways; in Fig. 22 (a) the section points are the maximum value of $\mathrm{Im} c_1$ for each cycle. The orbit shown can be found to emerge from a simple periodic orbit in a Hopf bifurcation (see discussion in Guckenheimer and Holmes[56]). In the Poincare section, the periodic orbit appears as a single point. This point spawns a circle at the bifurcation point which initially grows in size in proportion to the square root of the change in the parameter from its value at the bifurcation. While mode 1 and mode 2 (not shown) are exhibiting asymmetric orbits, mode 3 has a symmetric quasiperiodic orbit as shown in Fig. 22 (b). Section points on this orbit are made simultaneously with those of mode 1. They occur twice each cycle because the basic period here is twice that of mode 1. The symmetry causes a restriction on the frequencies that appear in the spectrum. The spectrum for mode 1 is shown in Fig. 22 (c). Here the allowed frequencies are all two component harmonics of the form $f_{mn} = mf_1 + nf_2$. The choice of f_1 and f_2 is not unique, but it is generally preferable to choose the two highest peaks. Fig. 22 (d) shows the

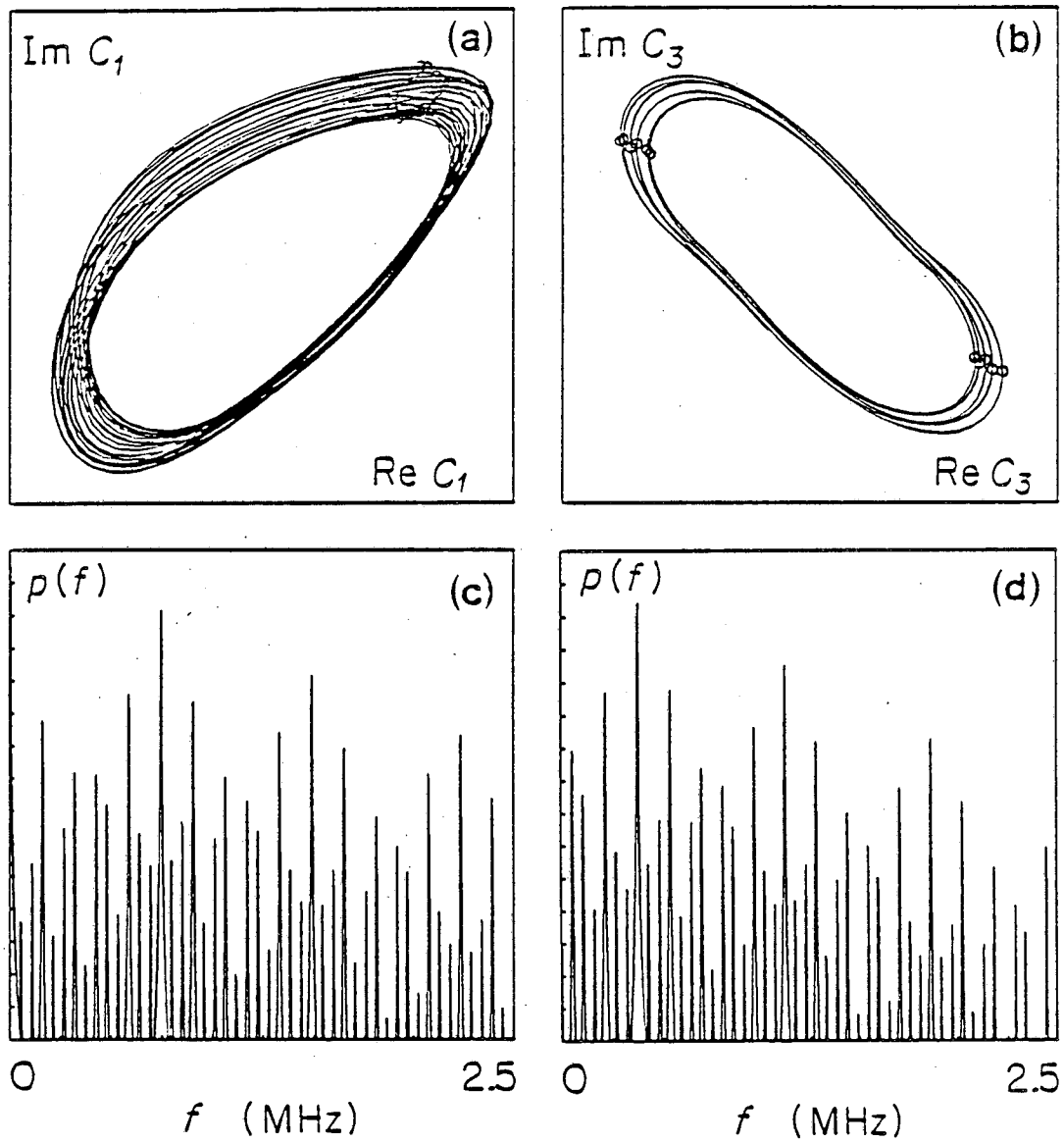

Figure 22. Computed quasiperiodic behavior for 3 modes: (a) Mode 1 for quasiperiodic orbit, circles mark Poincare section. (b) Mode 3: this mode exhibits a symmetrical orbit while mode 1 is asymmetrical. Mode 2 is similar to mode 1. (c) Fast Fourier Transform for mode 1, vertical range 150dB. Contains two component harmonics $f_{mn} = mf_1 + nf_2$, where f_1 and f_2 may be chosen to be the largest peaks in the spectrum. (d) Fast Fourier Transform for mode 3. Symmetry restricts peaks to those for which $m + n$ is odd. All figures have P_{in} = 0.027W, Δf_1 = -336kHz, Δf_2 = 164kHz, Δf_3 = 664kHz, $S_{kk'} = 3.971\times10^{19}G^{-2}s^{-2}$ for $k = k'$ and = $4.265\times10^{19}G^{-2}s^{-2}$ for $k \neq k'$, and other parameters same as in Fig. 20.

spectrum for mode 3. Here the allowed peaks are those for which $m + n$ is odd. This can be

shown to result from the symmetry of the orbit – see the detailed discussion in Part 2, Sec. 2.3. An alternate labeling scheme is very useful when the quasiperiodic orbit has just emerged from a periodic orbit following a Hopf bifurcation. This is to choose f_1 to be the fundamental frequency from before the bifurcation, and choose f_2 to be the difference between this and a nearby incommensurate peak. In this case the symmetry condition is that m must be odd, while n is unrestricted.

By changing the parameter values away from the Hopf bifurcation point, the 2-torus on which the orbit lies grows larger and becomes less smooth. At a certain critical point the orbit may become chaotic and the torus becomes fractal. This is the quasiperiodic route to chaos.[40,41] In Fig. 23 is shown a Poincare section of such a chaotic orbit and its power spectrum. This was reached by shifting the frequencies of the three modes synchronously, to simulate the effect of shifting the d.c. magnetic field in the experiment. The orbit is near to a period 5 phase locking, as can be seen in the 5 pointed character of the section and in the spectrum. There remain some surprisingly sharp peaks in the spectrum considering the complexity shown in the section.

More complicated versions of the relaxation oscillations are sometimes seen for three modes (as well as the variety previously described). In Fig. 24 is a case in which only the third mode (shown) is of the "weak" variety, while the other two modes are normally oscillating at a high level. The excitation which the weak mode receives from the pump and from the "strong" modes is just sufficient to allow it to grow at a slow rate from an initially very small amplitude. This growth may extend over several orders of magnitude in amplitude, lasting for a hundred cycles or more of the strong mode oscillation. Finally, when the size of the orbit becomes comparable to the size of the strong mode orbits, a rapid interaction phase occurs involving all three modes and leads to the return of the weak mode to a very low amplitude and then the process repeats. This appears to be an orbit of the "Silnikov" or spiral saddle type (see Guckenheimer and Holmes[56]), for which the existence of "horseshoes" and other complex behavior have been

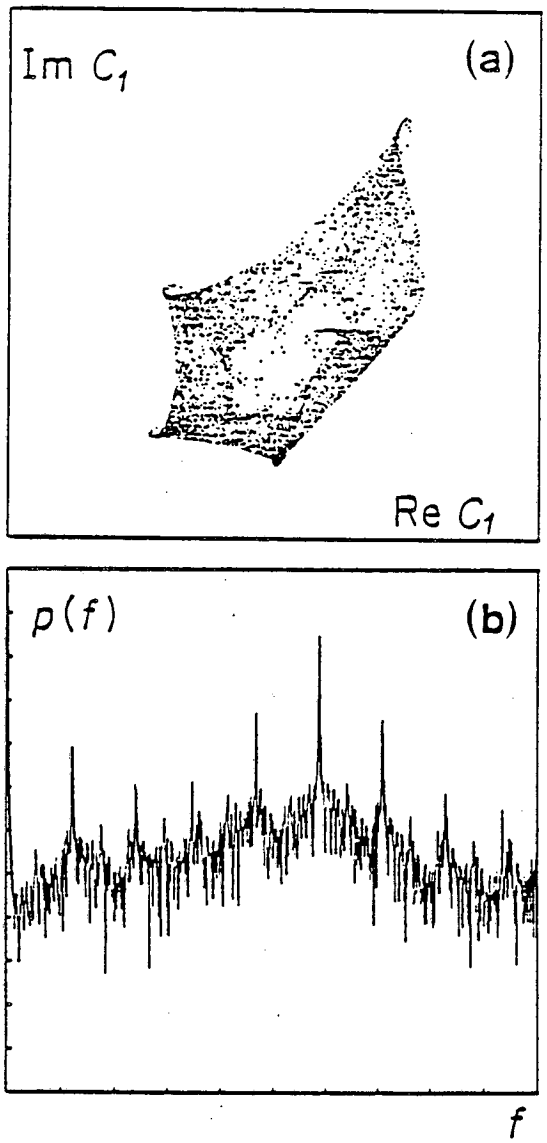

Figure 23 (a) Poincare section of chaotic orbit, following quasiperiodic transition to chaos. Proximity to period 5 locking produces five points on figure, Δf_1 = -334.5kHz, Δf_2 = 165.5kHz, Δf_2 = 665.5kHz, other parameters same as in Fig. 22. (b) FFT for orbit in (a).

explicitly shown.

This concept of a series of equally spaced modes may be taken to the limit of an infinite series. The reason that this works is that only those modes with relatively small detuning can

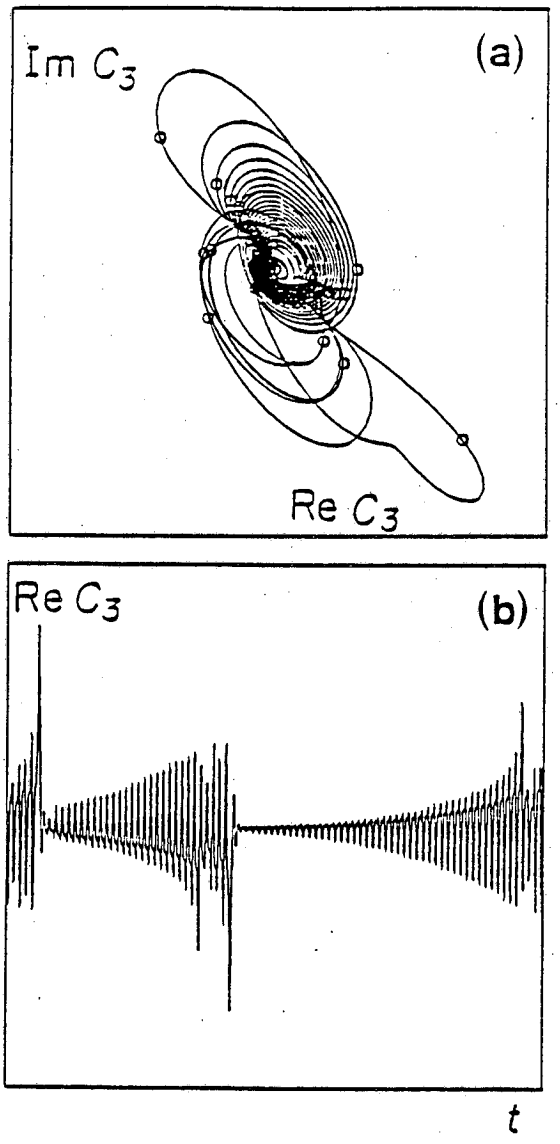

Figure 24. (a) Computed Silnikov type orbit for 3 modes. Only mode 3, the "weak mode", is shown. P_{in} = 0.02429W, Δf_1 = -300kHz, Δf_2 = 200kHz, Δf_2 = 700kHz, other parameters same as Fig. 20. (b) Time series for this orbit.

become excited and interact with the other excited modes. Modes which decay to zero have no effect on the excited modes. Thus we need to include in the computer simulation only those modes in the series with sufficiently small detuning (positive or negative) to become excited. The necessary number may be found by extending the series one mode at a time until the new

modes added are observed to be inactive. Since the series is infinite, its behavior in parameter space is periodic with respect to synchronously shifting the frequencies by the mode spacing. In Fig. 25 one period of the parameter space is shown. In this region, all of the types of behavior discussed previously may be found: stable fixed points (zero and nonzero), hysteresis, auto-oscillations, period-doubling, quasiperiodicity, chaos, and relaxation oscillations.

5 SUMMARY AND CONCLUSION

Excited spin waves in YIG form a weakly damped – nearly Hamiltonian – system, which displays a great variety of interesting nonlinear phenomena. The study focussed on the behavior of spin waves excited parametrically in a spherical sample via the first order Suhl instability. Data is primarily for perpendicular pumping, and with the d.c. field parallel to the [111] or easy axis of the crystal, but with some data for other orientations of pumping and crystalline axes. Observed phenomena includes: 1) fine structure – the excitation of single spin wave modes; 2) dynamics in the fine structure regime, involving the interaction of a small number (1, 2, 3, ...) of spin wave modes; these typically exhibit such phenomena as periodic auto-oscillations (typically 100 kHz), cascades of period doublings to chaos, and quasiperiodicity; 3) low frequency relaxation oscillations (Order 1 kHz) and aperiodic spiking (typically at somewhat higher frequencies); 4) high amplitude collective oscillations (presumably) involving the cooperation of many modes; these exhibit period doubling quasiperiodicity and phase locking of multiple frequencies, and various types of chaotic orbits; 5) abrupt emergence of high frequency noise; 6) hysteresis at the Suhl threshold in which the system jumps from a quiescent to a turbulent state; 7) in some cases a systematic increase in auto-oscillation frequency with pumping power is observed.

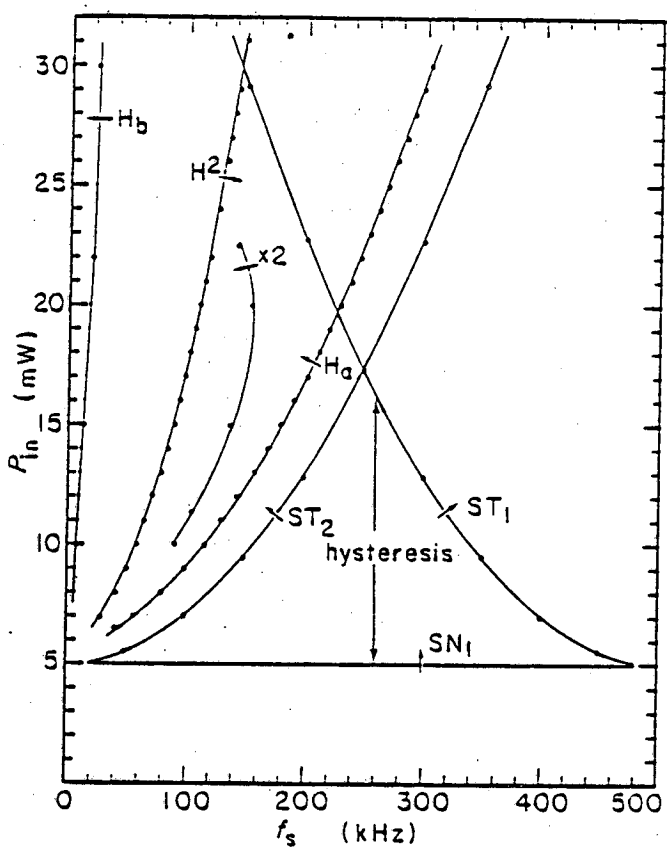

Figure 25. Computed parameter space diagram for mode series. Frequency shift f_s vs. applied power P_{in} (shift corresponds to change of d.c. field in experiment). The dynamics involve the active participation of zero, one, two, or three modes. At higher powers than shown in the figure additional modes may become involved. We label the modes as follows: mode 1 has $\Delta f_1 = f_s - 500\text{kHz}$, mode 2 has $\Delta f_2 = f_s$, mode 3 has $\Delta f_3 = f_s + 500\text{kHz}$. ST_1 and ST_2 are the Suhl thresholds for excitation of modes 1 and 2 respectively when all other modes are set to zero (this is actually a symmetry breaking bifurcation for the stable fixed point at zero). SN_1 is a saddle node bifurcation of nonzero fixed points below Suhl threshold [see Fig. 18 (b)]. Hysteresis is observed when traversing the region between SN_1 and ST_1. Crossing H_a in the direction of the arrow a Hopf bifurcation occurs in which a limit cycle involving modes 1 and 2 emerges from a fixed point. This is of the type shown in Fig. 20 (a) and (b). This oscillation undergoes a period doubling bifurcation upon crossing the line labeled ×2. Beyond this a cascade of period doublings occurs on route to chaos. On approach to the line H^2, mode 3 becomes active and the two mode solution we have been following is abruptly lost. H^2 actually corresponds to a secondary Hopf bifurcation from a 3 mode periodic orbit (on the left side) to a 3 mode quasiperiodic orbit (on the right side), of the type shown in Fig 22. H_b corresponds to another primary Hopf bifurcation, this time involving modes 2 and 3. Relaxation oscillations occur above the line ST_1 in the section below its intersection with ST_2. Onset appears to occur at the Suhl threshold ST_1.

A first principles theoretical analysis has been presented, based on the many earlier works on parametric excitation of spin waves, but developed here explicitly for the study of the nonlinear dynamics of excited spin wave modes. The theory explicitly includes the effects of crystalline and shape anisotropy. Also included are the interactions with the resonator (used to intensify the microwave field) and coupling to the waveguide. The result is a set of nonlinear equations coupling the spin wave modes with each other and with the pump, each mode being represented by a complex amplitude.

While the main analysis is made in the plane wave approximation an attempt is made to determine the effects of the true spherical spin-modes on the dynamics. A surprising result is that for very low order modes, the excitation may involve a pair of counter circulating waves with *different frequencies*. The sum of the two frequencies would have to very nearly equal the pumping frequency for resonance. For higher order modes however, the frequencies should be nearly the same, as they are for the plane wave approximation. It is not known as yet whether or not this effect can be detected experimentally.

An analysis has been made of trivial and nontrivial fixed points and it has been shown how this can lead to hysteresis at the Suhl threshold, an effect which was observed in the experiment.

Some theory is presented regarding relaxation oscillations and aperiodic spiking behavior, based on the concept of weak modes which are only active during short burst phases which may be instigated by the strong mode or modes reaching a critical threshold. An interesting result is that this is a natural way for stochasticity to enter into the experimental dynamics because during the dormant phase of the weak mode it can easily decay to the thermal magnon level. After this the subsequent dynamics become unpredictable. This analysis may be related to the work on irregular periods by Waldner et al.[54,55]

The possibility of generating microwave subharmonics at half of the pumping frequency is discussed based on the possibility of parametrically exciting either the uniform mode or a low order Walker mode which could couple directly as well as parametrically to the external field.

Finally a detailed study is made of the behavior of the spin wave equations of motion using numerical simulations. As a guide to comparison between the experimental data and numerical simulations, Table 5 is presented, which summarizes the work showing which data can be compared to which simulation.

Table 5: Guide to Data and Simulation Figures

Phenomena	Experimental Data	Simulation
Parameter space	Figs. 6, 7, 8	Fig. 25
Auto-oscillations	Fig. 9(a)	Fig. 20(a), (b)
Period-doubling	Fig. 9(b), (c), Fig. 13	Fig. 20(c)
Chaos	Fig. 9(d), (e)	Fig. 20(e)
Quasi-periodicity	Fig. 10	Fig. 22
Relaxation oscillations	Fig. 11	Fig. 21, Fig. 24
Phase locking	Fig. 14	---
Auto-osc. freq.	Fig. 15(a)	Fig. 15(b)
Broad band noise	Fig. 12	Fig. 21(e)

A series of equally spaced (in frequency) modes is studied, similar to that which was observed experimentally. For two modes auto-oscillations are observed which may exhibit some interesting symmetry characteristics. Relaxation and spiking behaviors are also observed, exhibiting the weak mode / strong mode behavior discussed in the theory. Cascades of period doubling bifurcations are also observed, leading to chaos. For three modes quasiperiodicity is first observed, along with phase locking phenomena, Hopf bifurcations, and the quasiperiodic route to chaos. Orbits nearly homoclinic to a spiral saddle point of the Silinkov type are also observed. The case of an infinite series of modes is also considered. It is possible to study due to the fact that only a few modes in the series have sufficiently small detuning to be excited. The type of behavior is periodic under a synchronous shifting of all of the frequencies of the modes by the frequency spacing of the modes. (This shifting corresponds to the effect of changing the d.c. field in the experiment.) A parameter space plot is made (pump power vs.

frequency shift) and compared with the behavior of parametrically excited surface waves.

Appendix: Computer Program Used in Sec. 4

The spin wave program numerically integrates and plots the spin wave dynamics as governed by Eq. (109) using a four point Runge Kutta algorithm, and can also accurately plot the Poincare section of the orbit and obtain the power spectrum using a fast Fourier transform. It is written in Fortran and uses double complex variables (this type is not available on all systems), as well as some real double precision variables. The subscripts k and k′ used in the text to refer to particular modes by their wavevectors are here converted to indices i and j since we will be dealing with the dynamics of some finite number of modes. The number of modes may be changed at any time by setting the variable nmag to the desired number. The spin wave variables c_i, are represented in the program by the complex variables ps(i), and their derivatives $\dot{c}_i$ by dp(i). The main parameters of interest in the program correspond to those used in the text as follows: pp corresponds to P_{in}, fp corresponds to $\omega_p/2\pi$, f0 corresponds to $\omega_0/2\pi$, gamc corresponds to Γ, gam0 corresponds to γ_0 (uniform mode damping, not used), gamk corresponds to γ_k (assumed equal for all modes), alpha corresponds to α, dfcav corresponds to $\Delta\Omega_R/2\pi$, df(i) corresponds to $\Delta\Omega_i/2\pi$, gk(i) corresponds to g_i, tkk(i,j) corresponds to T_{ij}, skk(i,j) corresponds to S_{ij}, rkk(i,j) corresponds to R_{ij}. Some control variables are: dt (the time step in seconds), nn0 (the number of steps per continue command 'c'), nnf (initial steps not displayed when using run command 'r'), imode (index of mode to be displayed graphically) imode1 (mode used to determine strobing positions), istrob (strobing control: 1=real peak, 2=imaginary peak, 3=real zero, 4=imaginary zero), it=trajectory display (1/0 = on/off), is=Poincare section display (1/0 = on/off). Values for most of these variables are to be put in a data file prior to running the program. This file is read at the beginning of the program (see code). New parameter

files may be stored and retrieved for desired operating points while running the program.

The program is designed utilize interactive graphics – commands entered at the terminal can generate a phase portrait, Poincare section, time series, or fast Fourier transform on a separate portion of the screen reserved for the graphics display. The mode being displayed is specified by the variable imode. The sequence of graphics commands is stored and can be retrieved later to generate a "hard copy" of the display on a laser printer. The graphics programs used were developed by Jim Crutchfield and Bruce McNamara. These graphics programs will not be listed here since the spin wave program could easily be modified to operate with any similar programs. The following subroutines in the spin wave program are for graphics: dpgraph (create graphics file which can be printed on a laser printer), exitgraph (end graphics), faxes (draw axes), fborder (draw border), fclear (clear display), fdomark (for making various symbols at specified position), fdotat (make dot at specified position), fgenwindow (also for initialization), flinewidth (set linewidth), fmove (move to specified position), fpendown (draw straight lines to subsequent positions given by fmove command), fpenup (no draw on subsequent move commands), fscale (set scale factor), ftriangle (make triangle at specified position), store (this is for initialization of the graphics display and for storage of graphics command sequence).

In addition to the graphics subroutines, their are a number of other subroutines which are used for the spin wave analysis. These are listed following the main part of the program below. They perform the following functions: "cavity" evaluates the dynamics of the cavity or resonator variable; "ssb" evaluates $\dot{c}_k$ using Eq. (109); "rk" evaluates the four point Runge-Kutta algorithm for specified timestep; "spctrm" determines the power spectrum; "four1" generates fast Fourier transform (used by subroutine spctrm); "datwin" generates chosen window function (used by subroutine spctrm);

Some of the main commands which can be given to the program are: l=list variables, parameters, Suhl threshold, and fixed points, q=quit, r=run, c=continue, cl=clear, ft=file trajectory data, fp=file Poincare section data, markfp=mark the fixed points on display, fft=generate fast Fourier transform, si=change size (or scale) of display, dump=generate PostScript file of display data for printing on laser printer, set=read parameter file, and save=create parameter file. In addition, any variable or parameter (with a few exceptions) may be changed by entering its name followed on the next line by the new value. For variables or parameters with indices enter the name without indices and the program will prompt for additional information. Complex quantities must be entered in the form (real, imaginary) even if chosen to be purely real.

```
****** Version magspec.f ************************************

      implicit double precision(a-h,o-z)
      double complex ps(100),ps0(100),dp(100),MM(100),NN(100),
     *gk(100),tkk(100,100),skk(100,100),tk(100,100),sk(100,100),
     *w0(100),w1(100),w2(100),w3(100),rlk(100),fl(100),Gk(100),
     *ck1(100),ck2(100),DD,EE,cav,cav0,ps1(100),rlci,
     *rkk(100,100),rkkp,skkp,tkkp,gkang
      character filename*20, command*20
      double precision df(100),ppthr(100),aa(100),bb(100),
     *cc(100),disc(100),w4(16384),w5(8192)
      common rlk,fl,sk,tk,gk,nmag
      common /a1/ xw0,xw1,yw0,yw1,aLW
      common /a2/ alpha,rlci
      external ssb
      twopi = 8.d0 * datan(1.d0)
      hbar=1.055d-27
      sizemk=.01
      xs=0.02
      ys=0.02
      aLW=1
      iAR=1
      do 1251 i=1,100
        ps(i)=(1d-8,1d-8)
        ps0(i)=(1d-8,1d-8)
        df(i)=0
        gk(i)=(1.414d7,0)
1251    continue
      do 1252 i=1,100
        do 1253 j=1,100
          tkk(i,j)=(0,0)
```

```
          skk(i,j)=(0,0)
          rkk(i,j)=(0,0)
 1253     continue
 1252   continue
      print*, 'version magspec.f  Aug. 22, 1987'
      print*,'parameter filename: '
      read*,filename
      open(unit=3,file=filename)
      read(3,*) dt,nn0,nnf,nmag
      read(3,*) pp,fp,f0,gamc,gam0,gamk,alpha,dfcav
      do 1051 i=1,nmag
        read(3,*) ps(i),df(i),gk(i)
        ps0(i)=ps(i)
 1051   continue
      do 1052 i=1,nmag
        do 1053 j=1,nmag
          read(3,*) tkk(i,j),skk(i,j)
 1053     continue
 1052   continue
      read(3,*) xw0,xw1,yw0,yw1,xs0,xs1,ys0,ys1
      read(3,*) x0,y0,xt,yt
      close(unit=3)
      g=alpha
      if(alpha .gt. 1.d0) alpha=0.045d0
      it=1
      is=1
      imod=1
      imode=1
      imode1=1
      istrob=1
      sign=1.d0
      iflag=1
      itick=1
      sign=1.d0
      call store(0)

* cl=clear and draw axes
      call fclear()
      call fgenwindow(xw0,yw0,xw1,yw1,iAR)
      call fscale(xs0,xs1,ys0,ys1)
      call flinewidth(aLW,aLWold)
      call fborder()
      call faxes(x0,y0,xt,yt,xs,ys)

*****************************************************************
   50 print*, 'command: '
      read*, command

* dimensionality
      if(command .eq. 'nmag') read*, nmag
```

```
* time step control
      if(command .eq. 'dt') read*, dt
      if(command .eq. 'nn0') read*, nn0
      if(command .eq. 'nnf') read*, nnf

* parameters
      if(command .eq. 'pp') read*, pp
      if(command .eq. 'fp') read*, fp
      if(command .eq. 'f0') read*, f0
      if(command .eq. 'gamc') read*, gamc
      if(command .eq. 'gam0') read*, gam0
      if(command .eq. 'gamk') read*, gamk
      if(command .eq. 'g') read*, g
      if(command .eq. 'alpha') read*, alpha

      if(command .eq. 'gk') then
        print*, 'index i: '
        read*, i
        print*, 'gk(i): '
        read*, gk(i)
      endif

      if(command .eq. 'tkk') then
        print*, 'index i: '
        read*, i
        print*, 'index j: '
        read*, j
        print*, 'tkk(i,j): '
        read*, tkk(i,j)
        tkk(j,i)=dconjg(tkk(i,j))
      endif

      if(command .eq. 'skk') then
        print*, 'index i: '
        read*, i
        print*, 'index j: '
        read*, j
        print*, 'skk(i,j): '
        read*, skk(i,j)
        skk(j,i)=dconjg(skk(i,j))
      endif

      if(command .eq. 'rkk') then
        print*, 'index i: '
        read*, i
        print*, 'index j: '
        read*, j
        print*, 'rkk(i,j): '
        read*, rkk(i,j)
      endif
```

```
      if(command .eq. 'rkkp') then
        print*, 'enter 1 for k=kp, 2 for k!=kp, 3 for all'
        read*, k
        print*, 'rkkp: '
        read*, rkkp
        do 460 i=1,nmag
          do 461 j=1,nmag
            if((k .eq. 1) .and. (i .ne. j)) go to 461
            if((k .eq. 2) .and. (i .eq. j)) go to 461
            rkk(i,j)=rkkp
461         continue
460       continue
      endif

      if(command .eq. 'skkp') then
        print*, 'enter 1 for k=kp, 2 for k!=kp, 3 for all'
        read*, k
        print*, 'skkp: '
        read*, skkp
        do 560 i=1,nmag
          do 561 j=1,nmag
            if((k .eq. 1) .and. (i .ne. j)) go to 561
            if((k .eq. 2) .and. (i .eq. j)) go to 561
            skk(i,j)=skkp
561         continue
560       continue
      endif

      if(command .eq. 'tkkp') then
        print*, 'enter 1 for k=kp, 2 for k!=kp, 3 for all'
        read*, k
        print*, 'tkkp: '
        read*, tkkp
        do 660 i=1,nmag
          do 661 j=1,nmag
            if((k .eq. 1) .and. (i .ne. j)) go to 661
            if((k .eq. 2) .and. (i .eq. j)) go to 661
            tkk(i,j)=tkkp
661         continue
660       continue
      endif

      if(command .eq. 'df') then
        print*, 'index: '
        read*, index
        print*, 'df(index): '
        read*, df(index)
      endif

      if(command .eq. 'dfcav') read*, dfcav
```

```
      if(command .eq. 's') then
        print*, 'amount of freq. shift: '
        read*, shift
        do 93 i=1,nmag
          df(i)=df(i)+shift
   93     continue
      endif

* initial values
      if(command .eq. 'ps') then
        print*, 'index: '
        read*, index
        print*, 'ps(index): '
        read*, ps(index)
      endif
      if(command .eq. 'ps0') then
        print*, 'index: '
        read*, index
        print*, 'ps0(index): '
        read*, ps0(index)
      endif
      if(command .eq. 'Set') then
        do 1005 i=1,nmag
          ps0(i)=ps(i)
 1005   continue
      endif

* fixed points
      if((command .eq. 'markfp').and.(imode.gt.0)) then
        call ftriangle(0.,0.)
        call ftriangle(dreal(ck1(imode)),dimag(ck1(imode)))
        call ftriangle(-dreal(ck1(imode)),-dimag(ck1(imode)))
        call ftriangle(dreal(ck2(imode)),dimag(ck2(imode)))
        call ftriangle(-dreal(ck2(imode)),-dimag(ck2(imode)))
      endif

* rescale=rescale frequencies
      if(command.eq.'rescale') then
        print*, 'new freq. = beta*old freq.'
        print*, 'beta= '
        read*, beta
        beta1=1/dsqrt(beta)
        dt=dt/beta
        gamk=beta*gamk
        pp=pp*beta*beta
        do 94 i=1,nmag
          ps(i)=ps(i)/beta1
          ps0(i)=ps0(i)/beta1
          df(i)=df(i)*beta
   94     continue
      endif
```

```
* plotting parameters
      if(command .eq. 'xw0') read*, xw0
      if(command .eq. 'xw1') read*, xw1
      if(command .eq. 'yw0') read*, yw0
      if(command .eq. 'yw1') read*, yw1
      if(command .eq. 'xs0') read*, xs0
      if(command .eq. 'xs1') read*, xs1
      if(command .eq. 'ys0') read*, ys0
      if(command .eq. 'ys1') read*, ys1
      if(command .eq. 'x0') read*, x0
      if(command .eq. 'y0') read*, y0
      if(command .eq. 'xt') read*, xt
      if(command .eq. 'yt') read*, yt

* print, trajectory, section, & variable control parameters
      if(command .eq. 'ip') read*, ip
      if(command .eq. 'it') read*, it
      if(command .eq. 'is') read*, is
      if(command .eq. 'itick') read*, itick
      if(command .eq. 'iflag') read*, iflag
      if(command .eq. 'sign') read*, sign
      if(command .eq. 'istrob') read*, istrob
      if(command .eq. 'imode') read*, imode
      if(command .eq. 'imode1') read*, imode1
      if((command .eq. 'imode').and.(iflag.eq.0)) iflag=2
      if(imode.lt.1) imode=0
      if(imode.gt.nmag) imode=nmag

* rescale gk to adjust threshold and make gk real
*   assumes all gk(i)'s are identical
      if(command .eq. 'rescalegk') then
        print*, 'desired pump threshold for df=0: '
        read*, ppth
        ppth2=ppth**0.5
        gk1=zabs(gk(1))
        gkang = gk(1)/gk1
        do 470 i=1,nmag
          ps(i)=ps(i)*gkang**-0.5
          gk(i)=dcmplx(gamk/ppth2,0)
  470     continue
        pp=pp*(gk1*ppth2/gamk)**2
        endif

* set rkk parameters in terms of gk and alpha
      if(command .eq. 'setrkk') then
      do 500 i=1,nmag
       do 501 j=1,nmag
        rkk(i,j)=(0,1d-7)*gk(i)*dconjg(gk(j))/(2*rlci*alpha**2)
  501   continue
  500  continue
      endif
```

```
* change quantum parameters to classical
      if(command .eq. 'change') then
        f=dsqrt(gamc*1.d7/(twopi*fp*hbar))
        DD=-g/(dcmplx(gamc,twopi*dfcav)*
     *  (dcmplx(gam0,twopi*df0)+g*g/dcmplx(gamc,twopi*dfcav)))
        EE=(0,-1)/
     *  (dcmplx(gam0,twopi*df0)+g*g/dcmplx(gamc,twopi*dfcav))
        hbar2=dsqrt(hbar)
        xs0=xs0*hbar2
        xs1=xs1*hbar2
        ys0=ys0*hbar2
        ys1=ys1*hbar2
        x0=x0*hbar2
        y0=y0*hbar2
        xt=xt*hbar2
        yt=yt*hbar2
        do 450 i=1,nmag
          do 451 j=1,nmag
            tkk(i,j)=tkk(i,j)/hbar
            skk(i,j)=skk(i,j)/hbar
            rkk(i,j)=EE*gk(i)*dconjg(gk(j))/hbar
 451        continue
 450      continue
        do 453 i=1,nmag
          ps(i) = ps(i)*hbar2
          gk(i) = (0,1)*DD*f*gk(i)
 453      continue
      endif

* determine converted parameters
      df0=f0-fp
      rlci=(1.d0,0.d0)/dcmplx(-gamc,-twopi*dfcav)
      do 1010 i=1,nmag
        rlk(i)=dcmplx(-gamk,-twopi*df(i))
        fl(i)=-gk(i)*dsqrt(pp)
        fthr=zabs(rlk(i)/gk(i))
        ppthr(i)=fthr*fthr
        do 1021 j=1,nmag
          tk(i,j)=(0.d0,-2.d0)*tkk(i,j)
          sk(i,j)=(0.d0,-1.d0)*(skk(i,j)+rkk(i,j))
1021      continue
        MM(i)= -rlk(i)/fl(i)
        NN(i)= (-tk(i,i)-sk(i,i))/fl(i)
        aa(i)=dreal(NN(i))*dreal(NN(i))+dimag(NN(i))*dimag(NN(i))
        bb(i)=dreal(MM(i))*dreal(NN(i))+dimag(MM(i))*dimag(NN(i))
        cc(i)=dreal(MM(i))*dreal(MM(i))+dimag(MM(i))*dimag(MM(i))
        disc(i)=bb(i)*bb(i)-aa(i)*(cc(i)-1)
        if(disc(i).gt.0) then
          ckt1= (-bb(i) -dsqrt(disc(i)))/aa(i)
          ckt2= (-bb(i) +dsqrt(disc(i)))/aa(i)
          if(ckt1.lt.0) then
```

```
            ck1(i)=(0,0)
          else
            ck1(i)=dconjg(zsqrt(ckt1*(MM(i)+NN(i)*ckt1)))
          endif
          if(ckt2.lt.0) then
            ck2(i)=(0,0)
          else
            ck2(i)=dconjg(zsqrt(ckt2*(MM(i)+NN(i)*ckt2)))
          endif
        else
          ck1(i)=(0,0)
          ck2(i)=(0,0)
        endif
 1010   continue

* l=list
* lb=list bare parameters
      if((command.eq.'l').or.(command.eq.'lb')) then
        print 900,'dt=',dt,'nn0=',nn0,'nnf=',nnf
  900     format(a4,d11.3,a4,i6,a4,i6)
        print 905,'nmag=',nmag
  905     format(a6,i3,a6,i3)
        print 901,'fp=',fp,'Hz ','f0=',f0,'Hz ','pp=',pp,'W '
  901     format(a4,d14.6,a4,a4,d14.6,a4,a4,d14.6,a4)
        print 902,'gamc=',gamc,'gam0=',gam0,'gamk=',gamk
  902     format(a6,d14.6,a6,d14.6,a6,d14.6)
        print 902,'alpha=',alpha,'dfcav',dfcav
        print*, 'i,j=          rkk='
        do 1081 i=1,nmag
          do 1082 j=1,nmag
            print*, i,j,rkk(i,j)
 1082       continue
 1081     continue
        print*, 'i,j=          skk='
        do 1181 i=1,nmag
          do 1182 j=1,nmag
            print*, i,j,skk(i,j)
 1182       continue
 1181     continue
        print*, 'i,j=          tkk='
        do 1281 i=1,nmag
          do 1282 j=1,nmag
            print*, i,j,tkk(i,j)
 1282       continue
 1281     continue
        print*, 'i=         ps='
        do 1008 i=1,nmag
          print*, i,ps(i)
 1008   continue
        print*, 'i=         df='
        do 1108 i=1,nmag
```

```
          print*, i,df(i)
 1108    continue
         print*, 'i=         gk='
         do 1208 i=1,nmag
          print*, i,gk(i)
 1208    continue
       endif

* lc=list converted parameters
       if((command.eq.'l').or.(command.eq.'lc')) then
         print 902,'df0=',df0
         print*,'Suhl thresholds, pump power in Watts'
         do 1011 i=1,nmag
          print 907,'ppthr(',i,')= ',ppthr(i)
  907     format(a6,i3,a3,d14.6)
 1011    continue
       endif

* ls=list state
       if(command.eq.'ls') then
         call cavity(cav,cav0,ps)
         print*, 'cav = ',cav
         print*, 'cav0= ',cav0
         do 1007 i=1,nmag
          print 903, 'ps(',i,')= ',ps(i)
  903     format(a4,i3,a4,d14.6,d14.6)
 1007    continue
         call ssb(tt,ps,dp,1+nmag)
         do 2007 i=1,nmag
          print 903, 'dp(',i,')= ',dp(i)
 2007    continue
       endif

* ls2=list sigma state
       if(command.eq.'ls2') then
         do 3007 i=1,nmag+1
          print 903, 'ps2(',i,')= ',ps(i)*ps(i)
 3007    continue
         call ssb(tt,ps,dp,1+nmag)
         do 4007 i=1,nmag+ncav
          print 903, 'dp2(',i,')= ',2*dp(i)*ps(i)
 4007    continue
       endif

* lfp=list fixed points
       if((command.eq.'l').or.(command.eq.'lfp')) then
       print*,'fixed points for mode i, with other modes at zero:'
         do 908 i=1,nmag
          print*, 'i           ck1            ck2'
          print*, i,ck1(i),ck2(i)
 908    continue
```

```
      do 909 i=1,nmag
        print*, 'i            MM            NN'
        print*, i,MM(i),NN(i)
 909   continue
      endif

* lw=list window parameters
      if((command.eq.'l').or.(command.eq.'lw')) then
        print*, 'window xmin, xmax, ymin, ymax:'
        print 906, 'xw0=',xw0,'xw1=',xw1,'yw0=',yw0,'yw1=',yw1
        print*, 'scale xmin, xmax, ymin, ymax:'
        print 906, 'xs0=',xs0,'xs1=',xs1,'ys0=',ys0,'ys1=',ys1
        print*, 'origin x0,y0   tick interval xt,yt'
        print 906, 'x0=',x0,'y0=',y0,'xt=',xt,'yt=',yt
  906     format(a6,d11.4,a6,d11.4,a6,d11.4,a6,d11.4)
      endif

* lcon=list control parameters
      if((command.eq.'l').or.(command.eq.'lcon')) then
        print*, 'control parameters 1=on  0=off: '
        print*, 'printing  ip=',ip
        print*, 'trajectory  it=',it
        print*, 'section  is=',is
        print*, 'mode number(0 for cavity) imode=',imode
        print*, 'file trajectory  ifilet=',ifilet
        print*, 'file poincare section ifilep=',ifilep
      endif

* lcom=list commands
      if((command.eq.'l').or.(command.eq.'lcom')) then
        print*, 'commands:'
        print*, 'l=list q=quit r=run c=continue cl=clear'
        print*, 'ft=file trajectory fp=file poincare section'
        print*, 'markfp=mark the fixed points on display'
        print*, 'fft=generate fast Fourier transform'
        print*, 'si=change size (or scale) of display'
        print*, 'dump=generate PostScript file of display data'
        print*, 'set=read parameter file'
        print*, 'save=create parameter file'
        print*, 'any variable (with a few exceptions)'
        print*, 'may be changed by entering its name'
        print*, 'followed on next line by the new value'
      endif

* read parameter file
      if(command .eq. 'set') then
        print*,'parameter filename: '
        read*,filename
        open(unit=3,file=filename)
        read(3,*) dt,nn0,nnf,nmag
        read(3,*) pp,fp,f0,gamc,gam0,gamk,alpha,dfcav
```

```
        g=alpha
        do 1061 i=1,nmag
          read(3,*) ps(i),df(i),gk(i)
          ps0(i)=ps(i)
 1061     continue
        do 1062 i=1,nmag
          do 1063 j=1,nmag
            read(3,*) tkk(i,j),skk(i,j)
 1063       continue
 1062     continue
        read(3,*) xw0,xw1,yw0,yw1,xs0,xs1,ys0,ys1
        read(3,*) x0,y0,xt,yt
        close(unit=3)
      endif

* create parameter file
      if(command .eq. 'save') then
        print*,'parameter filename: '
        read*,filename
        open(unit=3,file=filename)
        write(3,*) dt,nn0,nnf,nmag
        write(3,*) pp,fp,f0,gamc,gam0,gamk,alpha,dfcav
        do 1071 i=1,nmag
          write(3,*) ps(i),df(i),gk(i)
 1071     continue
        do 1072 i=1,nmag
          do 1073 j=1,nmag
            write(3,*) tkk(i,j),skk(i,j)
 1073       continue
 1072     continue
        write(3,*) xw0,xw1,yw0,yw1,xs0,xs1,ys0,ys1
        write(3,*) x0,y0,xt,yt
        close(unit=3)
      endif


* fp=file poincare data
      if(command .eq. 'fp') then
        print*, 'filename of data (n = do not file) ? '
        read*, filename
        if(ifilep .eq. 1) close(unit=1)
        if(filename.ne.'n') then
          open(unit=1,file=filename)
          ifilep=1
        else
          ifilep=0
        endif
      endif

* ft=file trajectory data
      if(command .eq. 'ft') then
```

```
        print*, 'filename of data (n = do not file) ? '
        read*, filename
        if(ifilet .eq. 1) close(unit=2)
        if(filename.ne.'n') then
          open(unit=2,file=filename)
          ifilet=1
        else
          ifilet=0
        endif
      endif


* cl=clear and draw axes
      if(command .eq. 'cl') then
        call store(3)
        call fclear()
        call fgenwindow(xw0,yw0,xw1,yw1,iAR)
        call fscale(xs0,xs1,ys0,ys1)
        call flinewidth(aLW,aLWold)
        call fborder()
        if(itick.eq.1) call faxes(x0,y0,xt,yt,xs,ys)
        if(iflag.eq.0) iflag=2
      endif

* dump=create PostScript file
      if(command .eq. 'dump') then
        call store(2)
        call exitgraph()
        call dpgraph(0)
        call exitgraph()
        call dpgraph(1)
        call store(1)
      endif

* fft=generate fft
      if(command.eq.'fft') then
        call spctrm(tt,ps,nmag,dt,ssb,w0,w1,w2,w3,w4,w5)
        if(iflag.eq.0) iflag=2
      endif

* line=set line width for laserprinter
      if(command .eq. 'line') then
        print*, 'linewidth: '
        read*, aLW
        call flinewidth(aLW,aLWold)
      endif

* si=size graphics
      if(command .eq. 'si') then
        print*, 'center on origin/strobing, enter 0/1: '
        read*, center
```

```
        print*, 'size'
        read*, size
        if(center .eq. 0) then
          xs0= -size
          xs1= size
          ys0= -size
          ys1= size
        else
          xs0= gxx-size
          xs1= gxx+size
          ys0= gyy-size
          ys1= gyy+size
        endif
        xt= size/10.
        yt= size/10.
        call store(3)
        call fclear()
        call fgenwindow(xw0,yw0,xw1,yw1,iAR)
        call fscale(xs0,xs1,ys0,ys1)
        call fborder()
        if(itick.eq.1) call faxes(x0,y0,xt,yt,xs,ys)
        if(iflag.eq.0) iflag=2
      endif

* q=quit
      if(command .eq. 'q') then
        if(ifilet .eq. 1) close(unit=2)
        if(ifilep .eq. 1) close(unit=1)
        call exitgraph()
      endif

* r=run (use c for continue)
      if(command .eq. 'r') then
        do 1006 i=1,nmag
          ps(i)=ps0(i)
 1006   continue
        if(imode.eq.0) then
          call cavity(cav,cav0,ps)
          axx=dreal(cav)
          ayy=dimag(cav)
        else
          axx=dreal(ps(imode))
          ayy=dimag(ps(imode))
        endif
        gwx=axx
        gwy=ayy
        tt=0.d0
        ikk=0
        kks=0
        par=0.5d0
        nn1=1
```

```
        iflag=2
        if(nnf.gt.0) iflag=1
      endif


* c=continue, r=run (re-initialize)
      if((command.eq.'c').or.(command.eq.'r')) then
      if(imode.eq.0) then
        call cavity(cav,cav0,ps)
        axx=dreal(cav)
        ayy=dimag(cav)
      else
        axx=dreal(ps(imode))
        ayy=dimag(ps(imode))
      endif
      if(iflag.eq.2) then
        call fpenup()
        call fmove(axx,ayy)
        call fpendown()
        iflag=0
      endif
      if(iflag.eq.3) then
        ecks=xs0
        wigh=(ys1-ys0)*(axx-xs0)/(xs1-xs0) +ys0
        call fpenup()
        call fmove(ecks,wigh)
        call fpendown()
      endif
      if(iflag.eq.4) then
        ecks=xs0
        wigh=ayy
        call fpenup()
        call fmove(ecks,wigh)
        call fpendown()
      endif
      do 700 istep=nn1,nn1+nn0-1
      call rk(tt,ps,nmag,dt,ssb,w0,w1,w2,w3)
      call ssb(tt,ps,dp,nmag)
  409 format(a6,4d14.6)
********** calculation of trajectory ***************************
      if(istep.le.nnf) go to 700
  510 ikk=ikk+1
      if(imode.eq.0) then
        call cavity(cav,cav0,ps)
        axx=dreal(cav)
        ayy=dimag(cav)
      else
        axx=dreal(ps(imode))
        ayy=dimag(ps(imode))
      endif
      if(it.eq.1) then
```

```
        if(iflag.eq.0) call fmove(axx,ayy)
        if(iflag.eq.1) then
          call fpenup()
          call fmove(axx,ayy)
          call fpendown()
          iflag=0
        endif
        if(iflag.eq.3) then
          ecks=(istep-nn1+1.d0)*(xs1-xs0)/nn0  +xs0
          wigh=(ys1-ys0)*(axx-xs0)/(xs1-xs0) +ys0
          call fmove(ecks,wigh)
        endif
        if(iflag.eq.4) then
          ecks=(istep-nn1+1.d0)*(xs1-xs0)/nn0  +xs0
          wigh=ayy
          call fmove(ecks,wigh)
        endif
      endif
      if(ifilet .eq. 1) write(2,1100) dcmplx(axx,ayy)
      if(ip .eq. 1) write(6,1100) dcmplx(axx,ayy)
      if(is.eq.0) go to 700
*****************************************************************

      if(istrob.eq.1) dp1=dreal(dp(imode1))
      if(istrob.eq.2) dp1=dimag(dp(imode1))
      if(istrob.eq.3) dp1=dreal(ps(imode1))
      if(istrob.eq.4) dp1=dimag(ps(imode1))

      if((sign*par.lt.0.d0).or.(sign*dp1.ge.0.d0)
     *.or.(istep.eq.1).or.(iflag.ne.0)) go to 600
      dp0=dp1
      do 95 i=1,nmag
        ps1(i)=ps(i)
   95 continue
      tsave=tt
      delt=dt
      do 96 i=1,6
        dsp=par-dp1
        if(dsp.ne.0.d0) then
          delt=delt*dp1/dsp
          call rk(tt,ps,nmag,delt,ssb,w0,w1,w2,w3)
          call ssb(tt,ps,dp,nmag)
          par=dp1
          if(istrob.eq.1) dp1=dreal(dp(imode1))
          if(istrob.eq.2) dp1=dimag(dp(imode1))
          if(istrob.eq.3) dp1=dreal(ps(imode1))
          if(istrob.eq.4) dp1=dimag(ps(imode1))
        endif
   96 continue
      if(imode.eq.0) then
        call cavity(cav,cav0,ps)
```

```
        gxx=dreal(cav)
        gyy=dimag(cav)
      else
        gxx=dreal(ps(imode))
        gyy=dimag(ps(imode))
      endif
      tsect=tt
      period=tsect-tsect2
      tsect2=tsect
      do 97 i=1,nmag
        ps(i)=ps1(i)
   97 continue
      tt=tsave
      dp1=dp0

      print 991,'period=',period,'sec ','freq=',1.d0/period,'Hz'
  991     format(a7,d14.6,a4,a5,d14.6,a2)
      if(it .eq. 0) then
        call fdotat(gxx,gyy)
      else
        call fdomark(gxx,gyy,0,sizemk)
      endif
      call fpenup()
      call fmove(axx,ayy)
      if(it .eq. 1) call fpendown()
      if(ifilep .eq. 1) write(1,1100) dcmplx(gxx,gyy)
  600 par=dp1
  700 continue
      nn1=nn1+nn0
      if(ifilet.eq.1) write(2,1100) dcmplx(axx,ayy)
      if(ip.eq.1) write(6,1100) dcmplx(axx,ayy)
      endif

      if(command.ne.'q') go to 50
      stop

 1100 format(4d14.6)
  100 format(10f8.4)
  270 format(10x,'total points=',i4)
  800 format(5x,'i=',i5,5x,'gxx=',f11.7,5x,'gyy=',f11.7)
 1270 format(10x,'total points=',i4)
 1800 format(5x,'i=',i5,5x,'axx=',f11.7,5x,'ayy=',f11.7)
      end

***** subroutines are given below ******************************

      subroutine cavity(cav,cav0,ps)
      implicit double precision(a-h,o-z)
      double complex ps(100),cav,gk(100),f1(100),tk(100,100),
     *sk(100,100),rlk(100),cav0,rlci
      common rlk,f1,sk,tk,gk,nmag
```

```
      common /a2/ alpha,rlci
      cav=(0.d0,0.d0)
      do 99 i=1,nmag
        cav=cav+dconjg(gk(i))*ps(i)**2
   99 continue
      cav=(0.d0,1.d0)*cav/(2*alpha)
      cav0=(0.d0,1.d0)*alpha*(pp**0.5)*rlci
      return
      end

      subroutine ssb(tim,vr,fn,jdim)
      implicit double precision(a-h,o-z)
      double precision n(100)
      double complex vr(100),fn(100),sum1,sum2,sig(100)
      double complex tk(100,100),sk(100,100),f1(100),rlk(100),
     *gk(100)
      common rlk,f1,sk,tk,gk,nmag
      sum1=(0.d0,0.d0)
      sum2=0.d0
      do 111 i=1,nmag
        vrR=dreal(vr(i))
        vrI=dimag(vr(i))
        n(i)=vrR*vrR+vrI*vrI
        sig(i)=vr(i)*vr(i)
  111   continue
      do 112 i=1,nmag
       sum1= rlk(i)
       sum2=f1(i)
       do 113 j=1,nmag
        sum1=sum1+dcmplx(dreal(tk(i,j))*n(j),dimag(tk(i,j))*n(j))
        sum2=sum2+sk(i,j)*sig(j)
  113   continue
       fn(i)=sum1*vr(i) +sum2*dconjg(vr(i))
  112  continue
      return
      end

      subroutine rk(time,state,idim,step,diffeq,u0,u1,u2,u3)
      implicit double precision(a-h,o-z)
      double complex u4,state(100),u0(100),u1(100),u2(100),
     *u3(100)
      external diffeq
      half=step*0.5d0
      sixth=step*0.16666666666666d0
      call diffeq(time,state,u1,idim)
      do 1 i=1,idim
      u0(i)=state(i)+dcmplx(half*dreal(u1(i)),half*dimag(u1(i)))
    1 continue
      time=time+half
      call diffeq(time,u0,u2,idim)
      do 2 i=1,idim
```

```
      u0(i)=state(i)+dcmplx(half*dreal(u2(i)),half*dimag(u2(i)))
    2 continue
      call diffeq(time,u0,u3,idim)
      do 3 i=1,idim
      u0(i)=state(i)+dcmplx(step*dreal(u3(i)),step*dimag(u3(i)))
      u3(i)=u3(i)+u2(i)
    3 continue
      time=time+half
      call diffeq(time,u0,u2,idim)
      do 4 i=1,idim
      u4=u1(i)+u2(i)+u3(i)+u3(i)
      state(i)=state(i)+dcmplx(sixth*dreal(u4),sixth*dimag(u4))
    4 continue
      return
      end

      subroutine spctrm(tt,ps,nmag,dt,ssb,w0,w1,w2,w3,w4,w5)
      implicit double precision(a-h,o-z)
      double complex ps(100),w0(100),w1(100),w2(100),w3(100)
      double complex aps, cav, cav0
      character filefft*20
      external ssb
      logical ovrlap,pdata,asym
      dimension p(4096),w4(16384),w5(8192)
      common /a1/ xw0,xw1,yw0,yw1,aLW
      twopi = 8. * datan(1.d0)
      print*, '# freq. bins (2**i, enter i<=12) : '
      read*, i
      if(i.gt.12) i=12
      if(i.lt.1) i=1
      mh=2**i
      m=mh+mh
      print*, 'time steps per data point: '
      read*, nsteps
      fmax= 1./(2.*dt*nsteps)
      print*, 'maximum freq=', fmax
      print*, 'number of segments to average initially: '
      read*, k
      print*, 'overlap segments? (enter t (true) or f (false)): '
      read*, ovrlap
      print*, 'mode to transform: '
      read*, mode
      print*, 'window type- '
      print*, '1=square,2=Hanning,3=Parzen,4=Welsh,5,6=special: '
      read*, itype
      if(itype.eq.5) print*,
     *  'datwin=dexp(-ak*(m*m/(4.*(j-.5)*(j-m-.5)))**2)'
      if(itype.eq.6) print*,
     *  'datwin=dexp(ak*m*m/(4.*(j-.5)*(j-m-.5)))'
      print*, 'enter power ak, 1=normal: '
      read*, ak
```

```
      print*, 'enter phase factor aph, 0=normal: '
      read*, aph
      print*, 'asymmetrize window? (enter t (true) or f (false)): '
      read*, asym
      if(asym) then
        print*, 'tilt factor (1.0=normal): '
        read*, b
      endif
      print*, 'printout data? (enter t (true) or f (false)): '
      read*, pdata
      print*, 'data source- '
      print*, '1=normal, 2=save, 3=retrieve, 4=test (constant): '
      read*, idat
      if((idat.eq.2).or.(idat.eq.3)) then
        print*, 'data filename: '
        read*, filefft
        open(unit=4,file=filefft)
      endif
      print*, 'window compression factor (>=1, 1=normal): '
      read*, wcom
      mm=m+m
      m4=mm+mm
      m44=m4+4
      m43=m4+3
      den=0.d0
      facm=m-1.d0
      facp=1./m
      sumw=0.d0
      do 11 j=1,m
        sumw=sumw+datwin(j,mh,itype,ak,b,asym,wcom)**2
        if(pdata) print*, 'datwin(',j,')=',
     *    datwin(j,mh,itype,ak,b,asym,wcom)
   11 continue
      p0=0.d0
      do 12 j=1,mh
        p(j)=0.d0
   12 continue
      if(ovrlap) then
        do 1 j=1,mh
          j2=j+j
          if((idat.eq.1).or.(idat.eq.2)) then
            do 2 i=1,nsteps
              call rk(tt,ps,nmag,dt,ssb,w0,w1,w2,w3)
    2       continue
            if(mode.eq.0) then
              call cavity(cav,cav0,ps)
              aps=cav-cav0
            else
              aps=ps(mode)
            endif
          endif
```

```
        if(idat.eq.2) write(4,*) aps
        if(idat.eq.3) read(4,*) aps
        if(idat.eq.4) aps= (1.,0.)
        w5(j2-1)=dreal(aps)
        w5(j2)=dimag(aps)
 1    continue
      endif
10  do 18 kk=1,k
      if(ovrlap) then
        do 13 j=1,mh
          j2=j+j
          if(aph.eq.0.) then
            w4(j2-1)=w5(j2-1)*datwin(j,mh,itype,ak,b,asym,wcom)
            w4(j2)=w5(j2)*datwin(j,mh,itype,ak,b,asym,wcom)
          else
            aph0=aph*(j2-m-1)*twopi/mm
            aph1=dcos(aph0)*datwin(j,mh,itype,ak,b,asym,wcom)
            aph2=dsin(aph0)*datwin(j,mh,itype,ak,b,asym,wcom)
            w4(j2-1)=w5(j2-1)*aph1-w5(j2)*aph2
            w4(j2)=w5(j2-1)*aph2+w5(j2)*aph1
          endif
          if(pdata)
     *    print*,'w4(',j2-1,')=',w4(j2-1),' w4(',j2,')=',w4(j2)
 13     continue
        do 31 j=1,mh
          j2=j+j
          if((idat.eq.1).or.(idat.eq.2)) then
            do 32 i=1,nsteps
              call rk(tt,ps,nmag,dt,ssb,w0,w1,w2,w3)
 32         continue
            if(mode.eq.0) then
              call cavity(cav,cav0,ps)
              aps=cav-cav0
            else
              aps=ps(mode)
            endif
          endif
          if(idat.eq.2) write(4,*) aps
          if(idat.eq.3) read(4,*) aps
          if(idat.eq.4) aps= (1.,0.)
          w5(j2-1)=dreal(aps)
          w5(j2)=dimag(aps)
 31     continue
        do 14 j=mh+1,m
          j2=j+j
          if(aph.eq.0.) then
            w4(j2-1)
     *       =w5(j2-1-m)*datwin(j,mh,itype,ak,b,asym,wcom)
            w4(j2)=w5(j2-m)*datwin(j,mh,itype,ak,b,asym,wcom)
          else
            aph0=aph*(j2-m-1)*twopi/mm
```

```
            aph1=dcos(aph0)*datwin(j,mh,itype,ak,b,asym,wcom)
            aph2=dsin(aph0)*datwin(j,mh,itype,ak,b,asym,wcom)
            w4(j2-1)=w5(j2-1-m)*aph1-w5(j2-m)*aph2
            w4(j2)=w5(j2-1-m)*aph2+w5(j2-m)*aph1
          endif
          if(pdata)
     *    print*, 'w4(',j2-1,')=',w4(j2-1),' w4(',j2,')=',w4(j2)
14        continue
        else
          do 41 j=1,m
            j2=j+j
            if((idat.eq.1).or.(idat.eq.2)) then
              do 42 i=1,nsteps
                call rk(tt,ps,nmag,dt,ssb,w0,w1,w2,w3)
42            continue
              if(mode.eq.0) then
                call cavity(cav,cav0,ps)
                aps=cav-cav0
              else
                aps=ps(mode)
              endif
            endif
            if(idat.eq.2) write(4,*) aps
            if(idat.eq.3) read(4,*) aps
            if(idat.eq.4) aps= (1.,0.)
            if(aph.eq.0.) then
              w4(j2-1)
     *         =dreal(aps)*datwin(j,mh,itype,ak,b,asym,wcom)
              w4(j2)=dimag(aps)*datwin(j,mh,itype,ak,b,asym,wcom)
            else
              aph0=aph*(j2-m-1)*twopi/mm
              aph1=dcos(aph0)*datwin(j,mh,itype,ak,b,asym,wcom)
              aph2=dsin(aph0)*datwin(j,mh,itype,ak,b,asym,wcom)
              w4(j2-1)=dreal(aps)*aph1-dimag(aps)*aph2
              w4(j2)=dreal(aps)*aph2+dimag(aps)*aph1
            endif
          if(pdata)
     *    print*, '.w4(',j2-1,')=',w4(j2-1),' w4(',j2,')=',w4(j2)
41        continue
        endif
16      continue
        call four1(w4,m,1)
        p0=p0+w4(1)**2+w4(2)**2
        print*, 'p(0)=',p0
        do 17 j=1,mh-1
          j2=j+j
          p(j)=p(j)+w4(j2+1)**2+w4(j2+2)**2
     *      +w4(mm+1-j2)**2+w4(mm+2-j2)**2
          if(pdata)
     *    print*, 'p(',j,')=',p(j)
17      continue
```

```
      p(mh)=w4(m+1)**2+w4(m+2)**2
      print*, 'p(',mh,')=',p(mh)
      den=den+sumw
   18 continue
      powmax=p0
      powmin=p0
      do 19 j=1,mh
        if(p(j).eq.0.) then
          print*, 'p(',j,')= 0'
        else
          if(powmax.lt.p(j)) powmax=p(j)
          if((powmin.gt.p(j)).or.(powmin.eq.0.)) powmin=p(j)
        endif
   19 continue
      denm4=den*m4
      powmax=10.d0*dlog10(powmax/denm4)
      powmin=10.d0*dlog10(powmin/denm4)
   60 print*, 'PSD range in dB: '
      print*, 'powmin= ',powmin,'powmax= ',powmax
      print*, 'enter desired plotting range: '
      print*, 'minimum= '
      read*, ys0
      print*, 'maximum= '
      read*, ys1
      iAR=1
      print*, 'plot from bin #: '
      read*, xs0
      print*, 'to bin #: '
      read*, xs1
      print*, 'freq range ',xs0*fmax/mh,' to ', xs1*fmax/mh
      call store(3)
      call fclear()
      call fgenwindow(xw0,yw0,xw1,yw1,iAR)
      call fscale(xs0,xs1,ys0,ys1)
      call flinewidth(aLW,aLWold)
      call fborder()
      xs=0.01d0
      ys=0.01d0
      yt=10.d0
      call faxes(xs0,ys0,xs1/10,yt,xs,ys)
      call fpenup()
      j=xs0
      if(j.eq.0)  yyy=10.d0*dlog10(p0/denm4)
      if(j.gt.0)  yyy=10.d0*dlog10(p(j)/denm4)
      if(yyy.gt.ys0) call fmove(xs0,yyy)
      if(yyy.lt.ys0) call fmove(xs0,ys0)
      call fpendown()
      do 20 xxx=xs0+1,xs1
        j=xxx
        yyy=10.d0*dlog10(p(j)/denm4)
        if(yyy.gt.ys0) then
```

```
        call fmove(xxx,yyy)
      else
        call fmove(xxx,ys0)
      endif
20  continue
    call fpenup()
50  print*, '0=quit fft, 1=continue fft,'
    print*, '2=dump fft to printer, 3=replot: '
    read*, command
    if(command.eq.1.) then
      print*, 'number of additional segments to average: '
      read*, k
      go to 10
    endif
    if(command.eq.2.) then
      call store(2)
      call exitgraph()
      call dpgraph(0)
      call exitgraph()
      call dpgraph(1)
      call store(1)
    endif
    if(command.eq.2.) go to 50
    if(command.eq.3.) go to 60
    if((idat.eq.2).or.(idat.eq.3)) close(unit=4)
    return
    end

    subroutine four1(data,nn,isign)
    implicit double precision(a-h,o-z)
    dimension data(16384)
    twopi = 8. * datan(1.d0)
    n=2*nn
    j=1
    do 11 i=1,n,2
      if(j.gt.i) then
        tempr=data(j)
        tempi=data(j+1)
        data(j)=data(i)
        data(j+1)=data(i+1)
        data(i)=tempr
        data(i+1)=tempi
      endif
      m=n/2
1     if((m.gt.2).and.(j.gt.m)) then
        j=j-m
        m=m/2
        go to 1
      endif
      j=j+m
11  continue
```

```
      mmax=2
    2 if(n.gt.mmax) then
        istep=2*mmax
        theta=twopi/(isign*mmax)
        wpr= -2.d0*dsin(0.5d0*theta)**2
        wpi=dsin(theta)
        wr=1.d0
        wi=0.d0
        do 13 m=1,mmax,2
          do 12 i=m,n,istep
            j=i+mmax
            tempr=wr*data(j)-wi*data(j+1)
            tempi=wr*data(j+1)+wi*data(j)
            data(j)=data(i)-tempr
            data(j+1)=data(i+1)-tempi
            data(i)=data(i)+tempr
            data(i+1)=data(i+1)+tempi
   12     continue
          wtemp=wr
          wr=wr*wpr-wi*wpi+wr
          wi=wi*wpr+wtemp*wpi+wi
   13   continue
        mmax=istep
        go to 2
      endif
      return
      end

      double precision function datwin(j,mh,itype,ak,b,asym,wcom)
      implicit double precision(a-h,o-z)
      logical asym
      pi = 4. * datan(1.d0)
      c=(j-mh-0.5d0)*wcom/mh
      if(dabs(c).lt.1.d0) then
*   Square window
        if(itype.eq.1) datwin=1.d0
*   Hanning window
        if(itype.eq.2) datwin=(1.d0+dcos(pi*c))**ak
*   Parzen window
        if(itype.eq.3) datwin=(1.0d0-dabs(c))**ak
*   Welch window
        if(itype.eq.4) datwin=(1.0d0-c**2)**ak
*   Special windows
        if(itype.eq.5) datwin=dexp(-ak/(1.d0 - c**2)**2)
        if(itype.eq.6) datwin=dexp(-ak/(1.d0 - c**2))
*   Asymmetrize
        if(asym) datwin=datwin*(1.d0+b*c)
      else
        datwin=0.d0
      endif
      return
```

```
end
```

REFERENCES FOR PART 1

1. Charles Kittel, "On the Theory of Ferromagnetic Resonance Absorption," *Phys. Rev.* **73** p. 155 (1948).
2. A.M. Clogston, H. Suhl, L.R. Walker, and P.W. Anderson, "Ferromagnetic Resonance Line Width In Insulating Materials," *J. Phys. Chem. Sol.* **1** p. 129 (1956).
3. L. R. Walker, "Magnetostatic Modes in Ferromagnetic Resonance," *Phys. Rev.* **105** p. 390 (1957).
4. L.R. Walker, "Ferromagnetic Resonance: Line Structures," *J. Appl. Phys.* **29** p. 318 (1958).
5. L. R. Walker, "Spin Waves and Other Magnetic Modes," pp. 299 in *Magnetism, Volume 1*, ed. George T. Rado and Harry Suhl,Academic Press, New York (1963).
6. P.C. Fletcher and R.O. Bell, "Ferrimagnetic Resonance Modes in Spheres," *J. Appl. Phys.* **30** p. 687 (1959).
7. P. Fletcher, I.H. Solt, Jr., and R. Bell, "Identification of the Magnetostatic Modes of Ferrimagnetic Resonant Spheres," *Phys. Rev.* **114** p. 739 (1959).
8. Robert L. White and Irvin H. Solt, Jr., "Multiple Ferromagnetic Resonance in Ferrite Spheres," *Phys. Rev.* **104** p. 56 (1956).
9. Robert L. White, "Spin Waves and Magnetostatic Modes," *J. Appl. Phys.* **31** p. 86S (1960).
10. R.W. Damon and J.R. Eshbach, "Magnetostatic Modes of a Ferromagnet Slab," *J. Phys. Chem. Sol.* **19** p. 308 (1960).
11. J.R. Eshbach and R.W. Damon, "Surface Magnetostatic Modes and Surface Spin Waves," *Psys. Rev.* **118** p. 1208 (1960).
12. Harry Suhl, "The Nonlinear Behavior of Ferrites at High Microwave Signal Levels," *Proc. I. R. E.* **44** p. 1270 (1956).
13. H. Suhl, "The Theory of Ferromagnetic Resonance at High Signal Powers," *J. Phys. Chem. Sol.* **1** p. 209 (1957).
14. H. Suhl, "Note on the Saturation of the Main Resonance in Ferromagnetics," *J.Appl. Phys.* **30** p. 1961 (1959).
15. N. Bloembergen and S. Wang, "Relaxation Effects in Para- and Ferromagnetic Resonance," *Phys. Rev.* **93** p. 72 (1954).
16. R.W. Damon, "Relaxation Effects in the Ferromagnetic Resonance," *Rev. Mod. Phys.* **25** p. 239 (1953).
17. P.C. Fletcher and Neal Silence, "Subsidiary Absorption Above Ferrimagnetic Resonance," *J. Appl. Phys.* **32** p. 706 (1961).

18. Frederic R. Morgenthaler, "Survey of Ferromagnetic Resonance in Small Ferrimagnetic Ellipsoids," *J. Appl. Phys.* **31** p. 95S (1960).

19. E. Schlomann, J.J. Green, and U. Milano, "Recent Developments in Ferromagnetic Resonance at High Power Levels," *J. Appl. Phys.* **31** p. 386S (1960).

20. M.I. Kaganov and V.M. Tsukernik, "Nonresonance Absorption of Oscillating Magnetic Field Energy by a Ferromagnetic Dielectric," *Sov. Phys. JETP* 37(10) p. 587 ().

21. Richard W. Damon, "Ferromagnetic Resonance at High Power," pp. 551 in *Magnetism, Volume 1*, ed. George T. Rado and Harry Suhl,Academic Press, New York (1963).

22. V.E. Zakharov, V.S. L'vov, and S.S. Starobinets, "Spin Wave Turbulence Beyond the Parametric Excitation," *Sov. Phys. Usp* **17** p. 896 (1975).

23. K. Nakamura, S. Ohta, and K. Kawasaki, "Chaotic States of Ferromagnets in Strong Parallel Pumping Fields," *J. Phys. C.* **15** p. L143 (1982).

24. K. Nakamura, S. Ohta, and K. Kawasaki, "Chaotic States in Driven Ferromagnets," *J. Phys. Soc. Jpn.* **52** p. 147 (1983).

25. S. Ohta and K. Nakamura, "Power Spectra of Chaotic States in Driven Magnets," *J. Phys. C.* **16** p. L605 (1983).

26. George Gibson and Carson Jeffries, "Observation of Period Doubling and Chaos in Spin Wave Instabilities in Yttrium Iron Garnet," *Phys. Rev. A* **29** p. 811 (1984).

27. X.Y. Zhang and H. Suhl, "Spin Wave Related Period Doublings and Chaos Under Transverse Pumping," *Phys. Rev. A* **32** p. 2530 (1985).

28. S.M. Rezende, O.F. de Alcantara Bonfim, and F.M. de Aguiar, "Model for Chaotic Dynamics of the Perpendicular Pumping Spin Wave Instability," *Phys. Rev. B* **33** p. 5153 (1986).

29. F.M. de Aguiar and S.M. Rezende, "Observation of Subharmonic Routes to Chaos in Parallel-Pumped Spin Waves in Yttrium Iron Garnet," *Phys. Rev. Lett.* **50** p. 1070 (1986).

30. W. Froncisz and James S. Hyde, "The Loop-Gap Resonator: A New Microwave Lumped Circuit ESR Sample Structure," *J. Mag. Res.* **47** p. 515 (1982).

31. S. Geller, "Crystal and Static Magnetic Properties of Garnets," pp. 1 in *Physics of Magnetic Garnets*, ed. A. Paoletti,North-Holland, New York (1978).

32. S. Geller, H. J. Williams, R. C. Sherwood, J. P. Remeika, and G. P. Espinosa, "Magnetic Study of the Lighter Rare-Earth Ions in the Iron Garnets," *Phys. Rev.* **131** p. 1080 (1963).

33. P. Hansen, "Magnetic Anisotropy and Magnetostriction in Garnets," pp. 56 in *Physics of Magnetic Garnets*, ed. A. Paoletti,North-Holland, New York (1978).

34. P. Hansen, "Anisotropy and magnetostriction of gallium-substituted yttrium iron garnet," *J. Appl. Phys.* **45** p. 3638 (1974).

35. P. Escudier, "L'Anisotropie de l'Aimantation: un Parametre Important de l'Etude de l'Anisotropie Magnetocristalline," *Ann. de Phys.* **9** p. 125 (1975). In French: 49 page work on anisotropy giving results for Ni, Fe and YIG between 2K and 300K, including coefficients K1, K2, and K3.

36. W. Jantz and J. Schneider, "High Resolution Spin-Wave Spectroscopy in YIG," *Solid State Commun.* **9** p. 69 (1971).

37. W. Jantz and J. Schneider, "Fine Structure of the Subsidiary Absorption in YIG," *Phys. Stat. Sol.* **31** p. 595 (1975).

38. B.Andlauer, W. Jantz, and J. Schneider, "Fine Structure of Spin-Wave Instabilities in YIG," *A.I.P. Conf. Proc.* **5** p. 1209 (1972).

39. W. Jantz, J. Schneider, and B.Andlauer, "Fine Structure of the Parallel Pump Instability in YIG," *Solid State Commun.* **10** p. 937 (1972).

40. M.J. Feigenbaum, L.P. Kadanoff, and S.J. Shenker, "Quasiperiodicity in Dissipative Systems: A Renormalization Group Analysis," *Physica D* **5** p. 370 (1982).

41. S. Ostlund, D. Rand, J. Sethna, and E. Siggia, "Universal Properties of the Transition from Quasi-periodicity to Chaos in Dissipative Systems," *Physica D* **8** p. 303 (1983).

42. H. Suhl and X.Y. Zhang, "Spatial and Temporal Patterns in High-Power Ferromagnetic Resonance," *Phys. Rev. Lett.* **57** p. 1480 (1986).

43. X.Y. Zhang, "Hopf Bifurcations on the Degenerate Spinwave Manifold and Auto-Oscillations at High Power," preprint (1986).

44. X.Y. Zhang and H. Suhl, "Theory of Auto-oscillation in High Power Ferromagnetic Resonance," *Phys. Rev. B*, ().

45. V.V. Zautkin, V.S. L'vov, and S.S. Starobinets, "Resonance Phenomena in a Parametric Spin Wave System," *Sov. Phys. JETP* **36** p. 96 (1973).

46. Ernst Schlomann, "Fine Structure in the Decline of the Ferromagnetic Resonance Absorption with Increasing Power Level," *Phys. Rev.* **116** p. 828 (1959).

47. V.E. Zakharov, V.S. L'vov, and S.S. Starobinets, "Instability of Monochromatic Spin Waves," *Sov. Phys. Solid State* **11** p. 2368 (1970).

48. V.E. Zakharov, V.S. L'vov, and S.S. Starobinets, "Stationary Nonlinear Theory of Parametric Excitation of Waves," *Sov. Phys. JETP* **32** p. 656 (1971).

49. T. Holstein and H. Primakoff, "Field Dependence of the Intrinsic Domain Magnetization of a Ferromagnet," *Phys. Rev.* **58** p. 1098 (1940).

50. Conyers Herring and Charles Kittel, "On the Theory of Spin Waves in Ferromagnetic Media," *Phys. Rev.* **81** p. 869 (1951).

51. J.A. Osborn, "Demagnetizing Factors of the General Ellipsoid," *Phys. Rev.* **67** p. 351 (1945).

52. Edmund C. Stoner, "The Demagnetizing Factors for Ellipsoids," *Phil. Mag. 7th series* **36** p. 803 (1945).

53. Carl E. Patton and Wolfgang Jantz, "Anomalous Subsidiary Absorption in Single Crystal YIG and Evaluation of Spin Wave Linewidth," *J. Appl. Phys.* **50** p. 7082 (1979).

54. F. Waldner, D. R. Barberis, and H Yamazaki, "Route to chaos by irregular periods: Simulations of parallel pumping in ferromagnets," *Phys. Rev. A* **31** p. 420 (1985).

55. F. Waldner, R. Badii, D. R. Barberis, G. Broggi, W. Floeder, P. F. Meier, R. Stoop, M. Warden, and H. Yamazaki, "Route to chaos by irregular periods," *J. Magn. Magn. Mat.* **54-57** p. 1135 (1986).

56. J. Guckenheimer and P. Holmes, *Nonlinear Oscillations, Dynamical Systems, and Bifurcations of Vector Fields*, Springer, New York (1983).

57. William H. Press, Brian P. Flannery, Saul A. Teukolsky, and William T. Vetterling, *Numerical Recipies: The Art of Scientific Computing*, Cambridge University Press, New York (1986).

PART 2:

DYNAMICS OF A MAGNETIC OSCILLATOR

1 INTRODUCTION AND OVERVIEW

In this part of the thesis, the results of a study of another magnetic system will be presented – this one very different from the spin wave system of Part 1. This is a low frequency experiment (~100 Hz) in which the nonlinear effects result from saturation and hysteresis of a magnetic core. This experiment was designed to study some of the wealth of phenomena associated with the emergence of a second frequency in a dynamical system and the subsequent interactions between those frequencies.

There has recently been considerable interest in nonlinear dissipative systems which exhibit quasiperiodic behavior and phase locking, and in particular how such systems make the transition from regular to chaotic motion. There have been several theoretical and computer-assisted studies of this problem[1-8] as well as a large amount of experimental work[9], primarily with fluids, and also in solid state systems.

Systems that display quasiperiodicity can often be pictured as equivalent to two or more coupled nonlinear oscillators or modes. For systems equivalent to only one nonlinear oscillator, the route to chaos is typically through a period doubling cascade. Simple systems of two or more oscillators have not been fully studied, particularly their complex behavior near resonances, where a new frequency is emerging that is rationally related to a previously existing frequency (by some factor M/N). This study is concerned with this complex behavior for a weakly

oscillating nonlinear oscillator that is being driven by a second oscillator which is a prime mover. A brief report of some of this work has been published earlier[10].

A comprehensive study of the behavior near "strong resonance" points is presented for the experimental system and compared with the theoretical work of V. I. Arnold and others. Although this is a local theory, it can aid in the understanding of much of the complex behavior observed, some of which extends far from the resonance points. A thorough understanding of the dynamics requires the study of unstable orbits and basins of attraction. This is accomplished through a novel technique of repeated initialization, which allows one to locate these unstable orbits and observe the stable and unstable manifolds of saddle points. The bifurcations occurring within regions of phase locking and those that mark their boundaries are also explored in detail.

Symmetry plays a very important role in this physical system. Resonance points can be separated into symmetric and asymmetric types. Symmetric quasiperiodic attractors occur for which certain peaks in the frequency spectrum are suppressed. Symmetry breaking bifurcations and complementary band mergings are observed as a consequence of symmetry. Much of this symmetry-related behavior is explained using the concept of a half-cycle map.

In addition to this study of the important dynamics observed, two models are developed and studied for the physical system itself. The first is an unusual differential equation model which is irreversible and leads to a noninvertible Poincare map of the plane. The folding of this mapping has important consequences and explains some of the unusual behavior observed in the phase locked regions. (Note: noninvertibility does not preclude use of Arnold's theory - see Sec. 4.3.2.) In the second model a planar (2-D) mapping is assumed and an approximation for this Poincare map is obtained directly from experimental data by expanding the map in a 2-D Taylor expansion. Compared to the first model, this model shows improved agreement with the bifurcation set measured experimentally. This method could be useful in modeling other sys-

tems, especially those for which differential equation models are inaccurate or too complicated to analyze.

In the remainder of this section a description of the physical system is presented, the experimental methods used are described, and an introduction to and preview of the experimental results is given (with full details in Sec. 3).

1.1 Description of the Dynamical System

This system is a forced symmetrical nonlinear oscillator. It contains a single nonlinear element, an inductor made by winding a coil on a toroidal magnetic core[11]. This element acts both as a nonlinear inductor (through core saturation) and as a nonlinear dissipator (through magnetic hysteresis). This is driven by a "linear exciter" consisting of an oscillating current source $I_S(t)$, a negative resistance R, and a capacitance C, connected in parallel as shown in Fig. 1. The current source is generated by an operational amplifier that is driven by a sine wave

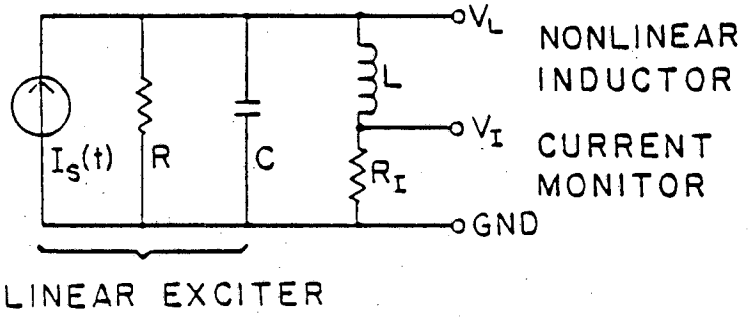

Figure 1. Schematic diagram of the forced magnetic oscillator. Note: R is a linear negative resistance.

generator of frequency ω_1, so that

$$I_S(t) = I_0 \sin\omega_1 t, \tag{1}$$

where I_0 is typically 1 mA and ω_1 is typically $2\pi \times 100$ Hz. The negative resistance is linear and is generated by another operational amplifier circuit. R is typically -500Ω and C is typically 7.5 μF. The negative resistance allows the system to be self-oscillatory for $I_0 = 0$ (typically 200 Hz) and to exhibit two-frequency oscillations for certain operating conditions with $I_0 \neq 0$.

In addition to these components there is a resistance R_I of one ohm in series with the inductor which is used as a current monitor by measuring the voltage V_I across it. R_I has been found (by decreasing its value) to have a negligible influence on the system's behavior, so we will not include it in our analysis below.

The effects of the linear components are easily combined in the relation:

$$I_L = -C\dot{V}_L - \frac{1}{R} V_L + I_S(t), \tag{2}$$

relating the inductor current (I_L) and voltage (V_L). Making the usual approximations about uniform magnetic induction B and magnetic field H in the core, we may write (in S. I. units):

$$V_L = nA\dot{B} \tag{3}$$

$$I_L = (L/n)\, H \tag{4}$$

where n = number of turns (100), A = effective core cross section ($1.51 \times 10^{-5} m$), and L = magnetic path length (0.1097 m). Substituting these into Eq. (2) we find the basic equation

$$\frac{L}{n} H = I_S(t) - \frac{nA}{R} \dot{B} - nAC\ddot{B} \tag{5}$$

The nonlinearity of the core effects the system through the relation between B and H, knowledge of which is required to solve Eq. (5), i.e. to find $B(t)$ or $H(t)$; this problem is treated in Sec. 4. At sufficiently low frequencies (so that the core is in quasi-equilibrium) there will be some nonlinear monotonic relation between B and H and this relation will change whenever $\dot{B}$ changes sign, i.e. when $V_L = 0$, due to magnetic hysteresis.

The state variables through which we usually observe the system behavior are the inductor current I_L, its voltage V_L, and the current source I_S. Since $I_S(t)$ is a sinusoidal oscillation ($I_0 \sin\omega_1 t$), its state (for fixed I_0 and ω_1) is given by its phase $\theta_S(t) \equiv \omega_1 t \pmod{2\pi}$. For convenience however, we observe $I_S(t)$ directly since this is equivalent to knowing θ_S if we also know the sign of $I_S(t)$. The magnetic induction B may be determined by integrating V_L [Eq. (3)] as we did to produce one of the figures in Sec. 1.3. However, for complicated behavior of the system, there is considerable difficulty caused by the arbitrary constant of integration, since one must stabilize the integral against any minute nonoscillatory part of V_L without introducing large fluctuating errors in the integral due to low frequency components of V_L.

The parameters by which we usually vary the behavior of the system are I_0, the peak amplitude of $I_S(t)$; τ_1, the period of $I_S(t)$; and R, the negative resistance. Normally we will be looking at some region of the I_0,τ_1 space with some fixed R. Varying other parameters such as C, n, and core parameters A and L is expected to yield no new behavior due to system scaling relations which we discuss in Sec. 4.2.

1.2 Methods of Observation

Most of the experimental data presented in this paper are periodically strobed phase portraits or Poincare sections. A simple periodic oscillation appears as a single point in the Poincare section. As parameters are varied, this oscillation may lose stability and some more complicated pattern may appear. Most of the Poincare sections presented in this paper are of I_L vs. I_S sampled when V_L crosses zero (i.e. a peak of I_L). The data points were collected using a trace storing oscilloscope and then photographed.

In order to fully understand the behavior of a nonlinear dynamical system, it is very helpful to be able to observe the transient behavior from some initial condition as well as the mode or modes of behavior that the system may exhibit after the transients have died away. For example, there may be two stable periodic oscillatory modes which can be reached from different initial conditions. Often there are unstable modes, slight perturbations from which (such as caused by noise) will grow exponentially with time.

For reasons explained in Sec. 4.3.1, the state of the system at a peak or turning point of I_L may be approximated by just two variables: I_L and I_S, provided the core is near saturation. Thus, if one can initialize the system to any desired I_S and I_L at a time when $V_L = 0$, then one has a simple and effective means of exploring the transient behavior of the system. This is accomplished by using an electronically controlled analog switch, which when activated, forces the system into a periodic oscillation at the driving frequency ω_1 but with amplitude and phase adjustable with respect to that of $I_S(t)$. One then electronically deactivates this at a turning point ($V_L = 0$), freeing the system to follow its own path from this initial condition.

With this initializer we can set I_S and I_L at the initial turning point. If the above approximation on core saturation is valid, then we have access to the entire Poincare space. But if not, this space has additional dimensions. In this case we might have difficulty finding an unstable node if it is also unstable on these extra dimensions. If, however, an unstable fixed point has at least one stable direction in the full Poincare space, then we can reach this point by initializing on the stable manifold[12] of the fixed point, provided this manifold intersects the subspace that we can access with the initializer. Thus, in general, an initializer can be useful even in cases where it cannot access all possible initial states.

In addition to phase space diagrams ("phase portraits") and Poincare sections of these diagrams, we also measure the frequency spectrum $V(\omega)$ of $V_L(t)$ with a scanning spectrum analyzer, an HP Model 3580A, with 90 dB dynamic range. The results are plotted as ω vs.

$V(\omega)$ in dBV, i.e. the peaks in the spectra are to be read in decibels above 1 volt rms (dBV = 20 log10 V rms). Unless otherwise specified, the resolution bandwidth used is 1 Hz.

1.3 Preview of Experimental Results

When we vary the parameters (I_0, ω_1, R) of the system, we find that there is a region in this parameter space where the system exhibits a symmetrical periodic oscillation at the driving frequency ω_1. This could be described as a relaxation oscillation, having a "slow phase" where V_L and I_L do not change much, alternating with a "fast phase" where V_L and I_L rapidly change sign. When one observes the behavior of the system in two or more state variables, such as I_L vs. I_S, one sees a closed curve as shown in Fig. 2a.

However, as one crosses a certain surface in the parameter space, one finds that the system begins to develop another oscillation at some new frequency ω_2. In the primary region of study this is in the range $\omega_1 < \omega_2 < 2\omega_1$. The ratio ω_2/ω_1 may be irrational, in which case the oscillation will no longer be periodic. When observed in the space of three or more state variables (e.g. I_L, V_L, I_S), the orbit will remain on a two-dimensional torus and will proceed to fill in this surface completely as $t \to \infty$ (Fig. 2b). We can examine a cross-section (or Poincare section) of this figure (say by strobing at appropriate intervals a storage oscilloscope) and will find a set of points forming a closed curve. A frequency spectrum (say of $V_L(t)$) will show the frequencies ω_1 and ω_2 and smaller components at all their "odd" linear combinations: $\omega_{mn} = m\,\omega_1 + n\,\omega_2$ where $n + m$ = odd integer (Fig. 2c). We discuss this further in Sec. 2.3.3. This change in stability, i.e. the onset of a second frequency ω_2, is known as a Hopf bifurcation. In a two-parameter space (say I_0, ω_1), the Hopf bifurcation occurs when one crosses a certain line. Across this line there are regions where ω_2/ω_1 is a rational ratio (M/N in lowest terms) and the

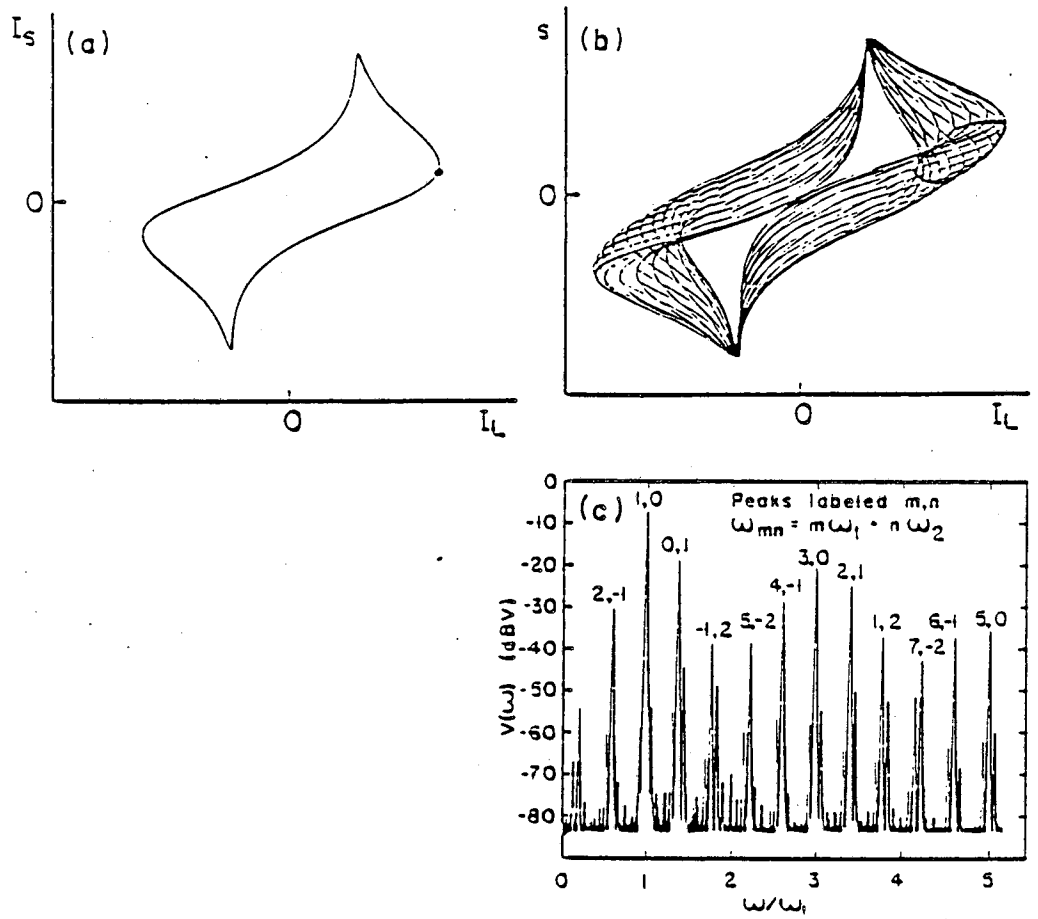

Figure 2. (a) Phase portrait of the inductor current I_L vs. the forcing current I_S. Strobing every cycle as the inductor voltage V_L crosses zero from positive to negative produces the point shown. Here there is a symmetrical 1:1 phase locking. (b) At another point in parameter space the system undergoes a Hopf bifurcation and a symmetrical quasiperiodic attractor emerges. By strobing, the Poincare section is seen to display an invariant circle. (c) Frequency spectrum of $V_L(t)$ – shows only odd 2-component harmonics (m+n = odd) due to symmetry.

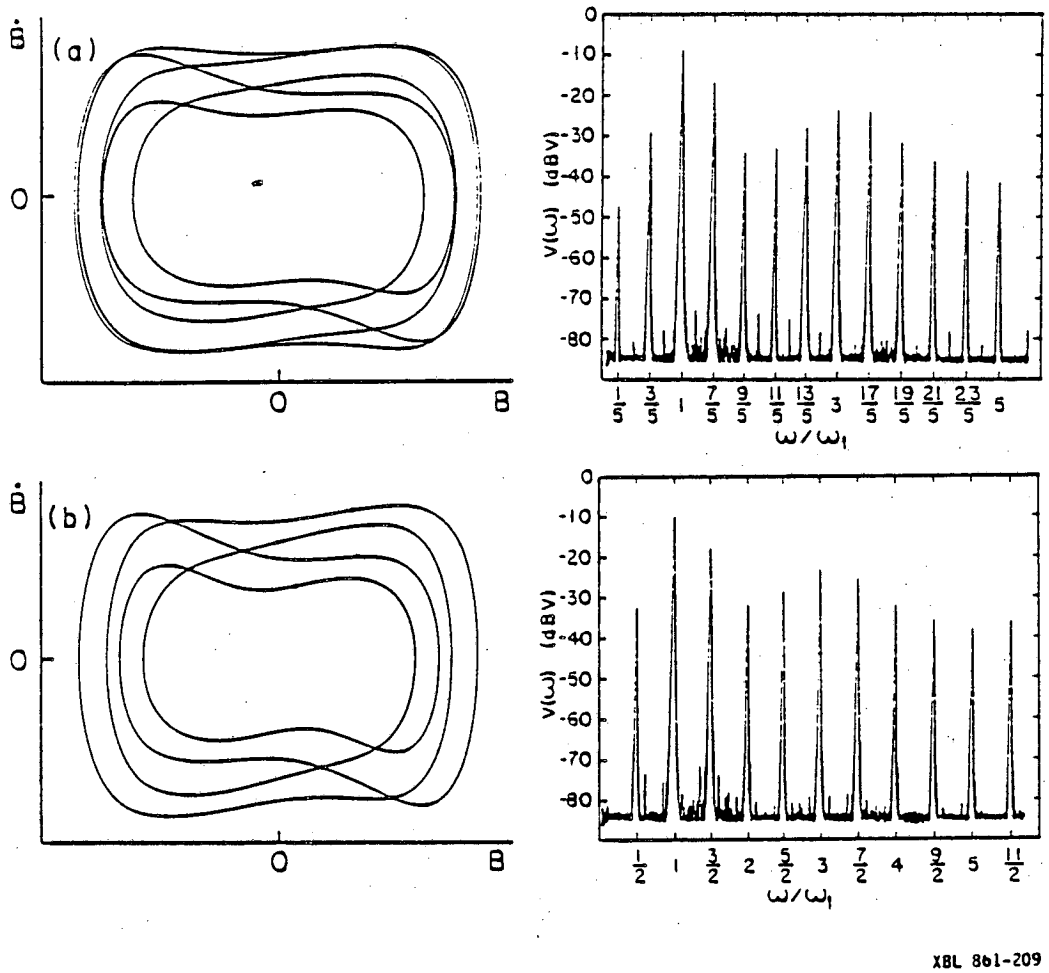

Figure 3. (a) Phase portrait and spectrum of $V_L(t)$ for the symmetric type of entrainment with $\omega_2/\omega_1 = 7/5$. (b) Asymmetric type: shows two complementary attractors (by double exposure) interwoven with each other. Each has $\omega_2/\omega_1 = 3/2$. The Poincare section of (a) is five points; of (b), it is two sets of two points.

behavior is again periodic. Here the system is said to be phase locked or entrained. We find that when M and N are both odd, that the behavior of the system is again symmetrical (e.g. $V_L(t_1) = -V_L(t_2)$ where $t_2 = t_1 + N\pi/\omega_1$) and the frequency spectra will contain only odd har-

monics of the frequency ω_1/N (see phase portrait and frequency spectrum in Fig. 3a). In all other cases of entrainment there are two complementary asymmetric modes in which the system can oscillate (see phase portrait and frequency spectrum in Fig. 3b).

If we define the order of the entrainment q as

$$q = N \quad \text{for symmetric behavior} \tag{6}$$

$$q = 2N \quad \text{for asymmetric behavior} \tag{7}$$

then we find that in a two-dimensional parameter space [we use I_0(rms) and $\tau_1 = 2\pi/\omega_1$], for $q \geq 5$ the entrainment regions all have a typical shape called a resonance horn or an entrainment horn or a tongue. The frequency ratio changes smoothly along the line of Hopf bifurcation and the horns emerge from this line at the points corresponding to rational ratios, called points of resonance. We show such a parameter space diagram in Fig. 4. The points of resonance are labeled by their order q. For resonances of order less than five, there are other characteristic patterns often involving the coexistence of more than one stable behavior pattern. The $q = 4$ resonance has a hornlike region emerging from it in this figure, but it also has many other forms, some of which are described in Sec. 3.1.4.

In this paper our primary emphasis is on behavioral changes that the system goes through as we vary its parameters near the points of resonance and the associated phase locked regions. We discuss both the theory (Sec. 2.2) and our experimental results (Sec. 3.1) for both the weak ($q \geq 5$) and strong ($q \leq 4$) resonances. An understanding of the theoretical behavior, particularly of the strong resonances, is found to be very important in predicting the qualitative behavior far from the resonance point. Moving within the horn away from its vertex one finds the system behavior becoming more complex, as described in Sec. 3.2. In Sec. 3.3 we describe what can happen when two phase locking domains overlap or coexist. In some cases we observe a Hopf bifurcation initiating from an entrainment. This will appear as a set of closed curves, which we describe in Sec. 3.4.

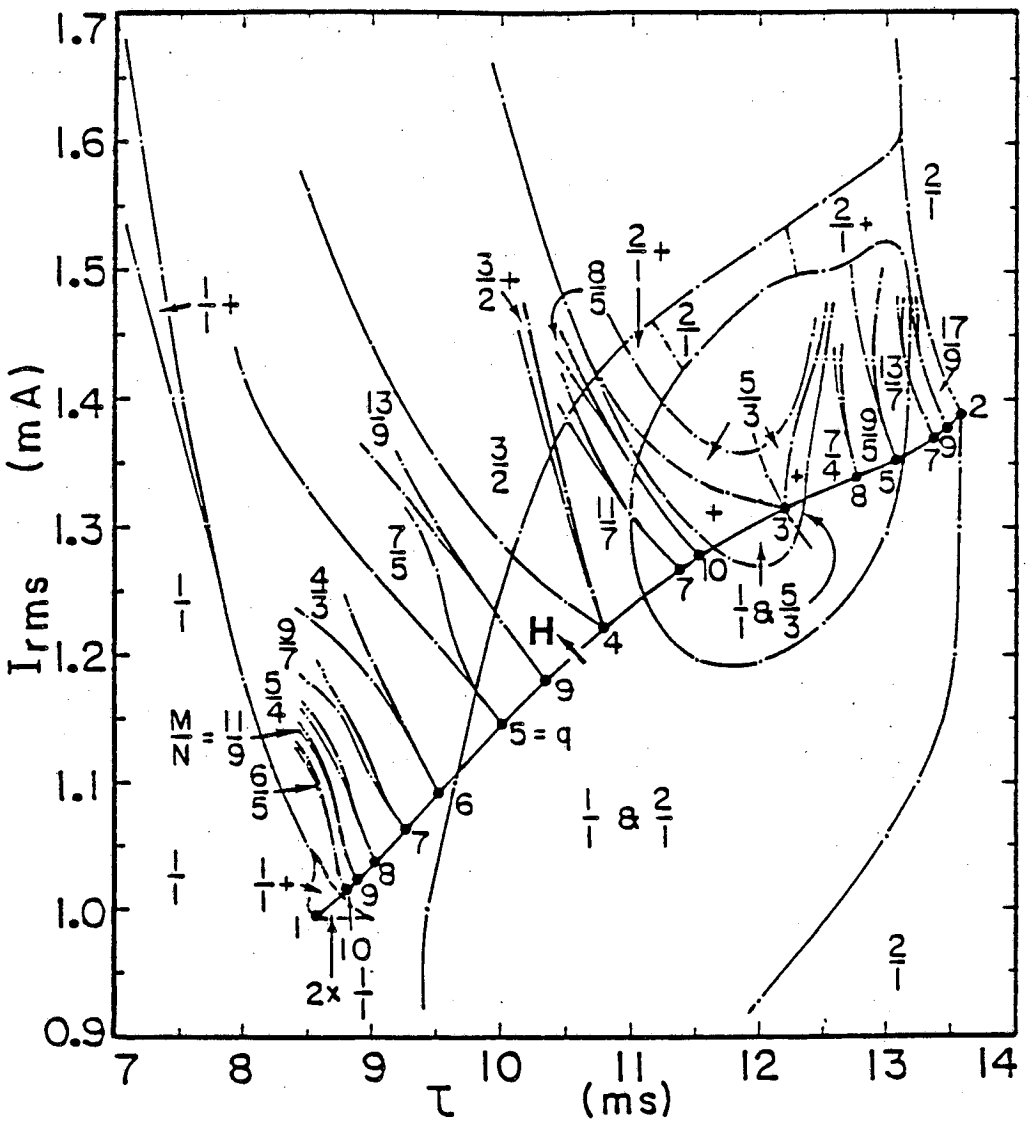

Figure 4. Parameter space diagram. Here τ is the period of the driving current $I_S(t)$ and I_{rms} is the rms aplitude of $I_S(t)$; for $R = -500\ \Omega$ and $C = 7.5\ \mu F$. Phase locked regions are labeled by ω_2/ω_1, points of resonance by order q (for $q \leq 10$), Hopf bifurcation by H. Portions of phase locked regions labeled with a plus sign have coexisting quasiperiodic attractors. In some regions two phase locked attractors coexist, e.g. the region labeled 1/1 and 5/3. The region labeled $2 \times 1/1$ has two distinct 1/1 type attractors. Hysteresis is observed when these multiple attractor regions are traversed. The region labeled 2/1 exhibits an asymmetric attractor with two complementary modes and is thus distinguishable from the symmetrical 1/1 attractor. In Sec. 3, many structures shown here are studied in great detail and are found to be related to the theoretical behavior of the points of "strong resonance". Note that the points labeled "1" and "2" are the end points of the Hopf bifurcation line.

Throughout the paper we will be emphasizing the importance of hidden behavior related to unstable oscillatory modes of the system and the transient behavior that couples the unstable orbits with stable ones. Knowledge of this "hidden behavior" is very important to the understanding of the "visible behavior" and how it changes with the parameters. Thus, for example, we experimentally investigate motion on both the unstable and stable manifolds of saddle orbits.

2 THEORETICAL CONCEPTS

2.1 Bifurcation Types

We expect that most readers of this paper will be familiar with the fundamental types of bifurcations (saddle-node, Hopf, period doubling, etc.), and therefore we restrict our discussion to some details which may be less commonly known. For a review of material not presented here we refer to Ref. 12.

Many different types of bifurcations, both local and global, are important to the dynamics of a system, like the present one, in which a second frequency is emerging. In order to fully understand the dynamics, it is necessary (in some cases) to study the bifurcations of unstable fixed points in the system. Although these bifurcations do not directly effect the attractor(s) of the system, they will effect the basins of attraction. Frequently, unstable fixed points emerging from such bifurcations will, at some other parameter setting, be involved in a bifurcation involving a stable attractor. In a two-dimensional Poincare space there are four types of period doubling bifurcations, two of which involve only unstable fixed points (in the Poincare section), as shown in Fig. 5. In each case a single fixed point splits into a period doubled pair, separated by a period one fixed point of altered stability (relative to the original fixed point). There are

TABLE 1 – NOTATION USED IN BIFURCATION DIAGRAMS

2-D bifurcation diagrams have a number of lines representing co-dimension 1 bifurcations, which separate regions of parameter space in which qualitatively different behavior patterns exist. The patterns drawn for each region represent typical 2-D Poincare sections. In them, solid dots represent stable points (sinks) and open dots (very small circles) represent unstable points (sources). Saddles have no dot but are clearly indicated by arrows on their stable and unstable manifolds. Foci are distinguished from nodes by a slight spiral on approach. The co-dimension 1 bifurcations are indicated by an arrow connecting the Poincare patterns of two adjacent regions or crossing a bifurcation line in the bifurcation diagram, and an abbreviation for the bifurcation. These are used both in the theoretical and experimental figures. The bifurcations occur as described below in the direction of the arrow.

Abbrev.	Description
A. The following are continuous bifurcations with no jump to another attractor and no hysteresis implied:	
H	Hopf: circle(s) emerge from point(s) in the Poincare section.
×2	Period doubling.
×4	2nd period doubling.
×∞	End of period doubling cascade.
bm1	Band merging: two-band chaotic attractor merges to one band.
sb	Symmetry breaking: one symmetric attractor splits into two complementary asymmetric attractors.
cbm	Complementary band merging: two complementary chaotic attractors merge into one symmetric one.
plc	Phase-locked circle: periodic nodes and saddles appear (in saddle-node pairs) on an invariant circle and then separate.
cr(i)	Interior crisis[27]: period n chaotic attractor contacts period n saddle point and loss of phase locking occurs in conjunction with a sudden increase in attractor size.
nf	Node changes to focus (trivial bifurcation).
lr	Left focus changes to right focus (iterates clockwise). This is usually with respect to the rotation of a periodic attractor encircling the focus (trivial bifurcation).
B. The following involve a jump (i.e., a discontinuous change in the observed variable) and imply hysteresis.	
sn	Saddle-node: a saddle and node appear together and separate. In reverse, a jump to another attractor occurs when the node is annihilated.

hc	Homoclinic: circle(s) contact periodic saddle(s) forming a homoclinic orbit; circle(s) are annihilated and a jump to another attractor occurs.
cr(b)	Boundary crisis[27]: chaotic attractor contacts the boundary of its basin of attraction, is annihilated, and a jump occurs.
×2(b)	Subcritical period doubling [see Fig. 5(b)]. In reverse a jump can occur after the stable node combines with the period doubled saddle to form a period one saddle, leaving no attractor locally.
sb(b)	Subcritical symmetry breaking, similar to 2(b).

C. The following involve only unstable fixed points.

su	Saddle and unstable node appear together and then separate.
×2(c or d)	Type (c) or (d) period doubling of unstable fixed points, see Figs. 5(c) or (d).
sb(c or d)	Type (c) or (d) symmetry breaking of unstable fixed points, similar to 2(c or d).

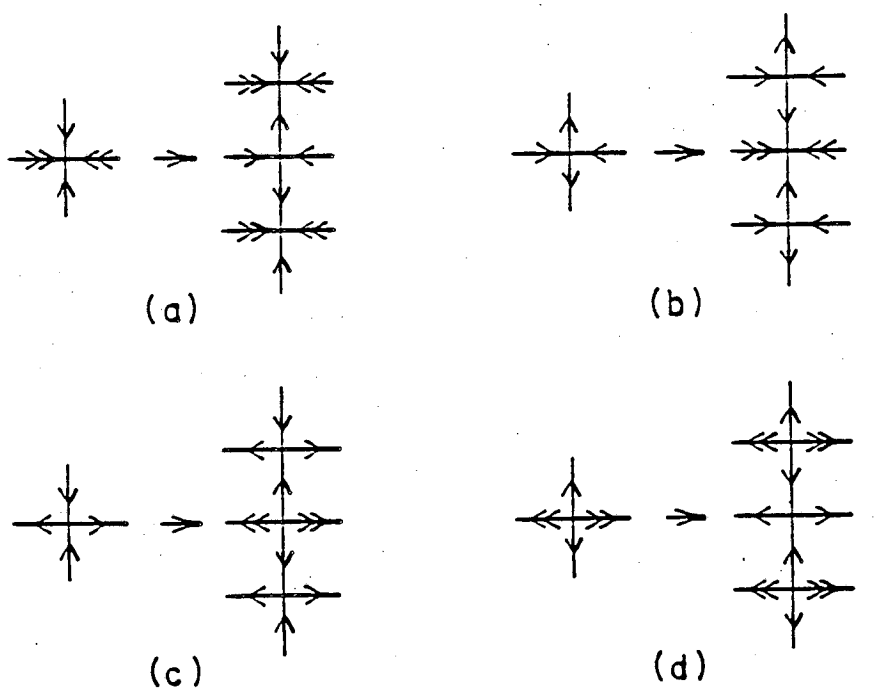

Figure 5. Structure of period doubling bifurcations for a 2-D Poincare section. There are four types: (a) The standard case involving a stable node. After bifurcation the two parts of the period 2 node are separated by a saddle point. (b) A saddle point bifurcates in its unstable direction to a period 2 saddle separated by a stable node. (c) A saddle bifurcates in its stable direction to a period 2 saddle separated by an unstable node. (d) An unstable node bifurcates to a period 2 unstable node separated by a saddle.

also four cases of symmetry breaking. These can also be represented by Fig. 5 except that in this case all fixed points are period 1. Saddle node bifurcations occur in two types, one of which involves a saddle and a stable node, the other a saddle and an unstable node. The second case has no attractors. An important type of global bifurcation is the homoclinic bifurcation[12]. Here, as parameters are varied, an invariant circle (corresponding to quasiperiodic motion) contacts a saddle orbit after which it is annihilated. In a nondegenerate case, this occurs as a point of tangency develops between the stable and unstable manifolds of the saddle point(s). We frequently observe, however, a (nearly) degenerate case where the stable and unstable manifolds

(nearly) coincide. In the nondegenerate case, the attractor becomes highly chaotic before it is annihilated, while in the degenerate case the circle remains relatively smooth (aside from a kink near the approaching saddle point). Table 1 presents a list of bifurcation types which have been observed in the experimental system, and defines a set of abbreviations which are later used in the bifurcation diagrams.

2.2 Bifurcations Near Points of Resonance

The case of bifurcation near points of resonance is discussed by Arnold[13-15], Iooss[16], and Takens[17]. In this case the bifurcating fixed point of the Poincare map has conjugate eigenvalues that are roots of unity ($\lambda = \exp 2\pi i p/q$). This fixed point is doubly degenerate since we are requiring both $|\lambda| = 1$ and $\arg(\lambda) = p/q$, and therefore we will have a bifurcation of codimension 2. This requires the variation of two parameters about the bifurcation point to be fully characterized. Arnold approaches this problem by making the connection between the bifurcation of a resonant fixed point in the Poincare map and the bifurcation of fixed points of vector fields in the plane. In the vicinity of the bifurcating orbit, the behavior may be approximated by a vector field of the plane that is determined by averaging in the Seifert foliation corresponding to the resonance being studied (see Arnold[13], page 170). In essence, this means we are looking at the behavior in a coordinate system which has one coordinate parallel to the bifurcating orbit (i.e. the angle indicating a particular point on the orbit) and two coordinates (x,y) transverse to the orbit with their origin at the orbit. These transverse coordinates rotate about the orbit at the same average rate as the nearby phase paths wind around it, i.e. p/q per cycle. This is the Seifert foliation. Averaging the behavior in the transverse coordinates over q cycles, one can represent the behavior as a vector field in the plane with symmetry under rotation by $2\pi/q$. This averaging is valid on the assumption that motion in these transverse

coordinates is very slow near the origin, occurring over many cycles. This will be true since at the bifurcation point the eigenvalues have unit magnitude there. For cases of order q greater than two, Arnold treats the problem in the plane of the complex variable $z = x + iy$. A Taylor's expansion of the vector field near the origin is made yielding $\dot{z} = \sum F_{jk} z^j \bar{z}^k$, where $\bar{z}$ is the complex conjugate of z. The rotational symmetry requires $j-k-1$ be divisible by q. Keeping the linear term, the lowest nonzero term with q symmetry and the lowest nonlinear term with no q dependence:

$$\dot{z} = \varepsilon z + Az|z|^2 + B\bar{z}^{q-1}, \quad q \geq 3, \tag{8}$$

where ε, A, and B are complex coefficients. Arnold refers to this as the principle deformation. The linear coefficient ε for this vector field must be zero at the bifurcation point (when $\lambda = e^{2\pi i p/q}$). Varying ε by a small amount around zero in the complex plane will determine the bifurcation sequence (i.e. varying Re ε and Im ε about zero can be assumed to be equivalent to varying any two parameters about the bifurcation point). We can assume that ε is much smaller than A and B so that they are effectively constant during the bifurcation process. However, different bifurcation patterns may be obtained for different values of A and B. These bifurcation patterns take the form of a sequence of co-dimension 1 bifurcations that are encountered as ε is varied around zero.

B can be set to one by rescaling the other parameters and the time. Letting $z = r\, e^{i\phi}$ and solving for fixed points ($\dot{z} = 0$) we find

$$\frac{\varepsilon}{r^2} = -A - r^{q-4} e^{-iq\phi}. \tag{9}$$

For $q \geq 5$ the last term is small for small r, and thus $\varepsilon \approx -Ar^2$ (i.e. ε and $-A$ must have nearly the same argument for there to be fixed points other than $z = 0$ since r must be real). When the last term is included, one finds that fixed points exist within a horn-shaped region, shown in Fig. 6. In this figure as in all other 2-D bifurcation diagrams throughout the rest of this paper, we use an abbreviated notation to describe co-dimension 1 bifurcation lines which is given in Table

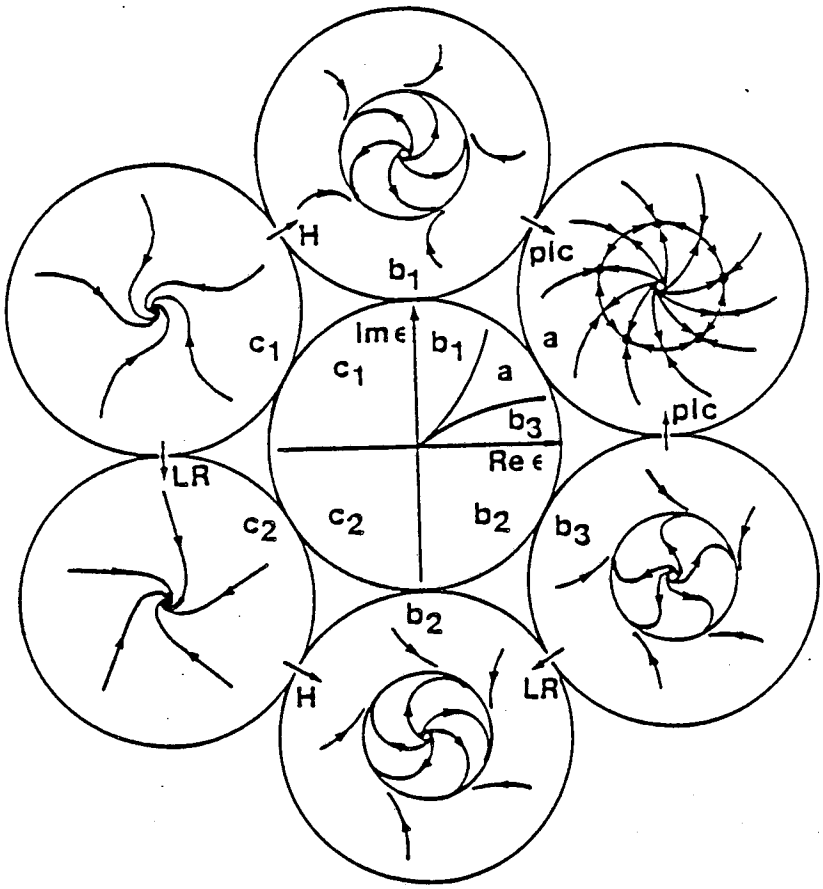

Figure 6. 2-D bifurcation diagram for resonant fixed point in the case of weak ($q \geq 5$) resonance with ReA and ImA < 0 (other cases related by symmetry). Central figure shows the bifurcation lines, in this case a horn, in the complex parameter space ε. Table 1 lists codimension 1 bifurcation abbreviations used in these figures. The surrounding figures represent the topological behavior pattern for a typical 2-D Poincare space for the indicated domains in the parameter space.

1. This horn (sometimes called a resonance horn or tongue) is centered on arg($-A$) and has an angular width θ that spreads with ε:

$$\theta \approx \frac{2|\varepsilon|^{(q-4)/2}}{|A|^{(q-2)/2}}. \tag{10}$$

Within the horn there are q nodes alternating with q saddles in a circle, as shown in Fig. 6.

This is sometimes called a circle in resonance or a phase-locked circle. Moving ε clockwise toward the horn boundary, the nodes approach the saddles which are clockwise from their positions. These annihilate and leave an invariant circle with clockwise rotation. Moving ε counterclockwise results in a counterclockwise approach and annihilation, and produces a counterclockwise invariant circle. Note that for the Poincare map this rotation of the invariant circle is with respect to the entrained rotation of p/q. The circle disappears (via inverse Hopf bifurca-

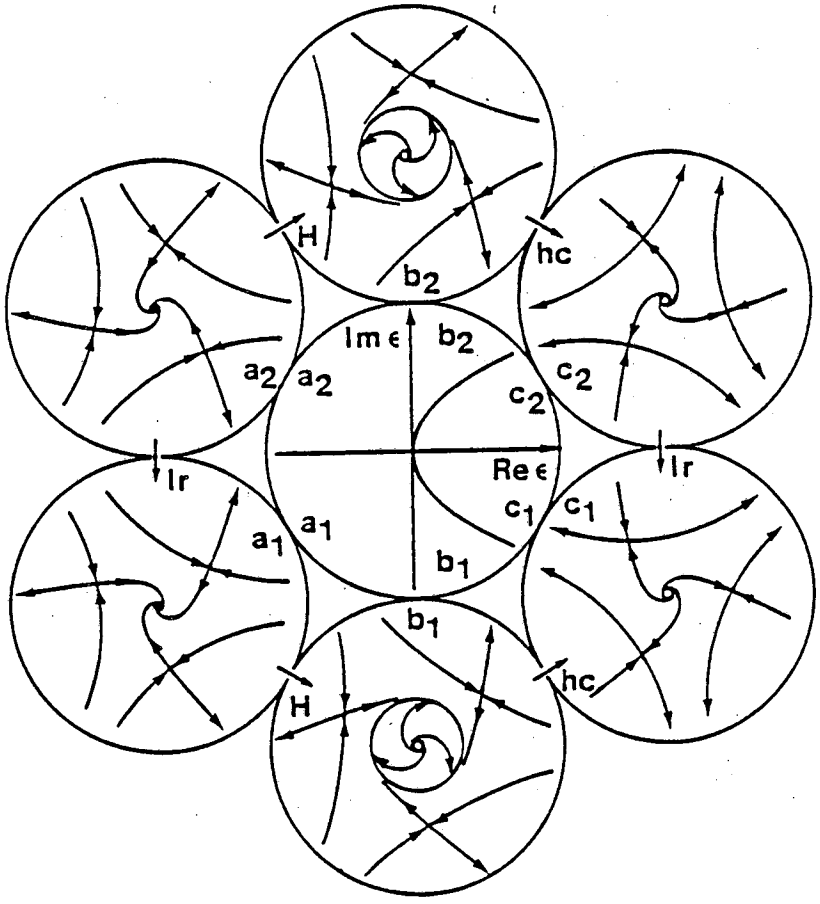

Figure 7. 2-D bifurcation diagram for $q = 3$. Involves no period 3 nodes, only period 3 saddles. Same diagramatic arrangement as discussed in caption of Fig. 6. Some regions have no attractors so a jump to some distant attractor must occur when entering these regions.

tion) when crossing Re $\varepsilon = 0$. Thus, except for the narrow horn-shaped region we have the same behavior as for an ordinary (nonresonant) Hopf bifurcation, in the case of weak ($q \geq 5$) resonance. This is not the case however for strong ($q \leq 4$) resonance. The cases $q = 3$ and 4 can also be studied using the complex equation:

$$q = 3: \quad \dot{z} = \varepsilon z + Az|z|^2 + B\bar{z}^2, \tag{11}$$

$$q = 4: \quad \dot{z} = \varepsilon z + Az|z|^2 + B\bar{z}^3, \tag{12}$$

For $q = 3$ there is only one bifurcation pattern [and its time (or arrow) reversed equivalent] which we show in Fig. 7. It should be noted that no stable period 3 fixed points are involved in this bifurcation. This fact will be explored further in Sec. 3.1. The $q = 4$ case, however, has not been completely characterized on a theoretical basis, although it is known that a large number of possibilities exist depending upon the choice of the parameters A and B[18-21]. Unlike $q = 3$, many of the $q = 4$ bifurcation patterns do involve stable period 4 points. For the cases $q = 1$ and $q = 2$, another approach is needed. Arnold shows that the principle deformations can be expressed in the x-y plane as:

$$q = 1: \quad \dot{x} = y, \ \dot{y} = \alpha + \beta x + Ax^2 + Bxy, \tag{13}$$

$$q = 2: \quad \dot{x} = y, \ \dot{y} = \alpha x + \beta y + Ax^3 + Bx^2y. \tag{14}$$

There is one type of $q = 1$ bifurcation (Fig. 8) and two types of $q = 2$ of which we show the one for $A > 0$, $B < 0$ (Fig. 9). The second type is not shown here (but see Ref. 13) since we have not observed this behavior in our system as we have for the other cases discussed above. The $q = 2$ case shown involves no stable period 2 points, while the other one does.

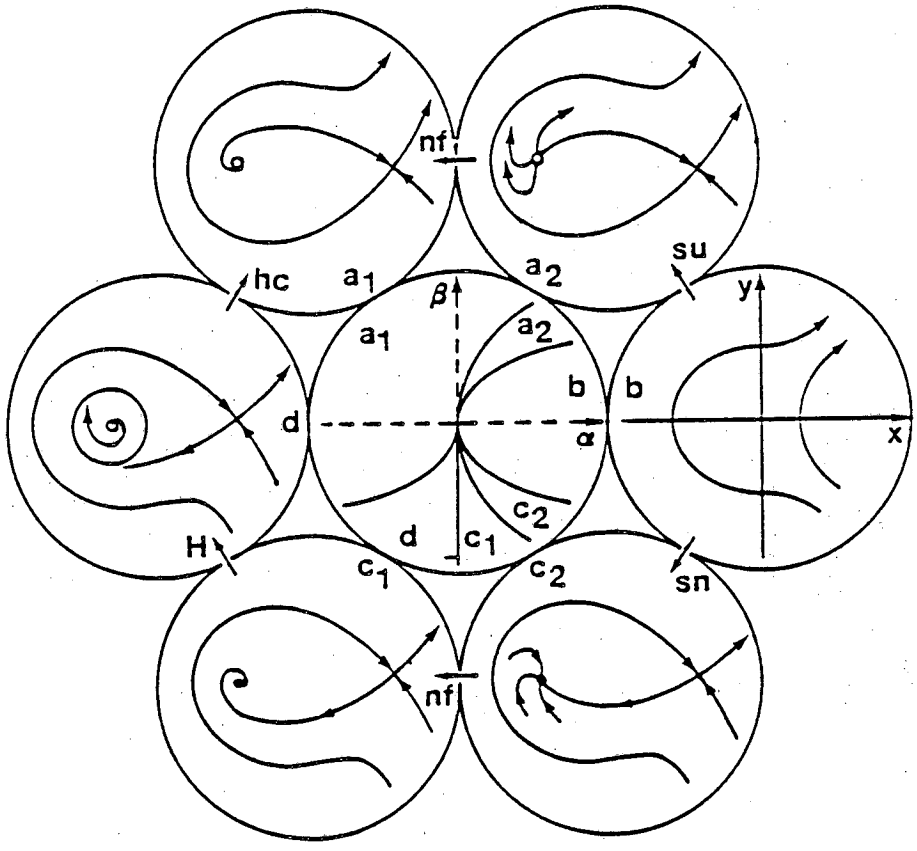

Figure 8. 2-D bifurcation diagram for $q = 1$ with $A > 0$, $B < 0$ (other cases related by symmetry). Same diagramatic arrangement as discussed in the caption of Fig. 6. Some regions have no attractors.

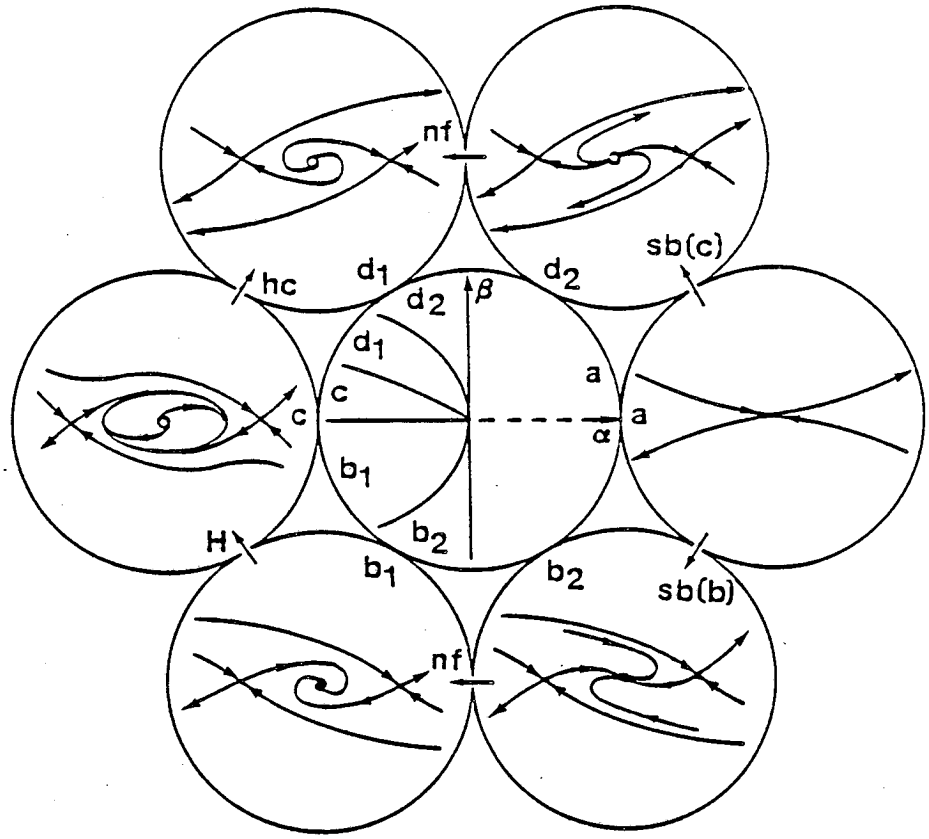

Figure 9. 2-D bifurcation diagram for $q = 2$ with $A > 0$ and $B < 0$. Same diagramatic arrangement as discussed in the caption of Fig. 6.

2.3 Behavior of a Symmetrical System

2.3.1 Half Cycle Map

We define a symmetrical system to be one which for any state x there is a complementary state x' such that if $x(t)$ is a possible phase path of system, then $x'(t)$ is also. We require that $x' \neq x$ for almost all x and also that $x'' = x$, where x'' is the complement of the complement of

x. The exact definition of the complementary state will depend on the type of symmetry involved. In our forced magnetic oscillator we assume that the magnetic core is perfectly symmetrical and that the complementary state satisfies: $B' = -B$, $H' = -H$, $V_L' = -V_L$, and the phase of the forcing oscillation (which is also considered part of the state) is shifted by 1/2 cycle. In our case the forcing oscillation must be symmetrical and contain no dc offset. (Note: the core exhibits complex memory effects as discussed in Sec. 4.1, and its state is not completely specified by B and H.)

Symmetry has important consequences for the behavior we can observe. First of all there are two types of attractors (or other invariant manifolds): those which are asymmetrical and have a complementary form, and those which are symmetrical and are their own complement. Symmetry breaking bifurcations become possible where one symmetrical attractor splits into two complementary ones. For a fixed point in the Poincare space, this can happen in the same way as period doubling except that the bifurcating eigenvalue passes through +1 instead of -1, and the bifurcated fixed points do not double in period (see Fig. 5). A symmetrical periodic oscillation clearly can only have odd harmonics in the frequency spectrum of V_L or I_L. This means that the ratio of any two frequencies exhibited by a symmetrical oscillation must be a ratio of odd integers; hence phase-locked states whose fundamental frequencies cannot be expressed as proportional to odd integers cannot be symmetrical.

As discussed in the previous section, the behavior of the bifurcation of a resonant fixed point is characterized by a symmetry under a rotation through an angle of $2\pi/q$ where q is the order of the resonance. When the frequency ratio corresponding to that fixed point is M/N and M and N are not both odd, then the order must be $q = 2N$ (instead of N) to allow for the division into two complements of anything that bifurcates from that resonant point.

Some of the behavior of a symmetrical system can be clarified through the concept of a half-cycle Poincare map[22]. We can define a complementary Poincare section as the intersection

of the orbit with the complement of the original Poincare space, e.g. for the space defined $V_L = 0$, $\dot{V}_L > 0$ we have the complement $V_L = 0$, $\dot{V}_L > 0$. We consider a situation where the orbit alternates crossing the two complementary sections. Mapping from the point X_0 in the original section to the subsequent point X_1 in the complement, we have the map $X_1 = F_+(X_0)$ and from this point to the subsequent point X_2 in the original we have the map $X_2 = F_-(X_1)$. But symmetry requires that

$$F_+(X_0) = X_1 \text{ implies } F_-(X_0') = X_1' \tag{15}$$

and therefore

$$X_{2n} = G^{(2n)}(X_0), \tag{16}$$

where $G^{(2n)}(X)$ is the 2nth iterate of X through the map G(X) and $G(X) \equiv F_+'(X) = F_-(X')$ is the half-cycle Poincare map. Thus one iteration of the full-cycle Poincare map can be expressed as two iterations of this half-cycle map G(X), which maps to the complementary section and then takes the complement of the result putting it back in the original Poincare space.

Note that if the half-cycle map has an invariant circle, its rotation number is not $\omega_2/2\omega_1$. This is because this map takes the complement of the state that actually occurs one-half cycle later. Thus,

$$\rho_{1/2} = [(\omega_2/2\omega_1) - \tfrac{1}{2}] \bmod 1, \tag{17}$$

where $\rho_{1/2}$ is the rotation number of the half-cycle map of a point inside the invariant circle.

The existence of this half-cycle map has important implications. If a fixed point is a fixed point for the half-cycle map (i.e. a symmetric oscillation), then we can study its bifurcation under this map. If an even number q of identical fixed points bifurcate from it, then we can state at once that a symmetry breaking bifurcation has taken place. This is because after q iterations of the half-cycle map, all points will have been visited, while at the same time only $q/2$ of them are visited by the full cycle Poincare map. Thus the attractor for the half-cycle map has period q, while the full-cycle map has two attractors of period $q/2$. However, if q is odd, q

iterations of the half-cycle map does not correspond to a whole number of iterations of the full-cycle map, and therefore the full-cycle map will visit all points resulting in a single (and hence symmetrical) attractor. For a phase-locked circle (as discussed in Sec. 2.2 in connection with bifurcations of order $q \geq 5$), we have symmetric and complementary asymmetric forms for odd and even numbers of nodes, respectively, as shown in Fig. 10.

Another important implication relates to the nature of symmetry breaking bifurcations. For a symmetric oscillation the attractor for the half-cycle map and the full-cycle map are the same. After a symmetry breaking bifurcation the full-cycle map iterates on one attractor or the other while the half-cycle map iterates back and forth between the two attractors. *Thus a symmetry breaking bifurcation is just a period doubling bifurcation for the half-cycle map.* It is to

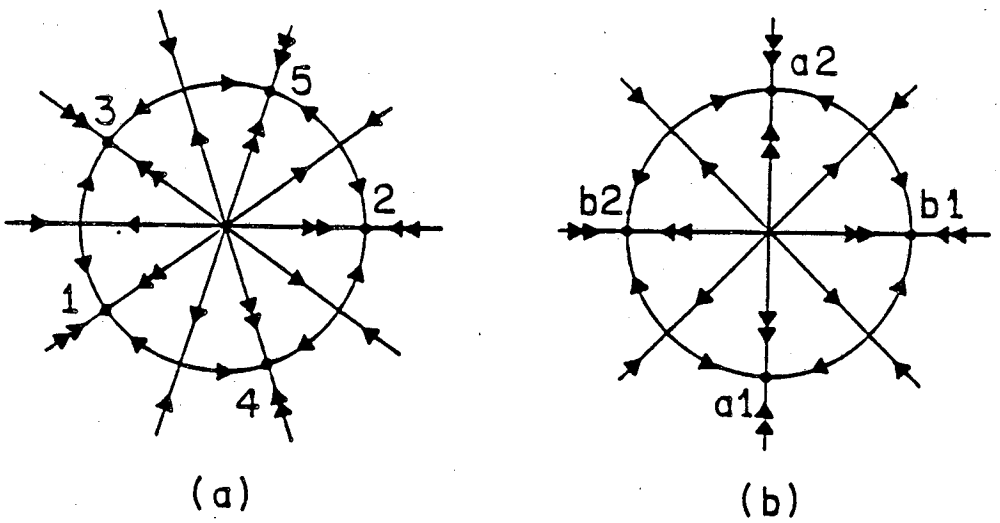

Figure 10. (a) Poincare map for symmetric phase-locked circle. Here the rotation number is 2/5 so an orbit through the stable nodes iterates in the sequence shown (i.e. 1, 2, 3, 4, 5, 1, 2, ...). (b) Complementary asymmetric phase-locked circle. Here the rotation number is 1/2 so the a orbit iterates in the sequence (a1, a2, a1, a2, ...) and the b orbit in the sequence (b1, b2, b1, b2, (b) could bifurcate from a $q = 4$ point.

be expected therefore that symmetric oscillations will ordinarily undergo a symmetry breaking bifurcation before (rather than simultaneously with) the first period doubling bifurcation, this being the second such bifurcation for the half-cycle map.

2.3.2 *Effects of Asymmetry*

While we are used to thinking of an inductor as a symmetrical component (i.e. when the leads are interchanged, it behaves the same), this will not necessarily be the case in a real inductor with a magnetic core. First, there may be a slight inherent anisotropy favoring the (average) alignment of domains in one direction over another. If we assume this is insignificant, there is still another problem: a small fraction of the domains may be very difficult to rotate and these may remain unchanged throughout the oscillatory cycle if the core is not being driven hard enough. If these have a net magnetization, they will produce an asymmetric perturbation on the system's behavior. This will be most strongly seen near a symmetry breaking bifurcation (see Secs. 2.3.1 and 3.2) where a symmetrical attractor splits into two complementary asymmetric attractors as a parameter is varied. The effect of the asymmetric perturbation will be to cause the system to choose a particular asymmetric attractor as shown in Fig. 11. Furthermore, if the behavior of the core is initially symmetric, it can develop asymmetry when it undergoes a symmetry breaking bifurcation. When one repeatedly passes the parameter through the bifurcation point, it is not uncommon to find it has developed a preference for a particular state. This net magnetization behaves much like a parameter that is very hard to control, it gets changed as we adjust other parameters but it doesn't return to its original value when they do. This peculiar property of the magnetic core is fairly weak in most of its effects on the behavior we have studied. However, it is very strong near the $q = 2$ bifurcation point (see Fig. 4 and Sec. 3.1) because of the strongly asymmetric orbits existing there and makes study of this region very

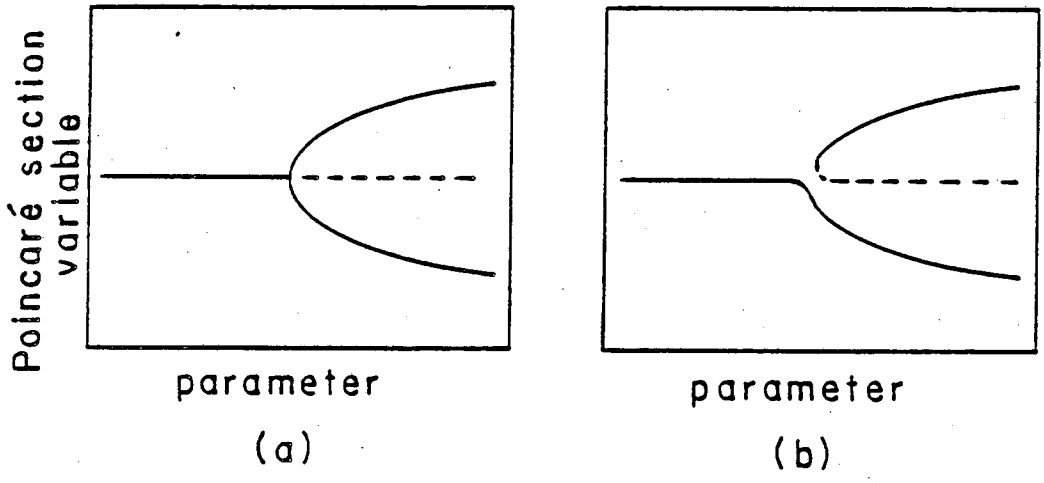

Figure 11. (a) Symmetry breaking bifurcation: the dotted line is an unstable symmetric attractor that separates the two complementary asymmetric attractors following bifurcation. (b) Asymmetric perturbation causes the original (nearly) symmetric attractor to go to a particular asymmetric (nearly) complementary attractor. The other (near) complement appears via saddle-node bifurcation. Thus symmetry breaking bifurcations are only to be expected in perfectly symmetric systems.

difficult.

2.3.3 Frequency Spectra for Quasiperiodicity

Motion on a 2-torus can be described by two angles: $\theta_1 = \omega_1 t$ and $\theta_2 = \omega_2 t$ corresponding to the two ways in which one can go around the torus. Thus the state of the system can be specified by these two angles:

$$\mathbf{X} = \mathbf{X}(\theta_1, \theta_2) = \text{state of system.} \tag{18}$$

We can express this as a Fourier series:

$$\mathbf{X} = \sum_{m=-\infty}^{\infty} \sum_{n=-\infty}^{\infty} \mathbf{X}_{mn} \exp[im\theta_1 + in\theta_2],$$

where

$$\mathbf{X}_{nm} = \frac{1}{(2\pi)^2} \int_0^{2\pi} d\theta_1 \int_0^{2\pi} d\theta_2 \, \mathbf{X}(\theta_1, \theta_2) \exp[-im\theta_1 - in\theta_2].$$

Thus we can get Fourier components at all integral linear combinations (two component harmonics) of ω_1 and ω_2,

$$\omega_{mn} = m\omega_1 + n\omega_2, \tag{19}$$

where m and n are integers.

Provided the torus remains intact, the amplitude of these components must fall off as m and n become large.

For a symmetrical oscillation we expect that

$$\mathbf{X}(\theta_1, \theta_2) = -\mathbf{X}(\theta_1 + \pi, \theta_2 + \pi),$$

provided that the complement of **X** is **–X** which is true at least for most components of **X** (like V_L or I_L). This results in the elimination of certain terms in the spectrum. If $m + n$ is even, then

$$\exp[-im\theta_1 - in\theta_2] = \exp[-im(\theta_1 + \pi) - in(\theta_2 + \pi)], \tag{20}$$

so the integral for $\mathbf{X}_{mn}$ vanishes by symmetry. *Thus only odd harmonics where $m + n$ is odd are allowed for a symmetrical oscillation.*

3 EXPERIMENTAL RESULTS

3.1 Bifurcation Patterns Near Points of Resonance

In this section we discuss the behavior of our system near points of resonance, particularly "strong" resonances of order $q \leq 4$, as well as the more familiar "weak" resonances of order

$q \geq 5$. Each of the strong resonance cases has its own characteristic behavior patterns, the theory for which we discussed in the previous section. An understanding of each of these cases is essential to obtaining an overall picture of the behavior in the parameter space. Associated with most cases of strong resonance there are regions in parameter space where two attractors coexist or overlap, each of which continues into some adjacent region where it is the only attractor. This results in the phenomenon of hysteresis: when traversing a path in parameter space, the system gets to a point where the attractor it is on is annihilated and a jump occurs to a coexisting attractor; but when the path is reversed, the jump occurs at the opposite end of the overlap region, so that the forward and reverse paths are different. This behavior is easily traced back to the behavior near the resonant fixed point which can be understood through the theory presented in Sec. 2.2. In addition to the cases $q = 1$ through 4, we also show a case involving strong hysteresis for $q = 5$ although in this case the hysteresis does not extend all the way to the bifurcation point. In each case we show the region of a two-parameter space [I_0(rms) and $\tau_1 = 2\pi/\omega_1$] in which behavior of the indicated order can be found. This is divided by lines indicating bifurcations of co-dimension 1. A number of these lines emerge from the resonant point while some others do not. To each subregion there corresponds a diagram which indicates qualitatively the behavior in each region (i.e. shows all attractors, saddle points, and their stable and unstable manifolds). In some cases we also show actual Poincare sections corresponding to these subregions or the transitions between them. The 2-D bifurcation diagrams given in this section use the abbreviations in Table 1 to label co-dimension 1 bifurcations as we did in Sec. 2.2.

3.1.1 Resonance of Order 1

The experimental bifurcation pattern we obtained in this case is shown in Fig. 12. This is essentially an enlargement of the region near the $q = 1$ point shown in Fig. 4 which marks one endpoint of the Hopf bifurcation line. It may surprise the reader to find that this line could abruptly stop in this manner. This behavior will normally occur only at first and second order resonance points as a consequence of the theory governing the dynamics near these points. We show some actual Poincare sections from region a_1 in Figs. 13(a) and (b). The regions labeled a_1, a_2, b, c_1, c_2, and d correspond to identically labeled regions in Fig. 8 which shows the theoretical behavior of a typical $q = 1$ bifurcation very near the bifurcation point. Note that the stable node present in each of these regions does not appear in Fig. 8. This is because it is not involved in the bifurcation of this resonant fixed point, i.e. it does not approach the resonant fixed point as $\varepsilon \rightarrow 0$, and it is effectively at infinity on the scale of the fixed points and limit cycles that do. Nevertheless, its presence can be inferred from the behavior at the bifurcation point: the unstable manifolds that point to infinity in Fig. 8 must in a real system connect to some other attractor. Since attractors bifurcate from the $q = 1$ point in regions c and d, they must coexist with this other attractor (in this case a node) and thus we see hysteretic behavior in these regions. The node is finally annihilated with the saddle point that was generated in the $q = 1$ bifurcation so that regions e and f have only one attractor. Guckenheimer and Holmes (Ref. 12, pp. 71-72) show a similar bifurcation pattern for a $q = 1$ point in the forced Van der Pol oscillator, which is based on earlier studies of this equation[23-26].

The sn (saddle node) and hc (homoclinic) bifurcation lines approaching the $q = 1$ point in our data do not appear to become tangent as in the theoretical diagram. It could be that this feature was destroyed due to some slight noise or fluctuations in the physical system.

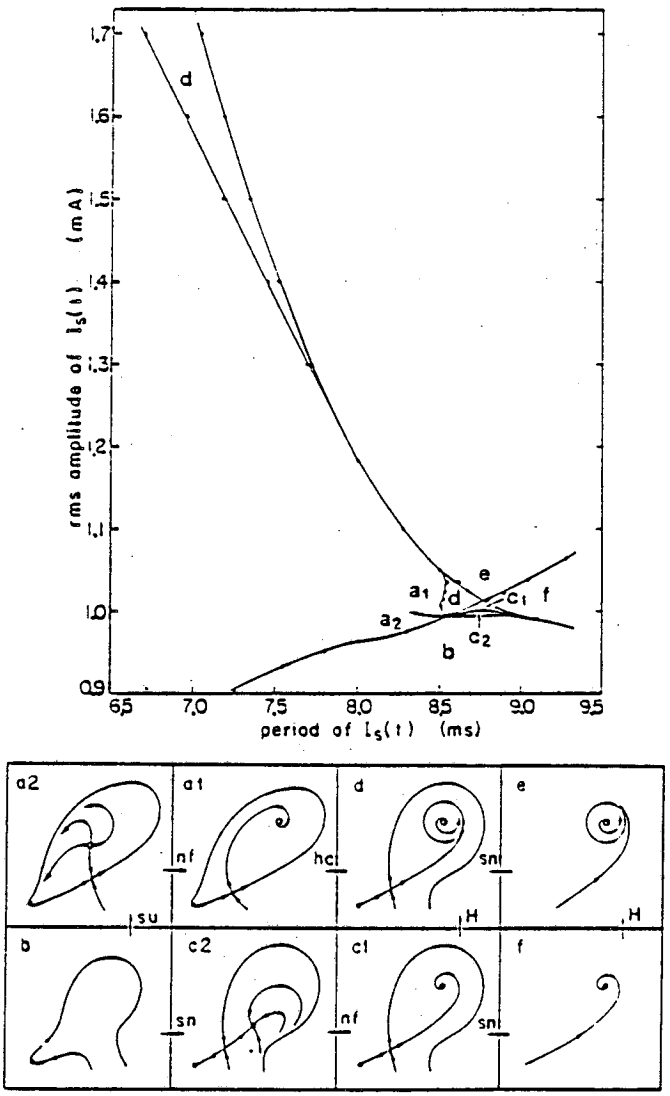

Figure 12. Experimental parameter space diagram near $q = 1$ resonance point. Coordinates are $\tau_1 = 2\pi/\omega_1$ vs. I_0(rms). Other parameters are fixed: R = -500 Ω, C = 7.5 μF. Small figures below show the structure in a typical 2-D Poincare space for each region of the parameter space. Regions a_1, a_2, b, c_1, c_2, and d correspond to the same regions in the theory, Fig. 8. The figures are constructed from data obtained from initialized Poincare sections.

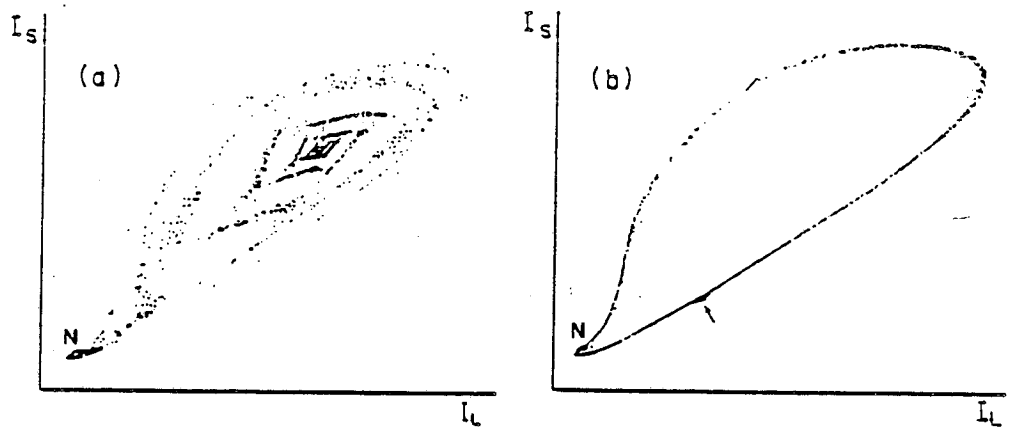

Figure 13. Initialized (see Sec. 1.2) experimental Poincare sections in region a_1 of Fig. 12. (a) Initialized at the unstable focus (arrow). (b) Initialized at the saddle point (arrow). Both cases approach the stable node (N) after a few cycles. Initialization is then repeated many times to produce continuous lines. Parameters for (a) and (b): I_0(rms) = 1.052 mA, τ_1 = 8.079 ms.

Note the homoclinic bifurcation occurring between regions d and a_1 (see discussion of homoclinic bifurcations in Sec. 2.1). This bifurcation is initially of a nearly degenerate form forming a saddle loop. Moving upwards in the parameter plot (I_0 increasing), the region d comes to an end and a_1 becomes adjacent to e. As we go further, however, the a_1-e line splits again and a new d region appears. The homoclinic bifurcation at this higher I_0 is not degenerate, however, as the dynamics are much more chaotic in this region. Here the chaotic attractor in regions e and d disappears upon the formation of a homoclinic tangency at the a-d boundary, as shown in Fig. 14.

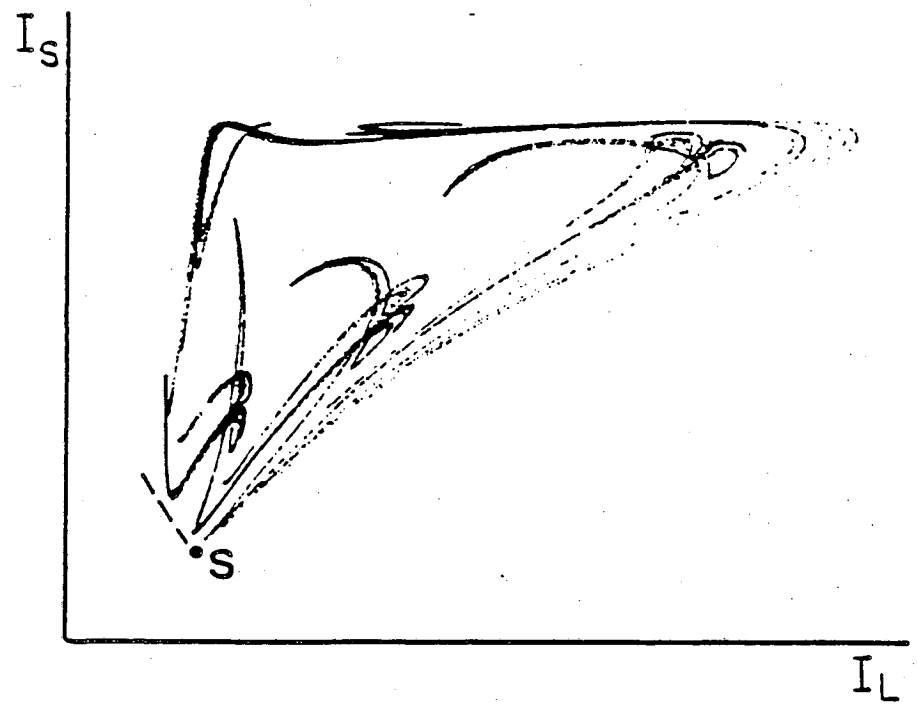

Figure 14. Experimental Poincare section I_L vs. I_S on approaching homoclinic tangency at d-a boundary in region d at high I_0. The oscillations in the attractor at the lower left will contact the stable manifold of a saddle point (dotted line), after which (in region a_1) the attractor will no longer exist, i.e., if initialized here the system will ultimately escape to some other attractor (a node in this case). Parameters: I_0(rms) = 1.700 mA, τ_1 = 6.800 ms, R = -500 Ω, C = 7.5 μF.

3.1.2 Resonance of Order 2

There are actually two possible bifurcation patterns for this case according to the theory, but we have only observed one of these. Like the q = 1 case, this point of resonance marks an end point to the Hopf bifurcation line.

In our system, this resonance corresponds to a frequency ratio of 2/1. Since this is not a ratio of odd integers, this is a complementary asymmetric type of resonance, and hence we multiply the denominator by 2 to get the order q (see Section 2.3.1). The experimental data are

presented in Fig. 15. The behavior near the bifurcation point agrees with the theoretical result given in Fig. 9. Here again (as for $q = 1$) there are nodes that do not approach the resonant fixed point as $\varepsilon \rightarrow 0$. The bifurcating 2/1 type points (asymmetric period 1) are all saddle points, and the bifurcation process is effectively a rearrangement of their separatrices. As in the $q = 1$ case, the presence of the nodes is implied by the theoretical picture in which unstable manifolds apparently go off to infinity. In a real system we expect these to connect to attractors which are very distant on the scale where the theoretical picture is accurate. This in turn implies that there will be hysteresis and ultimately a boundary line where these attractors disappear. As is easily seen, the hysteresis in this case covers a very large area. There is a large hole in the center of the hysteretic regions which is possibly an attempt to avoid the 5/3 entrainment domain (see Fig. 4). It does slightly overlap a hysteretic region of this domain, however, and in that small region there are four coexisting attractors: a pair of asymmetric (2/1) nodes, a period 3 (5/3) node, and an invariant circle. On approaching this hole from regions b_1, c, or d, period doubling bifurcations occur (not shown) for the pair of 2/1 nodes. These become chaotic and a crisis[27] occurs at the hole boundary. In b_1 and c this is a boundary crisis and a jump occurs to the coexisting symmetrical oscillation. In d_1 this is an interior crisis in which the two complementary asymmetric attractors contact the separatrix between them and a loss of phase locking occurs. There is no jump or hysteresis in this case. It is important to note that an asymmetric 2/1 entrainment is not distinguishable from a symmetry broken 1/1 entrainment. In fact one can get from the 1/1 region to the 2/1 region via symmetry breaking bifurcation at low current levels (<0.65 mA rms) as shown in Fig. 15.

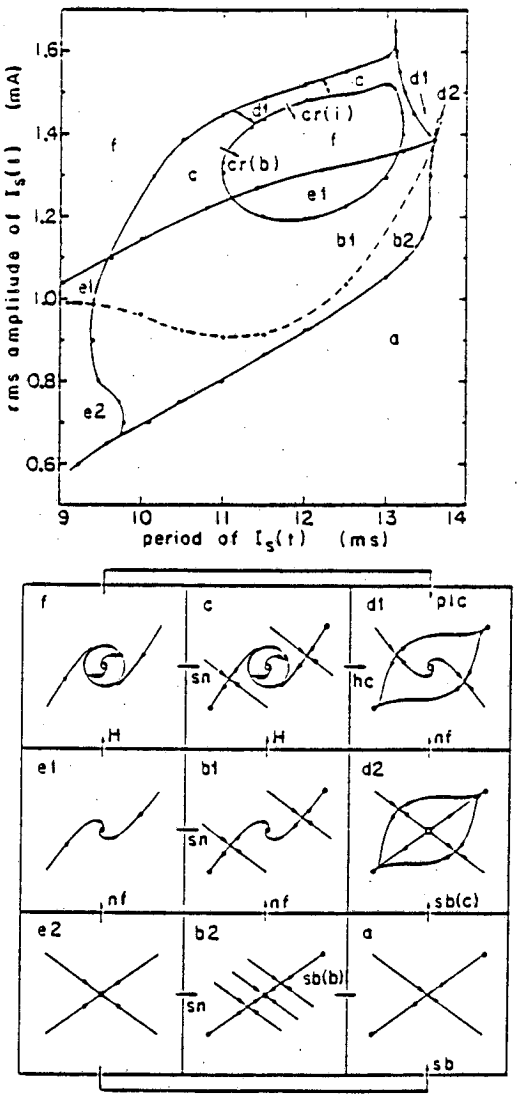

Figure 15. Experimental parameter space diagram near q = 2 resonance point. Coordinates are τ_1 vs. I_0(rms). Other parameters are fixed: R = -500 Ω, C = 7.5 μF. Small figures below show the structure in a typical 2-D Poincare space for each region of the parameter space. Regions labeled a, b_1, b_2, c, d_1, and d_2 correspond to same labeled regions in Fig. 9 (theory). The difference between b_1 and b_2 and between d_2 and d_1 is a trivial change of a node to a focus. The figures are constructed from initialized Poincare sections.

3.1.3 Resonance of Order 3

This case is different from the first and second orders in that it occurs in the middle rather than at an end point of the Hopf bifurcation line. It is different from weak resonances in that it

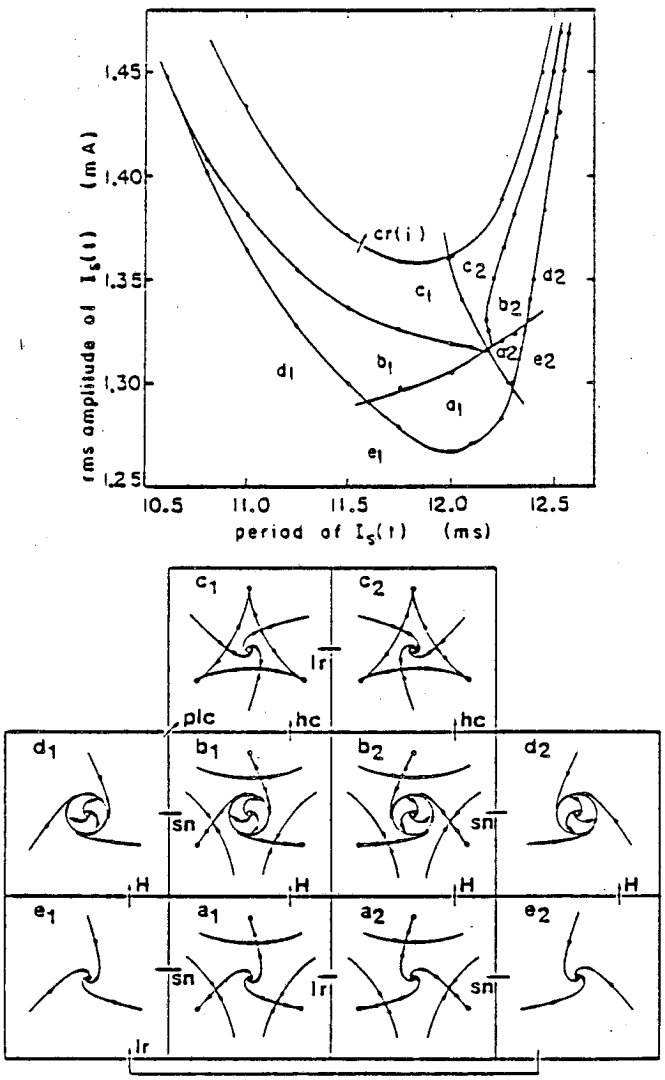

Figure 16. Experimental parameter space diagram for $q = 3$ resonance point. Coordinates are τ_1 vs. I_0(rms). Other parameters are fixed: R = -500 Ω, C = 7.5 μF. Small figures below show the structure in a typical 2-D Poincare space for each region of the parameter space. Regions labeled a_1, a_2, b_1, b_2, c_1, and c_2 correspond to same labeled regions in Fig. 7 (theory). The figures shown in these regions are constructed from initialized Poincare sections.

exhibits hysteresis, that the entrainment region is not horn shaped, and that entrainment is found on both sides of the Hopf bifurcation line.

The case we studied corresponds to a frequency ratio of 5/3. The bifurcation diagram is given in Fig. 16 and some observed Poincare sections are shown in Fig. 17. There is agreement with the theoretical treatment shown in Fig. 7. Similar to the q = 1 and 2 cases, no period 3 nodes are involved in the bifurcation at the resonance point, only saddle points and invariant circles. As before, there are period 3 nodes not involved in this bifurcation whose presence can be inferred from the unstable manifolds going towards infinity in Fig. 7. The result, as in the previous cases, is the formation of hysteretic regions, here a_1, a_2, b_1, and b_2. The attracting circle in the b_1 and b_2 regions disappears in a homoclinic bifurcation at the b_1-c_1 and b_2-c_2 boundaries when it contacts the period 3 saddle point. A distinctive feature of this case is that the bifurcation diagram is symmetric about a center line (lr) across which the focus (and the circle in the b and d regions) changes from left rotation to right rotation with respect to the rotation of the period 3 attractor. Otherwise, the (1) regions and corresponding (2) regions are the same. The period 3 nodes undergo period doubling bifurcations (not shown in Fig. 16) as we move towards the line labeled cr(i). This becomes a period 3 chaotic attractor which loses phase locking through an interior crisis[27] at cr(i).

3.1.4 Resonance of Order 4

This is the last of the strong resonance cases. It can occur in a wide variety of forms – sometimes being similar to the weak resonance cases, sometimes having similar characteristics to the third order case, and sometimes exhibiting other complex patterns.

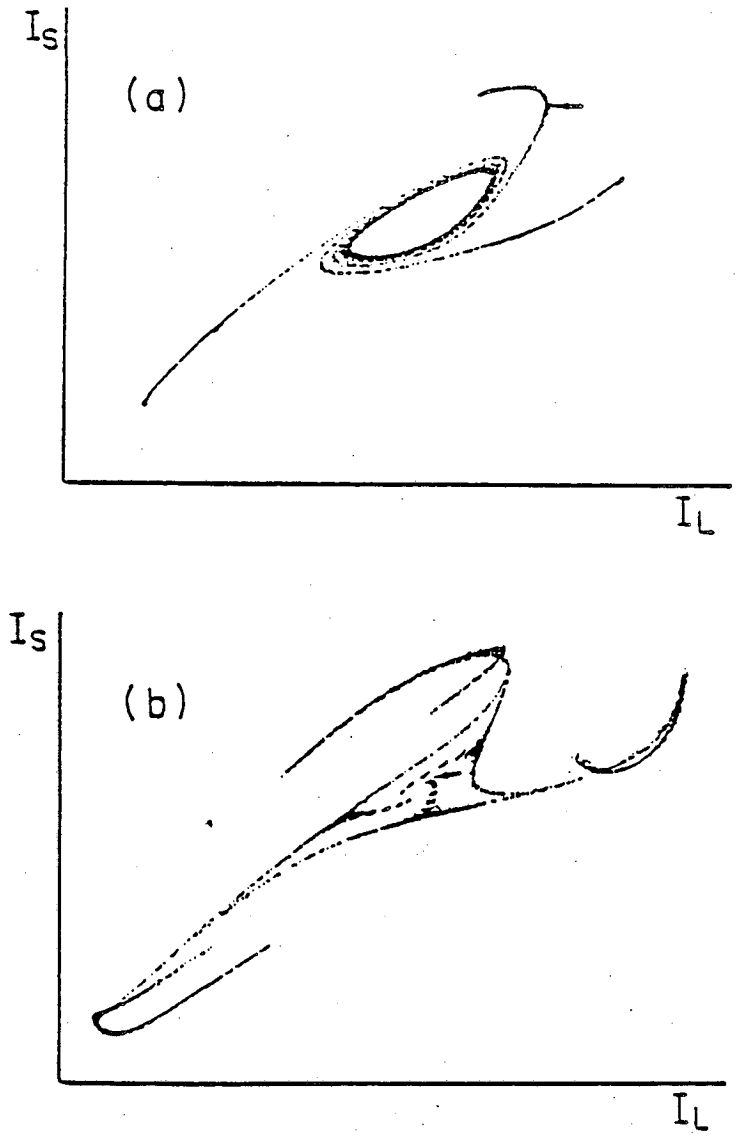

Figure 17. Initialized Poincare sections. (a) Parameters set in region b_1 of Fig. 16 [I_0(rms) = 1.325 mA, τ_1 = 11.75 ms] initialized on period 3 saddle point (arrow) – shows its unstable manifold going out to period 3 node and in to circle. (b) Parameters set in region c_1 (1.346 mA, 11.78 ms). Central circle has disappeared in a homoclinic bifurcation. The period 3 attractor has become chaotic through a period doubling sequence. Produced by initializing near central focus on route to period 3 attractor via a near pass by the period 3 saddle.

The case studied corresponds to a frequency ratio of 3/2. It is an asymmetric type where a complementary pair of period 2 fixed points can bifurcate from the resonant point, thus giving

an order of $q = 4$. This case is the least well understood theoretically. Arnold[13] gives two possible bifurcation patterns, neither of which have we seen. However, the three patterns we have seen are nevertheless compatible with the present theoretical understanding. It was possible to observe more than one pattern by setting a third parameter (R) at different values. This has the effect of changing A and B in Eq. (12). B can, in fact, be eliminated from Eq. (12) by a change of variables, but since A is complex, one actually needs two additional parameters to explore all possible bifurcation patterns in this case. The first case is the one shown in Fig. 4 for R = -500 ohms where the appearance is that of an ordinary resonance horn except that it emerges in a vee at the base. There is some slight hysteresis on the right boundary of the horn, but it seems to disappear as one approaches the bifurcation point. For R slightly more negative (~ –600 Ω), this hysteresis is stronger and does appear to go all the way to the bifurcation point, giving us a second case. In the hysteretic region the entrained solution and the quasi- periodic solution coexist with different basins of attraction.

For R more negative still, a third case occurs when this hysteresis extends below the line of Hopf bifurcation, as shown in Fig. 18. Note that unlike the resonances of second, and third order shown previously, these cases of fourth order resonance do involve stable nodes in the bifurcation of the resonant point. The saddle node and homoclinic bifurcations at the d-b_1 and d-a_1 boundaries, respectively, are shown in progress in Figs. 19(a) and (b). The dots are the jump that occurred as the parameter (τ_1) was adjusted across the bifurcation point.

3.1.5 Resonance of Order 5 and Above

While resonance of order $q \geq 5$ always follows the entrainment horn form very near the bifurcation point, there can still be strong hysteresis that extends nearly to that point. Such is the case with the 7/5 resonance at R = -800 ohms shown in Fig. 20. Here the phase-locked

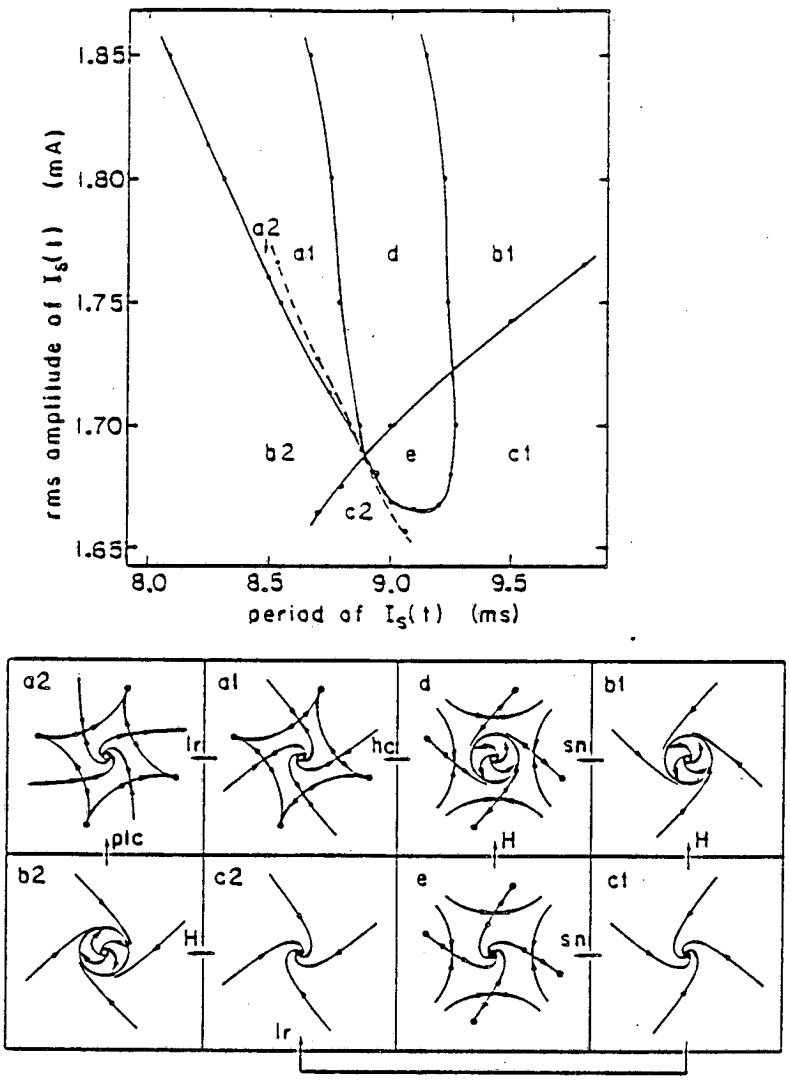

Figure 18. Experimental parameter space diagram near $q = 4$ resonance point (third case). Coordinates are τ_1 and I_0(rms) with R = -750 Ω, C = 7.5 μF fixed. Small figures below show the structure in a typical 2-D Poincare space for each region of the parameter space. Note: in the second case, region e is absent, and regions b_1 and d both emerge as wedge-shaped regions from the resonant point.

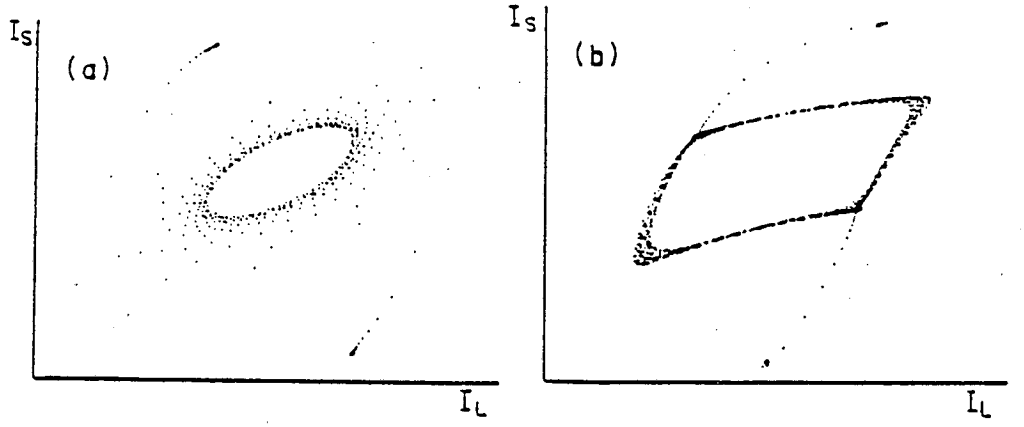

Figure 19. Experimental Poincare sections, I_L vs. I_S, near $q = 4$. (a) Saddle node bifurcation at d-b_1 boundary of Fig. 18. The system was on one of the two complementary period 2 nodes in region d near the boundary. The parameter was τ_1 moved across the boundary and this orbit annihilated with a period 2 saddle. The dots are a single trajectory (a jump) to the invariant circle. (b) Homoclinic bifurcation at the d-a_1 boundary. System was on the circle in region d near the boundary. Proximity of a pair of period 2 saddles to the circle produces corners. As the parameter is moved across the boundary, stability is lost and the trajectory jumps along the unstable manifold of one of the period 2 saddles (chosen at random) to the corresponding period 2 node. The initialization (Sec. 1.2) was not used in these figures.

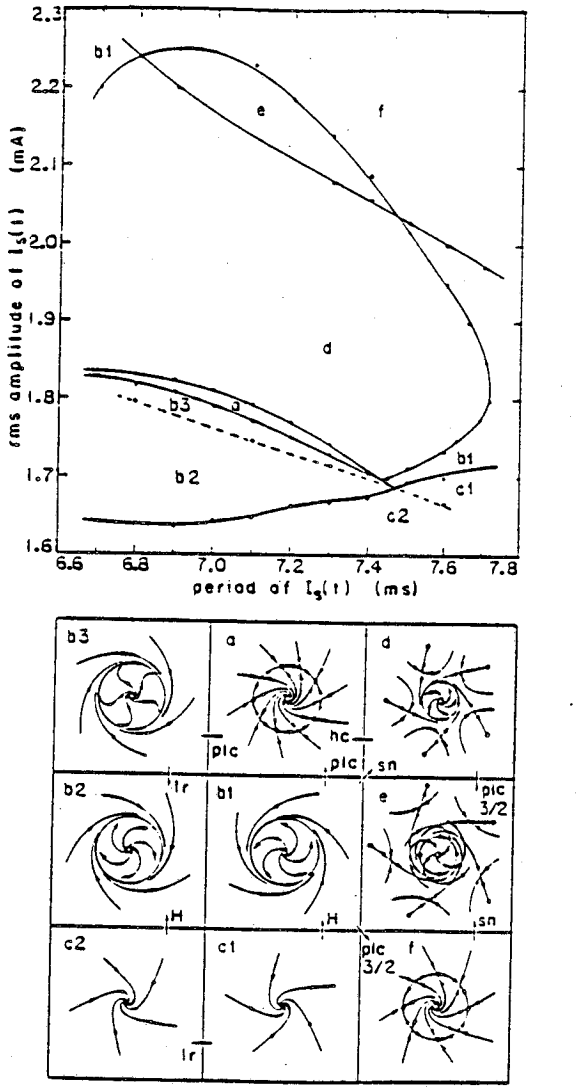

Figure 20. Experimental parameter space diagram [I_0(rms), τ_1] near q = 5 resonance point with R = -800 Ω, C = 7.5 μF. Small figures below show the structure in a typical 2-D Poincare space for each region of the parameter space. Note strong hysteresis (region d) and also overlap of 7/5 and 3/2 domains (region e) discussed in Sec. 3.3. The figures are inferred from Poincare section data.

circle exists only in a very narrow horn (a), while there is a very large region (d) where a 7/5 entrainment coexists with an invariant circle. This region actually overlaps another entrainment domain (3/2), and we will be discussing this region (e) in Sec. 3.3.

3.2 Internal and Boundary Bifurcations of Entrainment Horns

3.2.1 Symmetry Breaking and Period Doubling Bifurcations

Period doubling bifurcations are the route by which the motion within a horn approaches chaos. These form a series of lines inside the horn that one crosses as one moves (in parameter space) away from the vertex inside the horn. In a case where the attractor is initially symmetric (i.e. the frequency ratio is M/N where M and N are both odd as discussed in Sec. 2.3.1) these period doubling bifurcations will be preceded by a symmetry breaking bifurcation where two asymmetric attractors emerge from the initial symmetric one. Figure 21 shows the 7/5 resonance horn at R = -392 ohms. Note that the symmetry breaking (sb) and period doubling ($\times 2$) lines do not run parallel to the sides of the horn as one might at first expect but can run directly into it. This feature is less pronounced in the horn for R = -500 ohms, but other features are very similar. This behavior can occur only for certain types of Poincare maps – see discussion in Sec. 4.3.2. Chaos is reached at the $\times\infty$ line. In Figs. 22(a) and (b) we show Poincare sections showing typical period doubling and symmetry breaking of a phase-locked circle. In both cases the bifurcating pairs of nodes split away from the circle, one going out and the other in. A saddle point is left on the circle.

3.2.2 Complementary Band Merging

It is well known that after an infinite sequence of period doubling bifurcations, a band merging sequence begins. A sequence of band merging (bm) lines could be found within a resonance horn starting with an infinite number of bands and decreasing by factors of two down to the original periodicity of the horn. However, in the initially symmetric case, there is an

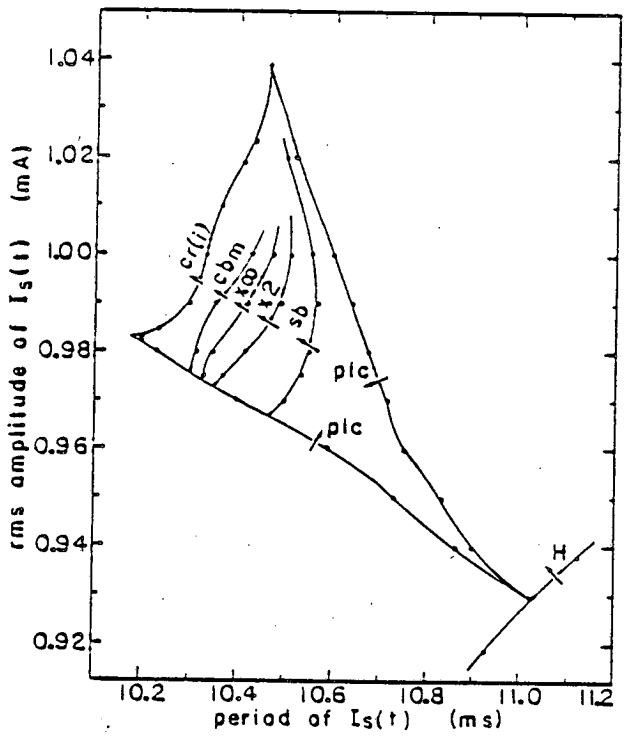

Figure 21. Experimental entrainment horn (7/5) showing internal and boundary bifurcations, in (I_0, τ_1) parameter space with R = -392 Ω, C = 7.5 μF fixed. Abbreviations are defined in Table 1.

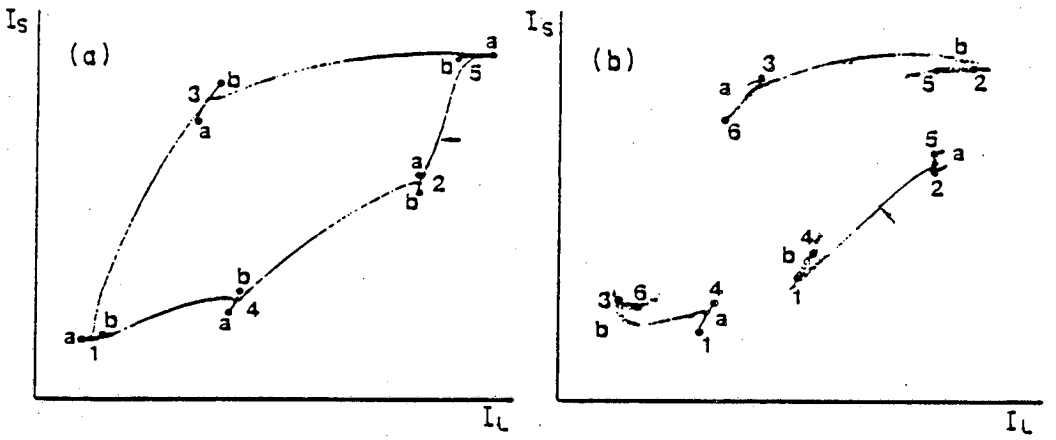

Figure 22. (a) Symmetry breaking bifurcation of 7/5 phase-locked circle. Poincare section initialized at period 5 saddle point (arrow). The two attracting period 5 nodes are labeled a and b and iterate in the sequence ((1,2,3,4,5,1,2,...). Parameters: I_0(rms) = 1.240 mA, τ_1 = 9.456 rms, R = -500 Ω, C = 7.5 μF. (b) Period doubling bifurcation of 4/3 phase-locked circle. Poincare section initialized at one of the period 3 saddle points (arrow). The missing manifolds can be reached from the complementary saddle. This is a complementary type of phase-locked circle with a and b attractors as marked. Each has period doubled and iterates in the indicated sequence. Parameters: I_0 = 1.210 mA, τ_1 = 8.855 ms, R = -500 Ω, C = 7.5 μF.

additional bifurcation where the two complementary bands contact each other and symmetry is restored. What one observes is that in crossing this complementary band merging line (cbm in Fig. 21) the attractor will suddenly double in size as the region previously on the complementary attractor becomes accessible. This bifurcation is completely analogous to the earlier symmetry breaking bifurcation, and it may be considered as simply the final band merging of the attractor for the half-cycle map (see Sec. 2.3.1). In Figs. 23(a) and (b) we show Poincare sections just before and after cbm.

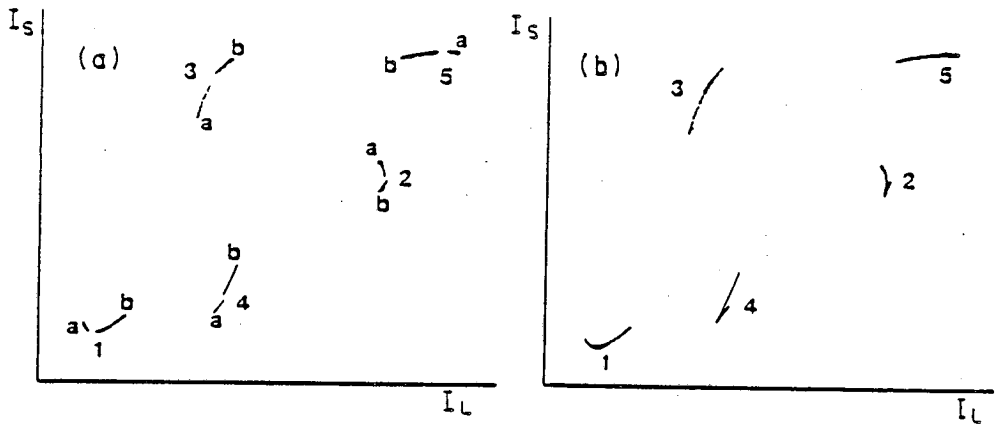

Figure 23. Poincare sections I_L vs. I_S. (a) Just before complementary band merging. Double exposure shows both a and b attractors which iterate in the sequence shown. Parameters: I_0(rms) = 1.245 mA, τ_1 = 9.354 ms, R = -500 Ω, C = 7.5 μF. (b) Just after cbm, now single symmetric attractor. Parameters: I_0(rms) was increased to 1.252 mA.

3.2.3 Boundary Bifurcations

Prior to crossing the first symmetry breaking or period doubling line, the boundary bifurcations of a resonance horn are simple saddle node bifurcations on the resonance circle as discussed in Sec. 2.2. Nevertheless, the invariant circle just outside the horn does not have to be smooth. For the Poincare section shown in Fig. 24 the horn has a symmetry breaking line just inside the boundary, so the stable eigenvalue (transverse to the circle) is very near one, and thus has little ability to quench the transverse oscillations. One sees a laminar or periodic phase as the system slowly slips by the old nodal site, followed by a chaotic burst. This is a form of the intermittency route to chaos[28,29].

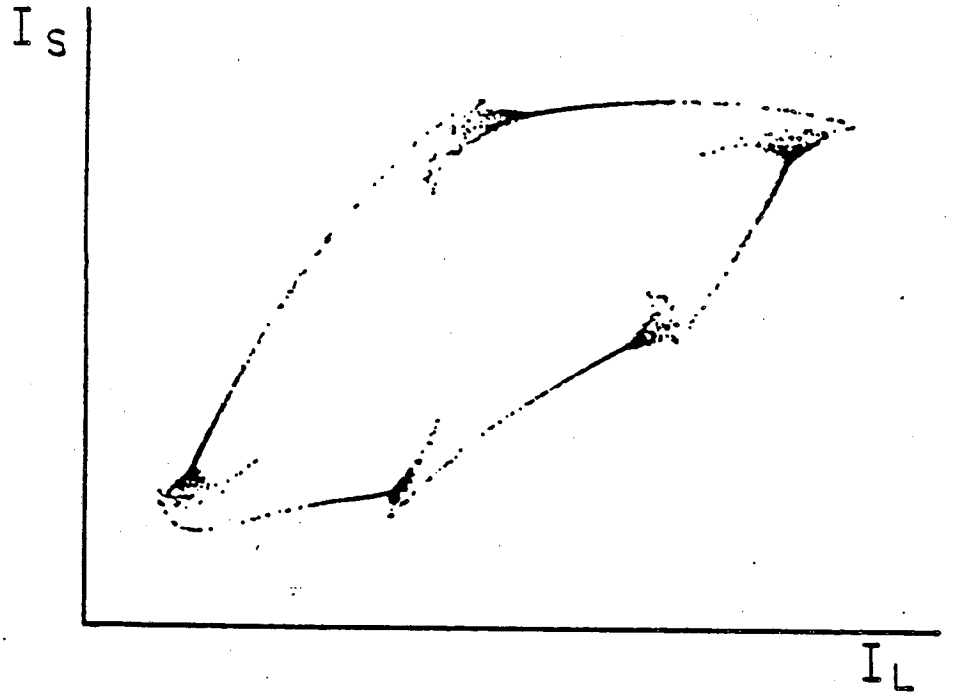

Figure 24. Poincare section showing intermittency at 7/5 horn boundary.

At the boundary of the horn in Fig. 21 between the sb line and the ×2 line the boundary is reached with broken symmetry. For this to happen the period 5 saddle must also break symmetry before the boundary (similar to the type C period doubling in Fig. 5) so that each set of attracting nodes can annihilate with a set of saddles. The general structure just before the boundary is shown in Fig. 25. Figure 26 shows a sequence of Poincare sections moving away from the horn boundary outside. The first (3.15a) clearly shows the remnant of the unstable manifolds of the complementary pair of period 5 saddles and their oscillatory approach towards the prior location of the pair of period 5 nodes. The following section (3.15b) shows how this wild oscillation at the old nodal site dies out and a circle develops.

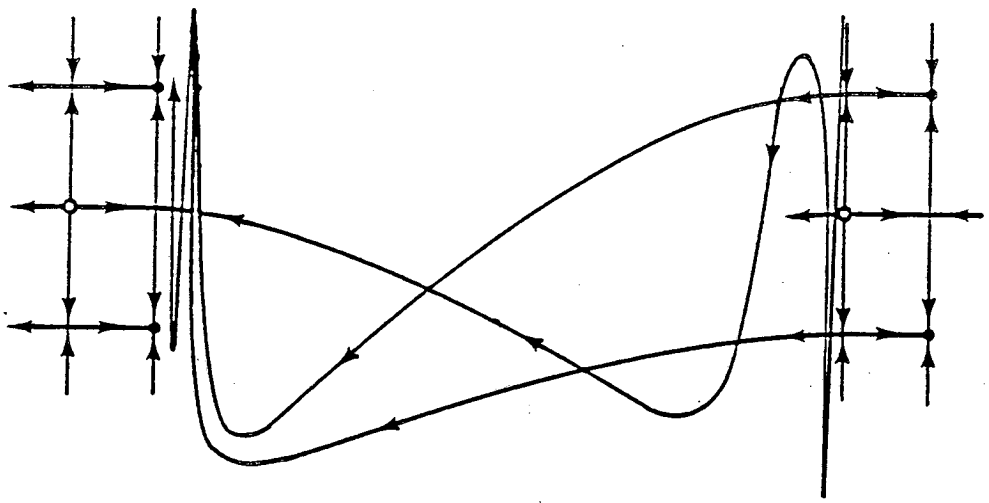

Figure 25. Drawing showing segment of phase-locked circle having broken symmetry saddles and nodes, near horn boundary and approaching saddle node annihilation. Shows heteroclinic crossing between the saddle points.

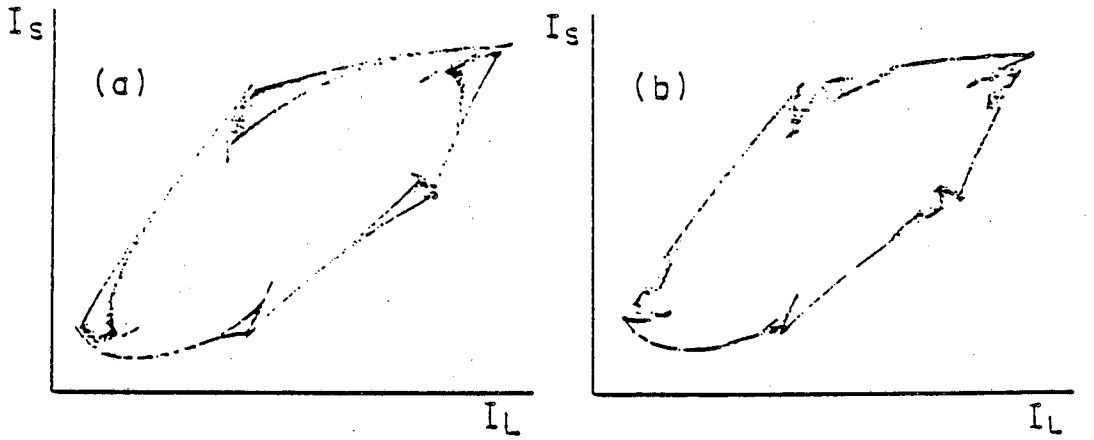

Figure 26. Sequence of Poincare sections after saddle node annihilation (in Fig. 25). All at R = -392 Ω, C = 7.5 μF, and τ_1 = 10.365 ms. (a) At a point nearest horn boundary (but outside), I_0(rms) = 0.971 mA. (b) 0.965 mA.

As we move farther up the horn boundary, we cross period doubling lines and presumably the saddle points here also period double although these cases cannot be studied in much detail experimentally due to noise in the system.

The upper boundary of the horn occurs when the expanding periodic attractor contacts the separatrix between it and the adjacent piece of the attractor. At this point an interior crisis[27] occurs and entrainment is lost. In Fig. 27 we show the attractor just below and just above this boundary. Above the boundary the attractor makes a sudden jump in size, each piece now contacting the adjacent piece.

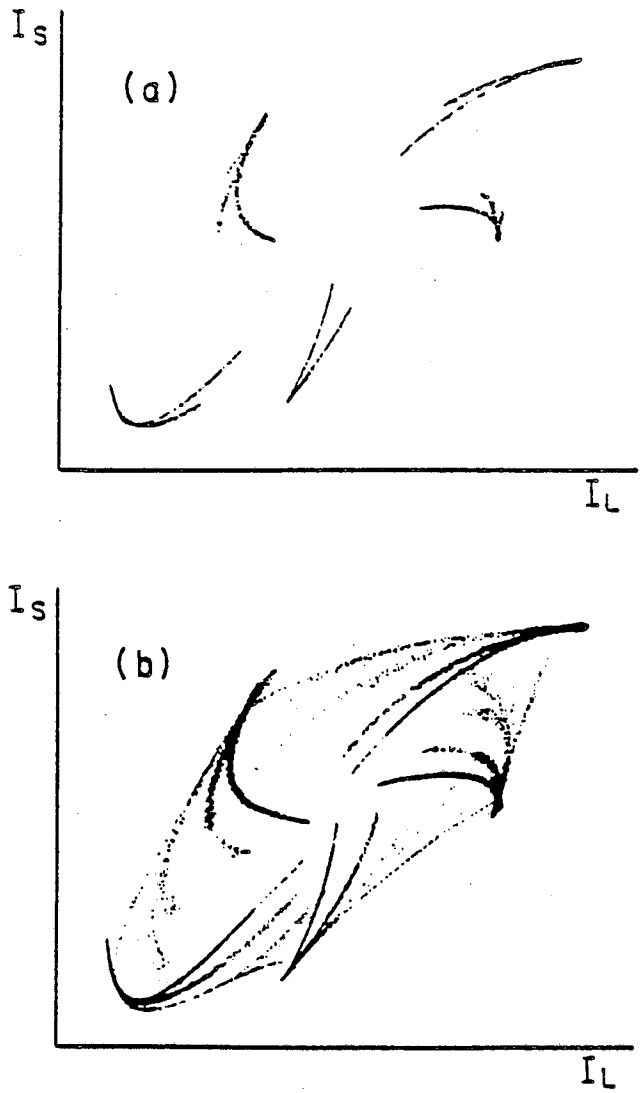

Figure 27. Poincare section showing crisis at upper boundary of horn. Both at R = -392 Ω, C = 7.5 μF, τ_1 = 10.300 ms. (a) Still phase locked, I_0(rms) = 0.989 mA. (b) Loss of phase lock, I_0(rms) = 0.991 mA.

3.3 Overlapping Entrainment Domains

It is possible for neighboring domains to overlap in some regions. When this occurs, the separatrices between the two attractors cannot be simple since they have different rotation numbers. We show such a case in Fig. 28, a Poincare section corresponding to the overlap of the 3/2 and 7/5 entrainment domains of region e, Fig. 20. Here there is a pair of period 2 attractors surrounded by a period 5 attractor. The unstable manifold of the period 5 saddle points are shown as it wraps around the period 2 attractors an infinite number of times. The stable manifold of the period 2 saddle points (not shown) crosses this manifold as it spirals outward (counterclockwise). Due to the peculiar kink in the period 5 manifold, the stable period 2 manifold crosses each winding of the shown manifold three times in succession.

3.4 Entrainment Islands

As is well known (e.g., see Ref. 30), Hamiltonian systems can exhibit "resonance islands." In Hamiltonian systems there are no attractors or repellers, rather the phase space is foliated into invariant manifolds by the invariants of the system, e.g. the energy. These manifolds can be tori and the case of a rational frequency ratio is referred to as a primary resonance. One can find an initial condition for which the Poincare section for this resonance is a series of points. But for a nearby initial condition, the Poincare section will have the appearance of a set of small circles or "primary resonance islands," one encircling each of the points for the previous initial condition. The Poincare map goes from one island to another with the same rotation number as before (the system is still in resonance) but now there is in addition a rotation about the islands for each iteration. When one looks closer, one finds "secondary resonances" and secondary islands located about these primary resonances, and so on ad infinitum.

It is interesting that dissipative systems can be attracted to such islands. In Fig. 29 we show an entrainment domain in part of which attracting period 3 islands are found. These

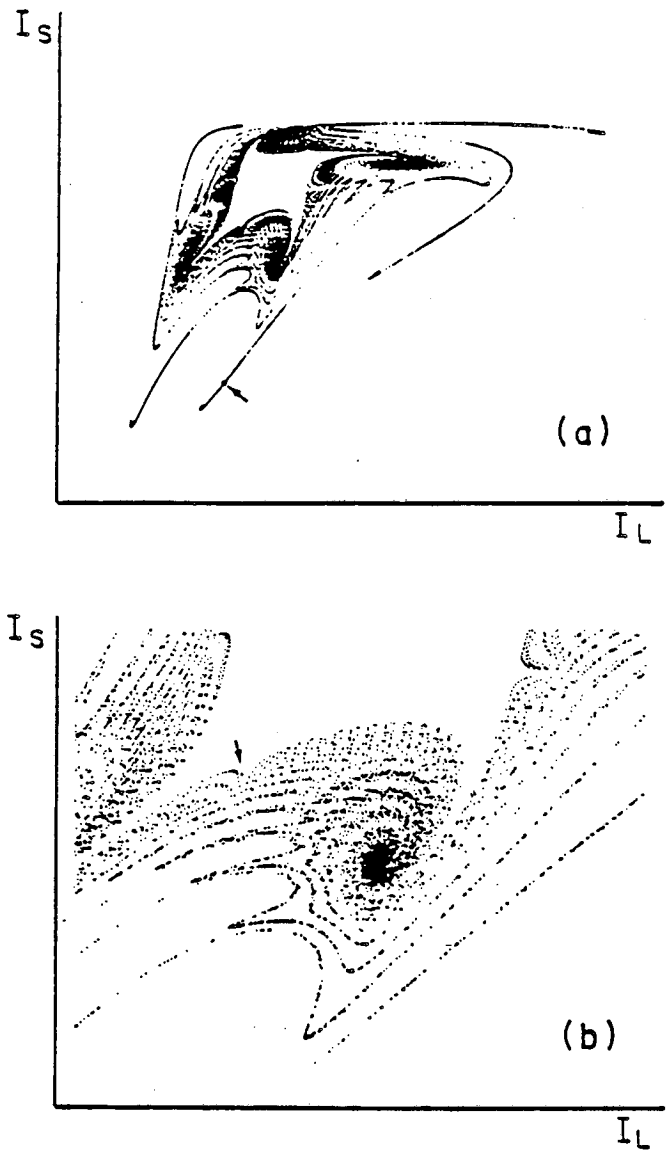

Figure 28. Overlapping entrainment domains (7/5 and 3/2) shown in initialized (see Sec. 1.2) Poincare sections. (a) Initialized at period 5 saddle point (arrow). Shows unstable manifold leading out to period 5 node and winding in to pair of period 2 foci. Parameters: I_0(rms) = 2.18 mA, τ_1 = 7.070 ms, R = -500 Ω, C = 7.5 μF (see Fig. 20). (b) Enlargement, showing fine structure and period 2 saddles (arrow). Note: initialization must be repeated many times (>100) to obtain these pictures.

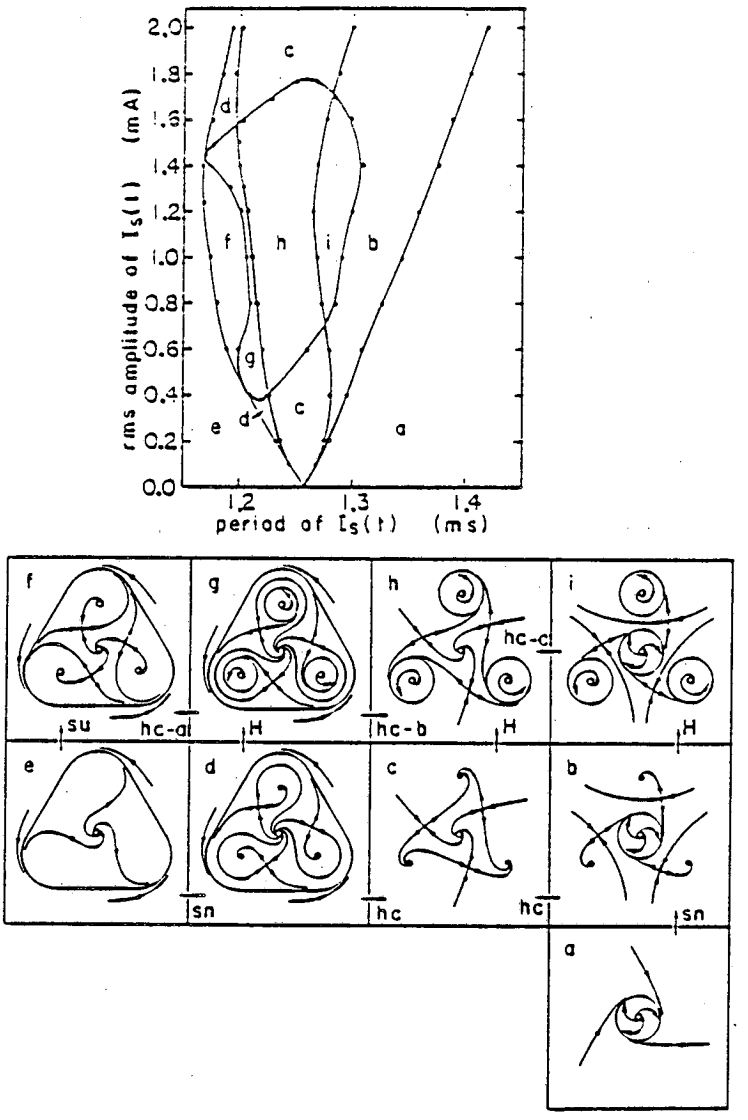

Figure 29. Entrainment domain (1/3) in which a Hopf bifurcation to periodic "islands" occurs. Fixed parameters: R = -500 Ω, C = 5.42 μF. Small figures below show the structure in a typical 2-D Poincare space for each region of the parameter space. Between the saddle-node (sn) and Hopf (H) bifurcations there must be a node-to-focus (nf) bifurcation which is not shown.

islands appear through a Hopf bifurcation of an ordinary period 3 entrainment. In Fig. 30(a) we show a phase portrait of the islands with strobing superimposed.

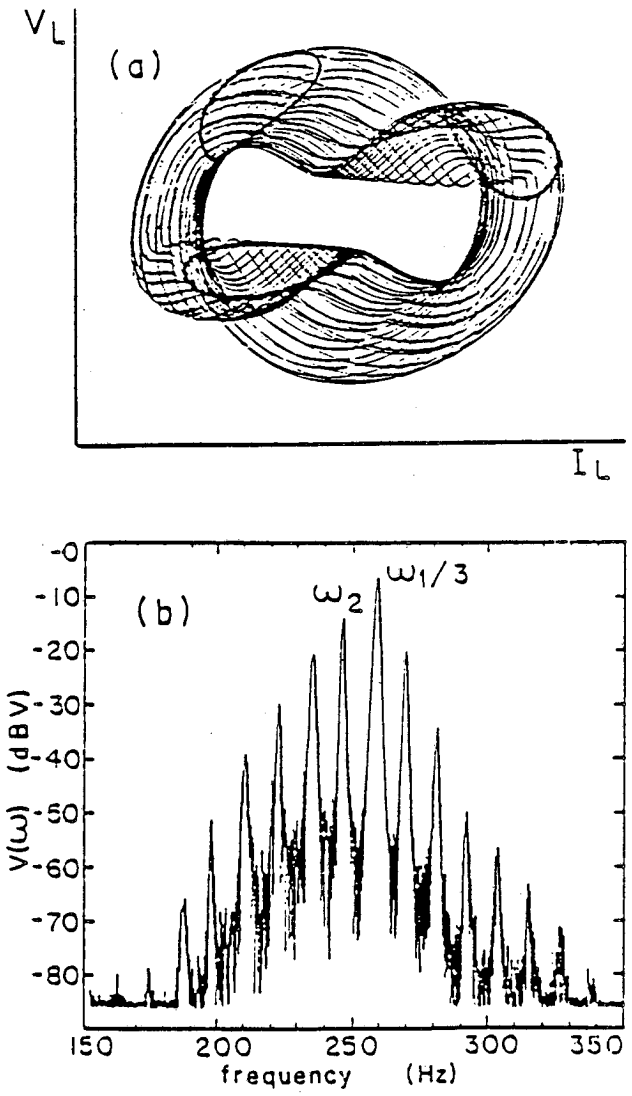

Figure 30. (a) Phase portrait with strobing superimposed, showing periodic "islands" for a point in region g of Fig. 29. (b) Frequency spectrum at same setting as in (a).

As in the case of a 2-torus, a point on the attractor can be described by two angles θ_1 and θ_2 (see Sec. 2.3.3). Only now $\theta_1 = \omega_1 t/3$ instead of $\omega_1 t$ since three cycles of ω_1 are required to get back to the original circle in the Poincare section. Thus the frequency spectra can contain the two-component harmonics of $\omega_1/3$ and ω_2. However, this is a symmetric attractor and so

only odd harmonics are found:

$$\omega_{mn} = \frac{m\,\omega_1}{3} + n\,\omega_2,$$

where m and n are integers and $m + n$ is odd. In the case presented, $\omega_1 \simeq 800$ Hz (much higher than the other experiments in this paper), and ω_2 is very close to $\omega_1/3$. The frequency spectrum corresponding to Fig. 30(a) is given in Fig. 30(b).

As seen in Fig. 29 there is strong hysteresis present. In one region the islands coexist with a surrounding circle, and in another they coexist with a circle that is centered between them. These hysteretic regions terminate through variations of the homoclinic bifurcation, in which either the circle or the islands contact the period 3 saddle forming a homoclinic orbit connecting the three saddles in a single loop, or three loops, respectively. Beyond this point (in parameter space) the circle or islands involved cease to exist. In Fig. 31(a)-(c) we show the three bifurcations of this type that were found. These Poincare sections were made by starting the system on one attractor just before its annihilation point and then adjusting the parameter through the bifurcation point. The data represent a single transient from the annihilated attractor to the other attractor. They follow the unstable manifold of the period 3 saddle point involved in this bifurcation.

4 ANALYSIS AND MODELING OF THE SYSTEM

Up to this point our theoretical "model" has been Arnold's rather abstract theory of bifurcations near points of resonance. That is, we have measured Poincare sections near points of resonance, both strong and weak, and compared them graphically to the theoretical model. We now present an entirely different kind of theoretical model and compare with the data: we return to the basic equation [Eq. (5)] of the physical system and numerically solve it under

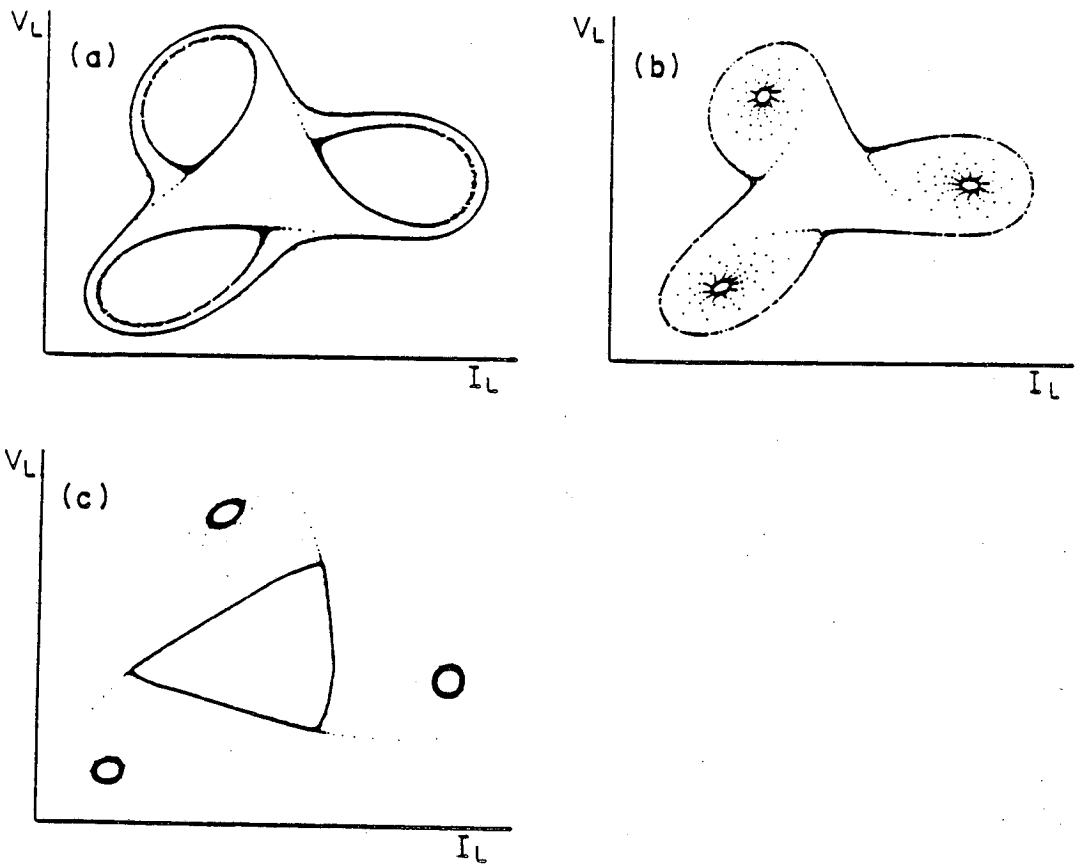

Figure 31. Poincare sections of homoclinic bifurcations in progress (shows loss of stability and jump). Initializing system (Sec. 1.2) not used. (a) Corresponds to hc-a in Fig. 29, three circles contact three saddle points, the attracting circles vanish and a jump occurs along the unstable manifold of the saddles to the coexisting external circle when crossing the boundary from region g to region f. (b) Reverse of (a) occurring at hc-b. Saddles contact outer circle and an inward jump occurs to the three islands when crossing the boundary from g to h. (c) Similar to (b) but here the circle losing stability does not surround the islands (hc-c). Jump occurs when crossing the boundary from i to h.

several approximations for the relationship between H and B. This model is shown to generate

a noninvertible Poincare map of the plane, with important consequences for the dynamical behavior. We also develop another model for our physical system – a 2-D map determined directly from experimental data. This is accomplished by expanding the map in a 2-D Taylor expansion, with coefficients determined from sets of experimental data points. The objective is to obtain a model which can predict specific behavior of the system, e.g. the locus of points of resonance, the boundaries of phase-locked regions, and period doublings.

4.1 Magnetic Core Behavior

Our basic problem here is to explore the relationship between the magnetic field H and the magnetic induction B in the core. This system is highly dependent on core dissipation due to magnetic hysteresis, as well as nonlinear inductance due to core saturation, so highly simplified models will be of little value.

In the most general case (assuming uniform B and H) we would expect that the present values of B and H would be some complicated functional of the previous excitation of the core [which could be specified by $I_L(t)$ or $V_L(t)$] and would also depend on the initial state of the core $S(t=0)$, which could be much more complicated than simply $H(0)$ and $B(0)$. Since $I_L(t)$ is related to $H(t)$ by Eq. (4) and $V_L(t)$ is related to $B(t)$ by Eq. (3), we could in principle find $H(t)$ as a functional of $B(t)$ or vice versa:

$$H(t) = H[B(t'), 0 < t' < t, S(0)]. \tag{21}$$

Dealing with such a functional would be very difficult even if we knew what it was, so instead we will examine the behavior of the core at very low frequencies. Here we can make the approximation (as discussed in Sec. 1.1) that H is a monotonic function of B which changes at the turning points of B, whenever $\dot{B}$ changes sign. At low frequency we can assume that H and B change sign simultaneously. This function can only depend on the previous turning points of

H (or equivalently of B) and the initial state of the core:

$$H = H[B, H_\pi, S(0)], \tag{22}$$

where H_π are all prior turning points of H (i.e. where H and $B = 0$). This behavior suggests that it may be fruitful in some cases to consider the behavior in terms of a map from the state at one turning point to the next. This idea is further developed in Sec. 4.3.1.

The complicated B–H behavior of the core is due to a combination of reversible (energy conserving) and irreversible (dissipative) changes in the polarization of the magnetic domains. Just following a turning point in B, the reversible processes tend to dominate. These are typically smooth Bloch wall motions (i.e. motion of the domain boundaries) at low B, and smooth domain rotation at high B. In this region $\partial B/\partial H$ is low. After a while these smooth motions tend to get stopped at imperfections in the core material. These are passed in irreversible jumps resulting in minute jumps in B. Here $\partial B/\partial H$ steepens. Ultimately B is limited by saturation when all domains point in the same direction. The work done on the core can be obtained using Eqs. (3) and (4):

$$W = \int V_L I_L \, dt = \int LAB\dot{H} \, dt = LA \int H \, dB. \tag{23}$$

This shows that the energy dissipated in a cycle is proportional to the area enclosed by the hysteresis loop.

4.2 Scaling Properties

In this section we will explore ways in which the system can be "scaled" to give equivalent behavior at some new set of parameters. In so doing we will discover how many parameters must be varied to cover all distinct modes of behavior.

From Eq. (5),

$$H = \frac{n}{L} I_0 \sin(\omega_1 t) - \frac{n^2 A}{LR} \dot{B} - \frac{n^2 AC}{L} \ddot{B}. \tag{24}$$

If B changes slowly enough, then H depends on the path taken by B (as could be specified by the turning points) but not how fast that path is traversed. This means that we can consider changing the frequency as well as the other parameters. Let $\theta = \omega_1 t$, then

$$H = \alpha_1 \sin\theta - \alpha_2 \frac{dB}{d\theta} - \alpha_3 \frac{d^2 B}{d\theta^2}, \tag{25}$$

where

$$\alpha_1 = \frac{n}{L} I_0, \; \alpha_2 = \frac{n^2 A \omega_1}{RL} \text{ and } \alpha_3 = \frac{n^2 AC \omega_1^2}{L}.$$

Thus in this approximation we need to vary only three parameters to cover all distinct behavior patterns. Any change in the parameters that leaves the α's unchanged will not effect the type of behavior the system exhibits; thus we obtain the scaling constraints:

$$\frac{\tilde{n}}{\tilde{L}} \tilde{I}_0 = 1, \; \frac{\tilde{n}^2 \tilde{A} \tilde{\omega}_1}{\tilde{R}} \tilde{L} = 1 \text{ and } \frac{\tilde{n}^2 \tilde{A} \tilde{C} \tilde{\omega}_1^2}{\tilde{L}} = 1. \tag{26}$$

where the $\tilde{}$ indicates that this is the ratio of the new value of the parameter to its original value. Using Eqs. (3) and (4) we find

$$\tilde{V}_L = \tilde{n} \tilde{A} \tilde{\omega}_1, \; \tilde{I}_L = \frac{\tilde{L}}{\tilde{n}} \text{ and } \tilde{t} = 1/\tilde{\omega}_1, \tag{27}$$

where the $\tilde{}$ indicates that this is the ratio of the variable with the new parameters (at the new time) to its original value (at the old time).

In the general case where H is some functional of the previous history of $B(t)$, we must also require $\tilde{\omega}_1 = 1$ in order to scale the system. In this case we need four parameters to fully explore the behavior of the system (e.g. I_0, ω_1, R, and C).

In the experiments presented in this paper (near 100 Hz) the low frequency scaling relations for $\tilde{\omega}_1 \neq 1$ are found to be only roughly correct. However, if R is varied slightly from the value it should have from Eq. (26), a value can be found for which nearly identical behavior is

found at the new frequency. It is believed that this adjustment can compensate for a slight change in dissipation per cycle in the magnetic core at the new frequency. For most of the data presented, only three parameters are varied: I_0, ω_1, and R.

4.3 Irreversible Differential Equation Model

In Section 4.2 we saw that the behavior of the forced system could be described by Eq. (25), a differential equation in H and B. Clearly we must be able to express H as a function of B in order to have a solvable model for the behavior of the system. Since we are operating at low frequencies (typically 100 Hz), we can make the approximation that the core is in quasiequilibrium. Then there will be some monotonic relation between B and H, and this relation will change (because of magnetic hysteresis) whenever $\dot{B}$ changes sign. The resultant equation of motion is irreversible. As B is changed continuously in one direction, and particularly as it approaches saturation, it is reasonable to expect the core to "forget" its previous history as the magnetic domains become aligned in nearly the same direction. $H(B)$ approaches the saturation curve $H_S(B)$ which is the same each cycle. The state of the core (under these conditions) can be described by a single variable, H or B, without any significant dependence on previous history. Thus, when the turning point of the magnetic induction, B_{TP}, occurs well into the saturation region, we can expect that the function $H(B)$ which is followed until the next turning point can be represented approximately as a function of B_{TP}, i.e. $H \simeq H(B, B_{TP})$.

Most of the dynamics described in this paper occur under conditions where the magnetic core is going from near saturation in one direction to near saturation in the other. We can therefore use the approximations just discussed to develop an empirical model for the $H(B)$ function which can be used in Eq. (25) to approximately describe the dynamics of this system. We have chosen a form roughly based on the observed dynamics in the B–H plane, but left certain

coefficients free to be varied (within reasonable limits) to obtain the best agreement between the Hopf bifurcation line of the model and that of the actual system (see Fig. 4). In this model the saturation hysteresis loop is represented by the function

$$H_S(B) = fB^5 + \frac{w}{2}, \tag{28}$$

where w and f are constants. This is the increasing branch of the loop, the decreasing one is related due to core symmetry, i.e. it is just $fB^5 - w/2$. The parameter w can be thought of as the width of the loop, since it is the difference between the increasing and decreasing branches. A fifth power was chosen for $H_S(B)$ because it was a good fit to the observed curve. However, the exact function is not critical to the behavior of the model; qualitatively very similar results can be obtained using a cubic function or even an inverse tangent function.

As stated previously, $H_S(B)$ must describe the asymptotic behavior of $H(B)$. Thus $H(B)$ is given by $H_S(B)$ plus a term which decays as B increases. In order to obtain a simple model we chose a decay function which decays completely to zero for some finite change in B, corresponding to the approximation that past history is completely eliminated beyond a certain point. The form used is

$$H(B) = H_S(B) + H_D(B), \tag{29}$$

where the decay term $H_D(B)$ is given by

$$H_D(B) = \begin{cases} -w(B_{TP} + B_D - B)^2/B_D^2 & \text{for } B \le B_{TP} + B_D \\ 0 & \text{for } B \ge B_{TP} + B_D \end{cases} \tag{30}$$

B_D is a decay constant, and B_{TP} is the last turning point for B. This model is only to be used when the oscillations always result in a change in B between turning points greater than B_D. Otherwise a more complicated model is required, such as one in which $H(B)$ depends on several (or all) previous turning points of B. The exact form of the decay function is of course very difficult to determine experimentally, but the dynamics do not appear to be strongly dependent on the form used, provided it merges smoothly (i.e. continuous first derivative) with the saturation curve and that the decay length (here B_D) can be adjusted. It should be emphasized

that this model for $H(B)$ results in making Eq. (25) an irreversible differential equation. This is because $H(B)$ depends on B_{TP}, the previous turning point. To follow the equation in reverse, we would need to know B_{TP} before reaching it. As it turns out, it is impossible to find the proper value of B_{TP} to use because the solution to the reversed equation is not unique. This will be discussed further in Secs. 4.3.1 and 4.3.2.

The dynamics of Eq. (25) were explored numerically using a 4th order Runge-Kutta method[31]. Our experimental estimates for the parameters are: $f \approx 60$, $W \approx 3.3$, and $B_D \approx 0.4$. In order to attempt to compensate for a variety of effects not included in the model, we adjusted these slightly, obtaining a reasonable fit to the experimental bifurcation set with $f = 60$, $W = 4.00$, and $BD = 0.357$. The resultant Hopf bifurcation line and points of resonance are compared with the experimental line in Fig. 32. The model also exhibits entrainment horns and other features in qualitative correspondence to those observed experimentally (Fig. 4). The main difference is the greater slope of the Hopf bifurcation line of the model relative to that observed. No reasonable adjustment of the three model parameters will correct this difference nor does any alternate form tried for the saturation curve such as a cubic function or an inverse tangent function. It is possibly the result of some departure of the real system from our quasistatic approximation.

In Fig. 33 we show typical phase portraits for the model for a 1:1 phase-locked case [Fig. 33(a)] and a quasiperiodic case [Fig. 33(b)]. As can be seen, these compare quite well with similar experimental results given in Figs. 2(a) and (b).

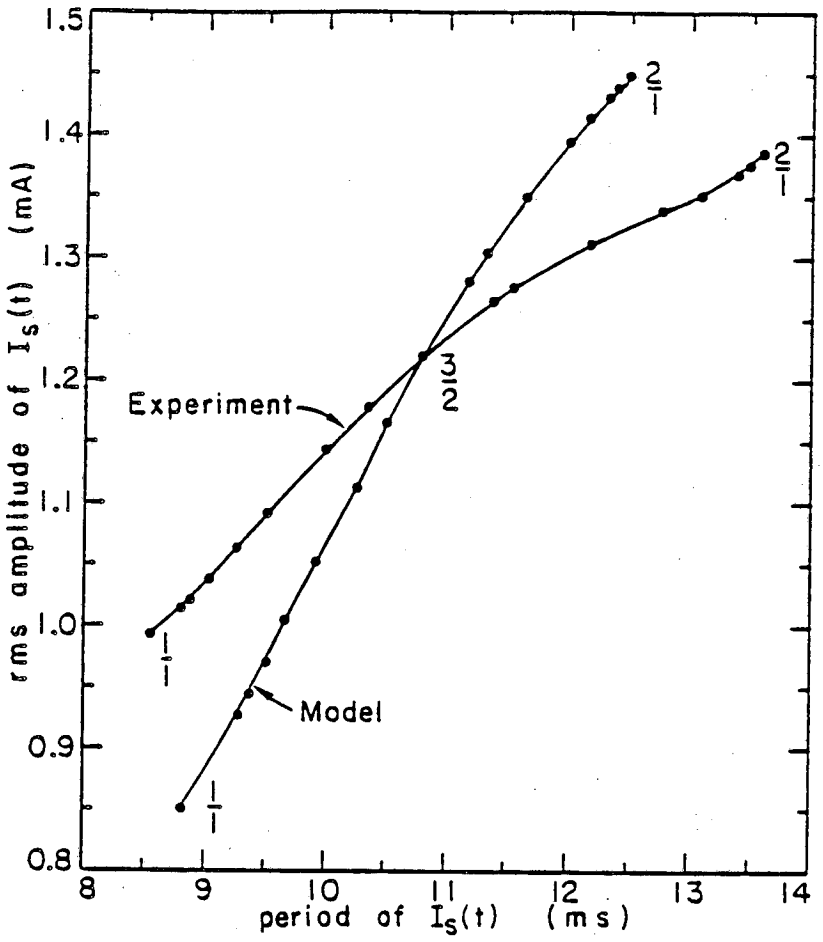

Figure 32. Comparison of points of resonance resulting from the differential equation model with those from the experiment. The same points are shown as on the H line in Fig. 4. The parameters were adjusted for exact agreement with experiment at the 3/2 point.

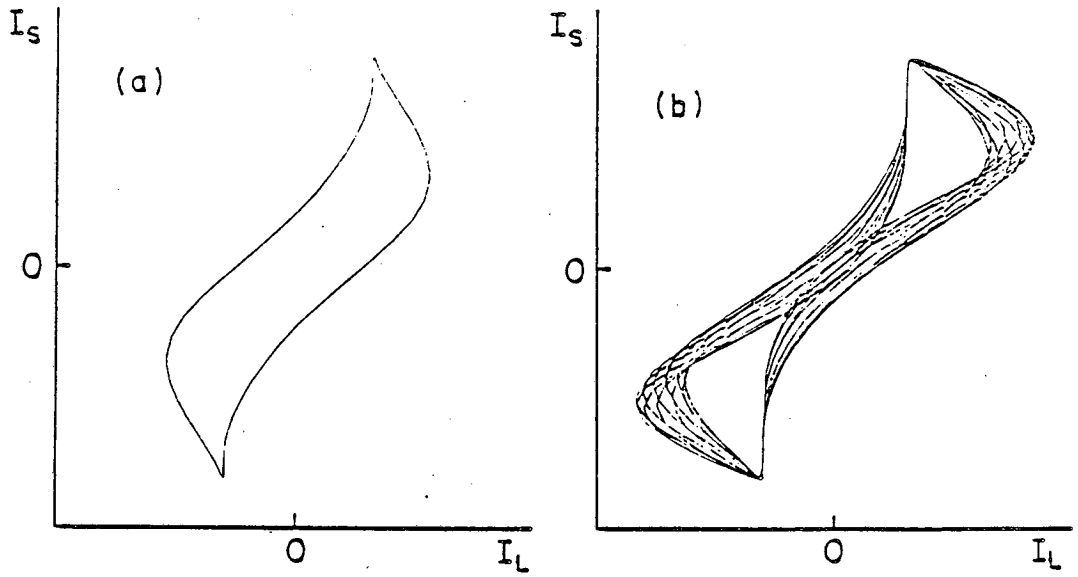

Figure 33. Typical phase portraits generated by the model. (a) 1:1 phase locking, below the line of Hopf bifurcation, cf. Fig. 2(a). (b) Quasiperiodic, above the line of Hopf bifurcation, cf. Fig. 2(b).

4.3.1 Reduction to a Noninvertible Planar Map

The process of merging with the saturation curve $H_S(B)$ corresponds to the contraction of the dynamical system to a lower dimensional phase space. Before the merging has occurred, we need to know B and B_{TP} – to represent the state of the core, and V_L and θ (the inductor voltage and the phase of the driver, respectively) – to represent the state of the driver and linear components. But after $H(B)$ merges with $H_S(B)$, the dependence of the model on B_{TP} vanishes and the phase space is three-dimensional. We can eliminate one dimension by defining a Poincare section and studying the dynamics of the mapping defined by successive intersections of the orbit with this surface of section. The logical choice is to use the section defined by $V_L = 0$,

since this is the turning point for the magnetic induction B and therefore the point of maximum saturation. Thus the Poincare space is two-dimensional – one dimension represents the state of the core (e.g. B or H or I_L), and one represents the state of the driver (e.g. θ or I_S). Note that most of the experimental Poincare section data given in this paper are in the (I_L, I_S) space strobed at $V_L = 0$.

The differential equation model [Eq. (25) with Eq. (29) for $H(B)$] can easily be used to generate the corresponding Poincare map. In Fig. 34 we show a typical example, produced by iterating a square grid through the mapping. This is actually a half cycle map (see Sec. 2.3.1), i.e., we follow the differential equation from a positive turning point initial condition to a negative turning point and then take the complement of the result (by changing the sign of I_L and I_S to give us another positive turning point state. This gridwork representation gives us a complete description of a two-dimensional map in a single figure. It is also the clearest way to show the noninvertibility of the mapping, since one can easily see that it folds over onto itself so that there are two choices for the pre-iterate of a given point. There is a line in the Poincare space where the Jacobian (defined in Sec. 4.3.3) of the mapping is zero, as shown in Fig. 34(a). This is the line which maps into the fold in Fig. 34(b). On one side of this line the Jacobian is positive (the right side), so the map is orientation preserving, while the other side of the line has negative Jacobian and is orientation reversing. This line is very important to the dynamics and is discussed further in Sec. 4.3.2.

4.3.2 *Effects of Irreversibility*

We would first of all like to point out the fact that Arnold's theory for diffeomorphisms may still be applied in spite of the global noninvertibility of the mapping. This is because the mapping may be considered locally invertible near the fixed point, i.e. for a given point near the

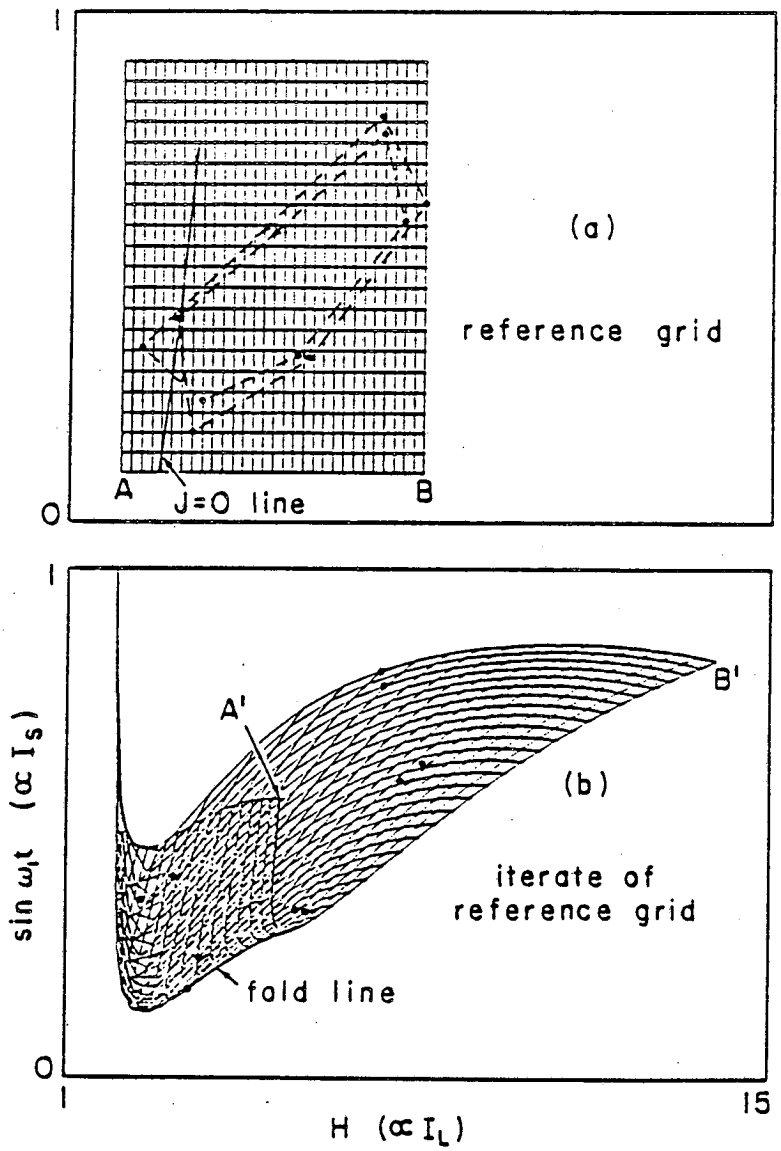

Figure 34. The 2-D Poincare map for the model, shown by iterating a grid pattern. At this parameter setting, the attractor is phase locked at a 1/5 rotation and has period doubled once. [This actually corresponds in the experiment to a point in the 7:5 horn just past symmetry breaking, see Eq. (17) and Fig. 22(a).] (a)Shows grid pattern, attractor (points) connected by dashed lines showing the iteration sequence, and zero Jacobian line. (b) Iterate of the grid pattern. The fold is the iterate of the zero Jacobian line.

fixed point the inverse mapping of this point is unique if we require that it also be near the fixed point. Typically there will be a second value for the inverse mapping, but it will be far from the

fixed point and will have no effect on the local dynamics.

While it is expected that high order phase lockings will follow circle map behavior[3-6] when near the critical "chaos" line in the parameter space, low order phase lockings can exhibit more complex behavior patterns not adequately described by a (1-D) circle map, requiring at least a 2-D map model. The irreversibility of the map can also play an important role in the dynamics. For an orientation preserving map, both eigenvalues of a fixed point (if real) must have the same sign. Also a 2-D map must always be orientation preserving near a focus (or spiral fixed point). In Fig. 22(a) we showed the symmetry breaking of a period 5 fixed point. This occurred when one eigenvalue of this periodic fixed point became less than -1. In a reversible orientation preserving map, the other eigenvalue would have to be negative as well, but this eigenvalue is observed (in the experimental system) to be positive. This is possible because one of the points on the period 5 orbit has (as we moved up the horn) crossed the line of zero Jacobian as shown for the model in Fig. 34. This makes the Jacobian negative and requires that the eigenvalues be of opposite sign. This can effect the qualitative structure of the bifurcations within the entrainment horns. The bifurcation pattern shown in Fig. 21 cannot occur for a 2-D reversible orientation preserving map. The reason is that the sequence of lines labeled sb, $\times 2$, ..., $\times\infty$, and cbm all intersect the left boundary of the horn. At the points of intersection we must have eigenvalues of +1 and -1 (+1 for the saddle-node at the boundary and -1 for the period doubling); hence the map must exhibit orientation reversal. We know that the map also exhibits a Hopf bifurcation; and since this is a bifurcation of a focus, it requires an orientation preserving map. In order for a map to exhibit both reversing and preserving regions, it must (for nondegenerate cases) exhibit a folding character as shown in Fig. 34 and hence be irreversible. This restriction does not apply to higher dimensional maps since these will have additional eigenvalues whose signs can be adjusted so as to maintain a positive Jacobian and allow a reversible map under the conditions described. Hence the experimental bifurcation pattern shown in Fig. 21 can be exhibited by invertible or noninvertible maps of dimension greater than

2, but only by noninvertible maps of dimension equal to 2.

4.3.3 Numerical Methods Used in the Model

The locations of the points of resonance for the model as shown in Fig. 32 were determined using the Jacobian matrix for the mapping. For an arbitrary mapping $\mathbf{X}' = \mathbf{F}(\mathbf{X})$ the Jacobian matrix is given by:

$$J_{\alpha\beta} = \frac{\partial F_\alpha}{\partial X_\beta}. \tag{31}$$

The determinant of this matrix is the Jacobian J. In the present application, the Poincare space is two-dimensional, so J is a 2×2 matrix. Since the mapping is defined by integrating the differential equation model, J must also be determined numerically. This can be done by iterating two points which are very close together, i.e.

$$J_{\alpha\beta}(\mathbf{X}) \approx [F_\alpha(\mathbf{X} + \mathbf{D}_\beta) - F_\alpha(\mathbf{X} - \mathbf{D}_\beta)] / 2D_\beta, \tag{32}$$

where $\mathbf{D}_\beta$ is a small displacement in the β direction. The first step to locate a particular point of resonance in the parameter space is to find the fixed point in the Poincare space for some parameter setting thought to be near the resonance point. It is quite impractical to do this by repeatedly iterating the map, because the fixed point is on the verge of instability and will exhibit exceedingly long decay times. However, if $\mathbf{X}_0$ is the fixed point, then locally the mapping is given approximately by the linear relation

$$\mathbf{X}' \approx \mathbf{X}_0 + \mathbf{J}\cdot(\mathbf{X} - \mathbf{X}_0). \tag{33}$$

thus

$$\mathbf{X}_0 \approx (\mathbf{1}-\mathbf{J})^{-1}\cdot[\mathbf{F}(\mathbf{X}) - \mathbf{J}\cdot\mathbf{X}]. \tag{34}$$

Successive iterations of this estimation procedure for $\mathbf{X}_0$ rapidly converge, provided the initial point was not too far away. The second step to locating the points of resonance is to look at the

eigenvalues of J. They must be of the form

$$e_{\pm} = \exp(\pm i\pi p/q) = A_0 \pm iB_0,$$

where p/q is the rational rotation number (for the half cycle map) corresponding to that point of resonance. If the eigenvalues of the fixed point for parameter setting P are actually $A(\mathbf{P}) + iB(\mathbf{P})$, then an estimate for the location of the resonance point $\mathbf{P}_0$ can be made by looking at the local variation of $A(\mathbf{P})$ and $B(\mathbf{P})$ with P. Define

$$\mathbf{C} = \begin{bmatrix} \partial A/\partial P_1 & \partial A/\partial P_2 \\ \partial B/\partial P_1 & \partial B/\partial P_2 \end{bmatrix}. \tag{35}$$

The components of C can be determined numerically using small deviations in the parameters P_1 and P_2, e.g., $\partial A/\partial P_1 \approx [A(P + \delta_{P1}) - A(P - \delta_{P1})]/2\delta_{P1}$ The location of the fixed point may change when P is changed by δ_{P1}, so it must be relocated before A and B can be determined. The estimate for P_0 is then given by

$$\mathbf{P}_0 \approx \mathbf{P} + \mathbf{C}^{-1} \cdot \begin{bmatrix} A_0 - A \\ B_0 - B \end{bmatrix}. \tag{36}$$

Successive iterations of this procedure rapidly determine $\mathbf{P}_0$ for a particular resonance point to high accuracy.

4.3.4 Corrections to the Model

We will now briefly discuss a few modifications which can be made to improve the model for $H(B)$, Eq. (29). These fall into three general categories: (1) functional changes, (2) time dependent effects, and (3) higher dimensional effects.

(1) The most obvious changes to consider are to improve the accuracy of the functions $H_S(B)$ and $H_D(B)$. We used a fifth power for $H_S(B)$, but this function could instead be expanded in a Taylor series of several terms, or represented by a sequence of data points deter-

mined experimentally: A similar improvement could be made for the function $H_D(B)$, e.g., the decay length B_D could be made dependent on the turning point B_{TP} and the functional form may be modified to more accurately agree with experimental measurements.

(2) Deviations from the approximation of quasistatic field changes in the core may be corrected for an improved model. It is found experimentally that H is slightly increased when $\dot{B}$ is nonzero. If we assume that $\Delta H \propto \dot{B}$, then this is equivalent to having an effective resistance R_E in parallel with the quasistatic model.

(3) Increasing the dimensionality of the model is to be avoided if possible, since this will complicate the numerical computations. However, a discussion of the higher dimensional effects is useful since it may lead to insight into how to correct the model to compensate for these effects without increasing its dimension. The higher dimensionality arises when the $H(B)$ function does not completely merge with the saturation curve $H_S(B)$, and when the core retains some "memory" of earlier turning points in B. In our model we have artificially eliminated such effects by making the decay term $H_D(B)$ go to zero when B has changed by B_D. In a more realistic model we would expect some kind of exponential decay, never going completely to zero. Thus there remains some remnant of past history, the true dimensionality being effectively infinite. However, so long as these higher dimensional effects are small, one can hope to compensate for them and retain a 2-D Poincare section for the model. One approach would be to apply some correction term to the Poincare map (as generated by the differential equation) which compensated for the fact that $H(B)$ for the experimental system was slightly displaced from the saturation curve $H_S(B)$.

4.4 Measuring the Map Coefficients – Experimentally Determined 2-D Taylor Expansion

The reduction from a flow to a mapping is a very useful one since the mapping exhibits all of the important dynamics of the flow while being much easier to analyze. Unfortunately, this reduction cannot be accomplished analytically for most differential equations. Instead, we have decided to try another approach here – expanding the map in a 2-D Taylor expansion and determining the coefficients. Since our differential equation model is not in perfect agreement with the observed behavior, we make this expansion directly from experimental data, attempting to improve the agreement between the bifurcation set of the model and of the experiment.

The expansion must be carried out in both parameter space and in Poincare variable space. We have chosen to make the parameter expansion about the center point on the line of Hopf bifurcation -- the 3:2 resonance point (see Fig. 4), and the Poincare variable expansion about the central focus which undergoes the Hopf bifurcation. Nonlinear terms through third order in the Poincare space are crucial to the dynamics when near the Hopf bifurcation. While it is true that the Hopf bifurcation of a map can be reduced to a complex normal form[12] having just a single nonlinear (cubic) term, we were also interested in folding (irreversibility) of the map, a proper description of which may require a more complex knowledge of the nonlinearities than a single term. Therefore, we have carried out a full expansion to third order. For a 2-D expansion in I_L and I_S, this entails four linear terms, six quadratic terms, and eight cubic terms:

$$
\begin{aligned}
I_L' &= A_{LL}\, I_L + A_{LS}\, I_S \\
&\quad + A_{LLL}\, I_L^2 + A_{LLS}\, I_L\, I_S + A_{LSS}\, I_S^2 \\
&\quad + A_{LLLL}\, I_L^3 + A_{LLLS}\, I_L^2 I_S + A_{LLSS}\, I_L\, I_S^2 + A_{LSSS}\, I_S^3 \\
I_S' &= A_{SL}\, I_L + A_{SS}\, I_S \\
&\quad + A_{SLL}\, I_L^2 + A_{SLS}\, I_L\, I_S + A_{SSS}\, I_S^2 \\
&\quad + A_{SLLL}\, I_L^3 + A_{SLLS}\, I_L^2 I_S + A_{SLSS}\, I_L\, I_S^2 + A_{SSSS}\, I_S^3
\end{aligned}
\tag{37}
$$

There are no constant terms because we have shifted the coordinates (I_L, I_S) so that the central focus is at (0, 0). We restrict the parameter dependence to the linear coefficients, A_{LL}, A_{LS}, A_{SL}, and A_{SS}. A linear expansion in the parameters τ_1 and I_0 requires three terms for each linear coefficient:

$$
\begin{aligned}
A_{LL} &= A_{NL}\, A_{LLO} + A_{LLT}\, \Delta\tau_1 + A_{LLI}\, \Delta I_0 \\
A_{LS} &= A_{NL}\, A_{LSO} + A_{LST}\, \Delta\tau_1 + A_{LSI}\, \Delta I_0 \\
A_{SL} &= A_{NL}\, A_{SLO} + A_{SLT}\, \Delta\tau_1 + A_{SLI}\, \Delta I_0 \\
A_{SS} &= A_{NL}\, A_{SSO} + A_{SST}\, \Delta\tau_1 + A_{SSI}\, \Delta I_0
\end{aligned}
\tag{38}
$$

where $\Delta\tau_1$ and ΔI_0 are the displacements from the location of the 3:2 resonance point (located at $\tau_1 \approx 10.8$ ms and $I_0 \approx 1.22$ mA), and A_{NL} is a nonlinear correction factor used to correct the curvature of the Hopf bifurcation line, which is approximately unity for small displacements. The form used for A_{NL} is:

$$
A_{NL} = 1 + A_{TT}\, \Delta\tau_1^2 + A_{TI}\, \Delta\tau_1\, \Delta I_0 + A_{II}\, \Delta I_0^2 \tag{39}
$$

The reason for keeping so many terms is to obtain some degree of quantitative agreement with experiment, both for the bifurcation set in parameter space and for the attractor(s) in Poincare space.

The linear coefficients and their parameter dependence were determined by examining the attractor for a number of parameter values. These parameter values were all chosen to be in the

quasiperiodic regime, slightly above the Hopf bifurcation line (hereafter referred to as the H line). Here the attractor is a set of points lying approximately on an ellipse which is centered on the unstable focus, which is the origin of our expansion. The four linear coefficients can be approximately determined from four features of this attracting ellipse: (1) the rotation number, i.e. the average angular jump around the ellipse between successive points; (2) the Jacobian of the mapping – this is approximately unity if very close to the H line (as is the case); (3) the eccentricity of the ellipse; and (4) the angular tilt of the major axis of the ellipse. The eccentricity and tilt are easy to determine by inspection and are found to only change slightly along the H line. The rotation number is known accurately from previous measurements locating the points of resonance (having rational rotation number). In addition to the behavior along the H line, we also need the behavior transverse to it. This is more difficult, since the Jacobian is no longer equal to unity when we move away from the H line. This generally requires using initialization techniques (see Sec. 1.2). For points above the H line we initialize the system near the central focus, and observe the outward spiral of the orbit. Sufficiently close to the central focus, the nonlinear terms will be negligible and the linear terms can be determined to fit the experimental sequence of points. Following this procedure the linear coefficients were determined:

$$A_{LLO} = 1.082499,\quad A_{LSO} = -7.576032,\quad A_{SLO} = 0.286668,\quad A_{SSO} = -1.082499,$$
$$A_{LLT} = -0.26553,\quad A_{LST} = 1.1066,\quad A_{SLT} = -0.0013991,\quad A_{SST} = -0.19248,$$
$$A_{LLI} = 1.0051,\quad A_{LSI} = -22.464,\quad A_{SLI} = 0.36103,\quad A_{SSI} = -4.7891.$$

Knowledge of the linear terms is all that is needed to locate the H line and points of resonance. The linear expansion in the parameters, however, is only accurate near the point in parameter space we are expanding about, i.e. the 3:2 resonance point. In order to obtain some degree of long range agreement, we found it necessary to modify the linear expansion. However, rather than going to a full quadratic expansion in the parameters, we have chosen instead to use a nonlinear correction factor A_{NL} [Eq. (39)] requiring only three additional coefficients,

rather than 12. These are adjusted mainly to correct the curvature of the H line to improve agreement with experiment. Using A_{TT} = -0.02266, A_{TI} = -0.37898, and A_{II} = -1.5512, we obtain the results shown in Fig. 35, in which the H line for the model is compared with the experimental H line. As can be seen, agreement is excellent near the 3:2 point, but deteriorates slightly towards the end points.

In order to determine all 14 nonlinear coefficients (through 3rd order), a more sophisticated approach must be taken than that used to determine the linear coefficients. By taking a sequence of points in the experimental Poincare section, which are sufficiently far from the origin to make nonlinear effects important, we use the method of least squares[31] to determine the

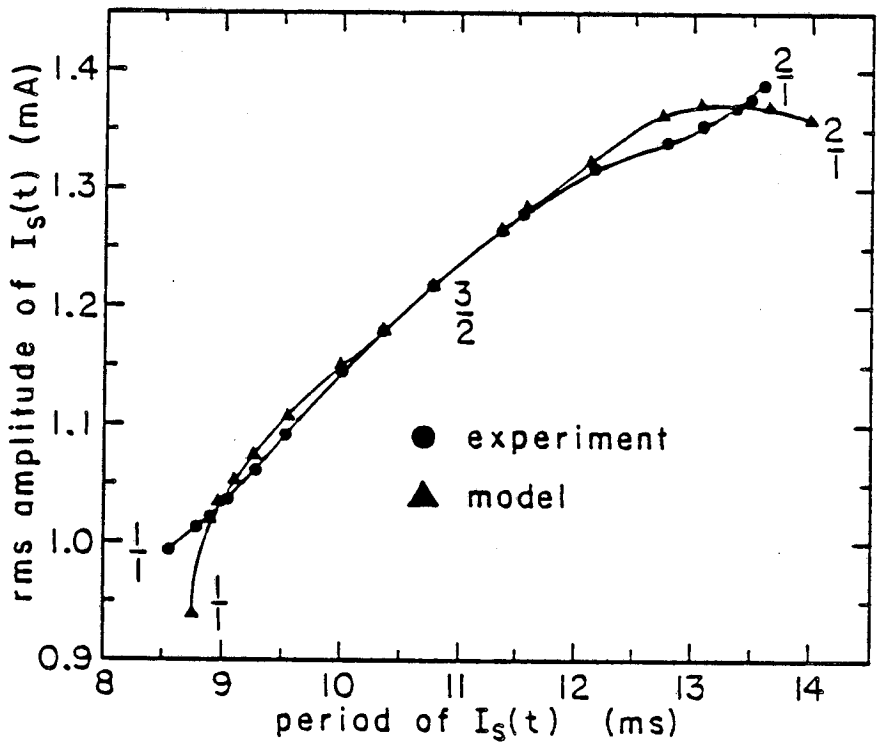

Figure 35. Comparison of the points of resonance resulting from the measured map coefficient model with those of the experiment (same points as in Figs. 32 and 4).

set of coefficients giving the best fit of the approximation to the experimental mapping between successive data points. This method requires one to invert a large matrix, and thus must be carried out on a digital computer. We took data for an outward spiraling transient (from which we used 13 successive data points) leading to a 19:13 phase-locked attractor (from which all 13 points were used). The atrractor was far enough out that it deviated significantly from a centered ellipse, but still close enough to the origin that higher order terms (beyond cubic) might reasonably be neglected. The transient was important for the proper determination of the linear coefficients. The result of this calculation is the set of nonlinear coefficients given below:

A_{LLL}=–0.014745, A_{LLS}=–0.42672, A_{LSS}=–3.1192,
A_{SLL}=–0.020851, A_{SLS}=0.23495, A_{SSS}=–1.5591,
A_{LLLL}=–0.047467, A_{LLLS}=0.15150, A_{LLSS}=0.094472, A_{LSSS}=1.0667,
A_{SLLL}=–0.0084103, A_{SLLS}=0.056690, A_{SLSS}=–0.12257, A_{SSSS}=–0.39779.

The mapping thus determined agrees quite well with the experimental data points, the rms error for all points being about 1% of the range of the data set.

In Fig. 36 we show the boundary of the 3:2 horn from experiment (solid line) and model (dashed line). Also shown is the interior line which marks the first period doubling bifurcation. Agreement is fairly good considering that we only carried out the parameter expansion for the linear coefficients.

This represents the first attempt (to the author's knowledge) to accurately measure the coefficients for a 2-D damping directly from a dynamical system. The approach of expanding as a Taylor series has shown some degree of quantitative agreement with a complex physical system. The accuracy of the results should be expected to improve dramatically if the order of the expansion is increased, with coefficients calculated from a larger data set. This approach may be valuable for other systems which, due to their complexity, cannot be modeled accurately with a differential equation based on first principles. High dimensional systems will generally exhibit low dimensional dynamics when near an instability, such as Hopf bifurcation, and thus can (when near the instability at least) be accurately described by a low dimensional

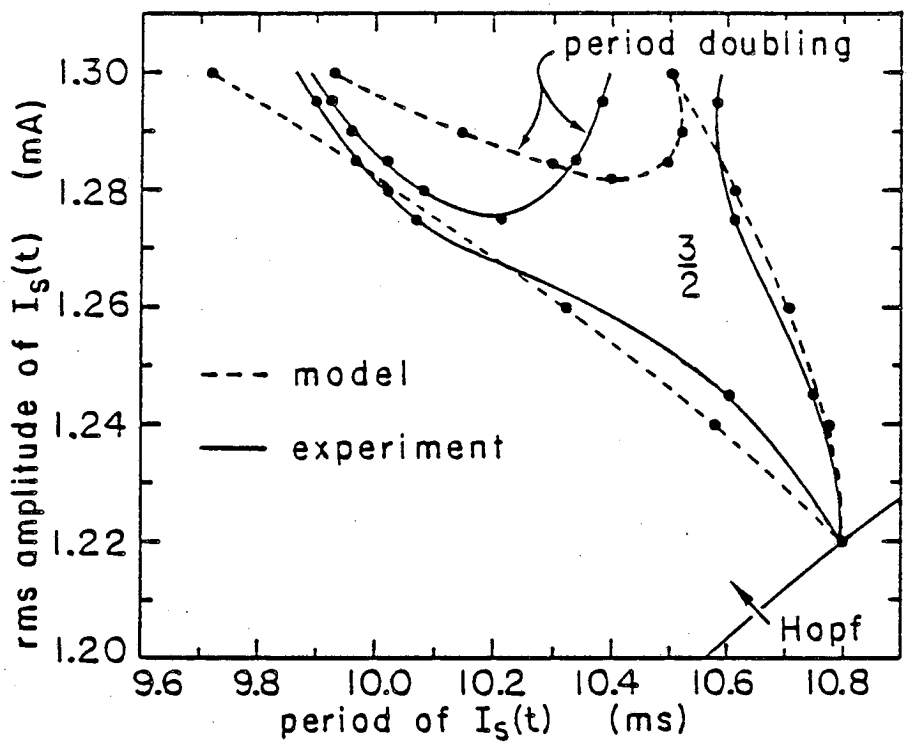

Figure 36. Boundary of 3/2 horn and first period doubling line in its interior. Solid lines - experimental data; dashed lines - computed for measured coefficient model.

mapping.

5 SUMMARY AND CONCLUSION

The driven symmetric nonlinear magnetic oscillator described by Eq. (5) has a very rich dynamical behavior, for which extensive data has been presented. An overall view of the behavior is given by Fig. 4, in the parameter space (I_0, τ_1). A dominant feature is the Hopf bifurcation to quasiperiodicity, together with the formation of entrainment horns and hysteresis. Within a horn there are period doubling cascades, internal crises, and loss of entrainment.

Between horns the system follows a quasiperiodic route: loss of smoothness of the Poincare section at an irrational rotation number followed onset of chaos. Also observed are symmetry-breaking bifurcations and homoclinic bifurcations. The system exhibits a Hopf bifurcation from an entrained state to periodic islands, similar to those found in Hamiltonian systems.

Phenomena near and on the phase locking boundaries have been explored in detail. Bifurcations near points of resonance are observed, and can be understood from Arnold's theory of versal deformations of the plane. By a novel technique of repeated initializations of the system we observe "hidden" behavior (e.g. motion on both unstable and stable manifolds of saddle points) in a 2-D Poincare space and compare to the theory, with excellent agreement. Much of the complex behavior observed, including multiple attractors and hysteresis, are found to result from the behavior at these resonance points. We believe that this is the first detailed study of strong resonance in a physical system.

Important properties of the behavior related to symmetry are explored. The concept of a half-cycle map is developed which explains much of the observed behavior such as the existence of two types of resonance points – symmetrical and asymmetrical, how their order q is related to the frequency ratio M/N, why a symmetry breaking bifurcation may precede a period doubling sequence, and why a complementary band merging may follow a band merging sequence (of the chaotic attractor). Symmetrical quasiperiodic attractors containing only odd 2-component harmonics are observed [Fig. 2(b) and (c)] and explained (Sec. 2.3.3).

In a second, and quite different, kind of theoretical analysis, a differential equation model is developed, based on empirical properties of the magnetic core, which gives good qualitative agreement with the physical system in terms of the bifurcation patterns observed and the locus in parameter space of the points of resonance. This model leads to a noninvertible map of the plane, with important consequences for some of the behavior exhibited.

Based on the assumption that a 2-D mapping could represent an accurate model for the physical system, this mapping has been expanded as a 2-D Taylor series with the *coefficients measured from experimental data.* The resultant model shows improved quantitative agreement with experiment for its bifurcation set over the differential equation model, as well as being faster to analyze numerically. Specifically, good agreement is found between this model and the data for the actual locus in parameter space of the Hopf bifurcation line, horn boundaries, and period doubling boundary line. Similar techniques could be useful in modeling other physical systems which are too complex to be described by a differential equation based on first principles. These modeling techniques may have applications in engineering as well as in the study of other nonlinear phenomena.

REFERENCES FOR PART 2

1. D. G. Aronson, M. A. Chory, G. R. Hall, and R. P. McGehee, in New Approaches to Nonlinear Problems in Dynamics, ed. P. Holmes (Philadelphia: S.I.A.M., 1980), p. 339, and Commun. Math. Phys. 83, 303 (1982).

2. D. G. Aronson, R. P. McGehee, I. G. Kevrekidis, and R. Aris, Phys. Rev. A 33, 2190 (1986).

3. M. J. Feigenbaum, L. P. Kadanoff, and S. J. Shenker, Physica 5D, 370 (1982).

4. S. J. Shenker, Physica 5D, 405 (1982).

5. S. Ostlund, D. Rand, J. Sethna, and E. Siggia, Physica 8D, 303 (1983).

6. M. H. Jensen, P. Bak, and T. Bohr, Phys. Rev. Lett. 50, 1637 (1983) and Phys. Rev. A 30, 1960 (1984); P. Cvitanovic, M. H. Jensen, L. P. Kadanoff, and I. Procaccia, Phys. Rev. Lett. 55, 343 (1985).

7. J. H. Curry and J. A. Yorke, Lecture Notes in Math. 668, 48 (1978).

8. D. Ruelle and F. Takens, Commun. Math. Phys. 20, 167 (1971); 23, 343 (1971).

9. J. P. Gollub and S. V. Benson, J. Fluid Mech. 100, 449 (1980); H. L. Swinney, Physica 7D, 3 (1983); J. Stavans, F. Heslot, and A. Libchaber, Phys. Rev. Lett. 55, 596 (1985);

C. D. Jeffries, Physica Scripta T9, 11 (1985); H. G. Winful, Y. C. Chen, and J. M. Liu, Appl. Phys. Lett. 48, 616 (1986).

10. P. Bryant and C. Jeffries, Phys. Rev. Lett. 53, 250 (1984).

11. In these experiments we have used a toroidal core manufactured by Magnetics (part no. 52039-1F). The core is of the "tape wound" type, made from 1 mil thick Supermalloy (79% Ni, 17% Fe, 4% Mo) tape. It has an effective cross- section of 0.151 cm^2 and a magnetic path length of 10.97 cm. The coil is 100 turns of 28 copper wire.

12. A general reference for some of this material is: J. Guckenheimer and P. Holmes, Nonlinear Oscillations, Dynamical Systems, and Bifurcations of Vector Fields (New York: Springer-Verlag, 1983).

13. V. I. Arnold, Geometrical Methods in the Theory of Ordinary Differential Equations (New York: Springer-Verlag, 1983), pp. 170, 280, 291.

14. V. I. Arnold, Usp. Mat. Nank 27, No. 5, 119 (1972) [Russ. Math. Surv. 27, 54 (1972)].

15. V. I. Arnold, Funkts Anal. Prilozh. 11, No. 2, 1 (1977) [Funct. Anal. Appl. 11, 85 (1977)].

16. G. Iooss, Bifurcation of Maps and Applications (New York: North-Holland Publishing Co., 1979), p. 105.

17. F. Takens, Comm. Math. Inst., Rijkuniversiteit Utrecht 3, 1 (1974).

18. A. I. Neishtadt, J. Appl. Math. Mech. 42, 895 (1978).

19. F. S. Berezovskaia and A. I. Khibnik, J. Appl. Math. Mech. 44, 663 (1980).

20. Y. H. Wan, Arch. Rat. Mech. Anal. 68, 343 (1978).

21. F. Lemaire-Body, C. R. Acad. Sci. Ser. A 287, 727 (1978).

22. This concept was developed independently by J. Swift and K. Wiesenfeld, Phys. Rev. Lett. 52, 705 (1984).

23. B. van der Pol, Pilos. Mag. 3, 65 (1927).

24. M. L. Cartwright, J. Inst. Elec. Eng. 95, 88 (1948).

25. A. W. Gillies, Quart. J. Mech. Appl. Math. 7, 152 (1954).

26. P. J. Holmes and D. A. Rand, Quart. Appl. Math. 35, 495 (1978).

27. C. Grebogi, E. Ott, and J. A. Yorke, Phys. Rev. Lett. 48, 1507 (1982), and Physica 7D, 181 (1983).

28. P. Manneville and Y. Pomeau, Phys. Lett. 75A, 1 (1979).

29. Y. Pomeau and P. Manneville, Commun. Math. Phys. 74, 189 (1980).

30. A. J. Lichtenburg and M. A. Lieberman, Regular and Stochastic Motion (New York: Springer-Verlag, 1983), p. 44.

31. S. D. Conte and C. deBoor, Elementary Numerical Analysis (New York: McGraw-Hill, 1980).

PART 3:

NOISE RISE IN JOSEPHSON JUNCTIONS

1 INTRODUCTION

This part of the thesis is concerned with a practical problem – an anomalous "noise rise" that was observed to occur in Josephson Junction parametric amplifiers. A theory is presented which offers an explanation for this effect. The theory is based on a "dynamical systems" approach to the problem, the results of which may be applied to a broad class of similar systems. Predictions are made which may be tested in future experiments.

About a dozen years ago, the first Josephson junction parametric amplifiers were built and studied.[1-6] These devices achieved good signal gain of electromagnetic radiation in the difficult frequency range ~ 1 - 100 GHz, a range important for astrophysical observations. Unfortunately, these amplifiers have proven impractical because of a noise problem – the so-called noise rise[5-7] – previously unseen in other kinds of parametric amplifiers. Typically, one expects the ratio of signal amplification G_s to broadband noise amplification G_n to be a constant for a given device, independent of parameter settings: this ratio is proportional to the noise temperature T characterizing the amplifier. The Josephson devices, however, display a noise temperature which is an increasing function of G_s: that is, the greater the signal gain, the worse the signal-to-noise ratio, until the noise output overwhelms the coherent signal.

Although a variety of explanations have been forwarded,[8-14] this noise rise phenomenon remains an open problem. The purpose of this paper is to examine a new mechanism that

results in a gain-dependent noise temperature. This theory exploits very recently developed insights linking parametric amplification to the generic properties of nonlinear dynamical systems near the onset of simple bifurcations.[15-17] Besides generating a noise rise like that observed in past experiments, the theory leads to a number of predictions to enable future experiments to determine whether the present mechanism is truly at play.

The idea that any time-periodic dynamical system can be used as a parametric amplifier near a simple bifurcation point has been supported by experiments involving nuclear magnetic resonance lasers,[16] electrical analog circuits,[15] Barium Sodium Niobate crystals,[18] and a mechanical "bouncing ball" system.[19,20] The reason why general quantitative statements can be made about small-signal amplification properties in such diverse physical systems rests on ideas from bifurcation theory. Near an instability, the relevant phase space dimension typically reduces to a very small number – for the cases relevant to this paper, the effective dynamics reduces to a one dimensional phase space. This reduction of dimension results in so-called "universal" behavior, with results that are independent of physical details. Although this universality holds only close to the bifurcation point, it is precisely near such points that parametric amplifiers achieve high gain. This happy coincidence is the linchpin of the theory presented in this paper.

Previous attempts to explain the origin of the noise rise have all examined directly the specific circuit equations governing the dynamics of Josephson junction parametric amplifiers.[8-14] A succinct and informative review of many of these theories may be found in Ref.10. With one exception, which suggested that the noise rise is due to deterministic chaos,[12,13] these explanations involve the presence of external noise, as we do here. Of these theories, the work presented here has most in common with the idea of the "phase instability" (invoked by Chiao et al. for the 4-photon mode[7]) and the noise-induced hopping picture (described by Miracky and Clarke for the 3-photon mode[14]). The essential ingredient in each of these is that the amplifier dynamics can have multiple solutions – in dynamical systems

parlance, there can be *coexisting attractors* – and external noise can "kick" the system back and forth between these stable solutions. In each case, analog simulations of the governing circuit equation supported this basic picture.

A major difference between previous work and the present paper is that, rather than proceed from a direct analysis of the circuit equations valid for the Josephson junction devices, we focus on the *universal dynamics* valid in the neighborhood of a bifurcation point. (The appropriate "universality class" depends only on the type of bifurcation encountered; consequently, the 3-photon mode is described by a different normal form than is the 4-photon mode, as explained in Sec. 3.) This new approach should be viewed as complementary to the body of work based on the detailed circuit equations. The present theory has certain advantages, both in its power to explain previous observations and to make several new, experimentally testable predictions. On the other hand, the weakness of this approach is that it only predicts the *scaling behavior* for the parameter dependence of various physical quantities, and not their absolute *magnitudes*. For example, we do not quote values for the noise temperature in degrees Kelvin, nor do we explain the physical origin of the random external fluctuations (e.g. shot noise, Johnson noise, etc.). Because of this complementary relationship, we try to make contact between the results of this study and previous theories wherever possible.

This paper is organized as follows. Sec. 2 briefly describes the previous noise-free theories of the 3- and 4-photon modes, and recaps the recent insights linking dynamical instabilities and parametric amplification. Sec. 3 discusses in detail the reduced "normal form" equations appropriate for each mode. The results of digital and analog simulations of these reduced equations are presented in Sec. 4, examining in detail the properties of the noise rise in each of the two modes. Analytic expressions for the signal gain and the noise gain, valid in certain limiting parameter regimes, are derived in Sec. 5, and compared with the simulations. Sec. 6 is devoted to a discussion of how to apply the results to experimental data, and provides a number of specific predictions for future experiments. Applying this general theory to two new

situations is the focus of Sec. 7. We discuss the possibility (and potential advantages) of operating the Josephson junction parametric amplifier in a 6-photon mode, and also discuss the relevance of the general theory to an entirely different system, namely modulated semiconductor lasers. Finally, the results are summarized in Sec. 8, with a brief look at what these results suggest about the theoretical optimal performance of parametric amplifiers.

2 BACKGROUND

Josephson junction parametric amplifiers have been built using a variety of arrangements, employing either single junctions (microbridges,[1] point contacts,[2] or tunnel junctions[6]) or an array of many junctions in series.[5] The noise rise has been observed in all of these designs. The fact that the noise-free performance is well understood theoretically for these devices suggests that the deterministic theories contain much of the essential dynamics. Therefore, it is worthwhile to review briefly these analyses – which are based on a direct attack on the governing circuit equations – and to compare them with the recent results revealed by the general approach to the nonlinear dynamics of bifurcating dynamical systems. We consider the 3- and 4-photon modes separately, with an emphasis on those aspects that have a bearing on the noise rise phenomenon.

2.1 Three-Photon Mode[21,22]

The basic model of the Josephson junction parametric amplifier is depicted schematically in Figure 1. In dimensionless form, the governing circuit equation has the form

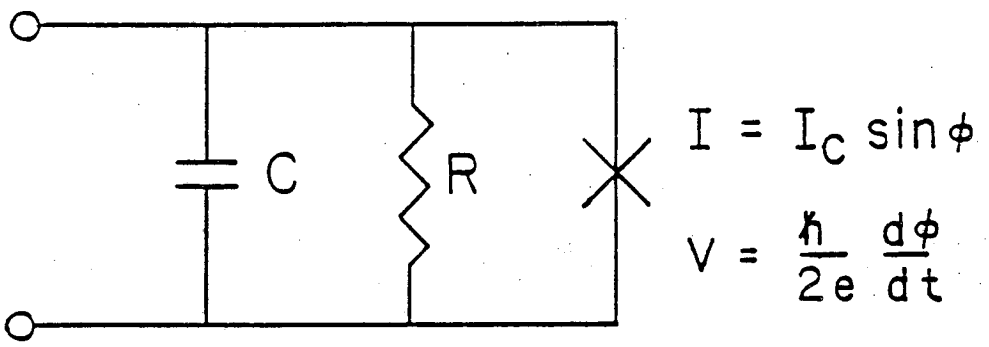

Figure 1. Schematic model of the resistively shunted Josephson junction parametric amplifier. The cross represents the idealized junction through which supercurrent flows. C, R, and I_c are the capacitance, resistance, and critical current, respectively.

$$\ddot{\phi} + \beta_c^{-1/2}\dot{\phi} + \sin\phi = A + B\cos(\omega_p t) + C\cos(\omega_s t + \theta) \qquad (1)$$

where ϕ is the difference between the phases of the wavefunction across the junction, β_c is the McCumber parameter, and A, B, C are the external voltage drives at zero, pump, and signal frequencies, respectively. The McCumber parameter can be expressed in terms of the system's critical current I_c, capacitance C, resistive shunt R, electron charge e, and the reduced Planck's constant $\hbar$, as $\beta_c = 2eR^2CI_c/\hbar$. Equation (1) represents an idealization of the physical system; for example it neglects the quasiparticle current across the junction, and ignores the presence of tuning circuit(s) necessary to couple the device to the external world. It is generally believed that these complications affect only the details of the amplifier's performance, and not its essential behavior. Of course, since the noise rise is not yet understood, the importance of these "details" cannot be ruled out; however, the mechanism discussed in this paper is insensitive to their presence.

In the 3-photon mode, the (small) signal has frequency ω_s nearly equal to one half the pump frequency ω_p. It is convenient to introduce the small parameter Δ which measures the detuning of ω_s from $\frac{1}{2}\omega_p$:

$$\Delta = \omega_s - \tfrac{1}{2}\omega_p \tag{2}$$

Direct analysis of nonlinear equations such as (1) is a notoriously difficult task; nonetheless, by truncating the contribution of higher harmonics generated by the sinϕ term, an expression for G_s can be derived, which is a complicated function of all the parameters appearing in Eq. (1): $G_s = G_s(\beta_c, A, B, \omega_p, \omega_s)$. In the limit of zero detuning, one can show that parameter values exist for which G_s diverges, leading to an "infinite gain" condition.[21,22] (The possibility of divergence stems from the fact that the calculations are linearized about the $C=0$ solution of Eq. (1).) It was also shown that the infinite gain condition coincides with the condition for the onset of a period doubling bifurcation. This fact has proved to be a useful rule of thumb for locating high-gain regions of parameter space in experiments.[14]

From the dynamical systems perspective, the coincidence of a bifurcation point and very high parametric gain is a *general* phenomenon.[15] For example, any T-periodic system close to a period doubling bifurcation will amplify small signals of frequency ω_s near π/T (or $3\pi/T$, $5\pi/T$, etc.). Moreover, the scaling of the expected gain is universal: a linearized theory[15] shows that the gain depends on two parameters only,

$$G_s \propto (\mu^2 + \delta^2)^{-1} \tag{3}$$

where δ is proportional to the detuning Δ, and μ is the bifurcation parameter, with μ=0 at the bifurcation point. For example, if Eq. (1) suffers a period doubling when $A = A_*$ – holding all other parameters fixed – then one takes $\mu \propto (A - A_*)/A_*$. The proportionality constants will depend on the details of the governing equation: experimental determination of these constants is discussed in Sec. 6.

From Eq. (3), we recover the infinite gain result for zero detuning at the bifurcation point. Of course, this formula must break down when the gain gets too large (i.e. for μ too close to zero), at which point nonlinear effects must be included. The appropriate nonlinear theory has been developed for period doubling systems, and a variety of interesting phenomena are observed.[23] For example, one effect is a shift of the bifurcation point away from μ=0, the

magnitude of this shift growing as the two-thirds power of the signal amplitude. Moreover, the direction of the shift is always such as to *suppress* the onset of period doubling, an effect which has been observed in electrical analog simulations of Duffing's Equation,[23] a mechanical "bouncing ball" experiment,[20] measurements on the oscillations of a magnetorestrictive ribbon to alternating magnetic fields,[24] and in digital simulations of Eq. (1).[25]

In contrast to the result Eq. (3) of the linearized theory, the scaling of G_s in the nonlinear theory depends explicitly on the input signal strength ε, (ε is proportional to C in Eq. (1)). A simple expression analogous to Eq. (3) cannot be written down; however, all the results follow from studying the simple first order nonlinear differential equation

$$\dot{x} = \mu x - x^3 + \varepsilon \cos \Delta t \tag{4}$$

where $x(t)$ may be pictured as the (slowly varying) amplitude of the period doubled component of the response of the system. We postpone a more detailed explanation of the precise meaning and justification of this equation until the next section.

2.2 Four-Photon Mode[1]

In the 4-photon mode, gain is achieved for signal frequencies nearly equal to the pump frequency, $\omega_s \simeq \omega_p$. One major difference with the 3-photon mode is that the system is normally operated with no dc bias, i.e. $A = 0$ in Eq. (1), (although this is not a requirement). Just as in the 3-photon theory, a harmonic balance calculation leads to an expression for G_s as a complicated function of all the system parameters.[1] And again, for zero detuning Δ,

$$\Delta \equiv \omega_p - \omega_s \tag{5}$$

there is the possibility of infinite gain, the conditions for which coincide with a dynamical instability; this time a saddle-node bifurcation.[1,26]

One important complication in the behavior of the 4-photon mode is the presence of *hysteresis*. This led to the central theoretical notion of the Infinite Nonre-entrant Gain (ING) curve.[1] The term "re-entrant" means that G_s is a multiply-valued function of a control parameter, so that as this parameter is swept back and forth the gain displays hysteresis (Figure 2a), which is an undesirable trait even though there exist theoretical infinite gain points. However, by tuning a second parameter, it is possible to eliminate the hysteresis (Figure 2b). The cost of doing this is great: eliminating the hysteresis also eliminates the infinite gain points. Thus, one's best strategy is to find the crossover between these two behaviors – by tuning both parameters (say, B and ω_p in Eq. (1)) it is possible to operate near a point of infinite, nonre-entrant gain (Figure 2c).

From the point of view of dynamical systems theory, this behavior is easy to understand. The infinite gain condition corresponds to a saddle-node bifurcation, and saddle-node bifurcations are generically accompanied by hysteresis as a *single* parameter is varied (i.e. this is a codimension-one bifurcation). The idea of tuning *two* parameters, the second allowing the disappearance of a saddle-node, leads to the familiar "cusp" bifurcation.[27] Figure 3 illustrates the unfolding of the cusp bifurcation in parameter space: two curves of saddle-nodes intersect to form the cusp point. According to the general theory of amplification in bifurcating dynamical systems,[26] the saddle-node curves correspond to infinite-gain points (in a linearized theory, and at zero detuning). Operating just below the cusp point gives the ideal; sweeping just a single parameter yields large gain while avoiding the hysteresis.

Again, near such "infinite gain" points, the linearized theory breaks down. No nonlinear noise-free amplifier theory analogous to the one for period doubling has been developed. As described in the next section, the appropriate noise-free reduced equation for this case differs from Eq. (4), insofar as it requires two bifurcation parameters μ and ν (as expected from the discussion above).

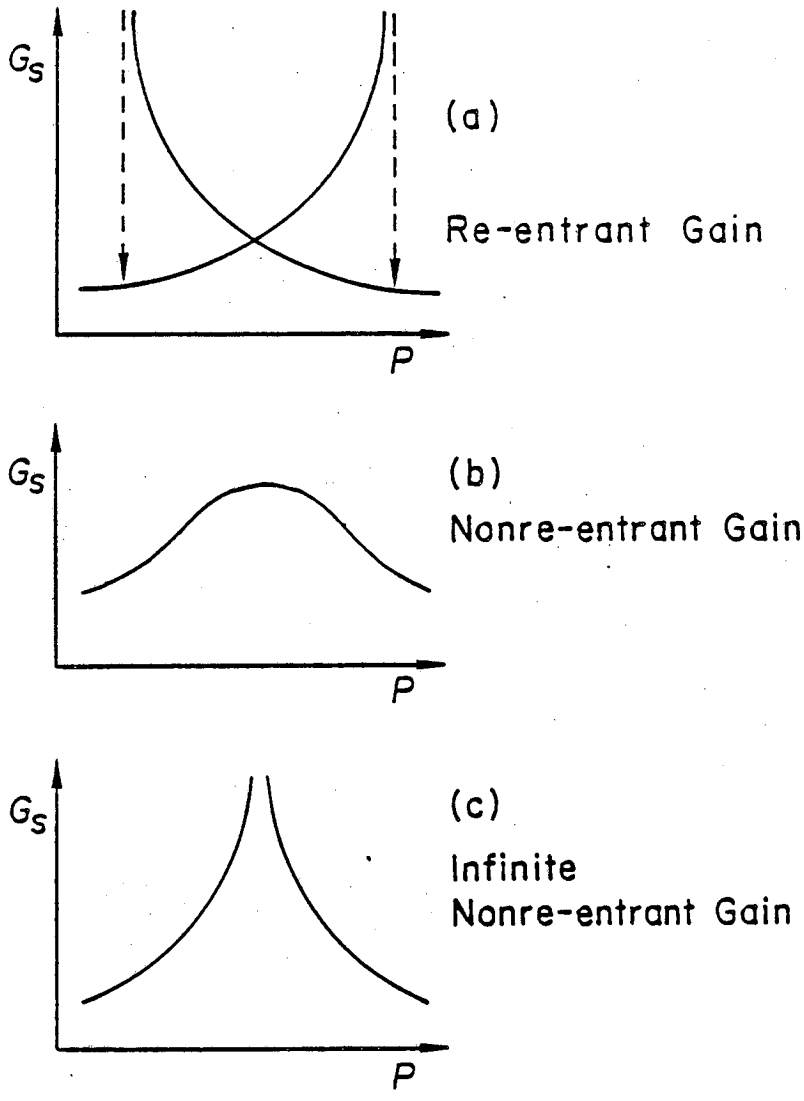

Figure 2. Sketch of signal gain versus control parameter P, illustrating the concept of "infinite nonre-entrant gain." The three different situations shown correspond to different values of a second control parameter. (a) Gain goes to infinity at saddle-node bifurcation points but hysteresis makes these operating points undesirable, since thermal noise may cause a transition to the coexisting low gain state. (b) Changing the second parameter eliminates the bifurcations for all values of P, now there is no hysteresis, but no infinite gain either. (c) Transition point from re-entrant to nonre-entrant – now we have infinite gain without hysteresis.

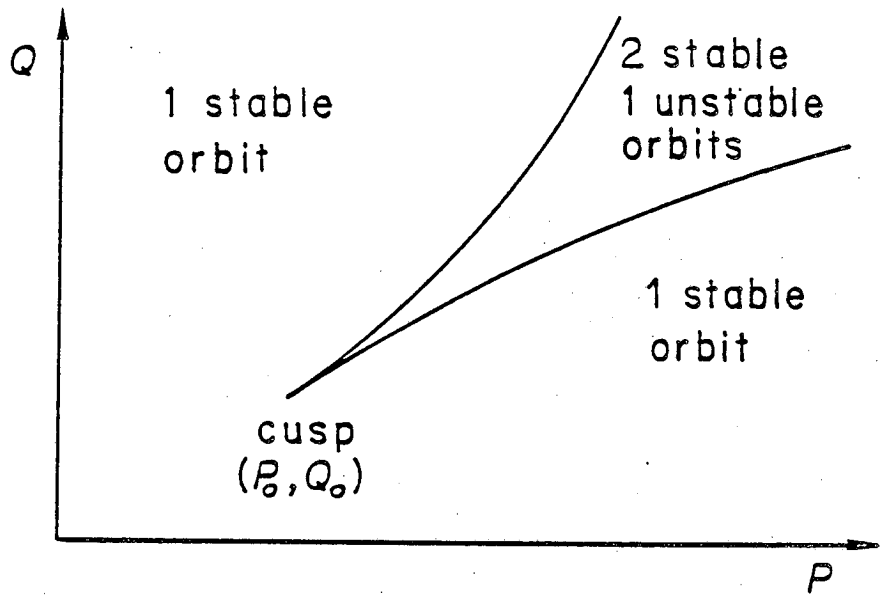

Figure 3. Typical Parameter space plot of a cusp bifurcation: two lines of saddle-node bifurcation points terminate at the cusp point (P_0, Q_0).

$$\dot{x} = \mu x + \nu - x^3 + \varepsilon\cos\Delta t \tag{6}$$

The cusp point occurs at $\mu=\nu=0$. We discuss how μ and ν can be related to experimental control parameters in Sec. 6.

Before moving on to the next section, we would like to point out two additional conclusions that follow readily from the present point of view, both concerning the unbiased Josephson junction parametric amplifier. The unbiased ($A=0$) case has always been identified with the 4-photon mode, but this really misses the essential point that *it is the kind of bifurcation* that matters and not the governing equation. Consequently, since it is known that Eq. (1) with $A=0$ can undergo period doubling bifurcations,[28] it is possible to operate the unbiased amplifier in the 3-photon mode (in the appropriate parameter regime). Moreover, the unbiased amplifier could be operated in yet a different mode, which is a 6-photon mode (with $\omega_s \simeq 2\omega_p$), a possibility which is discussed further in Sec. 7. The latter possibility is due to the occurrence of a

symmetry-breaking bifurcation[29, 11] in the unbiased dynamics, a class of instability distinct from either period doubling or cusp bifurcations.

3 THE REDUCED EQUATION

The results of this paper follow from the study of the reduced equations (4) and (6) in the presence of noise for the 3- and 4-photon modes of the Josephson junction parametric amplifiers. In this section it is explained why these equations predict the important dynamical behavior of the much more complex system (1), or indeed *any* parametric amplifier operated in these modes. The basic behavior of the reduced equations is introduced with emphasis on the effects of the signal and the noise. In the next section the results of computer simulations demonstrate that the reduced equations can provide detailed understanding of the noise rise.

Before we discuss the derivation of the reduced equation we will discuss its interpretation in terms of the full dynamical variable Φ. We assume for the moment that we are considering the period doubling case. For Eq. (1) the state of the full system (excluding the perturbation) is three dimensional; that is, $\Phi=(\phi,\dot{\phi},\theta_p)$ where θ_p is the phase of the pump. However, in general Φ may have any dimension greater than two. (We do assume here that the system is driven, that is, the fundamental frequency ω_p is fixed. The analysis for autonomous systems is slightly more complicated.) In this space we assume that the unperturbed system has a periodic orbit $\Phi_0(t)=\Phi_0(t+T)$, $T=2\pi/\omega_p$ that is near a period doubling bifurcation. We further assume that the period doubling bifurcation is *supercritical*, so that past the bifurcation point the orbit Φ_0 still exists but is now unstable, and nearby there is a stable period-two orbit. Because we are near the bifurcation point, the period doubled solution and any long lived transients are confined to the center manifold of the bifurcation.

Regardless of the dimension of the phase space of Φ, the dimension of the center manifold is two, parameterized by a phase θ_p and another variable x. Transients relax rapidly back to the center manifold, then slowly onto the stable solution. One can visualize the center manifold as a band centered on the orbit $\Phi_0(t)$ which, in the case of a period doubling bifurcation, undergoes a half twist between $\theta_p = 0$ and $\theta_p = 2\pi$. Thus it is in the form of a Mobius strip. A general orbit on this manifold can be expressed approximately as

$$\Phi(t) = \Phi_0(t) + x(t)\Phi_1(t) \tag{7}$$

where $x(t)$ is a slowly varying function describing deviations of the orbit from $\Phi_0(t)$, and $\Phi_1(t)$ is a symmetric function of period $2T$ satisfying $\Phi_1(t) = -\Phi_1(t+T)$. In the steady state x will be zero below the bifurcation and a non-zero constant above it. Due to the slow nature of dynamics on the center manifold, a small, near resonant perturbation may have a significant influence on $x(t)$, while having little ability to deviate the orbit off of the center manifold, so that Eq. (7) remains a good description of the behavior. Thus the dynamics may be well approximated by understanding the behavior of the reduced scalar variable $x(t)$. As will be shown below, when perturbed by a periodic signal near the resonant frequency $\omega_p/2$, the amplitude x responds as if driven at the difference frequency $\Delta = \omega_s - \omega_p/2$. Furthermore, when the system is randomly perturbed, it is the part of the noise spectrum near to $\omega_p/2$ which has the dominant effect on the variable x.

As introduced in the previous section, $x(t)$ satisfies the reduced equation

$$\dot{x} = \mu x - x^3 + \varepsilon\cos\delta t + \xi(t) \tag{8}$$

for the period doubling and symmetry breaking bifurcations, and

$$\dot{x} = \nu + \mu x - x^3 + \varepsilon\cos\delta t + \xi(t) \tag{9}$$

for the cusp bifurcation. Here μ and ν are bifurcation parameters, ε is proportional to the perturbation amplitude, δ is proportional to the detuning frequency Δ, and $\xi(t)$ is white noise of unit strength. Henceforth we will often work only with Eq. (9), since Eq. (8) may be considered a special case of it. The reduced variable may be directly observed in an experiment by making

a Poincare section in which the phase portrait is strobed every *two* cycles of the pump. The sequence of points will be closely spaced and can be approximated by a continuous function that is proportional to $x(t)$. Taking a Poincare section eliminates the phase variable θ_p and further reduces the dimension of the problem from two to one.

Qualitatively, what behavior might be expected for this system? From the theory of noisy precursors,[30,31] it is clear that just before and just after the bifurcation, the power spectrum will display a noise bump with a Lorentzian shape centered at $\omega_p/2$ (in the three photon case) for the full system and at $\omega=0$ in the reduced equation. As μ passes through 0, the bump will grow taller and become narrower. Likewise, the theory of parametric signal amplification in bifurcating systems[26] predicts a gain profile for coherent signals with a similar Lorentzian shape that grows and narrows as μ approaches 0 in the same way. Why then do we observe noise gain increasing faster than signal gain in the Josephson junction parametric amplifier? The above mentioned theories for noise and signals are based on a linearized analysis, valid in the limit of small signal and noise. For extremely small detuning δ – where signal gain is greatest – however, nonlinear effects cannot be ignored. Above $\mu=0$, there are two attracting basins, near $+\sqrt{\mu}$ and $-\sqrt{\mu}$. The barrier between them, at $x=0$ grows more formidable as μ gets larger. The presence of noise causes the system to switch aperiodically between these two basins – a process which can be approximated as telegraph noise. This fact is exploited in Sec. 5 to obtain analytic expressions for signal and noise gains. As μ is increased (or applied noise decreased) switching becomes less frequent confining the power of this noise driven square wave to lower frequencies, i.e., the noise bump grows narrower and taller approaching (but never exactly reaching) a delta function. The bifurcation point is not well defined in the presence of noise, since this normally corresponds to the point where the delta function appears. Surprisingly, the signal gain is not maximized at $\mu=0$ (as predicted by a linearized analysis), but continues to increase for $\mu>0$ for sufficiently small detuning. The signal is able to achieve high gain in this region by altering the transition rates for the noise driven switching – favoring the positive basin during

the positive phase of the signal and the negative basin during the negative phase. However, this mechanism is only effective when the switching rate is greater than or approximately equal to the detuning of the signal. As μ is increased, the switching rate decreases and the noise bump eventually becomes narrower than the detuning frequency, after which point signal gain falls off. The noise rise results from the fact that the height of the noise bump increases more rapidly than the signal gain. The signal gain for sufficiently small signals is linear, whereas the noise level at the signal frequency is a highly nonlinear function of the applied noise spectrum.

We now proceed with the derivation, again concentrating on the period doubling case. For no perturbation, $x(t)$ exhibits a symmetry breaking bifurcation when the actual dynamical variable exhibits period doubling. Thus it can be described by the normal form for a symmetry breaking bifurcation:

$$\dot{x} = \mu x - x^3 + \text{higher order terms} \tag{10}$$

where μ=0 is the bifurcation point. (One way to derive this is to start with the normal form for the period doubling of a mapping $x' = -(1+\mu)x + x^3 + O(x^5)$ and approximate the second iterate as a flow in the limit of small μ.) For sufficiently small signal, the effect of the signal is essentially linear. We can think of the perturbation between time t and time $t+2T$ as being made up of small sub-intervals, each of which is assigned an average value of the perturbation over that sub-interval. In the linear approximation each of these will have a linear influence on the value of x at time $t+2T$. The ratio between the influence and the perturbation need not be constant over the cycle but will in general be a function $g(t)$ of the phase of the subharmonic period. The Mobius strip nature of the center manifold requires that $g(t) = -g(t+T)$, for example $g(t)$ might be something like $\cos\omega_p t/2$. Thus, for an arbitrary (but small) perturbation $f(t)$,

$$\dot{x} = \mu x - x^3 + F(t) \tag{11}$$

where

$$F(t) = \frac{1}{2T}\int_{t-T}^{t+T} g(t')f(t')dt' \tag{12}$$

The function $g(t)$ can have Fourier components at frequencies $\omega_n = n\,\omega_p/2$, where n is odd, i.e.:

$$g(t) = \sum_{n\ odd} g_n e^{i\omega_n t} \tag{13}$$

Thus, only perturbations with frequencies near one of these Fourier components can produce a slowly varying $F(t)$, which can in turn have a significant influence on the dynamics of the slowly varying $x(t)$. For a periodic perturbation $C\cos(\omega_n + \Delta)t$ detuned by an amount Δ, we find from Eq. (12) that

$$F(t) = C\,|\,g_n\,|\cos[\Delta t - \mathrm{Arg}(g_n)] \tag{14}$$

For the case where $f(t)$ is noise, we can compute the spectral density of $F(t)$. We define the power spectral density $F(\omega)$ as

$$2\pi F(\omega) = \lim_{t\to\infty}\frac{1}{t} < |\int dt e^{i\omega t} F(t)|^2 > \tag{15}$$

where the brackets <> indicate an ensemble average. Inserting the expression for $F(t)$, Eq. (12), one can obtain (we assume here that $F(t)$ varies continuously rather than discretely to simplify the calculation):

$$2\pi F(\omega) = \lim_{t\to\infty}\frac{1}{t} < |\frac{1}{2T}\int_{-T}^{T} dt' e^{-i\omega t'}\int_{t'}^{t+t'} dt'' \sum_n e^{i(\omega+\omega_n)t''} g_n f(t'')|^2 > \tag{16}$$

The limits on the t'' integral can be changed to 0 to t for sufficiently large t (t' becomes insignificant). For $\omega \ll 1/T$ we can approximate the t' integral as unity. This yields the expression

$$2\pi F(\omega) = \lim_{t\to\infty}\frac{1}{t} < |\sum_n F_n(\omega)|^2 > \tag{17}$$

where

$$F_n(\omega) = g_n \int e^{i(\omega_n+\omega)t'} f(t')dt'$$

Assuming the F_n's to be uncorrelated, we can express $F(\omega)$ in terms of $f(\omega)$, the power spectral density of the applied noise:

$$F(\omega) = \sum_n |\,g_n\,|^2 f(\omega_n+\omega) \tag{18}$$

Since only low frequencies can effect the slowly varying $x(t)$, we can approximate $F(\omega)$ as

white noise with spectral density equal to $F(0)$ in Eq. (18). When signal and noise are both applied, the reduced equation takes the form:

$$\dot{x} = \mu x - x^3 + \varepsilon_s \cos(\Delta t + \theta) + \varepsilon_n \xi(t) \tag{19}$$

where ε_s is proportional to the signal amplitude, ε_n is proportional to the noise amplitude, and $\xi(t)$ is white noise with unit delta autocorrelation.

Proper choice of time origin can eliminate the phase factor θ. We wish to consider the case where the noise is much stronger than the signal, as it is in this limit where the noise rise becomes a severe problem in the experimental situation. We therefore perform a rescaling of the equation to set ε_n to unity:

$$\frac{dx_1}{dt_1} = \mu_1 x_1 - x_1^3 + \varepsilon \cos\delta t_1 + \xi(t_1) \tag{20}$$

where $\varepsilon_s = \varepsilon_n^{3/2}\varepsilon$, $x = x_1\sqrt{\varepsilon_n}$, $\mu = \mu_1\varepsilon_n$, $t = t_1/\varepsilon_n$, and $\Delta = \delta\varepsilon_n$. Note that $\xi(t_1/\varepsilon_n)$ has the same spectral density as $\sqrt{\varepsilon_n}\xi(t_1)$. Equation (20) is the fundamental equation we wish to study. In the interest of simplifying the notation, the subscript 1 will not be used explicitly throughout the rest of the paper. One may assume that the rescaled variables are used unless stated otherwise. Except in special cases[20] it is quite difficult to obtain analytic expressions for the parameters in Eq. (20) in terms of those in the full equations of motion. However, one may always estimate these relationships in linear approximation from numerical or experimental data as discussed in Sec. 6.

Extension of these results to the cusp and symmetry breaking bifurcations is quite simple – we just use the appropriate normal form in place of Eq. (10). For the cusp the normal form is

$$\dot{x} = \mu x + \nu - x^3 + \text{higher order terms} \tag{21}$$

and the result with perturbations is

$$\frac{dx_1}{dt_1} = \mu_1 x_1 + \nu_1 - x_1^3 + \varepsilon \cos\delta t_1 + \xi(t_1) \tag{22}$$

where $\nu = \nu_1\varepsilon_n^{3/2}$. The interpretation of Eq. (7) is now slightly different – both Φ_0 and Φ_1 have

period T. If Φ_0 is a symmetrical orbit then Φ_1 will in general also be – i.e.: $\Phi_0(t) = -\Phi_0(t+T/2)$ and $\Phi_1(t) = -\Phi_1(t+T/2)$. This case occurs in the unbiased Josephson junction and it represents the breaking up of one symmetrical orbit in two coexisting symmetrical orbits. Asymmetrical cases are also possible however. The symmetry breaking bifurcation has the same normal form as the period doubling bifurcation, Eq. (10). Now, however, Φ_0 in Eq. (7) is a symmetrical orbit ($\Phi_0(t) = -\Phi_0(t+T/2)$) and $\Phi_1(t)$ represents the asymmetric part of the orbit ($\Phi_1(t) = \Phi_1(t+T/2)$).

4 SIMULATIONS

Three kinds of simulations were performed in order to study the noise rise phenomenon and determine how it is affected by the various parameters in the equation. First, the full pendulum equation (1) was integrated on an analog computer. An analog, as opposed to digital, simulation has the advantages of high speed and tremendous ease in varying parameters. The basic phenomenon, noise gain increasing faster (with increasing μ) than signal gain, was observed and the importance of using a very small detuning frequency δ was quite clear. In a second set of simulations, the reduced equations (8) and (9) were studied on an analog computer. This provided clear evidence that these simpler equations can capture the important features of the noise rise. Finally, extensive digital simulations of the reduced equations were performed for various values of μ and δ. These again confirmed the presence of the noise rise in the reduced equations and suggest a number of predictions, presented in Sec. 6, about how real systems such as the Josephson junction parametric amplifier will perform.

4.1 Analog Simulations

To reproduce the noise rise in the pendulum equation (1), an analog computer was constructed using low offset, low drift operational amplifiers and a Josephson junction box to implement the $\sin\phi$ nonlinearity. A 33 bit digital feedback shift register was used to generate noise with adequate low and high frequency characteristics. To observe a significant noise rise, a sinusoidal signal of very small detuning Δ and small amplitude C was required. Thus the signal generators for ω_p and ω_s were selected to have especially stable signals. To place the analog computer in the 3-photon mode, the parameters were varied to put the system near a period doubling bifurcation and as far as possible from any other bifurcations.

Figure 4 shows results taken with a spectrum analyser monitoring the variable $\dot{\phi}$. With a

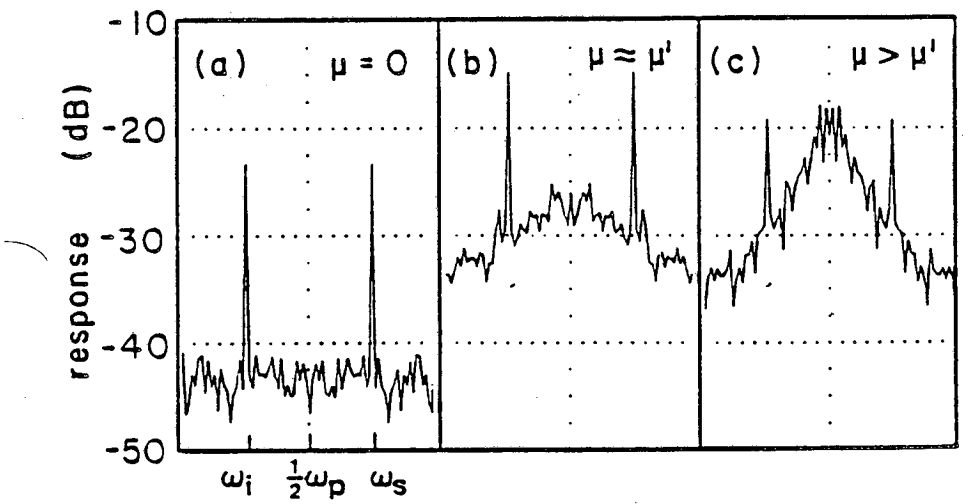

Figure 4. Power spectra from analog simulation of Eq. (1) with noise added for the 3-photon case with $\Delta = 5\times10^{-4}\omega_p$. (a) $\mu=0$; this is the period doubling bifurcation point in the absence of noise. (b) $\mu=\mu'$; this is the point of maximum signal gain. The noise bump is starting to move inside the detuning frequency. Note the diminished signal to noise ratio. (c) $\mu>\mu'$; signal gain falls off, noise rise continues.

detuning of 0.1% from $\frac{1}{2}\omega_p$, as the parameter A was increased the signal gain G_s was seen to increase by 8 dB but the signal-to-noise ratio fell from 20 dB to 14 dB. Similar results have been published using actual Josephson junction amplifiers.[6]

The 4-photon mode was studied by tuning the analog computer near a cusp bifurcation, and a similar noise rise was observed there. In Figure 5 the noise rise – the ratio of G_n (at ω_s) to G_s – is plotted against the signal gain, as the parameters are varied. The curve shown corresponds approximately to varying μ with ν set to zero (see Eq. (9)). When μ is positive one enters the "switching regime" in which noise induces a hopping between two coexisting attractors. When ν is zero, the equation is symmetrical and hence equal time (on the average) is

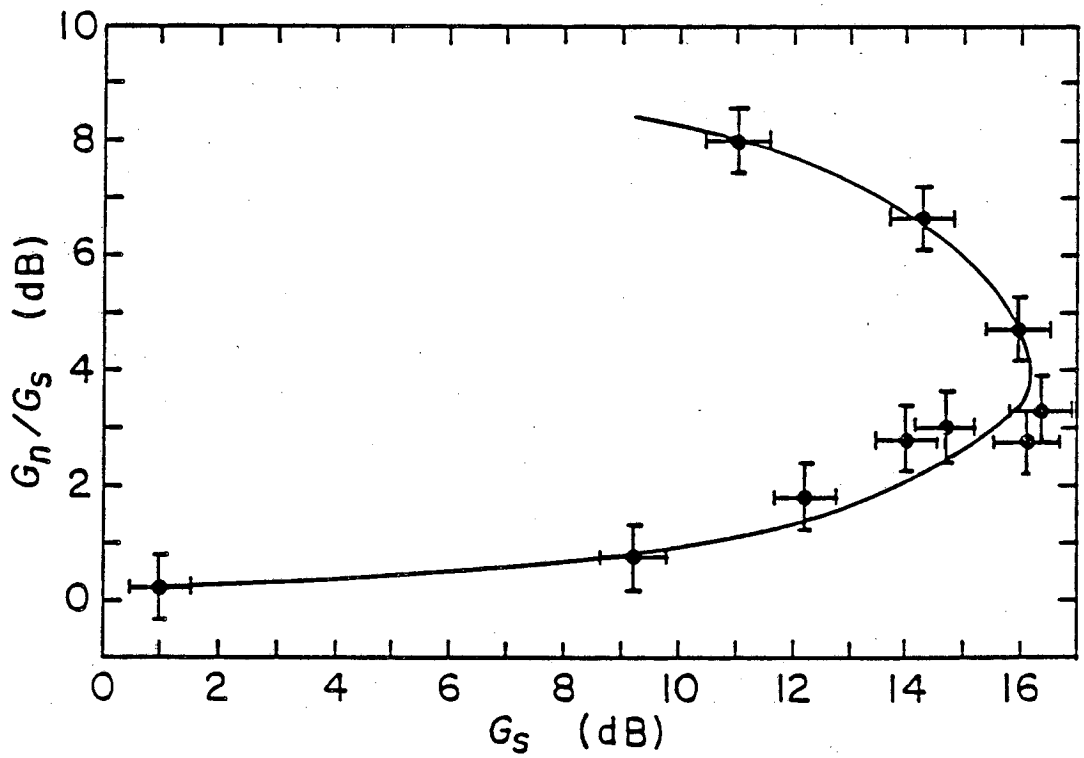

Figure 5. Signal gain vs. noise rise from analog simulation of Eq. (1) with noise added for the 4-photon case. Note that the noise rise continues as we go beyond the point of maximum signal gain. The detuning for this data is $\Delta=1.25\times10^{-3}\omega_p$.

spent in each of the two states. We use this fact to obtain the data in the simulations – we adjust one parameter to some new value and then a second parameter is adjusted to symmetrize the hopping. Signal and noise gains are recorded at this parameter setting and then the process is repeated to obtain a sequence of data points (see Figure 5). In the linear approximation, G_n/G_s would be exactly unity for all values of G_s. Instead, along the line $\nu=0$ the ratio G_n/G_s gradually increases and continues to do so even after the signal gain has begun to fall off.

The reduced equation (8) for the 3-photon mode was integrated with a similar analog computer. Without a pump signal and with just a cubic nonlinearity, the first order reduced equation is much simpler to instrument that the full pendulum equation Eq. (1). However, the need for low drift elements continues, and for $\nu=0$ it is especially important to maintain low offsets. Figure 6 shows the switching behavior which occurs for positive μ. In this regime the

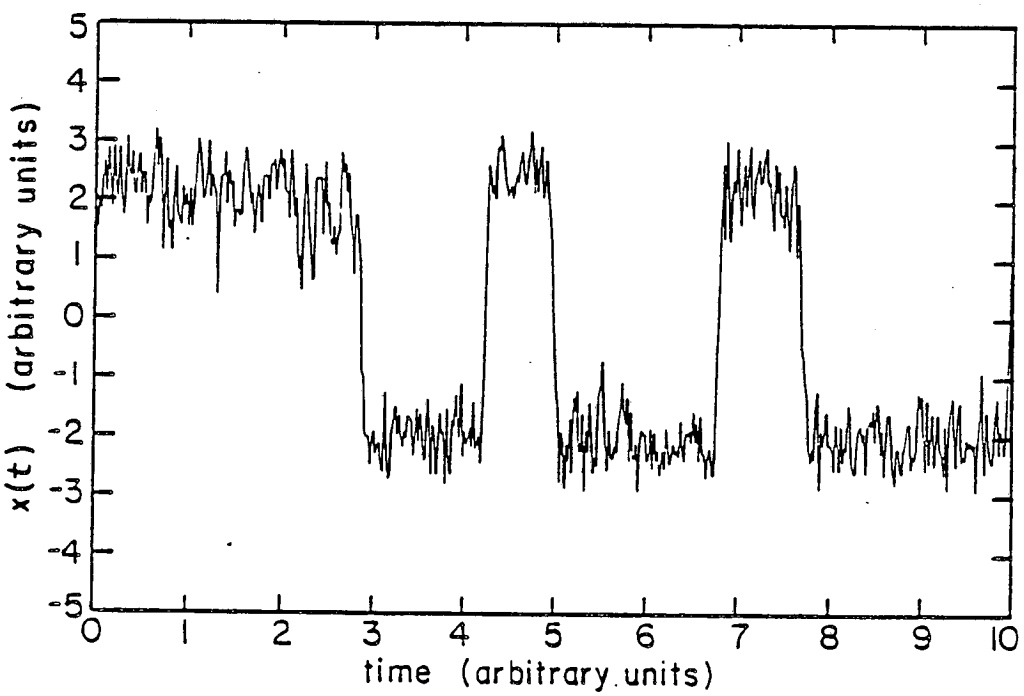

Figure 6. Behavior of $x(t)$ in the "switching regime" $\mu>0$ for the reduced Eq. (8).

dynamics can be approximated as a telegraph process (random switching between fixed levels) and analytic results may be obtained (see Sec. 5). In Figure 7 we show the power spectrum of $x(t)$ for three values of μ. Again a noise rise is clearly apparent as μ is increased. The effect is somewhat larger than in Figure 4 because the effective detuning δ is smaller in this case.

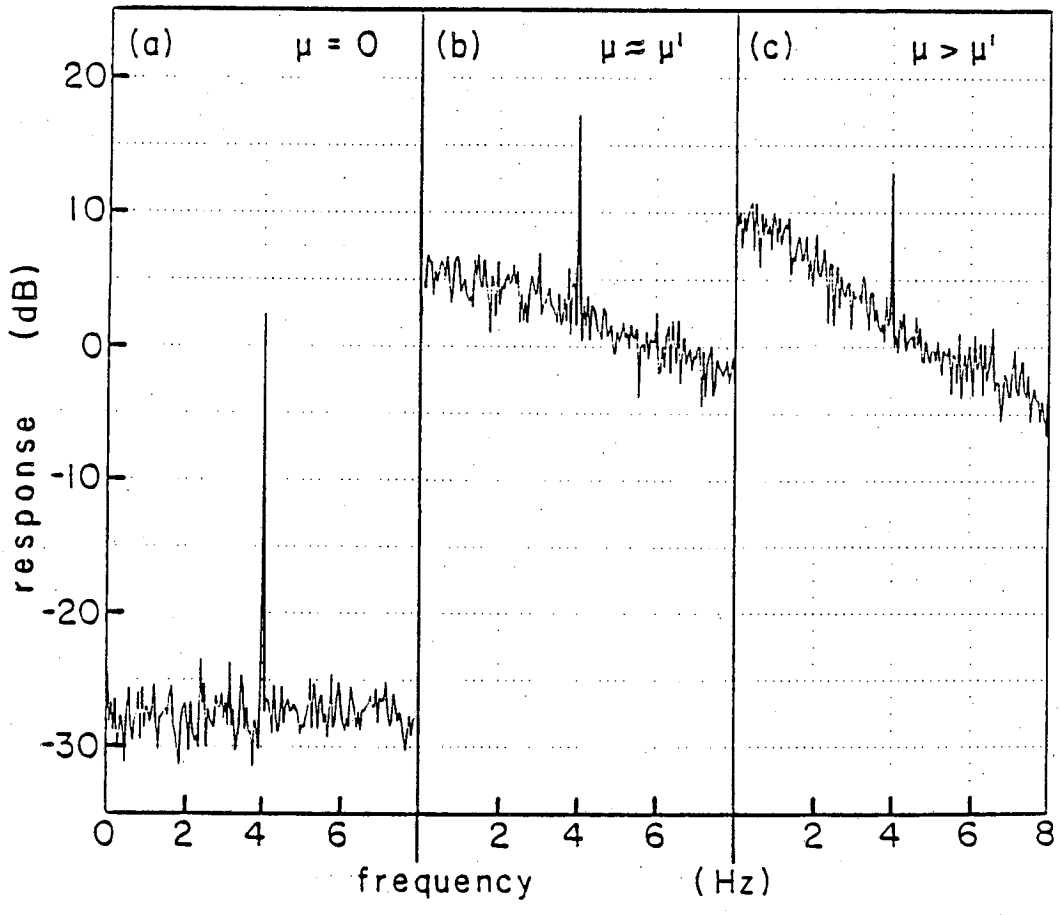

Figure 7. Power spectra from analog simultation of the reduced Eq. (8). Zero frequency here corresponds to ω_p for the dynamical variable (see Fig. 4). Noise-rise is greater than in Fig. 4 because the effective detuning is smaller here. (a) μ=0; this is the period doubling bifurcation point in the absence of noise. (b) $\mu=\mu'$; this is the point of maximum signal gain. The noise bump is starting to move inside the detuning frequency. Signal to noise ratio has fallen from 30dB to 15dB. (c) $\mu>\mu'$; signal gain falls off, noise rise continues.

4.2 Digital Simulations

While digital integration is considerably slower than analog, it provides far greater precision and flexibility for determining the behavior of the reduced equations. Happily, our particular problem has certain characteristics and symmetries which allow significant improvement in speed over a standard approach. The details of the method used are discussed in the Appendix. The goal is to estimate the signal and noise gains as functions of the parameters μ and δ. For sufficiently small signal amplitude ε, we expect the quantities G_n and G_s to be essentially independent of ε. This was verified in the simulations.

In Figure 8 a, b and c we plot G_n (at the signal frequency), G_s, and noise rise, all as functions of the bifurcation parameter μ for several values of the (rescaled) detuning δ. As can be seen, for finite detuning G_s reaches a maximum at some value $\mu=\mu'$. G_n continues to increase however, reaching its maximum beyond μ'. While the G_n and G_s are both sensitive functions of δ, their ratio is insensitive to δ. A significant difference (from $\delta=0$) shows up only when well beyond the μ of maximum G_s. In Figure 9 we plot noise rise versus G_s for several values of δ. These curves show that the noise rise continues to increase as we pass the point of maximum G_s. We also see how the maximum G_s increases as $|\delta|$ is decreased, but so does the noise rise at the point of maximum G_s. The bandwidth of the G_s decreases very rapidly with increasing μ. This effect is shown in Figure 10 where we plot G_s versus detuning for several values of μ.

In summary, the simulations verify our expectation that the reduced equations capture the important dynamical properties responsible for the noise rise in the full dynamical system Eq. (1). Of course, the validity of the reduced equations is much wider, applying in the high-gain limit of all other weak-signal parametric amplifiers. Which reduced equation is appropriate depends solely on the bifurcation involved, i.e. solely on the "mode" of operation. In this sense, these dynamical properties are *universal*, so that the results of the simulations can be

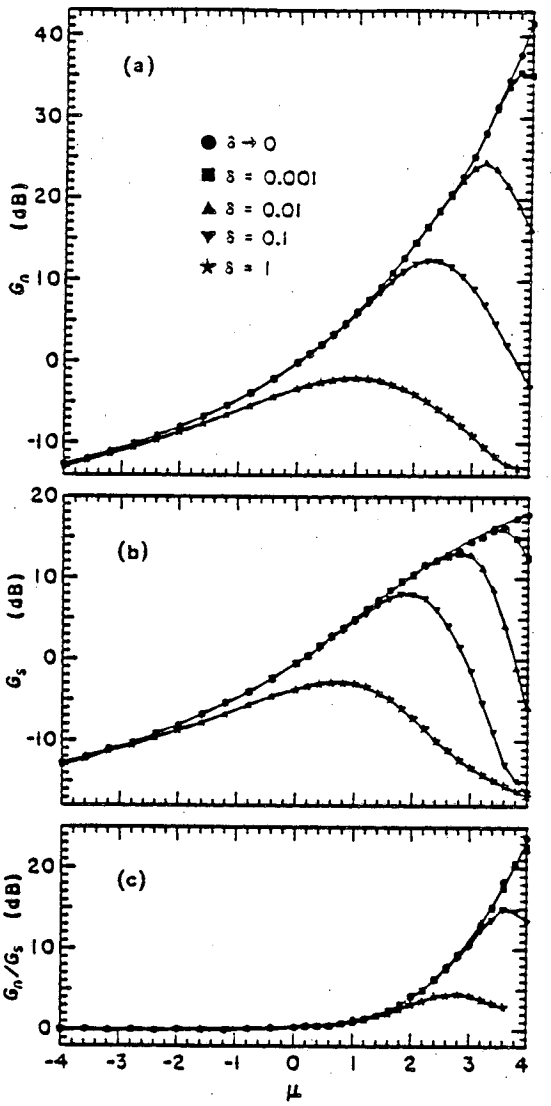

Figure 8. Numerically generated data from the reduced equation Eq. (8). (a) Noise gain G_n vs. bifurcation parameter μ. (b) Signal gain G_s vs. μ. (c) Noise-rise G_n/G_s vs. μ. In (a) and (b) the highest curve corresponds to the limit of zero detuning ($\delta = 0$), with successively lower curves following the sequence: $\delta = 0.001, 0.01, 0.1, 1$. In (c) the cases of $\delta = 0, 0.001$, and 0.01, are indistinguishable and form the highest curve shown, with successively lower curves in the sequence: $\delta = 0.1, 1$.

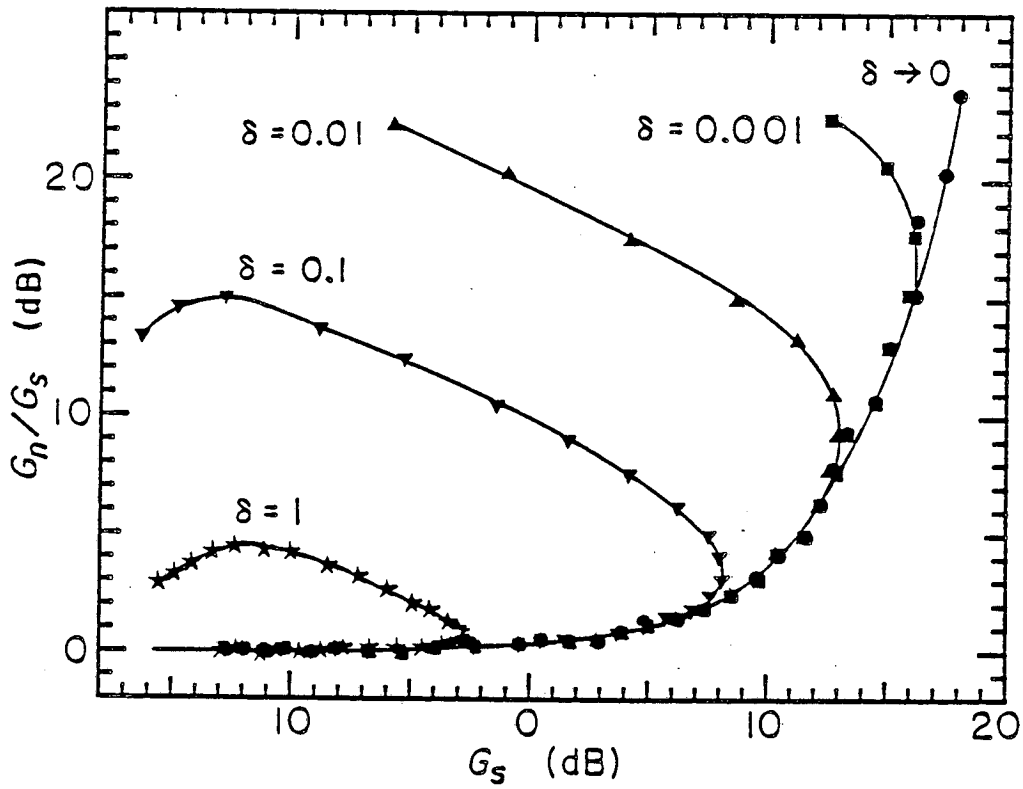

Figure 9. Numerical data showing noise rise G_n/G_s as a function of G_s. Comparing with the analog data in Fig. 5 we would estimate that this previous result corresponds approximately to δ=0.1.

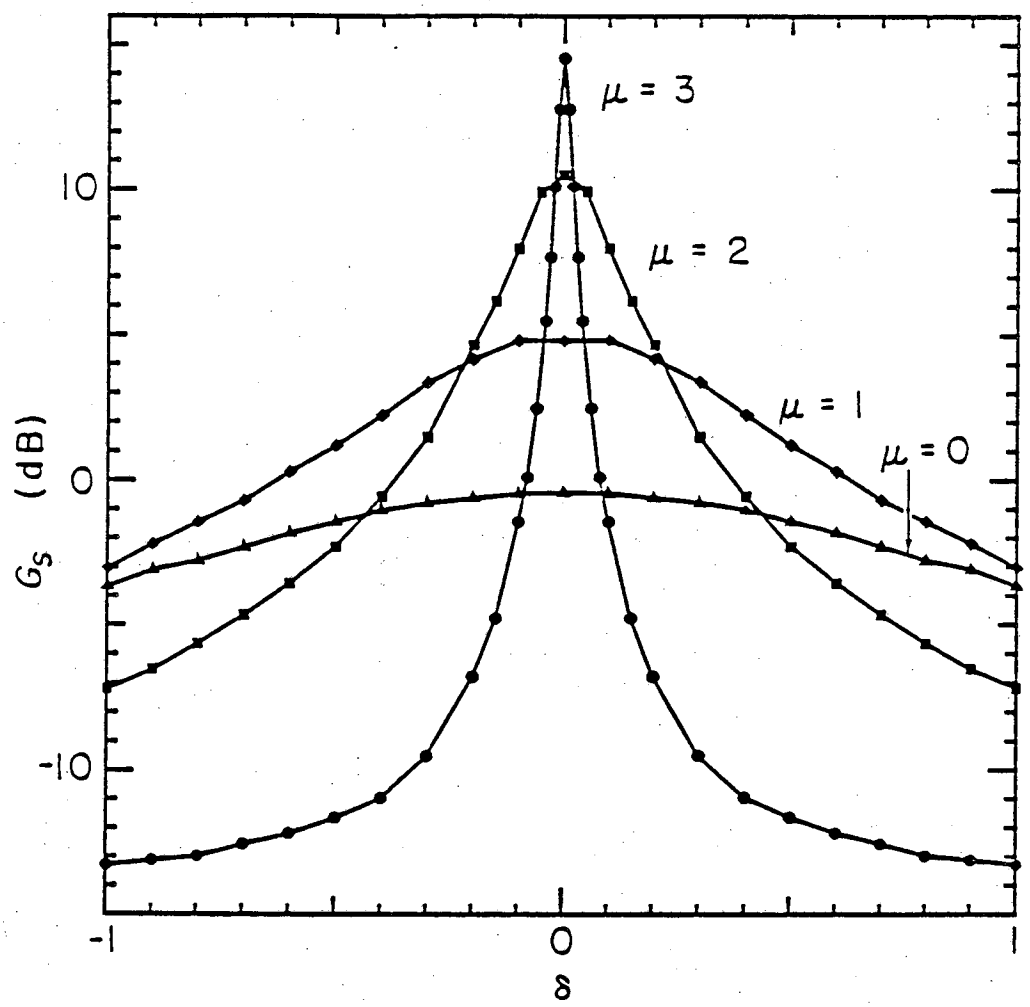

Figure 10. Numerical data showing signal gain as a function of detuning for several values of the bifurcation parameter μ. Note that the bandwidth decreases very rapidly.

used to make *quantitative* predictions about the behavior of parametric amplifiers in this regime. We discuss many such predictions in Sec. 6.

5 ANALYTICAL RESULTS

Using the tools of bifurcation theory, we were able to reduce the full phase space dynamics to a study of the one dimensional center-manifold dynamics. As disarmingly simple as the reduced equations appear, their analysis requires computer simulations near the bifurcation point $\mu=0$. However, there are two limiting regimes where one *can* derive analytic results: for sufficiently negative μ a linearized analysis is possible, and for sufficiently positive μ the dynamics is well-approximated by a switching process.

In the linear regime, the cubic term may be ignored due to the low amplitude of the response. The resulting analysis yields identical signal and noise power gains at the signal frequency,

$$G = (\mu^2+\delta^2)^{-1}, \tag{23}$$

and thus there is no noise rise. As one increases μ toward $\mu=0$, the linear theory breaks down – as it must, since G_n and G_s cannot go to infinity (for $\delta=0$) as predicted by the linear theory – and one must rely on numerical analysis or simulations like those of Sec. 4.

Upon increasing μ to sufficiently positive values, the system enters the switching regime where one can again make analytic headway: the remainder of this section is devoted toward this end. Before launching into the detailed calculations, we give a brief description of the dynamics in this regime and an overview of the results.

In the switching regime, the undriven system ($\varepsilon=0$, $\xi=0$) has two stable equilibria x_+ and x_-. In the 3-photon mode, these correspond to different branches of the same phase-space attractor, while in the 4-photon mode (and the 6-photon mode – see Sec. 7) these correspond to two distinct attractors. The addition of a noise term induces switching between x_+ and x_-, as was shown in Figure 6. For sufficiently large μ, this behavior is well approximated by a telegraph process,[32,33] i.e. random switching between two fixed levels. The effect of the small sig-

nal ($\varepsilon \neq 0$) is to periodically alter the escape rates from the two equilibria; the x_+ state being favored while the signal is positive, the x_- state while negative.

To obtain analytic results for the switching regime, we first calculate the mean lifetimes τ_+ and τ_- for the x_+ and x_- states respectively by solving the Fokker-Plank equation in the limit of low diffusion between states. We find

$$\frac{1}{\tau_\pm} = \frac{1}{2\pi}\sqrt{2\mu^2 \pm 3\sqrt{\mu}S}\,\exp(-\tfrac{1}{2}\mu^2 \mp 2\sqrt{\mu}S) \tag{24}$$

where $S = v + \varepsilon\cos\delta t$. This result compares quite well with numerical simulations: for $\mu=3$ and $\delta=0$ we obtain $\tau=133.3$ from Eq. (24) and 132.0 from simulations. The noise gain is then determined from the autocorrelation function of the associated telegraph process, with result

$$G_n = \frac{\pi\sqrt{2}e^{\mu^2/2}}{\cosh(2v\sqrt{\mu})}\left[1 + \frac{\omega\pi^2}{2\mu^2}e^{\mu^2}\cosh^2(2v\sqrt{\mu})\right]^{-1} \tag{25}$$

This is compared with numerical data in Fig. 11(a). Agreement is good above $\mu=2$ with errors of 0.5 dB or less (for small detuning).

The signal gain receives its main contribution in the switching regime from the ability of the (slowly varying) signal to slightly alter $\tau_\pm$. This yields the result:

$$G_s = \frac{4\mu^2}{\cosh^4(2v\sqrt{\mu})}\left[1 + \frac{\delta^2\pi^2}{2\mu^2}e^{\mu^2}\cosh^2(2v\sqrt{\mu})\right]^{-1} \tag{26}$$

This result is compared with numerical data in Fig. 11(b). Here the convergence is somewhat slower, the numerical result being 1.5 dB low at $\mu=2$, but within 0.5 dB at $\mu=4$. We define the noise rise NR as the ratio G_n/G_s evaluated at $\omega=\delta$:

$$NR = \pi e^{\mu^2/2}\cosh^3(2v\sqrt{\mu})/2\sqrt{2}\mu^2 \tag{27}$$

Note that the noise rise is independent of δ. This behavior is also exhibited by the numerical data as shown in Fig. 11(c). Deviations from this rule occur only after μ is well past the point of maximum G_s. It is worthwhile to consider simplified versions of Eqs. (25) - (27) which result in certain special cases of interest. For $v=0$ they reduce to:

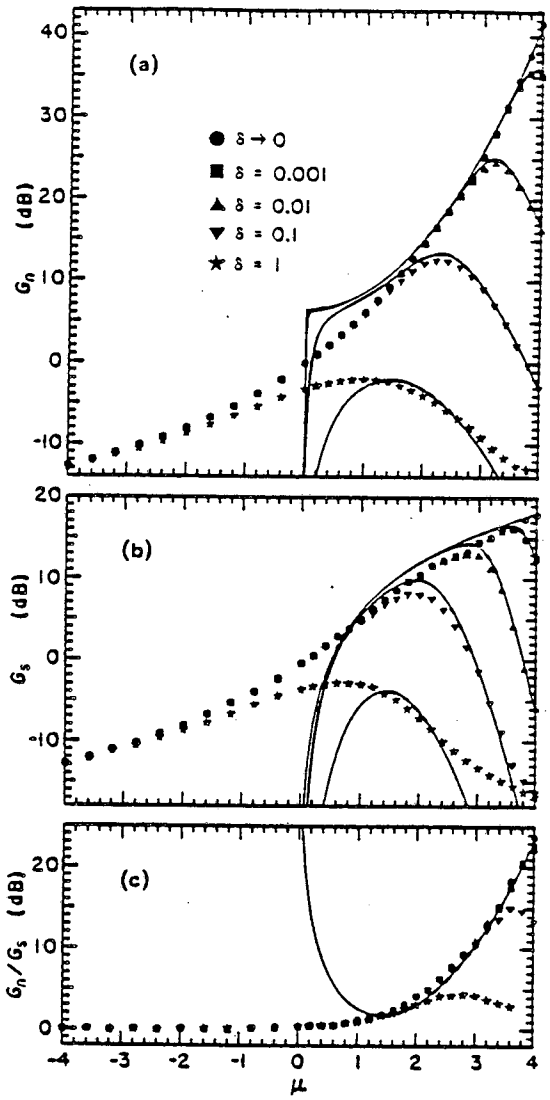

Figure 11. Comparison of the asymptotically correct theory (solid lines) with the data generated numerically from the reduced equation.

$$G_s = 4\mu^2 / (1 + \delta^2\pi^2 e^{\mu^2}/2\mu^2) \tag{28}$$

$$G_n = \pi\sqrt{2}e^{\mu^2/2} / (1 + (\omega^2\pi^2 e^{\mu^2}/2\mu^2)) \tag{29}$$

$$NR = \pi e^{\mu^2/2} / 2\sqrt{2}\mu^2 \tag{30}$$

These equations apply to the period doubling (3-photon) and symmetry breaking (6-photon)

cases which do not require the parameter ν. It also turns out that it is preferable to operate the cusp (4-photon) case with ν=0. For non-zero ν the behavior is always less desirable – the signal gain decreases while the noise rise increases, as can be seen in Eqs (26) and (27).

If we consider the limit of δ and ω approaching zero (still with ν=0) we obtain the particularly simple results:

$$G_s = 4\mu^2 \tag{31}$$

$$G_n = \pi\sqrt{2}e^{\mu^2/2} \tag{32}$$

Thus both G_s and G_n increase monotonically with μ, but with G_n increasing much more rapidly. The bandwidth over which this level of gain may be achieved is easily seen to be

$$BW = \frac{2\sqrt{2}}{\pi}\mu e^{-\mu^2/2} \tag{33}$$

Thus the gain-bandwidth product (for signal gain) is not a constant in the switching regime, but rather it decreases exponentially with increasing μ. This behavior can be seen quite dramatically in the numerical results shown previously in Fig. 10. In all of the results presented here one can explicitly include the effect of input noise amplitude ε_n. This is accomplished by reversing the transformation used in Eqs. (20) and (22). That is, replace μ with μ/ε_n, ν with $\nu/\varepsilon_n^{3/2}$, δ with δ/ε_n, ω with ω/ε_n, G_s with $\varepsilon_n^2 G_s$, G_n with $\varepsilon_n^2 G_n$, NR with NR, and BW with BW/ε_n. Thus, for example, Eq. (31) becomes $G_s = 4\mu^2/\varepsilon_n^4$, which shows that a slight reduction in noise level can result in a dramatic improvement in signal gain.

In the remainder of this section we present a derivation of $\tau_\pm$ and then, using this result, we determine G_n and G_s. We start with the reduced equation for the cusp or 4-photon case since it is the most general:

$$\dot{x} = \nu + \mu x - x^3 + \varepsilon\cos\delta t + \xi(t) \tag{34}$$

This starting equation can be rewritten as

$$\dot{x} = -\partial_x \psi(x,t) + \xi(t) \tag{35}$$

which is a Langevin equation for a heavily damped particle moving in the slowly-modulated

quartic potential

$$\psi(x,t) = -\tfrac{1}{2}\mu x^2 + \tfrac{1}{4}x^4 - Sx \tag{36}$$

where $S = v + \varepsilon\cos\delta t$. In the present case, ψ is a double-well potential, with minima at x_- and x_+ separated by a maximum at x_0 (see Fig. 12). As before, we take $\xi(t)$ to be delta-correlated noise with unit strength,

$$\langle \xi(t)\xi(t') \rangle = \delta(t-t') \tag{37}$$

The Fokker-Plank equation corresponding to Eq. (35) is

$$\partial_t W = -\partial_x j \tag{38}$$

where W is the probability density and j is the probability current

$$j = -W\partial_x \psi - \tfrac{1}{2}\partial_x W \tag{39}$$

For j constant, we can integrate this between the two minima to get an explicit expression for j

$$j = \frac{\tfrac{1}{2} W \exp(2\psi) \Big|_{x_+}^{x_-}}{\int_{x_+}^{x_-} \exp(2\psi)dx} \tag{40}$$

If we assume that the system starts near the state x_-, with initially no probability of being at x_+ (i.e.: $W(x_+)=0$), we can interpret j as $1/\tau_-$ where τ_- is the mean lifetime of the state x_-.

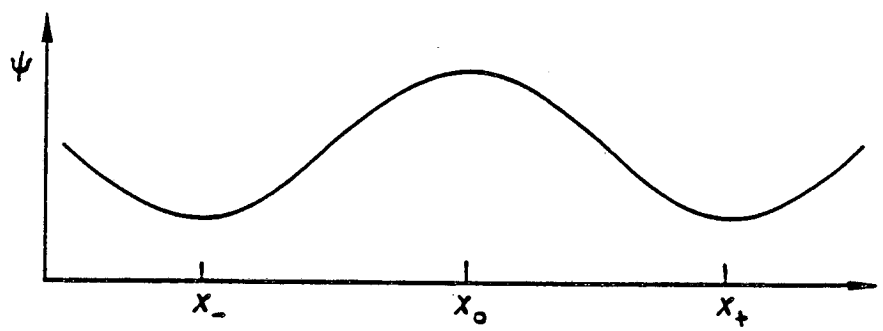

Figure 12. The potential ψ vs. x, showing two wells separated by a barrier.

For x near x_-, we can approximate Eq. (39) as

$$j = -(x_- - x)k_- W - \tfrac{1}{2}\partial_x W \tag{41}$$

where k_- is the curvature of $\psi(x_-)$. Since we assume j is very small (high barrier limit), we can solve immediately for W

$$W(x) = \text{const} \cdot \exp(-k_-(x-x_-)^2) \tag{42}$$

Proper normalization of $W(x)$ implies that

$$W(x_-) = \sqrt{k_-/\pi} \tag{43}$$

The integral in Eq. (40) receives its dominant contribution near x_0 where $\psi(x) \approx \frac{1}{2}k_0(x-x_0)^2$. Thus,

$$\int_{x_-}^{x_+} \exp(2\psi)dx = \sqrt{\pi/-k_0} \tag{44}$$

Combining Eqs. (43) and (44), with k_0, k_- determined from Eq. (36), we can evaluate Eq. (40) for j:

$$j = \frac{1}{\tau_-} = \frac{1}{2\pi}\sqrt{2\mu^2 - 3\sqrt{\mu S}}\,\exp[-\tfrac{1}{2}\mu^2 + 2\sqrt{\mu S}\,] \tag{45}$$

Similarly, we can write

$$\frac{1}{\tau_+} = \frac{1}{2\pi}\sqrt{2\mu^2 + 3\sqrt{\mu S}}\,\exp[-\tfrac{1}{2}\mu^2 - 2\sqrt{\mu S}\,] \tag{46}$$

which is just Eq. (45) with the sign of S changed. For large μ, the prefactor can be approximated by $\mu\sqrt{2}$, so that

$$\frac{1}{\tau_\pm} = \frac{\mu}{\pi\sqrt{2}}\exp[-\tfrac{1}{2}\mu^2 \mp 2\sqrt{\mu S}\,] \tag{47}$$

where $S = \nu + \epsilon\cos\delta t$.

Although S is assumed small, the S dependence of τ is crucial to the determination of signal gain. This is because the primary contribution to signal gain in the switching regime comes from the ability of the signal to slightly alter the transition probabilities, favoring the positive state while the signal is positive and favoring the negative state while the signal is negative.

We now calculate expressions for the noise and signal gains. Let n_+ and n_- be the fractions of the ensemble in the states x_+ and x_- respectively, so that $n_+ + n_- = 1$. If the offset term S is small, these states have constant amplitudes $x_\pm = \pm\sqrt{\mu}$ in the telegraph noise approximation ($\mu \gg 1$). Thus the ensemble average response is

$$\langle x \rangle = \sqrt{\mu}(n_+ - n_-) \tag{48}$$

The rate of change of n_+ obeys

$$\dot{n}_+ = \frac{n_-}{\tau_-} - \frac{n_+}{\tau_+} \tag{49}$$

so that

$$\langle \dot{x} \rangle = -\left[\frac{1}{\tau_-} + \frac{1}{\tau_+}\right]\langle x \rangle + \left[\frac{1}{\tau_-} - \frac{1}{\tau_+}\right]\sqrt{\mu} \tag{50}$$

For convenience, we assume a complex representation for the applied signal, i.e. we use $\varepsilon e^{i\delta t}$ instead of $\varepsilon\cos\delta t$. For sufficiently small ε we have

$$\frac{1}{\tau_-} + \frac{1}{\tau_+} = a_1 + \varepsilon b_1 e^{i\delta t} \tag{51}$$

$$\sqrt{\mu}\left[\frac{1}{\tau_-} - \frac{1}{\tau_+}\right] = a_0 + \varepsilon b_0 e^{i\delta t} \tag{52}$$

where the coefficients a_0, a_1, b_0, b_1 follow from expanding Eq. (47) to first order in ε,

$$\begin{bmatrix} a_1 \\ a_0 \\ b_1 \\ b_0 \end{bmatrix} = \frac{\mu\sqrt{2}}{\pi} e^{-\mu^2/2} \begin{bmatrix} \cosh(2v\sqrt{\mu}) \\ \sqrt{\mu}\sinh(2v\sqrt{\mu}) \\ 2\sqrt{\mu}\sinh(2v\sqrt{\mu}) \\ 2\mu\cosh(2v\sqrt{\mu}) \end{bmatrix} \tag{53}$$

First we analyze the steady state solution of Eq. (50) to determine the signal response. Let

$$\langle x \rangle = A + \varepsilon B e^{i\delta t} \tag{54}$$

Substitution of Eqs (51), (52), (54) into Eq. (50) and ignoring $O(\varepsilon^2)$ terms yields

$$A = a_0/a_1; \quad B = \left[\frac{b_0 a_1 - b_1 a_0}{a_1^2}\right]\left[1 + \frac{i\delta}{a_1}\right]^{-1} \tag{55}$$

Since B is the signal amplitude gain, the power gain G_s is equal to $|B|^2$. Using Eq. (53), this becomes

$$G_s = \frac{4\mu^2}{\cosh^4(2v\sqrt{\mu})}\left[1+\frac{\delta^2\pi^2}{2\mu^2}\exp(\mu^2)\cosh^2(2v\sqrt{\mu})\right]^{-1} \tag{56}$$

and the phase shift of the signal response is

$$phaseshift = -\arctan(\delta/a_1)$$

In the small signal limit, the response of the system to the signal is a linear amplification of that signal, with the power spectrum being unaffected at other frequencies. Thus we calculate the noise gain with ε set to zero, and Eq. (50) reduces to

$$\langle\dot{x}\rangle = -a_1\langle x\rangle + a_0 \tag{57}$$

In equilibrium, $\langle x\rangle_{eq} = a_0/a_1$ which implies:

$$n_{+eq} = \frac{a_0}{2a_1\sqrt{\mu}} + \frac{1}{2}, \quad n_{-eq} = \frac{1}{2} - \frac{a_0}{2a_1\sqrt{\mu}} \tag{58}$$

When initialized in the state x_+ the solution for $\langle x\rangle$ is:

$$\langle x\rangle_+ = \frac{a_0}{a_1} + (\sqrt{\mu} - \frac{a_0}{a_1})e^{-a_1 t} \qquad t \geq 0 \tag{59}$$

The corresponding $\langle x\rangle_-$ solution is:

$$\langle x\rangle_- = \frac{a_0}{a_1} - (\sqrt{\mu} + \frac{a_0}{a_1})e^{-a_1 t} \qquad t \geq 0 \tag{60}$$

The autocorrelation function is

$$G(\tau) = \langle x(0)x(\tau)\rangle = \sqrt{\mu}(n_{+eq}\langle x\rangle_+ - n_{-eq}\langle x\rangle_-) \tag{61}$$

$$= \left[\frac{a_0}{a_1}\right]^2 + \left[\mu - \left[\frac{a_0}{a_1}\right]^2\right] e^{-a_1|\tau|}$$

The noise power gain G_n is given by the Fourier transform of $G(\tau)$:

$$G_n = \frac{2}{a_1}\left[\mu - \left[\frac{a_0}{a_1}\right]^2\right]\left[1+\frac{\omega^2}{a_1^2}\right]^{-1} \tag{62}$$

or, using Eq. (53),

$$G_n = \frac{\pi\sqrt{2}\exp(\mu^2/2)}{\cosh(2v\sqrt{\mu})}\left[1 + \frac{\pi^2\omega^2}{2\mu^2}\exp(\mu^2)\cosh^2(2v\sqrt{\mu})\right]^{-1} \tag{63}$$

Note that the frequency dependence is the same as for G_s (compare Eq. (56)).

Equations (56) and (63) are the main results of this section. We can extend this analysis to include an approximation for non-telegraph processes. In the $\mu \gg 1$ limit, the noise and signal driven oscillations about a given equilibrium (which we previously ignored) can be determined by a linear analysis. The signal amplitude gain for this effect can be expressed in complex notation as $1/(i\delta+2\mu)$, and should be added to the previous result for the signal amplitude gain Eq. (55). For the noise, the power gain of this effect is the same as for the signal, i.e. $1/(\delta^2+4\mu^2)$ and it should be a good approximation (for high μ) to add this to the expression for G_n calculated in the telegraph approximation. These additional terms are not significant near the maximum gain point for a given detuning. *In fact they could be misleading* as there are other small corrections which have not been included which may be of comparable size. The new terms only become important as μ is increased well beyond the maximum gain point where they fall off much less rapidly with increasing μ than the original expressions.

6 DISCUSSION AND PREDICTIONS

Discussion

Understanding the dynamics near bifurcation points is essential to the theory of parametric amplification since it is only near such points that very high gain levels may be achieved. Fortunately, the dynamics near such points is focussed onto a low dimensional center manifold and can be understood through a relatively simple reduced equation (9). The case studied in this work, where the system is driven by both signal and noise, has been shown to generate a noise rise as one increases the signal gain. The study shows that for sufficiently small signals linear amplification of the signal occurs at all parameter settings in spite of the highly nonlinear processes which lead to the noise rise. Another unexpected result is that gain continues to increase as one passes the bifurcation point ($\mu=0$). This is in contrast to the linearized theory

which says that the gain should be a maximum at $\mu=0$.

In order to clarify the connection between the experimental parameters and those of the theory, we now discuss some procedures by which one might change from one set of parameters to the other. The period doubling (3-photon) and symmetry breaking (6-photon, see Sec. 7) cases are the simplest because here the parameter ν is absent. The parameter μ will be given approximately by a linear transformation of any convenient parameter of the real physical system, i.e. $\mu \approx \gamma(P - P_0)$. Here P is some convenient experimental parameter, P_0 is the bifurcation point, and γ is a scale factor. Both P_0 and γ are initially unknown, and it is typically very hard to calculate these values analytically for a specific equation. However, one can estimate them by fitting experimental data to the numerical results. (Note that the exact location of P_0 will obscured by the presence of noise unless this can be turned off completely.) One approach is to compare the noise rise measured experimentally with the numerical results given in Fig. 8c which plot G_n/G_s vs μ. A few well chosen data points should determine estimates for γ and P_0.

Once μ has been determined, the scaling factor for δ is easily estimated. For example, for fixed μ, one can measure the 3 dB bandwidth of the noise peak and compare this with either the numerical results (Fig. 10), or use the analytic expression (33) to determine δ/Δ. The noise gain G_n will be related by some scale factor to the experimentally measured spectral density, which is easily found once δ and μ are known. The signal gain G_s will be related by yet another scale factor to the measured signal *power* gain. For the present purposes, it is unimportant to determine the relation between ε and the input signal amplitude because the results assume linear signal gain, which occurs for sufficiently small ε. Of course, the reduced equation *is* valid for larger ε, where nonlinear amplification and saturation can be expected, and in this regime this scaling factor is very important.

In the cusp bifurcation (or 4-photon case), two experimental bifurcation parameters P and Q must be used. The choice is somewhat arbitrary – to be determined by the experimenter. Near the cusp point, these will be related to μ and ν by some linear approximation

$$\begin{bmatrix} \mu \\ \nu \end{bmatrix} = \begin{bmatrix} P_\mu & Q_\mu \\ P_\nu & Q_\nu \end{bmatrix} \begin{bmatrix} P - P_0 \\ Q - Q_0 \end{bmatrix}$$

where P_μ, Q_μ, P_ν, Q_ν, P_0 and Q_0 are constants to be determined. There will be a horn shaped region in the (P, Q) parameter space where there exist two different attractors (see Fig. 13). Hysteresis will be observed when traversing the horn. Near the cusp of the horn these attractors will be sufficiently close that we may observe hopping between them, driven by the input noise.

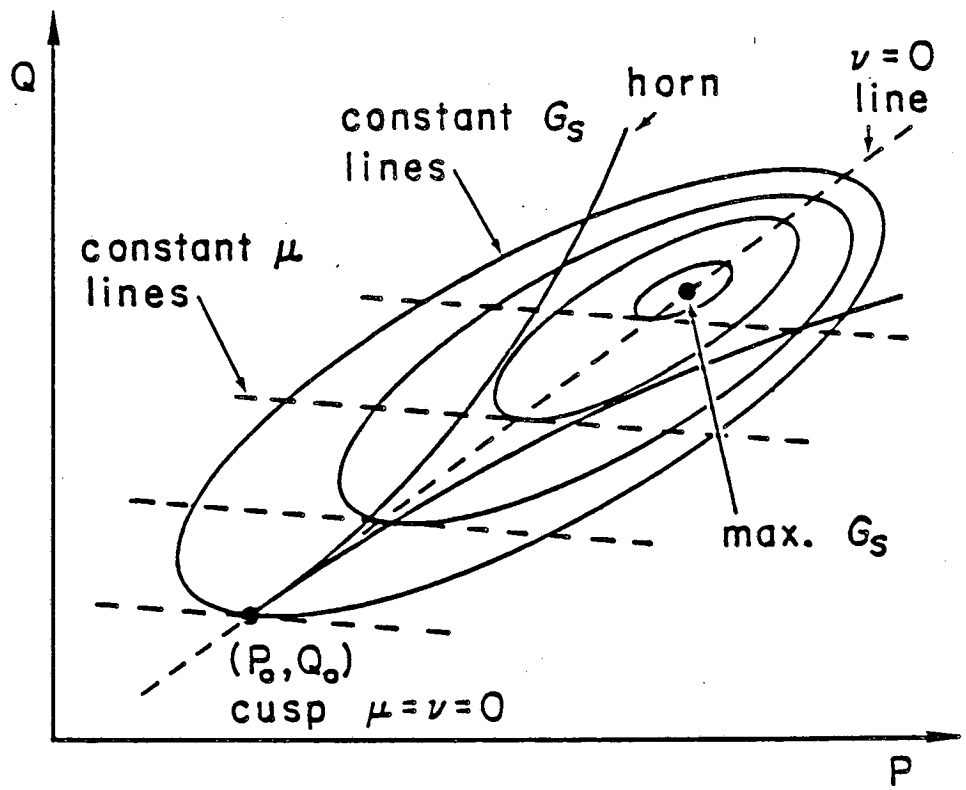

Figure 13. This sketch shows qualitatively the relationship between arbitrary system parameters P and Q and the parameters μ and ν of the reduced equation.

The line in the (P, Q) plane along which equal time on average is spent on each of the attractors corresponds to $\nu=0$. Values of μ along this line may be determined by the method outlined previously. The point (P_0, Q_0) is the cusp of the horn. Its exact location will be obscured by the noise, however, so it must be determined by the process of fitting experimental results with the numerical data. Normally one will not be interested in nonzero values of ν since, as has been shown, the behavior of the amplifier is always inferior. However, if desired, values of ν may be determined as follows: First, plot contours of constant signal gain in the (P, Q) plane. At the crossing point with the $\nu=0$ line, the noise rise should be a minimum (this is another method of locating the $\nu=0$ line). Straight lines tangent to these contours at the crossing points with $\nu=0$ are (in linear approximation) lines of constant μ. Values of ν along these lines may be determined by comparison of the behavior with the analytic formulas.

It is important to remember that the theory is based on certain limiting approximations. Specifically, to obtain the reduced equation we assume that the perturbation (signal and noise) is small, that the detuning is small, and that the system is close to the bifurcation point. For all results presented in this paper, it is further assumed that the signal is small relative to the noise in the sense that the telegraph or switching process is primarily noise driven. While $\varepsilon\cos\delta t$ is positive there will be a slight preference to the "+" state over the "-" state. However this effect should be small (say up to 10% shift in the mean lifetimes of these two states) because otherwise the signal gain will start to become nonlinear and deviations from the theory presented here may be expected. Another important consideration is the possibility of higher order degeneracies. For example, the cubic term in the reduced equation might vanish for some combination of parameters. This would then have to be replaced by the next nonzero term (typically x^5) which we have been neglecting. It is quite possible that the dynamics in this case would be improved in regard to maximum achievable signal gain, and therefore the experimenter in trying to optimize the amplifier performance might be drawn towards a degenerate operating point where some deviations from the theory presented here might again be expected.

We emphasize that the dynamics in the switching regime is very sensitive to the level of input noise. We have used the term "noise gain" or G_n in numerous places in the text, but this is *not* a linear gain and thus quite different behavior can be expected when the input noise level is changed. In fact, all of the scaling factors relating the experimental parameters to those of the reduced equation will change when the input noise level is changed. This rescaling can be determined quite precisely and is the same as the rescaling used at the end of Sec. 3 (Eq. (20)).

As was pointed out in Sec. 3, amplification will occur when the signal is slightly detuned from one of a discrete set of "resonant" frequencies. Furthermore, the response to the signal will have components near each of these frequencies. For the 3-photon or period doubling mode, these frequencies are $n\omega_p/2$ where n is odd. For the 4-photon or cusp mode these are $n\omega_p$. (However, this mode can occur for a symmetrical oscillation in which case n must be odd, i.e. if $\Phi(t)$ shows no even harmonics of ω_p near the bifurcation point then the restriction applies.) For the symmetry breaking bifurcation the frequencies are $2n\omega_p$. In addition, the case $n=0$ is suppressed in the driven pendulum (Josephson model) in cases where $\phi(t)$ is phase locked with the pump. This is because the junction voltage V_J is proportional to $d\phi/dt$ and hence V_J has an invariant constant component (the phase ϕ itself is not an observable dynamical variable).

The optimal operating frequency will be the one for which $\Phi_1(t)$ and $g(t)$ (defined in Sec. 3) have the largest components. This will usually be the lowest allowed frequency – i.e. $\omega_p/2$ for period doubling, ω_p for cusp, and $2\omega_p$ for symmetry breaking. Operation at the higher harmonics will usually result in a worsened signal-to-noise ratio. Frequency conversion is possible, i.e. a response at $\omega_p/2$ will result from a signal at $3\omega_p/2$ in the period doubling mode. If one does not want a response to these frequencies, care must be taken to filter them out of the signal before it reaches the device. In cases where $n=0$ is suppressed, it is not possible to use these devices as "detectors" i.e. to produce a low frequency response (near zero) to a high fre-

quency signal. In other cases, however, it is possible to combine the amplification and detection of a high frequency signal.

The mechanism of the noise rise we have been discussing occurs over a relatively short interval in parameter space – near the bifurcation point. However, when parameters are varied by more substantial amounts there are other sources of noise rise which are important. One of these, which we refer to as "idler noise" results from the emergence of an idler frequency as the bifurcation point approached. Noise frequencies near the idler can produce a response near the signal. This effectively doubles the power spectral density of the noise. Thus the emergence of the idler peak will result in a 3 dB noise rise. A similar effect – "harmonic noise" – results from conversion of noise near the other harmonics of the fundamental resonant frequency to a response near the signal frequency. This effect will usually be fairly small when operating near the fundamental frequency. Finally, an effect which is often overlooked is that signal and noise may be coupled to the amplifier in different ways. Substantial changes in operating point may then cause differing changes in gain for signal and noise. *This effect can be very large, easily amounting to 10 dB or more of noise rise.*

Predictions

In a previous work[34] A number of predictions were made which could be tested in an experimental system. These will now be discussed in greater detail:

(1) For $\mu<0$ the noise temperature is essentially constant (i.e. no noise rise), even as G_s increases. This statement is based on the numerical results. It is not precisely true in a mathematical sense – in fact the numerical study *did* show a noise rise at $\mu=0$, but it was only 0.4 dB, and therefore negligible for most practical applications. The result is not surprising since a linearized analysis (valid for large negative μ) results in *no* noise rise.

(2) For $\mu>0$ (and nonzero detuning), there exists a μ of maximum signal gain, μ', while the noise gain at the signal frequency also reaches a maximum which is beyond μ' (this behavior is

clearly shown in the numerical results). Moreover, μ' increases either with increasing noise input or decreasing detuning. The effect of changing the noise input can be determined from the rescaling given in Sec. 3 Eq. (20), while the effect of changing the detuning is evident from the numerical results – see Fig. 8.

(3) The noise rise is insensitive to changes in detuning – both G_n and G_s fall off initially in the same way as the detuning is increased from zero. The analytic result Eq. (27) shows this is exactly true for high μ values. For sufficiently large δ, however, the noise rise must fall off – when δ is much greater than the average hopping rate, $1/\tau$, a linearized treatment becomes possible which yields no noise rise.

(4) For sufficiently small detuning and large negative μ we find $G_s \propto G_n \propto \mu^{-2}$ (this follows from Eq. (23)), while for large positive μ and (ν=0) the behavior is $G_s \propto \ln G_n + \text{const} \propto \mu^2$ (this follows from the analytic results for the switching regime, Eqs. (28) and (29)). Furthermore G_s and G_n increase monotonically with μ including in the crossover region near μ=0. This result was obtained from the numerical data – it has not been rigorously proven. Note that for any nonzero detuning G_s and G_n reach maximum values as discussed in prediction (2).

(5) The bandwidth BW over which the gain indicated in (4) may be achieved is proportional to $|\mu|$ for large negative μ and to $\mu\exp(-k\mu^2)$ for large positive μ where k is a positive constant (these follow from Eqs. (23) and (33) respectively). Thus we cross over from a region of constant gain-bandwidth product $G_s^{1/2}BW$ to one which rapidly diminishes and may explain the unexpectedly small values for this product previously reported for the Josephson devices.[10] (Note that $G_s^{1/2}$ is the signal *amplitude* gain.) This effect is easily seen in Fig. 10 from the numerical study.

(6) A variety of theoretical curves have been generated numerically and were presented in Sec. 4. Through the use of appropriate scaling factors experimental data may be compared graphically with the theoretical model.

7 SIX-PHOTON MODE AND SEMICONDUCTOR LASERS

As has been emphasized, the results presented above are based on quite general dynamical arguments: the underlying physical details of the amplifying system are unimportant, the crucial element being the type of dynamical instability involved. This fact leads us, in this section, to go beyond the immediate subject of noise rise in 3- and 4-photon Josephson junction parametric amplifiers. We first examine the possibility of a "6-photon mode" that ought to occur in unbiased Josephson junction parametric amplifiers. Although this mode also displays a noise rise, it may have certain advantages over the 3- and 4-photon modes. We then discuss a semiconductor laser parametric amplifier which, though a very different physical system, should also display the noise rise. As we discuss below, the semiconductor system may be a good experimental system to test the predictions of Sec. 6.

Amplification in the Six-photon Mode

The occurrance of a period doubling bifurcation allows amplification in the 3-photon mode, while the saddle-node (and cusp) allows operation in the 4-photon mode. However, there is a third kind of simple bifurcation the Josephson junction parametric amplifier can suffer, which has associated with it a third mode of operation. This is the *symmetry breaking* (or *pitch-fork*) bifurcation, which can occur in certain parameter regimes of the unbiased system ($A = 0$ in Eq. (1)).[29,11]

A discussion of the small-system amplification properties near the onset of a symmetry breaking bifurcation is presented in Ref.26. The basic features are as follows. The experimental signature of this instability is the onset of power at even multiples of the pump frequency ω_p (Figure 14). Near this instability, high gain can be achieved for signals $\omega_s \approx 2\omega_p$. The idler ω_i will also appear near $2\omega_p$, so that $\omega_s + \omega_i = 4\omega_p$; keeping with previous nomenclature this

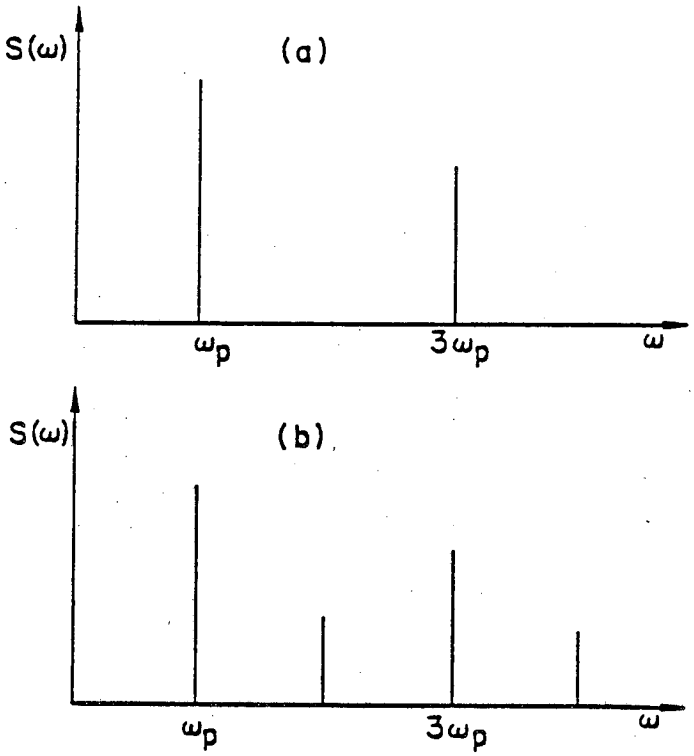

Figure 14. Signature of symmetry-breaking bifurcation. (a) below bifurcation, odd harmonics only. (b) above bifurcation, even harmonics appear.

would be called a 6-photon mode.

It appears that experiments have never tried to operate in this mode, although it should be possible: symmetry breaking for Eq. (1) has been reported in analog and digital simulations,[28, 29, 12] and has been suggested as well by the analytic work of Levinsen.[11] Aside from its novelty, this mode may have desirable characteristics: since gain is achieved near twice the pump frequency, this mode operates at higher frequencies than the other modes; as an unbiased mode, it does not require contacts needed to supply the dc voltage; since ω_s is not near ω_p, it is easier to separate the signal output from the pump-frequency output. There is also no hysteresis associated with the symmetry breaking bifurcation. Whether these advantages are realized in a practical sense is an open question, and must await actual experiments.

In any event, the 6-photon mode also displays a noise rise. The appropriate normal form equation is the same as for the period doubling case, Eq. (8), but now the decomposition Eq. (7) involves functions Φ_0 and Φ_1 such that

$$\Phi_0(t+\frac{\pi}{\omega_p}) = -\Phi_0(t) \; ; \quad \Phi_1(t+\frac{\pi}{\omega_p}) = +\Phi_1(t) \tag{64}$$

and the detuning Δ is defined by

$$\Delta = \omega_s - 2\omega_p \tag{65}$$

Moreover, the reduced Eq. (8) is now the continuous-time limit of the *first* iterate of the Poincaré return map, while it corresponded to the second iterate in the 3-photon case.

With the appropriate interpretations (64) and (65), all of the results for the noise rise in the 3-photon case go through. For example, the noise rise illustrated in Figure 7 will be seen in the 6-photon mode, with zero frequency in Figure 7 corresponding to $2\omega_p$ in the full system's power spectrum.

Noise-Rise in Modulated Semiconductor Injection Lasers

In 1976, Grothe et al. demonstrated experimentally that a semiconductor laser, pumped by an injection current modulated at 9 GHz, could act as a small-signal parametric amplifier.[35] They called this behavior "parametric sideband amplification", an effect which has been predicted theoretically.[36] It was shown later that the experimental parameter values which yielded high gain nearly coincided with those for the onset of a period doubling bifurcation.[37] (The amplifier operated in the 3-photon mode.)

The basic idea of the semiconductor injection laser is depicted in Figure 15. By injecting, say, holes across a p-n junction, one can induce electron-hole recombinations. There is a threshold dc injection current beyond which *stimulated recombination* produces strong coherent radiation. (The cleaved surfaces at either end act as reflective "mirrors" in analogy with gas lasers.) In the modulated injection laser, the injected current has a small ac component in

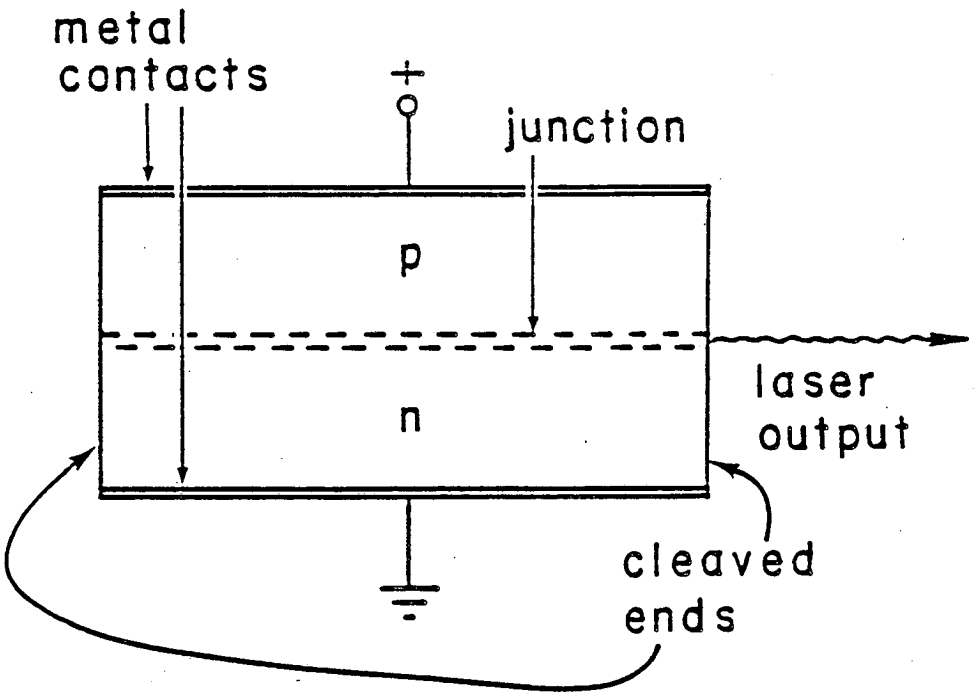

Figure 15. Semiconductor injection laser.

addition to a large dc component. As in gas lasers, varying the parameter values leads to instabilities in the output light intensity, $I(t)$. (The variations in $I(t)$ are at much lower frequencies – typically GHz – than the optical radiation frequencies, allowing for a semiclassical rate-equation description of the dynamics.) A variety of bifurcations have been documented for injection lasers,[38-40] including the period doubling essential to the parametric amplification experiment of Grothe et al.

It appears that this so-called parametric sideband amplification has not been pursued beyond the original experiments a decade ago. In the present context, it may be a good system to re-examine, for two reasons. First of all, it can test whether the noise rise occurs in systems other than the Josephson junction amplifiers: as a high frequency device, it should be possible to achieve small detunings, enhancing the range over which a noise rise might be observed.

Second, the semiconductor device has the technical advantage of not requiring low temperatures, so the experiments may be relatively inexpensive to perform.

8 CONCLUSION

It has been shown how the presence of external noise can be responsible for the "anamolous" noise rise observed in Josephson junction parametric amplifiers. The essence of the theory is the synthesis of two observations: (1) the high-gain limit of a parametric amplifier coincides with the onset of a dynamical instability, and (2) it is precisely near such bifurcation points that the effective phase space dimension is drastically reduced. This last fact implies that certain "universal" behavior is expected for parametric amplifiers of all kinds; the appropriate universality class depends only on the kind of bifurcation involved. The familiar 3- and 4-photon modes correspond to period doubling and cusp bifurcations, respectively, while the newly proposed 6-photon mode corresponds to a symmetry-breaking bifurcation. In all cases the noise rise phenomenon is found to occur as the result of noise-induced switching: in the 3-photon mode the switching occurs between branches of a single phase space attractor, while the 4- and 6-photon modes display switching behind coexisting multiple attractors.

The regime studied was that of weak signal and relatively strong noise. Weak signal implies that the system response at the signal frequency is a *linear* function of input signal, while "strong noise" simply means that the random perturbations are sufficiently large to excite a *nonlinear* dynamical response. That this is the relevant noise regime in the Josephson junction experiments is supported by a recent paper[25] which demonstrates that the experimental noise level is sufficient to wash out the distinctly nonlinear phenomenon of period-doubling suppression.[23]

The powerful tools of bifurcation theory – in particular the center manifold construction – allowed us to reduce the full dynamical system to the study of the appropriate first order nonlinear equation. Except in certain limiting cases, the solution of the reduced equations required digital and analog simulations. Together with the analytic results presented in Sec. 5, this analysis leads to a number of predictions which can be readily tested by future parametric amplifier experiments, using either Josephson junctions, semiconductor lasers, or other devices.

Whether or not the theory presented underlies previous noise rise observations must be determined by future experiments – for this reason, the predictive nature of the theory has been emphasized. Since the noise rise phenomenon appears to be a universal property (in the small-detuning limit), there is no simple prescription for avoiding this undesirable characteristic. Nevertheless, dynamical systems theory provides invaluable insights into understanding the optimally achievable performance of parametric amplifiers.

APPENDIX

Accurate determination of power spectral density in a numerical simulation typically requires a great deal of processor time because the stochastic fluctuations can only be averaged out by using a large amount of data. However, our particular problem has certain characteristics and symmetries which allow significant improvement over the standard approach. In general, to calculate the spectral density $S(\omega)$ at a particular frequency ω we may evaluate

$$2\pi S(\omega) = \lim_{T\to\infty} \frac{1}{T} < \left| \int_0^T x(t) e^{-i\omega t}\, dt \right|^2 >_{ensemble} \tag{66}$$

Thus to approximate $S(\omega)$ we must integrate an ensemble of data sets over a long time T. The accuracy of the result is proportional to $1/\sqrt{K}$, where K is the number of elements in the ensemble. One cannot obtain an accurate result without the ensemble average regardless of

how large T is – the error will always be of the same order as the measurement. This is because the distribution of $\int_0^T x(t)e^{-i\omega t}\,dt$ for the ensemble is a Gaussian in the complex plane, centered on zero. Thus the ensemble average measures the *variance* of this distribution. To achieve 1% accuracy on this measurement we need $K \approx 10000$. Once this has been realized, we see that the way to improve efficiency is through reduction of the time T. As we will now show, if the time intervals are properly chosen, substantial improvement is possible.

The key is to break up the time sequence for each ensemble element into a series of intervals each of which starts and ends at $x=0$ (these intervals may have different lengths of course). To avoid the complication of having very short intervals we require that $|x|$ be greater than some threshold value at some point during each interval. Let t_n be the interval endpoints, and define Y_n as:

$$Y_n = \int_{t_n}^{t_{n+1}} x(t)e^{-i\omega(t-t_n)}dt \tag{67}$$

In terms of the Y_n's, we find

$$2\pi S(\omega) = \lim_{T\to\infty}\frac{1}{T}<\left|\sum_n Y_n e^{-i\omega t_n}dt\right|^2> \tag{68}$$

$$= \lim_{T\to\infty}\frac{1}{T}\sum_{m,n}<Y_n Y_m^* e^{-i\omega(t_n-t_m)}>$$

since each interval is chosen by the same criteria and since each starts in the same state ($x=0$) we can expect the Y_n's to be uncorrelated. (This assumes that the signal is very small and can be neglected when calculating the noise response.) However, there may be a correlation between Y_n and τ_n, where $\tau_n \equiv t_{n+1}-t_n$. Thus we may write:

$$2\pi S(\omega) = \lim_{T\to\infty}\frac{1}{T}\{\sum_n<|Y_n|^2> \tag{69}$$

$$+\sum_{m>n}<Y_n e^{+i\omega\tau_n}><Y_m^*><e^{+i\omega(t_m-t_{n+1})}>$$

$$+\sum_{m<n}<Y_n><Y_m^* e^{-i\omega\tau_m}><e^{-i\omega(t_n-t_{m+1})}>\}$$

We can now use the symmetry of our system to simplify this expression. For the v=0 case, Eq.

(9) has inversion symmetry. Recall that nonzero values of ν are permitted only for the cusp bifurcation (4-photon mode) and in this case nonzero values are of little interest since they produce inferior amplifier performance. This symmetry combined with the symmetrical nature of our interval selection scheme has the important consequence that $<Y_n>=0$. Thus the last two terms drop out of Eq. (69) leaving:

$$2\pi S(\omega) = \lim_{T\to\infty} \frac{1}{T} \sum_n <|Y_n|^2> \tag{70}$$

What we have accomplished is to divide each element in the ensemble into a large number of sub-elements. Now it is the total number of these sub-elements which will determine the overall accuracy of the measurement. All of the sub-elements are equivalent regardless of which primary element they belong to. Thus we may write:

$$2\pi S(\omega) = \frac{1}{\sum_n \tau_n} \sum_n |Y_n|^2 \tag{71}$$

To achieve 1% accuracy we need 10000 intervals but the average length of these intervals is much shorter than would normally be possible for direct evaluation of Eq. (66), resulting in a significant improvement in efficiency. Note: since the applied noise has unit delta autocorrelation, the noise gain G_n is given by $2\pi S(\omega)$.

REFERENCES

1. M.J. Feldman, P.T. Parrish, and R. Y. Chiao, *J. Appl. Phys.* 46 p. 4031 (1975).
2. Y. Taur and P. L. Richards, *J. Appl. Phys.* 48 p. 1321 (1977).
3. O. H. Soerensen, J. Mygind, and N. F. Pedersen, *AIP Conf. Proc.* 44 p. 246 (1978).
4. J. Mygind, N. F. Pedersen, and O. H. Soerensen, *Appl. Phys. Lett.* 32 p. 70 (1978).
5. S. Wahlstein, S. Rudner, and T. Claeson, *J. Appl. Phys.* 49 p. 4248 (1978).
6. J. Mygind, N. F. Pedersen, O. H. Soerensen, B. Dueholm, and M. T. Levinsen, *Appl. Phys. Lett.* 35 p. 91 (1979).
7. R. Y. Chiao, M. J. Feldman, D. W. Peterson, B. A. Tucker, and M. T. Levinsen, *AIP Conf. Proc.* 44 p. 259 (1978).
8. M. J. Feldman, *J. Appl. Phys.* 48 p. 1301 (1977).
9. M. J. Feldman and M. T. Levinsen, *Appl. Phys. Lett.* 36 p. 854 (1980).
10. M. J. Feldman and M. T. Levinsen, *IEEE Trans. Magn.* MAG-17 p. 834 (1981).
11. M. T. Levinsen, *J. Appl. Phys.* 53 p. 4294 (1982).
12. B. A. Huberman, J. P. Crutchfield, and N. H. Packard, *Appl. Phys. Lett.* 37 p. 750 (1980).
13. N. F. Pedersen and A. Davidson, *Appl. Phys. Lett.* 39 p. 830 (1981).
14. R. F. Miracky and J. Clarke, *Appl. Phys. Lett.* 43 p. 508 (1983).
15. K. Wiesenfeld and B. McNamara, *Phys. Rev. Lett.* 55 p. 13 (1985).
16. B. Derighetti, M. Ravani, R. Stoop, P. F. Meier, E. Brun, and R. Badii, *Phys. Rev. Lett.* 55 p. 1746 (1985).
17. J. Heldstab, H. Thomas, T. Geisel, and B. Radons, *Z. Phys. B* 50 p. 141 (1983).
18. S. Martin and W. Martienssen, *Phys. Rev. A* 34 p. 4523 (1986).
19. P. Pieranski and J. Malecki, *Phys. Rev. A* 34 p. 582 (1986).
20. K. Wiesenfeld and N. B. Tufillaro, *Physica D*, (to appear).
21. N. F. Pedersen, M. R. Samuelsen, and K. Saermark, *J. Appl. Phys.* 44 p. 5120 (1973).
22. O. H. Soerensen, B. Dueholm, J. Mygind, and N. F. Pedersen, *J. Appl. Phys.* 51 p. 5483 (1980).
23. P. Bryant and K. Wiesenfeld, *Phys. Rev. A* 33 p. 2525 (1986).
24. H. Savage and C. Adler, unpublished.
25. H. Svensmark, J. B. Hansen, and N. F. Pedersen, *Phys Rev A* 35 p. 1457 (1987).
26. K. Wiesenfeld and B. McNamara, *Phys. Rev. A* 33 p. 629 (1986).
27. J. Guckenheimer and P. Holmes, *Nonlinear Oscillations, Dynamical Systems, and Bifurcations of Vector Fields*, Springer, New York (1983).
28. B. A. Huberman and J. P. Crutchfield, *Phys. Rev. Lett.* 43 p. 1743 (1979).
29. D. D'Humieres, M. R. Beasley, B. A. Huberman, and A. Libchaber, *Phys. Rev. A* 26 p. 3438 (1982).
30. K. Wiesenfeld, *J. Stat. Phys.* 38 p. 1071 (1985).

31. C. D. Jeffries and K. Wiesenfeld, *Phys. Rev. A* **31** p. 1077 (1985).
32. S. O. Rice, *Bell Syst. Tech. J.* **23** p. 282 (1944).
33. S. Machlup, *J. Appl. Phys.* **25** p. 341 (1954).
34. P. Bryant, K. Wiesenfeld, and B. McNamara, *Phys. Rev. B*, (to appear).
35. H. Grothe, W. Harth, and P. Russer, *Electron. Lett.* **12** p. 522 (1976).
36. P. Russer, H. Hillbrand, and W. Harth, *Electron. Lett.* **11** p. 87 (1975).
37. K. Wiesenfeld, *Phys. Rev. A* **33** p. 4026 (1986).
38. G. Arnold and P. Russer, *Appl. Phys.* **14** p. 255 (1977).
39. D. Siemsen, *Int. J. Electronics* **45** p. 63 (1978).
40. C.-H. Lee, T.-H. Yoon, and S.-Y. Shin, *Appl. Phys. Lett.* **46** p. 95 (1985).

LAWRENCE BERKELEY LABORATORY
TECHNICAL INFORMATION DEPARTMENT
UNIVERSITY OF CALIFORNIA
BERKELEY, CALIFORNIA 94720